# DESIGN AND PERFORMANCE ANALYSIS OF NEXT GENERATION HETEROGENEOUS CELLULAR NETWORKS FOR THE INTERNET OF THINGS

**Hazem Mohamed Saad Ibrahim**

A DISSERTATION SUBMITTED TO THE FACULTY OF GRADUATE STUDIES IN PARTIAL FULFILMENT OF THE REQUIREMENTS FOR THE DEGREE OF

DOCTOR OF PHILOSOPHY

GRADUATE PROGRAM IN DEPARTMENT OF ELECTRICAL
ENGINEERING AND COMPUTER SCIENCE
YORK UNIVERSITY
TORONTO, ONTARIO

November 2019

# Abstract

The Internet of Things (IoT) is a system of inter-connected computing devices, objects and mechanical and digital machines, and the communications between these devices/objects and other Internet-enabled systems. Scalable, reliable, and energy-efficient IoT connectivity will bring huge benefits to the society, especially in transportation, connected self-driving vehicles, healthcare, education, smart cities, and smart industries.

Multi-tier heterogeneous cellular networks have been a key technology in the development and implementation of the IoT. In this dissertation, we study heterogeneous cellular networks that are composed of two tiers: Tier 1 consists of macro base stations (MBSs) with higher transmission power and lower deployment density. Tier 2 consists of small base stations (SBSs) with lower transmission power and higher density deployment. SBSs are also termed *aggregators* in the context of several IoT applications that involve heavy data traffic in the uplink direction from devices to the core network.

The objective of this dissertation is to model and analyze the performance of large-scale heterogeneous two-tier IoT cellular networks, and offer design insights to maximize their performance. Using stochastic geometry, we develop realistic yet tractable models to study the performance of such networks. In particular, we propose solutions to the following research problems:

- We propose a novel analytical model to estimate the mean uplink device data rate utility function under both spectrum allocation schemes, full spectrum reuse (FSR) and orthogonal spectrum partition (OSP), for uplink two-hop IoT networks. The model takes into account the aggregator spatial density, aggregator association bias and spectrum partition ratio across the MBS tier and the aggregator tier, and device and aggregator power control fractionals (PCFs). We develop constraint gradient ascent optimization algorithms to obtain the optimal aggregator association bias (for the FSR scheme) and the optimal joint spectrum partition ratio and optimal aggregator association bias (for the OSP scheme).

- We study the performance of two-tier IoT cellular networks in which one tier operates in the traditional sub-6GHz spectrum and the other, in the millimeter wave (mm-wave) spectrum. In particular, we characterize the meta distributions of the downlink signal-to-interference ratio (sub-6GHz spectrum), the signal-to-noise ratio (mm-wave spectrum) and the data rate of a typical device in such a hybrid spectrum network. We characterize the conditional success probability (CSP) and its $b^{\text{th}}$ moment for (1) a typical device when it associates with a sub-6GHz MBS (direct transmission), (2) a typical device when it associates with a mm-wave SBS (access transmission), and (3) the tagged SBS when it associates with a sub-6GHz MBS (backhaul transmission). Finally, we characterize the meta distributions of the SIR/SNR and data rate of a typical device by substituting the cumulative moment of the CSP of a user device into the Gil-Pelaez inversion theorem.

- We propose to split the control plane (C-plane) and user plane (U-plane) as a potential solution to harvest densification gain in heterogeneous two-tier networks while minimizing the handover rate and network control overhead. We develop a tractable mobility-aware model for a two-tier downlink cellular network with high density small cells and a C-plane/U-plane split architecture. The developed model is then used to quantify the effect of mobility on the foreseen densification gain with and without C-plane/U-plane splitting.

# Acknowledgments

First and foremost, I thank “Allah” for giving me the patience, strength, and confidence to complete my doctoral studies.

I have to start by thanking my PhD supervisor Prof. Uyen Trang Nguyen, for her patient guidance, constant encouragement, and excellent advice throughout my PhD study. Without her invaluable help, encouragement, and experience this work would not be possible.

I would like to express my sincere appreciations to my supervisory committee members, Prof. Andrew Eckford and Prof. Hina Tabassum for their great personality, insightful comments, friendly advice and valuable guidance. I wish to thank my thesis defense committee members, Prof. Sebastian Magierowski, Prof. Xavier Fernando, and Prof. Regina Lee for accepting to be members of the committee. Their thoughtful comments and insight during the defense have resulted in a manuscript that is clearer, more compelling, and much improved.

I would like to thank Prof. Hina Tabassum for her collaboration on developing Chapter 4. I really learnt a lot from her technical skills. Her suggestions significantly improved the quality of Chapter 4.

Finally, I take this opportunity to express my profound gratitude to my beloved mother, Sayda Wahbi, my father, Mohamed Saad Ibrahim, for endless encouraging, understanding, support, and endless love during my study. To you I dedicate this thesis. My special thanks go to my dear wife, Eman Mohamed. Through your love, patience, support, and unwavering belief in me, I’ve been able to complete my long PhD journey. Lastly, I would like to thank my new born baby “Yoseph Hazem Ibrahim” who was born while I am writing this thesis. I love you so much.

# Table of Contents

# List of Tables

# List of Figures

# List of Symbols

| | |
|---|---|
| $\setminus$ | set exclusion operator |
| $\lambda$ | node density |
| $\mathbf{\Phi}$ | point process |
| $\epsilon$ | uplink power control fractional |
| $B$ | device association bias |
| $P$ | node power transmission |
| $\alpha$ | path loss exponent |
| $\mathbb{P}(.)$ | probability measure |
| $\mathcal{A}$ | association probability |
| $W$ | spectrum bandwidth |
| $\mathbb{E}_X(.)$ | expectation operator with respect to X |
| $\mathbb{1}(.)$ | indicator function |
| $j$ | imaginary number $\sqrt{-1}$ |
| $\Im(w)$ | imaginary part |
| $\min(.,.)$ | the minimum value |
| $\lfloor . \rfloor$ | floor function |
| $\mathbf{dom}(.)$ | domain of function |
| $\nabla U(\mathbf{Q})$ | gradient of $U$ in direction of $Q$ |
| $\Delta\eta$ | finite difference displacement in direction of $\eta$ |
| $\lVert . \rVert$ | Euclidean norm distance |
| ${}_2F_1(.,.;.;.)$ | Gauss Hyper-geometric function |

| | |
|---|---|
| $\mathcal{V}$ | mobile device velocity |
| $HO_{ij}^{(c)}$ | mean number of handovers per unit length from tier $i$ to $j$ for conventional network |
| $MHO^{(s)}$ | mean number of inter-anchor handovers per unit length for CP/UP split network |
| $VHO^{(s)}$ | mean number of intra-anchor handovers per unit length for CP/UP split network |
| $\mu_{\mathbf{C}}$ | control data overhead fraction in overall network capacity |
| $\theta$ | predefined threshold for correct signal reception |
| $D_{HO}^{(c)}$ | handover cost in conventional network |
| $D_{HO}^{(s)}$ | handover cost in CP/UP split network |
| $\mathcal{X}$ | probability of having X2 interface in conventional architecture handovers. |
| $\mathcal{Z}$ | probability of having X2 interface in CP/UP split architecture handovers |
| $d^{(c)}$ | delay per non X2 handover in conventional network |
| $\tilde{d}^{(c)}$ | delay per X2 handover in conventional network |
| $d_m^{(s)}$ | inter-anchor handover delay without X2 interface |
| $\tilde{d}_m^{(s)}$ | inter-anchor handover delay with X2 handover in CP/UP split network |
| $d_v^{(s)}$ | intra-anchor handover delay for CP/UP split network |
| $AT^{(c)}$ | average per-device throughput in the conventional network |
| $AT^{(s)}$ | average per-device throughput in CP/UP split network |
| $\mathcal{A}_j$ | association probability of a typical device $\mathcal{U}_j$ |
| $\mathcal{T}_j^{(c)}$ | BS throughput in each association state category for conventional network |
| $\mathcal{T}_j^{(s)}$ | BS throughput in each association state category for CP/UP split network |
| $\mathcal{SE}^{(c)}$ | spectral efficiency for conventional network |
| $\mathcal{SE}^{(s)}$ | spectral efficiency for CP/UP split network |
| $\bar{F}_{P_s}(x)$ | the meta distribution of SIR |
| $p_L$ | mm-wave blockage LOS probability |
| $p_N$ | mm-wave blockage NLOS probability |
| $P_s(\theta)$ | conditional success probability (CSP) |
| $M_b$ | the $b^{th}$ moment of $P_s(\theta)$ |
| $m_l$ | Nakagami-m fading parameter where $l \in \{L, N\}$ denotes LOS and NLOS links |

|  |  |
|---|---|
| $h_l$ | Gamma fading channel gain for mm-wave SBSs |
| $\alpha_{2,L}$ | path loss exponent of LOS SBS |
| $\alpha_{2,N}$ | path loss exponent of NLOS SBS |
| $G_1^o$ | $\mu$wave MBSs omnidirectional antenna gain |
| $G_2^{max}$ | main lobe gain for mm-wave SBS |
| $G_2^{min}$ | side lobe gain for mm-wave SBS |
| $\theta_a$ | 3 dB beamwidth for mm-wave SBS |
| $\mathcal{N}$ | number of elements in square antenna array |

# List of Abbreviations

| | |
|---|---|
| AWGN | additive white Gaussian noise |
| BPP | binomial point process |
| BSs | base stations |
| cMTC | mission-critical machine-type communication |
| C-RAN | cloud radio access network |
| CDF | cumulative distribution function |
| CSP | conditional success probability |
| C-plane | control plane |
| DRUF | data rate utility function |
| D2D | device to device |
| FSR | full spectrum reuse |
| HCPP | hard core point process |
| IoT | internet of things |
| IoE | internet of everything |
| i.i.d. | independently and identically distributed |
| LOS | line-of-sight |
| mMTC | massive machine-type communication |
| mm-wave | millimetre wave |
| MBSs | macro base stations |
| MIMO | multiple-input and multiple-output |
| MAC | medium access control |

| | |
|---|---|
| Mbps | megabits per second |
| NLOS | non-line-of-sight |
| OSP | orthogonal spectrum partition |
| PCF | power control fraction |
| PP | point process |
| PDF | probability density function |
| PPPs | poisson point processes |
| PCP | poisson cluster process |
| PMF | probability mass function |
| QoS | quality-of-service |
| RAN | radio access network |
| SIR | signal-to-interference ratio |
| SINR | signal-to-interference and noise ratio |
| SNR | signal-to-noise ratio |
| SBSs | small base stations |
| U-plane | user plane |
| $\mu$wave | microwave |
| 4G | fourth generation of wireless mobile communications |
| 5G | fifth generation of wireless mobile communications |

# Publications from the Dissertation

Peer-reviewed Journal Papers:

[**J1**] Hazem Ibrahim, Hina Tabassum, and Uyen T. Nguyen, "The Meta Distributions of the SIR/SNR and Data Rate in Coexisting Sub-6GHz and Millimeter-wave Cellular Networks," *IEEE Transactions on Wireless Communications , 2019.* [Submitted, under review]. [Impact Factor: 6.394]

[**J2**] Hazem Ibrahim, Wei Bao, Uyen T. Nguyen, "Data Rate Utility Analysis for Uplink Two-Hop Internet-of-Things Networks.". *IEEE Internet of Things Journal, 24 December, 2018.* [Impact Factor: 9.515]

[**J3**] Hazem Ibrahim, Hesham ElSawy, Uyen T. Nguyen, and Mohamed-Slim Alouini, "Mobility-Aware Modeling and Analysis of Dense Cellular Networks with C-plane/U-plane Split Architecture", *Volume: 64 , Issue: 11 , Nov. 2016, IEEE Transactions on Communications.* [Impact Factor: 5.69]

Peer-reviewed Conference Papers:

[**C1**] Hazem Ibrahim, Hina Tabassum, and Uyen T. Nguyen, "Meta Distribution of SIR in Dual-Hop Internet-of-Things (IoT) Networks, "*IEEE International Conference on Communications (ICC) 2019, Shanghai, China.*

[**C2**] Hazem Ibrahim, Hesham ElSawy, Uyen T. Nguyen, and Mohamed-Slim Alouini. "Modeling virtualized downlink cellular networks with ultra-dense small cells", *IEEE International Conference on Communications (ICC) 2015, London, England.*

# Chapter 1

# INTRODUCTION

## 1.1 Introduction

The Internet of Things (IoT) is defined as the ever-growing network of smart physical objects and devices that are capable of sensing and acting on their environment, and the communications between these devices and other Internet-enabled systems. The IoT is growing so fast such that every object or device eventually needs a connection to the Internet. The IoT enables smart devices to be more actively involved in people's everyday life, industry, business, healthcare, and transportation.

IoT networks will connect washing machines, smoke detectors, fridges, farm animal sensors, fleets of cars, fitness bands, thermostats, smart watches, sleep monitors, garbage bins and street lights with sensors for monitoring traffic, air pollution, noise and parking. Hence, it will result in a more intelligent *connected society* and that creates *smart cities*.

Everyone, from consumers to large corporate companies, is embracing the changes brought by the revolutionary IoT. It has changed the world in more ways than we could imagine until a few years ago. Already the numbers are staggering: billions of sensors connected with billions of devices are redefining almost everything in our daily life. It is estimated that around 75 billion devices will be interconnected by 2025 [1].

Due to the ever increasing number of devices and thus network traffic demands, several trends have emerged in future cellular networks such as network densification, heterogeneous multi-tier networks, and the use of the millimeter-wave spectrum to complement the traditional sub-6GHz spectrum.

State-of-the-art 5G networks are expected to achieve thousandfold capacity improvements with at least hundredfold increases in data rates and one order of magnitude delay reduction [2]. Network densification, via deployment of small base stations (SBSs), is among the key solutions to achieve this ambitious performance goal in 5G cellular networks [2]. Network densification via deployments of SBSs is preferred over deployments of macro base stations (MBSs) due to lower cost and faster deployment. It is expected that cellular network operators will significantly densify their networks by deploying SBSs to meet the 5G performance requirements.

A multi-tier heterogeneous cellular network comprises a tier of conventional MBSs, overlaid with a diverse set of lower-power base stations (BSs) such as picocells, small bases stations (SBSs), femtocells, and relay BSs [3]. Multi-tier heterogeneous cellular networks are expected to be a key deployment method of 5G cellular networks to increase network capacity and end user throughput [4] as well as to provide expanded indoor and cell edge coverage. The tiers of BSs are ordered based on transmission power of BSs with tier 1 consisting of MBSs which have the highest transmitted power. In general, due to differences in deployment, they also will have different path loss exponents and spatial densities (e.g., the number of BSs per square kilometre).

Figure 1.1 shows an example of a two-tier network. Tier 1 consists of MBSs with higher transmission power (in the downlink direction) and lower deployment density. Tier 2 consists of small bases stations (SBSs) with lower transmission power (in the downlink and uplink directions) and high density deployment. In order to provide relief to the MBS tier, which is and will continue to be the main bottleneck, the SBSs should be designed to have a bias towards connecting more users to itself [3], since they typically carry lighter loads than MBSs due to their smaller coverage areas.

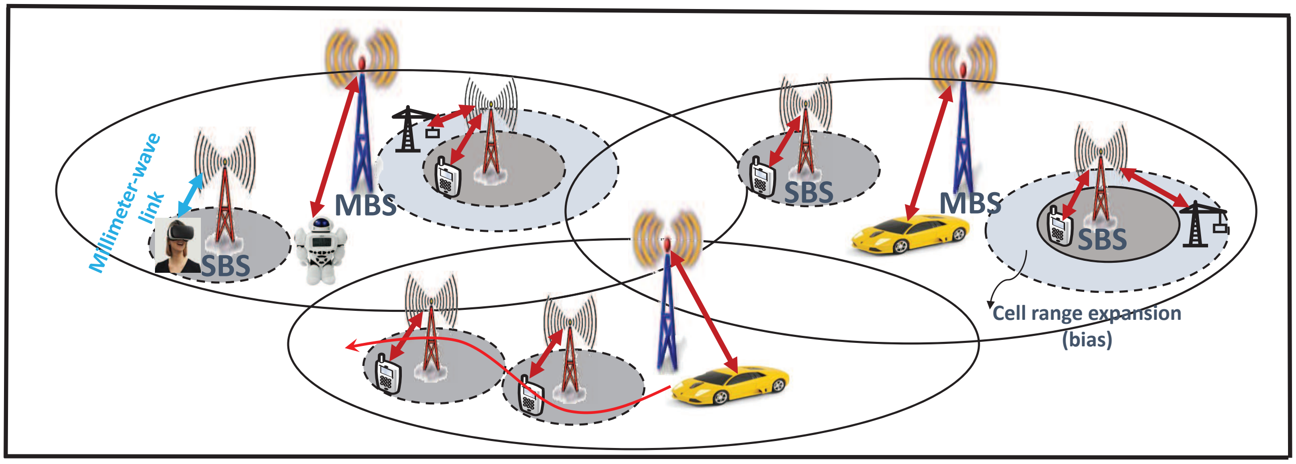

Figure 1.1: Large-scale heterogenous two-tier IoT networks.

A *heterogeneous network* uses a mixture of MBSs tier and low power BSs tier such as picocells, femtocells, and relays. The BSs in each tier communicate with devices with different transmitted power and are deployed with different densities. These networks with multiple tiers will improve spatial reuse and coverage in order to achieve higher data rates, while retaining seamless connectivity and mobility. Another source of heterogeneity is the coexistence of multiple spectrum; for example, the MBSs operate on the traditional sub-6GHz spectrum, while the SBSs communicate with user devices on the millimeter-wave spectrum.

As the sub-6GHz spectrum is running out of bandwidth to support a huge number of devices, operators of the upcoming 5G networks will tap into the millimeter-wave (mm-wave) spectrum. The mm-wave spectrum has wider bandwidths that can meet higher traffic demands and support data rates into the order of gigabits per second [5]. Millimeter wave (mm-wave) communication is one of the a key enabling technologies for future next generation wireless communications due to its abundant spectrum resources, which can lead to data rates of multiple of gigabits per second [6, 2]. Millimeter wave brings a positive effect on the network performance, which is the mitigation of the overall interference [4].

Since the mm-wave transmissions are highly susceptible to blockages and penetration losses, mm-wave spectrum and sub-6GHz spectrum will coexist in 5G networks [7, 8]. However, mm-wave communication has unique features such as directivity, sensitivity to blockages, and higher path losses. Therefore, mm-wave communications have fundamental differences compared with the current sub-6GHz communications [4].

Due to these differences, the unique features of mm-wave communications are required to be thoroughly considered in the design of network architectures and protocols in order to fully exploit the potentials benefits of mm-wave communications.

The overarching goal of the research in this dissertation is to model and analyze the performance of large-scale heterogeneous two-tier IoT networks with new design, technologies, and algorithms. Following are the motivations behind our research and the contributions of the dissertation.

## 1.2 Motivations and Contributions of the Dissertation

Large-scale heterogeneous cellular networks is very important and will be deployed widely in a near future to implement and support the IoT. The focus of the thesis is to use tools from stochastic geometry to model and analyze the performance of heterogeneous IoT cellular networks.

### 1.2.1 Motivations

We have identified gaps in existing research in several areas such as data rate analysis for uplink two-hop networks, the meta distributions of the SIR/SNR and data rate in coexisting sub-6GHz and mm-wave cellular networks, and the effect of mobility on the foreseen densification gain with a C-plane/U-plane split architecture.

Existing works on performance modeling and analysis of IoT networks have focused on estimating the coverages and data rates of different transmission schemes for multi-hop uplink communications in M2M networks [9,10,11]. Recently, works on performance modeling and analysis of two-hops IoT networks have appeared in [12,13,14,15,16]. Among these [12] and [13] address the problem of scheduling in uplink two-phase cellular-based massive machine type communication (mMTC) networks. Kim et al. [14] study the optimal settings of the network parameters in terms of the number of aggregators and packet-bundle size. Rigazzi et al. [15] investigate trade-off between the packets latency and the transmission power. Rao et al. [16] study the performance of different device-aggregator association schemes. Research on resource allocation and energy efficiency of two-hop IoT networks has recently appeared [17,18,19,20,21,22]. An energy-efficiency cluster head selection scheme and resource allocation to perform device grouping were proposed in [17,18,19,20,21] to maximize the network life. However, the problem of determining the mean uplink data rate utility over two consecutive hops in the uplink direction (i.e., from devices to aggregators to MBSs) has not been addressed in the literature.

Having identified this gap in the literature, we develop a novel analytical model to estimate the *mean data rate utility function* (DRUF) in the uplink direction of a two-hop IoT network to ensure rate fairness among devices (i.e., by maximizing the log of the uplink DRUF) and to improve device data rates. To the best of our knowledge, our work is the first that proposes an analytical model to estimate the log of the uplink DRUF of a two-hop IoT network. This estimate is critical in the design and deployment of IoT networks in order to improve the data rate of IoT links and to ensure rate fairness among devices.

A variety of research works study the *coverage analysis of mm-wave only cellular networks* [23, 24, 25, 26]. For instance, Di Renzo et al. [23] propose a general mathematical model to analyze multi-tier mm-wave cellular networks. Bai et al. [24] derive the coverage and rate performance of mm-wave cellular networks. Turgut and Gursoy [25] investigate heterogeneous downlink mm-wave cellular networks consisting of $K$ tiers of randomly located BSs where each tier operates in a mm-wave frequency band. Deng et al. [26] derive the success probability at the typical receiver in mm-wave device-to-device (D2D) networks.

Some recent studies analyze the *success probability* of coexisting $\mu$wave and mm-wave cellular networks. A hybrid cellular network is considered by Singh et al. [27] to estimate the uplink and downlink coverage and rate distribution of self-backhauled mm-wave networks. Elshaer et al. [28] develop an analytical model to characterize decoupled uplink and downlink cell association strategies. Singh et al. [27] and Elshaer et al. [28] model the fading power as Rayleigh fading to enable better tractability.

To the best of our knowledge, our work is the first to characterize the meta distributions of SIR/SNR and data rate for coexisting $\mu$wave and mm-wave IoT networks. Different from previous research in [25, 29, 28, 30, 26, 24, 28], we propose a stochastic geometry framework that focuses on modeling and analyze the meta distributions of the downlink SIR/SNR and data rate of a typical device in a coexisting $\mu$wave and mm-wave cellular IoT networks taking in consideration (i) coexistence of two different network tiers with completely different channel propagation, interference, and fading models, (ii) dual-hop transmissions enabled by two different spectrums, one in each network tier, and (iii) Nakagami-m fading model with shape parameter $m$ for LOS mm-wave channels. Nakagami-m fading is a generic and versatile distribution that includes Rayleigh distribution (typically used for non-LOS fading) as its special case when $m = 1$ and can well approximate the Rician fading distribution for $1 \leq m \leq \infty$ (typically used for LOS fading).

**Mobility-Aware Modeling and Analysis of Dense Cellular Networks with C-plane/U-plane Split Architecture**

The past five years have witnessed a plethora of stochastic geometry based models that tackles different aspects in cellular networking [31,32,3,33,34,35,36,37,38,39,40]. However, the majority of these models do not account for mobility and focus on the performance of stationary devices. For instance, coverage probability and rate performance are characterized for single-antenna downlink connections in [31,32,3], for single-antenna uplink connections in [34], and for downlink connections with multiple antennas in [35,36]. Stochastic geometry also helps characterizing the performance of CP/UP split architecture in cellular networks. For instance, the effect of vertical offloading and BS sleeping on the energy efficiency for the CU/UP split architecture is studied by Zhang et al. [39]. In [40], the throughput of the CU/UP split architecture is studied. However, none of the aforementioned studies incorporates the effect of mobility and handover into the analysis.

Surprisingly, few models can be found in the literature that exploit stochastic geometry to characterize mobility in cellular networks. The handover rate in cellular networks is first characterized by Lin et al. [41], in which expressions for the handover rate are derived for random waypoint mobility model in a single-tier cellular network. The handover rate for multi-tier cellular networks is characterized by Bao and Liang [42] for arbitrary mobility model. However, neither [41] nor [42] investigates the effects of handover on important performance metrics such as coverage, rate, or delay. The handover effects on coverage and rate are investigated by Sadr and Adve [43] for random way point mobility model. Note that the handover cost factor in [43] is considered as a network parameter that reflects the SINR degradation during handovers. Zhang et al. [44] investigate the effect of delay-reliability tradeoff in dense cellular networks for static and high mobility devices under a time slotted transmission scheme. However, the results in [44] may be misleading because the model only captures the positive impact of mobility and overlooks the performance degradation that may occur due to handover signaling and delay.

Different from the existing literature, our proposed mobility-aware paradigm captures the handover effect on the devices throughput in the conventional and CP/UP network architectures. Different from [43], the handover cost is not assumed and is rigorously derived from the system model. Also, different from [44] and [45], the developed model accounts for the handover effect and is not tailored to a specific mobility model. Furthermore, the developed model accounts for signaling overhead, flexible device association scheme via association biasing, the availability of X2 interface between BSs, and almost blank subframes (ABS) coordination between MBSs and SBSs.

Having identified gaps in existing research, we propose solutions in order to address them. In particular, our contributions in this dissertation are as follows

### 1.2.2 Detailed Contributions

**Data Rate Utility Analysis for Uplink Two-Hop Internet-of-Things Networks:**

High interference is a critical factor in large-scale IoT networks due to dense deployments and a huge number of devices such as sensors, actuators and machinery which are deployed in the manufacturing and supply chain industry for monitoring products, data aggregation and analysis, asset management, maintenance planning, and plant control and optimization. High interference in the uplink direction would reduce the uplink data rate. Therefore, minimizing interference and improving the data rate are critical factors to study for IoT networks. Therefore, we study the fundamental problem of spectrum allocation and device association in uplink two-hop IoT networks under two schemes of spectrum resource allocation: a) orthogonal spectrum partition (OSP) and b) full spectrum reuse (FSR).

We propose a model to estimate the mean uplink data rate utility that takes into account different key network parameters, namely, power control fraction (PCF) and spatial density of aggregators. In the proposed model, we propose a framework for maximizing the mean uplink data rate utility using stochastic geometry and based on the uplink device coverage probability. The uplink device coverage probability is a function of the aggregator bias for device association and spectrum partition ratio across the macro base station (MBS) tier and the aggregator-tier. We use constraint gradient ascent optimization to obtain the optimal aggregator association bias (for the FSR scheme) and the optimal joint spectrum partition ratio and aggregator association bias (for the OSP scheme). We confirm the accuracy of the developed constraint gradient ascent optimization algorithms using simulations.

Using the proposed model, we study the impact of device and aggregator PCFs and the spatial density of aggregators on the mean uplink data rate utility function, and obtain network design insights such as the optimal aggregator association bias and spectrum partition ratio. Simulation results show that the proposed optimized OSP and FSR schemes, by reducing interference, outperform other benchmark schemes such as the minimum-distance based association scheme and the maximum-SIR based association scheme in terms of uplink mean per-device data rate distribution.

### The Meta Distributions of the SIR/SNR and Data Rate in Coexisting Sub-6GHz and Millimeter-wave Internet of Things Cellular Networks:

The meta distribution is a unified performance metric that captures important network performance measures such as the coverage (or success) probability and the mean local delay as its special cases. We characterize the meta distribution of the downlink signal-to-interference-ratio (SIR)/signal-to-noise-ratio (SNR) and data rate of a typical device in a coexisting sub-6GHz and millimeter wave (mm-wave) cellular network using tools from stochastic geometry. Macro base stations (MBSs) transmit on sub-6GHz channels (which we term “microwave” channels for short), whereas small base stations (SBSs) communicate with devices on mm-wave channels with Nakagami-m fading. The SBSs are connected to MBSs via a microwave ($\mu$wave) wireless backhaul. A typical device associates itself with either a MBS or a SBS, depending on the biased received signal power criterion.

We first characterize the association probabilities of a typical device to a $\mu$wave MBS, a line-of-sight (LOS) mm-wave SBS and a non-LOS (NLOS) mm-wave SBS. Then we characterize the conditional success probability (CSP) and its $b^{\text{th}}$ moment for (a) a typical device when it associates with a $\mu$wave MBS (direct transmission), (b) a typical device when it associates with a mm-wave SBS (access transmission), and (c) the tagged SBS when it associates with a $\mu$wave MBS (backhaul transmission). Finally, we characterize the meta distribution by substituting the cumulative moment of the CSP of a device into the Gil-Pelaez inversion theorem. We provide closed-form approximations of the meta distribution using the Beta distribution. We then characterize special cases such as the mean local delay, variance of the CSP, and success probability of a typical device. Following similar steps, we characterize the meta distribution of the downlink SIR of a typical device in a $\mu$wave-only network where access and backhaul transmissions are conducted on orthogonal $\mu$wave (sub-6GHz) frequency channels and mm-wave-only IoT networks where access and backhaul transmissions are conducted on orthogonal mm-wave frequency channels. We present numerical results which are corroborated by Monte-Carlo simulations, and provide valuable insights into the mean local delay, variance of CSP, and success probability of a typical device.

**Mobility-Aware Modeling and Analysis of Dense Cellular Networks with C-plane/U-plane Split Architecture:**

Mobility has a big impact on per-device throughput in high dense cellular environments. The unrelenting increase in the population of mobile devices and their traffic demands drive cellular network operators to densify their network infrastructure. Network densification shrinks the footprint of base stations (BSs) and reduces the number of devices associated with each BS, leading to an improved spatial frequency reuse and spectral efficiency, and thus, higher network capacity.

However, the densification gain come at the expense of higher handover rates and network control overhead. Hence, devices mobility can diminish or even nullifies the foreseen densification gain. In this context, splitting the control plane (C-plane) and user plane (U-plane) is proposed as a potential solution to harvest densification gain with reduced cost in terms of handover rate and network control overhead. Therefore, we use stochastic geometry to develop a tractable mobility-aware model for a two-tier downlink cellular network with ultra-dense small cells and C-plane/U-plane split architecture. The developed model is then used to quantify the effect of mobility on the foreseen densification gain with and without C-plane/U-plane split.

To this end, we shed light on the handover problem in dense cellular environments, show scenarios where the network fails to support certain mobility profiles, obtain network design insights, and show effect of the handover delay problem in dense cellular environments and show the potential delay mitigation via the CP/UP split architecture.

## 1.3 Organization of the Dissertation

The remainder of the thesis is organized as follows. We provide a review of background and related work in Chapter 2. In Chapter 3, we present analytical model and simulation results that characterize the data rate utility for uplink two-hop IoT networks. In Chapter 4, we develop a systematic framework to characterize the meta distributions of the downlink SIR/SNR and data rate of a typical device in an IoT cellular network with coexisting sub-6GHz and millimeter-wave spectrums. In Chapter 5, we propose a novel mobility-aware analytical model of the C-plane/U-plane split radio access network architecture with flexible device association for future highly dense heterogeneous cellular networks. We conclude the thesis, and outline future research directions in Chapter 6.

# Chapter 2

# Literature Review

This chapter begins with an overview of background about key performance indicators (KPIs) used in stochastic geometry to characterize the performance of wireless communications networks and stochastic point processes used to represent different network deployments. Then we survey existing related works on performance modeling and analysis of large-scale IoT networks.

## 2.1 Background

Wireless communication engineers used to model 1G, 2G, and 3G cellular networks by modeling base stations according to a hexagonal grid and mobile users are distributed deterministically or distributed uniformly as Poisson point processes (PPPs) [46, 47, 48, 49]. These types of models were widely used to analyse and design old cellular networks, but they are extremely idealized and not tractable. Therefore, complex extensive simulations are used to calculate key performance metrics such as coverage probability for a specified target rate or average data rate.

The research on the fourth generation of wireless mobile communications (4G) [50, 51] aimed to provide such a large-scale IoT connectivity. However, the urgent necessity to serve high volumes of human-generated communication traffic, e.g. web browsing, IoT connectivity was excluded from the major design objectives of 4G wireless networks [52]. The first attempts for creating IoT connectivity were made during the transition period from 3G to 4G by companies outside the 3rd Generation Partnership Project (3GPP). Those early IoT solutions operated over the unlicensed spectrum, e.g., SigFox, before the public introduction of 4G networks [52]. Enabling large-scale IoT connectivity became a crucial subject in industry and academia after the successful and widespread deployment of 4G networks. The research on large scale IoT was embedded in most big projects aimed at shaping 5G networks, e.g., METIS I and II [53].

Recently, 4G cellular networks suffers from the scarcity of the available licensed and unlicensed radio spectrum. These reasons lead to 1) deployment of lower power BSs such as micro BSs, pico BSs, femto BSs, aggregators, phantom BSs, and relays, distributed antennas underlaid, 2) needs for new tools to design, model, and analyse the new cellular networks with the random deployment nodes' locations. Therefore, modern heterogenous cellular network topologies are more suitably represented by random deployments than by deterministic deployments, especially those that involve deployments of several types of low power BSs.

Using stochastic geometry to model, analyze, and design cellular networks with random deployments has gained much popularity in industry and academia recently due its tractability [54]. Point processes are used to model the locations and channel access of base stations and mobile users. Stochastic geometry is a very suitable tool to model, design, and analyze this kind of random deployments [54]. The main idea is to use random spatial models, i.e., point processes to represent locations of base stations based on probability distributions instead of fixed locations assumed in commonly used deterministic models such as grid-based models [55, 54, 56, 57, 58, 59, 60, 61].

Future cellular networks 5G and beyond (6G) are characterized by randomly deployed and heterogeneous deployments with high densities of base stations. Therefore, base stations and mobile users locations are modeled using stochastic point processes, which allow the application of powerful tools of stochastic geometry to network performance analysis.

Stochastic geometry is a powerful mathematical tool that captures the irregular deployment of heterogenous cellular networks with several types of low power BSs. It provides spatial averages (i.e., averages taken over a large number of nodes at different locations or over many network configurations) of important performance metrics such as interference, signal to interference plus noise ratio (SINR), outage probability, and average data rate. In other words, stochastic geometry is used to study the average behavior over many spatial realizations of a cellular network where its BSs in each tier are located according to some probability distribution. Stochastic geometry uses point process or random point pattern to statistically describe patterns produced by points in the n-dimensional space [55, 54, 56, 57, 58, 59, 60, 61].

### 2.1.1 Key Performance Indicators

Wireless communications engineers have used the following performance metrics for cellular network operations:

- **Coverage probability:** the probability that the SINR at the mobile users greater than a predefined threshold value T which defines correct signal reception. The coverage probability $P_c$ is a function of SINR, which is defined as $P_c = P(SINR > T)$. The outage probability $P_{out}$ is defined as $P_{out} = 1 - P_c$.
- **Spectral efficiency:** the average rate at which data can be sent over a given channel bandwidth. The spectral efficiency is a function of the SINR as follows: $R = \log_2(1 + SINR)$.
- **Mean local delay:** the average amount of time required to successfully transmit a packet. Specifically, the average time for retransmissions required to transmit a packet from a transmitter to a receiver successfully. The delay can be inferred as $\frac{1}{P_c}$.
- **Spectral frequency reuse efficiency:** an indication of how many times the frequency is being reuse over the spatial domain of the entire network.

- **Energy efficiency:** the rate at which data can be delivered between a transmitter and a receiver per power unit. Interference management helps to increase the energy efficiency of the cellular network because it reduces interference without increasing the power of the desired signal. When you have low interference this leads to higher SINR, higher delivered average data rate, higher coverage probability using the same transmitted power without any increase.

- **Link reliability:** The distribution of the conditional success probability of the transmission link, conditioned on the locations of the wireless transmitters, i.e., what fraction of devices can achieve $x\%$ transmission success probability?

The impact of the SINR parameter on the performance of cellular networks is very significant. This fact is demonstrated in the definitions of the most commonly used KPIs shown above, as SINRs appear in most definition.

### Signal to Interference Plus Noise Ratio (SINR) Model

In cellular networks, signals are modulated and transmitted from the transmitter to the receiver as electromagnetic waves. In the three-dimensional space, the signal power (wave energy) of these waves attenuates as a function of the distance between the transmitter and the receiver based on the following power law:

$$P_r(y) = P_t(x) A h_{xy} r^{-\alpha} \tag{2.1}$$

where $y \in \mathcal{R}^d$ is the location of the receiver, $P_r(y)$ is the received power, $x \in \mathcal{R}^d$ is the location of the transmitter, $P_t(x)$ is the transmitted power, A is a propagation constant, $h_{xy}$ is a random variable that represents the random channel gain between the transmitter located at $x$ and the receiver located at $y$, $r = \parallel x - y \parallel$ where $\parallel . \parallel$ is the Euclidean norm, and $\alpha$ is the path loss exponent. The decay or attenuation of signals is modeled as the product of a large-scale path gain component and a small-scale multi-path fading gain component as shown in Eq. (2.1). For multi-path fading, we consider a fading channel (for example

Rayleigh fading) model in the desired link, i.e, signal attenuation due to multi-path fading is modeled using an independent Rayleigh distribution such that the channel power gain $h_{xy} \sim \exp(1)$. For the large-scale path gain, the received power decays with $r^{-\alpha}$. It is worth noting that Eq. (2.1) represents the unbounded path loss model because of the singularity[1] at $r = 0$. This path loss model is often used in the literature because of its tractability. It is only valid for calculating the received power in the case of the far-field region (large $r$) [62]. There is a more realistic model called bounded path loss model that removes the singularity at the origin. The bounded path loss model is given by

$$P_r(y) = \frac{P_t(x) A h_{xy}}{r^{\alpha} + \delta} \tag{2.2}$$

where $\delta > 0$ is added to avoid the singularity. We will assume the unbounded path-loss model given by Eq. (2.1) due to its simplicity.

When a set of channels is active simultaneously, the interference from other channels is considered as noise. Therefore, the signal-to-interference-plus-noise (SINR) metric is used to measure the theoretical rate of information transfer, or the upper bound on channel capacity in wireless networks. From the unbounded pass loss law described by Eq. (2.1), we can infer that the desired signal can get drowned in noise if the interferer is closer to the receiver than the transmitter, assuming that the transmitter and the interferer transmitting with equal power level. Therefore, the relative distances between the transmitter and the receiver and between the interferer BSs and the receiver are very important to determine the performance of wireless networks due to distance dependent signal power decay and the shared nature of wireless media. Therefore, the topology of the network has a big impact on the receiver‘s SINR and, overall, on the network performance. The SINR of a receiver in a wireless network

---

[1] A singularity is in general a point at which a given mathematical object is not defined, or a point of an exceptional set where it fails to be well-behaved in some particular way, such as differentiability. For example, the function $f(x) = \frac{1}{x}$ on the real line has a singularity at $x = 0$, where it seems to ”explode” to $\pm\infty$ and is not defined

can be calculated as follows:

$$SINR(y) = \frac{\overbrace{P_t(x_0)Ah_{x_0y} \parallel x_0 - y \parallel^{-\alpha}}^{\text{Desired signal}}}{\underbrace{W}_{\text{Noise}} + \underbrace{\sum_{x\in\mathcal{I}} P_t(x)Ah_{xy} \parallel x - y \parallel^{-\alpha}}_{\text{Aggregation interference}}} \tag{2.3}$$

where $y$ is the location of the receiver, $x_0$ is the location of the transmitter, $\mathcal{I} = \{x_1, x_2, x_3, ....\}$ is the group of interferers that transmit simultaneously using the same frequency as the transmitter, and $W$ is the noise power. The term $\sum_{x\in\mathcal{I}} P_t(x)Ah_{xy} \parallel x - y \parallel^{-\alpha} = I_{agg}$ is the aggregate interference at the receiver due to the interferers that transmit simultaneously using the same frequency band used by the transmitter. It is clear that the statistical characteristics of $I_{agg}$ depend on the statistics of each interferer‘s signal power, which depends on the propagation effects, the location of the interferer, and user activities (traffic model) as shown in Fig. 2.1. The distances between the receiver and the interferers play an important role in the modeling of the performance of wireless networks. Therefore, based on the network model, wireless network characteristics such as the topology, available channels, traffic model, association model, and medium access control (MAC) protocol determine the statistic characteristics of the aggregate interference signal. The aggregate interference can be considered as finite or infinite. Aggregate interference is considered finite when only the interferers inside a certain area (such as a disk) are included and interferers outside the disk are excluded. Aggregate interference is considered infinite when all interferes in the wireless network are included in the analysis.

We consider two-tier networks where the first tier consists of macro BSs (MBSs) that transmit with the same power level $P_1$ and the second tier consists of small cell BSs (SBSs) that transmit with the same power level $P_2$ where $P_2 < P_1$. Therefore, a mobile users is associated with the BS (tagged BS) that offers the highest received power to the mobile user. Assume that a mobile user is associated with a MBS where the mobile user receives the higher power from this MBS than from other MBSs or SBSs. The distance between the mobile user and the tagged MBS is $d$. Assume that the MBS tier and the SBS tier have the

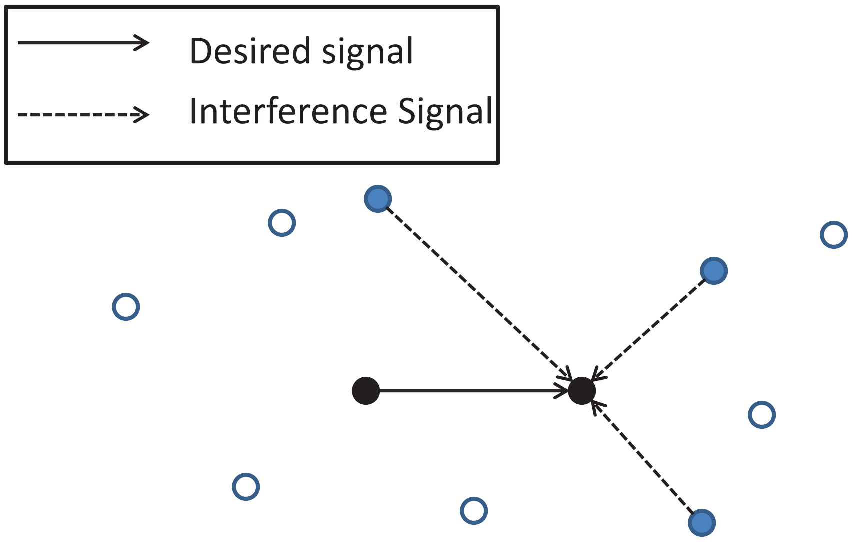

Figure 2.1: A snapshot of a network. A signal is transmitted from a transmitter to a receiver (solid black dots). Interferers transmit on the same frequency of the transmitter and the receiver simultaneously. Interferers (blue dots) cause interference to the receiver.

same path loss exponent $\alpha_1 = \alpha_2 = \alpha$. Therefore, the nearest interfering MBS is located at a distance $d_{int_{MBS}} > d$ and the nearest interfering SBS will be located at a distance $d_{int_{SBS}} > d\left(\frac{P_2}{P_1}\right)^{\frac{1}{\alpha}}$. Similarly, if the mobile user is associated with a SBS, the mobile user receives the highest power from this SBS. The distance between the user and the SBS is $d$. The MBS tier and SBS tier have the same path loss exponent $\alpha_1 = \alpha_2 = \alpha$. Therefore, the nearest interfering SBS is located at a distance $d_{int_{SBS}} > d$ and the nearest interfering MBS will be located at a distance $d_{int_{SBS}} > d\left(\frac{P_1}{P_2}\right)^{\frac{1}{\alpha}}$.

The wireless network topology and the instantaneous channel fluctuation gain have a big impact on the SINR experienced by each receiver at a certain point of time. Therefore, the SINR experienced by each receiver is a random variable that mainly depends on the wireless network topology and it changes from one time instance to another [63]. Stochastic geometry is a mathematical tool that averages over all network realizations seen from a arbitrary node weighted by their probability of occurrence [64] and [61]. In other words, stochastic geometry provides spatial averages, i.e., averages taken over a large number of BSs at different locations or over many network realizations, of the metric of interest (e.g., interference, SINR, coverage probability, outage probability, and achieved data rate)[56].

### Shannon Limit

The SINR is also used to compute the Shannon limit of a wireless communication channel in cellular systems. Let $C$ denote the capacity of an additive white Gaussian noise (AWGN) channel. The key factors that govern the performance of a wireless cellular network are shown in the following equation:

$$R < C = M \left( \frac{W}{N} \right) \log_2 (1 + SINR) \ \ bits/sec, \tag{2.4}$$

where W is the available BS spectrum bandwidth, N is the number of mobile users connected to the BS or the load and $N \geq 1$, and M is number of spatial streams between the BS and its mobile users. The data rate $R$ of a mobile user is upper bounded by the capacity of the AWGN channel as shown in Equation (2.4). From Equation (2.4), we can show that in order to increase the capacity of the cellular network, we have to consider three main factors: 1) increasing the number of BSs, 2) increasing the channel bandwidth, and 3) increasing number of special streams (spatial multiplexing factor). The spectrum bandwidth W can be increased by adding more spectrum such as the available unlicensed spectrum. The load factor N can be reduced through cell splitting or shrinking the coverages of BSs by deploying small cells and distributing mobile user traffic as evenly as possible among all the BSs [65]. We can increase the spatial multiplexing factor M by adding more antennas to BSs and mobile devises via the multiple-input and multiple-output (MIMO) technology.

## 2.1.2 Stochastic Point Processes

Using stochastic geometry, a network is modeled as a point process (PP) that represents and captures the network characteristics and properties by using a mathematical model to represent the location of the network BSs. A PP is selected to match the locations of the BSs in the wireless network and to represent the medium access control characteristics of the wireless network. The most commonly used PPs to model wireless networks are Poisson point process (PPP), binomial point process (BPP), hard core point process (HCPP), and Poisson cluster process (PCP).

### Poisson Point Processes

A PP $\psi = \{x_i; i = 1, 2, 3, 4, .......\} \subset \mathbb{R}^d$ is a PPP with intensity $\lambda$ if 1) the number of points N(B) falling inside any compact set $B \subset \mathbb{R}^d$ is a Poisson random variable with a mean $\lambda\|B\|$ where $\|.\|$ is the Lebesgue measure in a two-dimension space and $\lambda$ is the expected number of points per unit area and, 2) the number of points in a disjoint sets is independent. Figure 2.2 shows an example of a PPP.

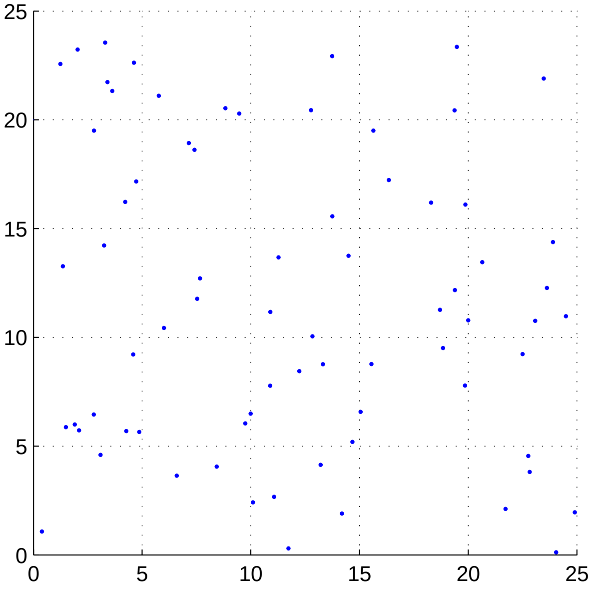

Figure 2.2: A Poisson point process in a 25m x 25m region with intensity 0.15 points/m$^2$.

The PPP is used to model a wireless network which consists of an infinite number of

BSs that are independently and randomly located in a finite or infinite area. The PPP is considered as the most important commonly used PP modeling wireless networks due to its independence property [66, 67, 68, 69, 70] . The PPP is widely accepted and well defined and understood as this has been confirmed by experimental data [54, 71] and theoretical proofs [72]. For instance, PPP can model BSs in a large scale wireless network and also can model mobile users in a wireless cellular networks. The PPP can capture the performance parameters for planned infrastructure based wireless networks that have coordinated spectrum access such as long term evolution (LTE) and LTE-Advanced. In such wireless networks, the PPP provides tight bounds for the performance parameters such as in the case of wireless network densification [54]. Network models based on the PPP are significantly more tractable than those based on traditional grid models. Moreover, network models based on the PPP are producing tightly close performance metrics such as probability of coverage and average data rate as the real measurments from cellular networks deployment. The PPP is the parent PP for different other point processes that have been used in the literature of modeling wireless communication networks such as Poisson cluster process and hard core point process (HCPP of type I and HCPP of type II).

Based on all above considerations, cellular network models based on PPP are currently used to design and analysis wireless cellular network networks. Di Renzo et al. [73] develop a comprehensive mathematical framework for the analysis of the average rate of multi–tier heterogeneous cellular networks. The authors assume that BSs in multi–tier heterogeneous cellular are distributed randomly as a PPP spatial distribution. The pioneer work done by Andrews et al. [54] to characterize the coverage probability and the average rate of PPP-based cellular networks as closed-form. In [74], the framework of [54] was extended to model multi-tier heterogeneous wireless networks as the superposition of many PPPs. Dhillon et al. [75] studied multi-tier heterogeneous cellular networks using a PPP-based network model by assuming a cell association criterion based on the maximum SINR. Dhillon et al. [76] incorporated a flexible notion of BS load characteristics in random spatial PPP models for K-tier heterogeneous wireless networks by introducing a conditionally thinning approach, conditional on the connection of a typical mobile user to its serving BS. Novlan et al. [77] studied the coverage probability and average rate in the cellular uplink. The probability density function (pdf) of the aggregated interference and the outage probability were characterized in [68] for PPP-based wireless networks with deterministic channel gains and pass loss exponent $\alpha = 4$. Mathar et al. [47] evaluated the cumulated instantaneous interference power in a Rayleigh fading channel for an infinite number of interfering stations when the positions of stations follow a one- or two-dimensional PPP. Weber et al. [78] studied the effect of channels fading, channel inversion power control, and threshold based scheduling on the transmission capacity. Weber et al. [79] developed a tractable framework for analyzing the performance and capacity improvement by using successive interference cancellations in wireless ad hoc networks which are modeled as PPP. Optimal capacity extension policies for a two-tier cellular network are developed in [37]. Lin at al. [41] determined handover rates due to random waypoint mobility in single-tier cellular networks. Bao and Liang [42] extended the results in [41] to multi-tier networks and mobility of arbitrary trajectories. Sadr and Adve, [43] calculated the handover rate in multi-tier cellular networks, and compared the coverage performance of stationary and mobile users. Syu and Lee, [80] studied the feasibility of device-to-device communications, while Lin et al. [81] propose an optimal spectrum partitioning between cellular and device-to-device users. Bai et al. [24] offered design insights for mmWave based cellular networks. Jindal et al. [82] applied fractional power control as a general approach to pairwise power control in decentralized networks, i.e., ad hoc or spectrum sharing. They modeled the cellular network as PPP. Then, they derived the transmission capacity using decentralized power control policy.

### Binomial Point Processes

A binomial point process (BPP) is a random pattern produced by locating a fixed number of points N(B) that are falling inside any compact set $B \subset \mathbb{R}^d$ with a finite Lebesgue measure $L(B) < \infty$, where $L(.)$ denotes the Lebesgue measure. The Lebesgue measure is a way of assigning a measure to subsets of an n-dimensional Euclidean space such as length, area, and volume. Assume that $\psi = \{x_i; i = 1, 2, 3, 4, .......\} \subset B$. If the number of points N(b) inside a compact set $b \subseteq B$ is a binomial random variable and the numbers of points falling inside a disjoint set are related via a multinomial distribution [83], then $\psi$ is considered a BPP.

The BPP is used to model a wireless network which consists of a finite number of BSs and the wireless network area is finite [84, 83], For instance, placing a set of wireless sensor nodes in a parking lot to count the number of vehicles in and out.

### Poisson Cluster Processes

A PCP point process is a random pattern produced by random clusters. A PCP is formed from a parent PPP $\psi = \{x_i; i = 1, 2, 3, 4, .......\}$ by exchanging each point $x_i \in \psi$ by a cluster of points $H_i$, $\forall x_i \in \psi$, where the points in $H_i$ are independently and identically distributed in a spatial domain.

The PCP is used to model a wireless network in which BSs are clustered according to social behaviour or by the MAC protocol [85, 64]. For instance, mobile users are gathered around a WiFi access point (AP). Figure 2.3(b) shows a PCP and its parent PPP.

### Hard-core Point Processes

A HCPP is a random pattern produced by a repulsive point process where no two points of that process are separated by a distance less than a predefined hard core distance $\delta \geq 0$. A point process $\psi = \{x_i; i = 1, 2, 3, 4, .......\} \subset \mathbb{R}^d$ is considered a HCPP if $\parallel x_i - x_k \parallel \geq \delta$, $\forall x_i, x_k \in \psi$, $i \neq k$.

The HCPP is used to model a wireless network in which BSs are separated by a minimum distance due to MAC layer characteristics, physical geographical constraints, or network planning. For instance, the Matern HCPP is used to model the spatial locations of BSs in wireless networks that use the carrier sense multiple access (CSMA) MAC algorithm [86, 87, 88, 89, 90].

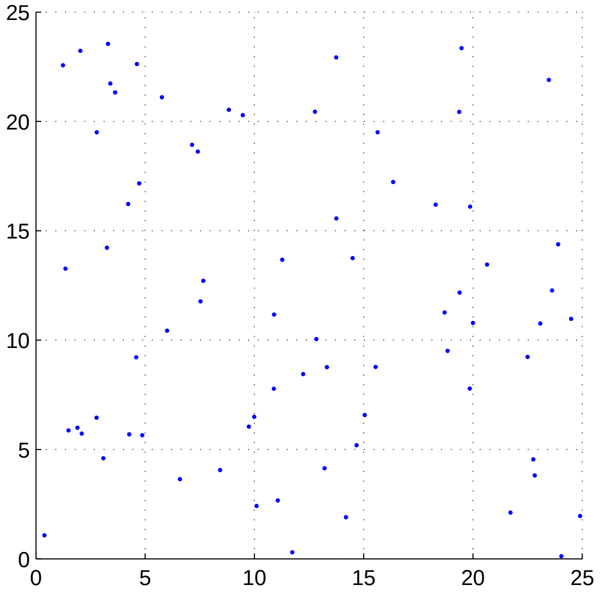

(a) A PPP in a 25m x 25m region with intensity 0.15 points/m2

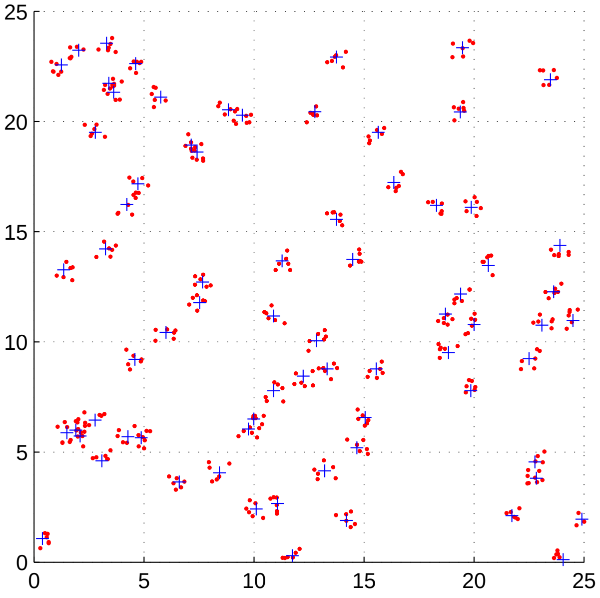

(b) A PCP in a 25m x 25m region generated from the parent PPP in (a). The parent PPP points are denoted by the blue crosses “+” while the added cluster points are denoted by the red dots.

Figure 2.3: Poisson cluster process

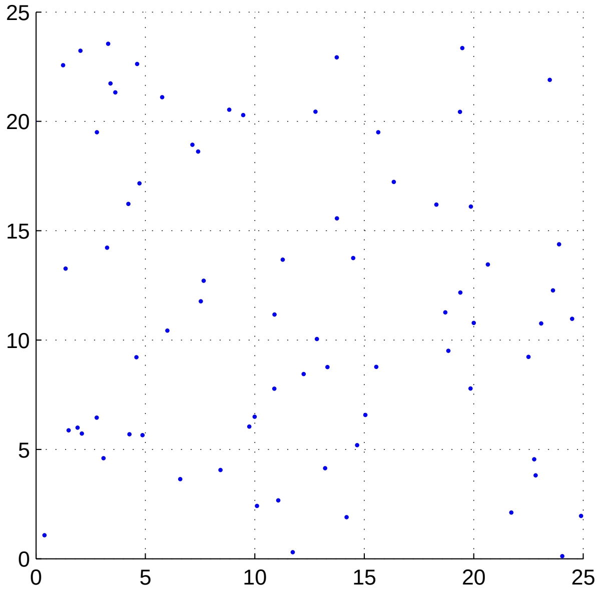

(a) A PPP in a 25m x 25m region with intensity 0.15 points/m2

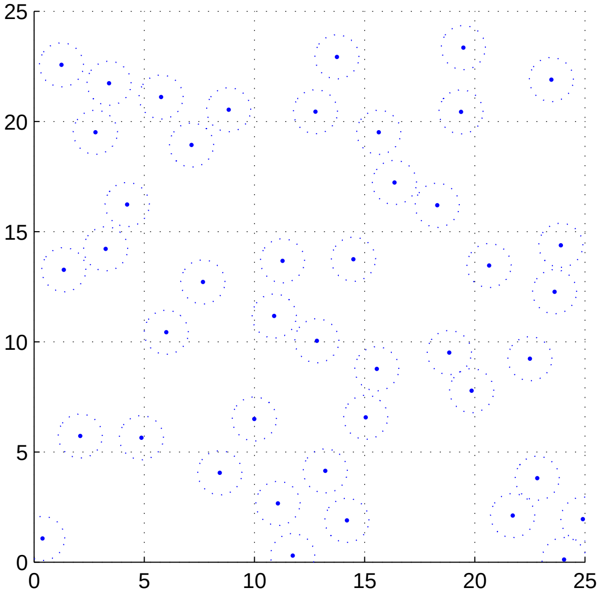

(b) A Matern HCPP of type I in a 25m x 25m region corresponding to the parent PPP in (a) and hard core distance $\delta = 2$m.

Figure 2.4: Hard core point process

There are two types of Matern HCPP, type I and type II. Both are based on a parent PPP of with intensity $\lambda_{PPP}$. In a Matern HCPP of type I , all nodes with a neighbor within the hard core distance $\delta$ are thinned (eliminated). However, in a Matern HCPP of type II, each node has a random associated mark, i.e, $t \in [0, 1]$ and a BS is thinned only if there is another BS within distance $\delta$ with a smaller mark point ($t = 0$) [91]. Figure 2.4(b) shows a Matern HCPP of type I with hard core distance $\delta = 2$m and its parent PPP.

A comprehensive tutorial and more detailed information about different types of PP can be found in [89].

## 2.2 Related Work

In this section, we review the relevant work in the literature on the design and performance analysis of next generation heterogeneous cellular networks for the IoT networks using stochastic geometry, divided into three main categories, i.e., uplink two-hop IoT networks, coexisting sub-6GHz and millimeter-wave IoT networks, and mobility modeling and analysis of dense cellular networks with C-plane/U-plane split architecture.

### 2.2.1 Performance Modeling and Analysis of Uplink Two-Tier IoT Networks

Existing works on performance modeling and analysis of large-scale IoT networks have considered *machine-to-machine (M2M) communications*. Malak et al. [9] develop models that characterize the coverage and rate of M2M devices under different transmission schemes. Malak et al. [10] extended the work in [9] to minimize the energy consumed through a joint optimization of the number of multi-hop stages and the fraction of aggregators. Haenggi and Puccinelli [11] investigate the effect of increasing the numbers of hops on the energy consumption introduced by relays.

Research on *performance modeling and analysis of two-hop IoT networks* has appeared recently, especially for uplink two-phase cellular-based massive machine type communication (mMTC) networks [12, 13, 14, 15, 16]. Guo et al. [12] study scheduling in uplink two-phase cellular-based mMTC network, where devices transmit to aggregators (i.e., aggregation phase) and the aggregated data is then relayed to base stations (i.e., relaying phase). Lopez et al. [13] extend the resource scheduling schemes proposed in [12] to study the system performance in terms of average success probability and average number of simultaneously served machine type devices. Rao and Shorey [16] study different device-aggregator association schemes, namely, fixed, random, and greedy association. The authors show that channel-aware resource scheduling (CRS) outperforms random resource scheduling (RRS) in terms of SIR.

*Delay performance of two-hop IoT networks* has been studied recently [15], [92], and [93]. Rigazzi et al. [15] study the trade-off between packet latency and the transmission power in the uplink direction of mMTC networks. Kim et al. [92] show that the use of aggregator nodes can reduce the per-hop delay as well as the device energy consumption by reducing the transmission distance from devices. Yang et al. [93] propose a stochastic geometry model to assess and characterize buffer-aided tandem networks consisting of relay nodes and multiple channels per hop. The authors observe lower latency requires an increase in the transmission power. Kim et al. [92] investigate the delay performance of two-stage of IoT uplink transmission with random access.

*Resource allocation and energy efficiency of two-hop IoT networks* have been recently investigated [17, 18, 19, 20, 21, 22, 16]. Resource allocation to perform device grouping and an energy-efficiency cluster head selection scheme was developed in [17, 18, 19, 20, 21] to maximize the network life. Wael and Rezki [22] study the reliability enhancement and resource allocation of smart metering systems using the millimeter wave technology in two-phase uplink networks with wireless gateways. Kim et al. [14] study the effect of packet bundling at the aggregator, which reduces the overhead and resource waste in mMTC networks when small packets are sent.

Despite previous research efforts, e.g., [92, 94, 9, 93, 10, 11, 12, 13, 14, 15, 16, 77, 22, 17, 18, 19, 20, 21], to the best of our knowledge, there has been no previous work that focuses on modeling and analysis of the mean DRUF of devices in the uplink direction of two-hop IoT cellular networks. Our work in **Chapter 3** is the first that mathematically models the log utility of data rate over two consecutive links in the uplink direction (i.e., data from a device to an aggregator to a MBS). Providing such a rigorous model which fills the gap in the literature is the main contribution of this thesis. The result will allow network operators to improve data rates of IoT links and ensure data fairness among devices.

### 2.2.2 Performance Modeling and Analysis of Coexisting Sub-6GHz and Millimeter-wave IoT Cellular Networks

A variety of research works studied the *coverage analysis of mm-wave only cellular networks* [23, 24, 25, 26]. For instance, Di Renzo et al. [23] proposed a general mathematical model to analyze multi-tier mm-wave cellular networks. Bai et al. [24] derived the coverage and rate performance of mm-wave cellular networks. They used a distance dependent line-of-sight (LOS) probability function where the locations of the LOS and non-LOS (NLOS) BSs are modeled as two independent non-homogeneous Poisson point processes, to which different path loss models are applied. The authors assume independent Nakagami fading for each link. Different parameters of Nakagami fading are assumed for LOS and NLOS links. Turgut and Gursoy [25] investigated heterogeneous downlink mm-wave cellular networks consisting of $K$ tiers of randomly located BSs where each tier operates in a mm-wave frequency band. They derived coverage probability for the entire network using tools from stochastic geometry. They used Nakagami fading to model small scale fading. Deng et al. [26] derived the success probability at the typical receiver in mm-wave device-to-device (D2D) networks. The authors modeled fading channel power as Nakagami fading and incorporated directional beamforming.

Some recent studies analyzed the *success probability* of coexisting $\mu$wave and mm-wave cellular networks. A hybrid cellular network was considered by Singh et al. [27] to estimate the uplink-downlink coverage and rate distribution of self-backhauled mm-wave networks. Elshaer et al. [28] developed an analytical model to characterize decoupled uplink and downlink cell association strategies. The authors showed the superiority of this technique compared to the traditional coupled association in a network with traditional MBSs coexisting with denser mm-wave SBSs. Singh et al. [27] and Elshaer et al. [28] modeled the fading power as Rayleigh fading to enable better tractability.

Compared to traditional coverage analysis conducted in [25,29,28], Deng and Haenggi [30] analyzed the meta distribution of the SIR in *mm-wave only single-hop* D2D networks using the *Poisson bipolar model* and simplified *Rayleigh fading channels* for analytical tractability.

To the best of our knowledge, our work in **Chapter 4** is the first to characterize the meta distributions of SIR/SNR and data rate for coexisting $\mu$wave and mm-wave networks. Different from previous research in [25,29,28,30], we develop a stochastic geometry framework that takes in consideration (i) coexistence of two different network tiers with completely different channel propagation, interference, and fading models, (ii) dual-hop transmissions enabled by two different spectrums, one in each network tier, and (iii) Nakagami-m fading model with shape parameter $m$ for LOS mm-wave channels. Nakagami-m fading is a generic and versatile distribution that includes Rayleigh distribution (typically used for non-LOS fading) as its special case when $m = 1$ and can well approximate the Rician fading distribution for $1 \leq m \leq \infty$ (typically used for LOS fading).

### 2.2.3 Mobility Modeling and Analysis of Dense Cellular Networks with C-plane/U-plane Split Architecture

Since future heterogenous cellular networks and large-scale IoT networks exhibit random topologies rather than idealized grids, stochastic geometry is widely accepted as a tool to model cellular networks [63]. The past five years have witnessed a plethora of stochastic geometry based models that tackles different aspects in cellular networking [63,31,32,3,33,34,35,36,37,38,39,40]. However, the majority of these models do not account for mobility and focus on stationary users performance. For instance, coverage probability and rate performance are characterized for single-antenna downlink connections in [31,32,3], for single-antenna uplink connections in [33, 34], and for downlink connections with multiple antennas in [35, 36]. Stochastic geometry also helps characterizing the performance of CP/UP split architecture in cellular networks. For instance, the energy efficiency gains provided by the CP/UP split architecture are characterized by Zakrzewska et al. [38]. The effect of vertical offloading and BS sleeping on the energy efficiency for CP/UP split architecture is studied by Zhang et al. [39]. In our pervious work [40], the throughput of the CP/UP split cellular architecture is studied. However, none of the aforementioned studies incorporates the effect of mobility and handover into the analysis.

Surprisingly, few models can be found in the literature that exploit stochastic geometry to characterize mobility in large-scale IoT networks and cellular networks. The handover rate in cellular networks is first characterized by Lin et al. [41], in which expressions for the handover rate are derived for random waypoint mobility model in a single-tier cellular network. The handover rate for multi-tier cellular networks is characterized by Bao and Liang [42] for arbitrary mobility model. However, neither [41] nor [42] investigates the effects of handover on important performance metrics such as coverage, rate, or delay. The handover effects on coverage and rate are investigated by Sadr and Adve [43] for random way point mobility model. The authors derive the probability of handover and use the coverage probability for stationary users multiplied by a handover cost factor to infer the coverage probability for users experiencing handovers. Note that the handover cost factor in [43] is considered as a network parameter that reflects the SINR degradation during handovers. Zhang et al. [44] investigate the effect of delay-reliability tradeoff in dense cellular networks for static and high mobility users under a time slotted transmission scheme. The authors show that high mobility users outperform static users because mobile users experience uncorrelated SINRs across different time slots. However, the results in [44] may be misleading because the model only captures the positive impact of mobility and overlooks the performance degradation that may occur due to handover signaling and delay. Finally, Ge et al. [45] develop a socialactivity aware mobility model, denoted as the individual mobility model, to represent the users clustering behavior in a two-tier cellular network. Assuming a single social community, located at the origin, which is covered by densely deployed SBSs, the coverage probability inside and outside the social community as well as the probabilities to arrive, depart, and stay in the social community are derived. However, the analysis in [45] is only valid for finite networks where the social community inhabits a non-negligible portion of the total network and overlooks the effect of handovers. It is worth mentioning that, similar to [43], the authors of [44] and [45] use the stationary SINR analysis to infer the coverage probability of moving users.

Different from the existing literature, in **Chapter 5**, we propose a mobility-aware paradigm that captures the handover effect on the devices throughput in conventional and CP/UP network architectures. Different from [43], the handover cost is not assumed and is rigorously derived from the system model. Also, different from [44] and [45], the developed model accounts for the handover effect and is not tailored to a specific mobility model. Furthermore, the developed model accounts for signaling overhead, flexible device association scheme via association biasing, the availability of X2 interface between BSs, and almost blank subframes (ABS) coordination between MBSs and SBSs.

# Chapter 3

# Data Rate Utility Analysis for Uplink Two-Tier IoT Networks

## 3.1 Motivations and Contributions

The Internet of Things (IoT) and machine-to-machine (M2M) communications will revolutionize the way we live our lives by all means. Aided by the ubiquitous wireless connectivity, decreasing communication costs, and the proliferation of cloud platforms, the deployment of IoT devices and services is accelerating [95, 96, 97, 98]. Therefore, integrating IoT and M2M communications in 5G cellular networks [99, 100, 101, 102, 40, 42, 103, 104] is a critical and important research area that must be addressed and well understood.

In this chapter, we study two-hop IoT cellular networks composed of two tiers. Tier 1 consists of macro base stations (MBSs) with higher transmission power (in the downlink direction) and lower deployment density. Tier 2 consists of aggregators with lower transmission power (in the downlink and uplink directions) and high density deployment. Fig. 3.1 shows an example of such a two-hop network. The aggrerators collect (aggregate) data from the devices and forward the data to MBSs. Energy-constrained devices can save energy by sending data to closer aggrerators (data aggregation) instead of transmitting to much farther

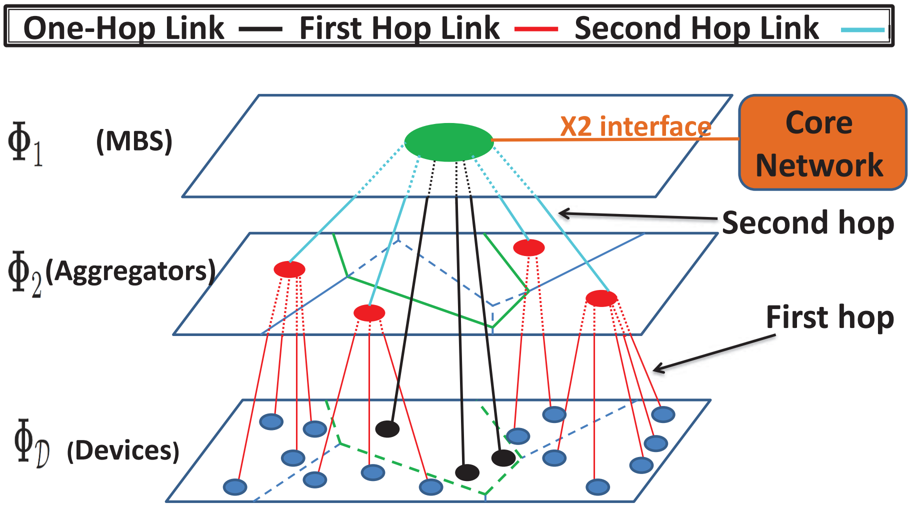

Figure 3.1: Uplink two-hop IoT communication networks. The blue devices communicate with the core network via two-hop communications. The black devices communicate with the core network via one-hop communications.

MBSs [10, 17, 18, 19, 20, 21].

In a two-hop IoT network, if a device (sensor or actuator) is connected to an aggregator, the device sends data to the core network via a two-hop connection: first to the aggregator, which then forwards the data to the MBS[1], which then forwards the data to the core network as shown in Fig. 3.1. Note that aggregators are not directly connected to the core network: an aggregator relays data from a device to a MBS, which then forwards the data to the core network, hence two-hop communications between the device and the core network. In Fig. 3.1, the blue devices communicate with the core network via two-hop communications.

Following is the main reason for using aggregators and two-hop communications in our IoT network architecture. There is usually a huge number of devices in IoT cellular networks. Therefore it would not be scalable (or would be too expensive) to provide direct wireless access between each device and a base station. Data aggregation has been proposed by

---

[1] We assume that MBSs are connected to the core network by separate high-capacity wired or wireless links X2 whose capacity has no impact on our performance analysis.

[105, 106, 107, 108] to deal with this massive connection problem. Using aggregators is a scalable and inexpensive approach to provide gateways and indirect Internet access to a huge number of IoT devices, and is widely accepted in the literature [12, 13, 14, 15, 16, 22].

Note that in the above IoT architecture, a device can connect directly to a MBS. In this case, the device can communicate with the core network via one-hop communication because the MBS is connected directly to the core network. This results in a hybrid network, in the sense that communications between devices and the core network can be either one-hop or two-hop, depending on whether a device is connected to a MBS (one-hop) or an aggregator (two-hop).

The above hybrid IoT architecture is different from conventional two-tier cellular networks, in which all MBSs in the upper tier and all small-cell base stations in the lower tier are directly connected to the core network. Therefore, in a conventional two-tier network, all communications between devices and the core network are via one-hop communications. The above difference distinguishes our work in this chapter from existing works [109, 31, 3] which focus on conventional two-tier networks using one-hop communications.

High density deployments of two-hop IoT networks face the serious challenge of mitigating interference caused by a huge number of devices. Interference reduces uplink data rates of devices, and as a result, negatively impacts their operational reliability. IoT devices need guaranteed minimum data rates in order to perform their tasks effectively and reliability. Thus our objective in this chapter is to improve the data rate of devices and to ensure the rate fairness among devices.

Existing works on performance modeling and analysis of IoT networks have focused on estimating the coverages and data rates of different transmission schemes for multi-hop uplink communications in M2M networks [9, 10, 11]. Recently, works on performance modeling and analysis of two-hops IoT networks have appeared in [12, 13, 14, 15, 16]. Among these [12] and [13] address the problem of scheduling in uplink two-phase cellular-based massive machine type communication (mMTC) networks. Kim et al. [14] study the optimal settings of the network parameters in terms of the number of aggregators and packet-bundle size. Rigazzi et al. [15] investigate trade-off between the packets latency and the transmission power. Rao et al. [16] study the performance of different device-aggregator association schemes. Research on resource allocation and energy efficiency of two-hop IoT networks has recently appeared [17,18,19,20,21,22]. An energy-efficiency cluster head selection scheme and resource allocation to perform device grouping were proposed in [17, 18, 19, 20, 21] to maximize the network life. However, the problem of determining the mean uplink data rate utility over two consecutive hops in the uplink direction (i.e., from devices to aggregators to MBSs) has not been addressed in the literature.

Having identified this gap in the literature, we develop a novel analytical model to estimate the *mean data rate utility function* (DRUF) in the uplink direction of a two-hop IoT network to ensure rate fairness among devices (i.e., by maximizing the log of the uplink DRUF) and to improve device data rates. To the best of our knowledge, our work is the first that proposes an analytical model to estimate the log of the uplink DRUF of a two-hop IoT network. This estimate is critical in the design and deployment of IoT networks in order to improve the data rate of IoT links and to ensure rate fairness among devices.

Following are the methodology and organization of our work in this chapter:

- In Section 3.3, we derive mathematical expressions for the uplink mean data rate utility functions (DRUF), expressed in terms of $\log_2$(Mbps), in two-hop IoT networks under both the FSR and OSP schemes.

- Since the DRUF expressions are not in closed form, optimal solutions in closed form are not attainable for the optimal aggregator association bias (for the FSR scheme) or the optimal joint spectrum partition ratio and aggregator association bias (for the OSP scheme). Therefore, in Section 3.4, we use constraint gradient ascent optimization to obtain the optimal aggregator association bias (for the FSR scheme) and the optimal joint spectrum partition ratio and aggregator association bias (for the OSP scheme). We confirm the accuracy of the developed constraint gradient ascent optimization algorithms using simulations.

- Using the above obtained optimal values and the proposed model, in Section 3.5, we validate the accuracy of the proposed analytical model. We then compare the performance of the optimized OSP and FSR schemes with the benchmark maximum-SIR based association scheme and minimum-distance association scheme in terms of the device uplink data rate.

The above model and analysis provide us with valuable design insights. By optimizing key network parameters, namely, the spectrum partition ratio and aggregator association bias, we can mitigate interference and enhance the mean uplink per-device data rate for both FSR and OSP spectrum allocation schemes. By determining the optimal aggregator association bias (the joint optimal uplink spectrum partition ratio and aggregators association bias) for two-hop IoT networks under the FSR (OSP) allocation scheme, we enhance the performance of devices in terms of the CDF of the uplink device data rate (Mbps) for different interference levels. Our proposed optimization method are expected to be used by cellular network operators providing 5G and IoT technologies to mitigate high interference in dense deployments of two-hop IoT networks, to improve the data rate and reliability of devices, and to ensure the rate fairness among devices (i.e., by maximizing the log utility function of data rate).

The remainder of the chapter is organized as follows. In Section 3.2, we describe the system model and assumptions. In Section 3.3, we define the analytical model that characterizes the device uplink mean DRUF for two-hop IoT networks under both the FSR and OSP schemes. In Section 3.4, we obtain the optimal aggregator association bias (for the FSR scheme) and the optimal joint spectrum partition ratio and optimal aggregator association bias (for the OSP scheme) using constraint gradient ascent optimization algorithms. We validate the accuracy of proposed analytical model and evaluate the optimized resource allocation schemes in Section 3.5. Section 3.6 concludes the chapter.

## 3.2 System Model and Assumptions

In this section, we describe the network model, assumptions, and important parameters, namely, association criteria (Section 4.2.4), pathloss model, power control, and transmission model (Section 3.2.3), spectrum allocation (Section 3.2.4), and uplink $SIR$ coverage probability (Section 3.2.5).

### 3.2.1 Network Model

We consider a hybrid two-tier IoT network as illustrated in Fig. 3.1. We assume that devices can connect directly to MBSs (one-hop communication) or indirectly via aggregators (two-hop communication). As in [109, 31, 3, 110], the location of the MBSs and aggregators are modeled as a two-dimensional homogenous Poisson point process (PPP) $\mathbf{\Phi}_k = \{\mathbf{y}_{k,1}, \mathbf{y}_{k,2}, ...\}$ of density $\lambda_k$, where $\mathbf{y}_{k,i}$ is the location of the $i^{th}$ MBS (when $k = 1$) or the $i^{th}$ aggregator (when $k = 2$). Let the MBS tier be tier 1 ($k = 1$) and the aggregators constitute tier 2 ($k = 2$). Let $\mathcal{D}$ denote the set of devices. The locations of devices in the network are modeled as independent homogenous PPP $\mathbf{\Phi}_{\mathcal{D}} = \{\mathbf{x}_1, \mathbf{x}_2, ....\}$ with density $\lambda_{\mathcal{D}}$, where $\mathbf{x}_i$ is the location of the $i^{th}$ device. We assume that $\lambda_{\mathcal{D}} >> \lambda_2 > \lambda_1$ as in [107]. Similar to [12], [10], [111], and [112], we do not model random access in the network and assume that the devices have been granted access to the network. We do not analyze the size of transmitted data, as in [10], because it is out of the scope of this chapter. A list of the key mathematical notations used in this chapter is given in Table 3.1.

A two-hop IoT network can be constructed from any configuration of the three PPPs $\mathbf{\Phi}_1$, $\mathbf{\Phi}_2$, and $\mathbf{\Phi}_{\mathcal{D}}$, where each device of the PPP $\mathbf{\Phi}_{\mathcal{D}}$ associates with either an aggregator from PPP $\mathbf{\Phi}_2$ or with a MBS from PPP $\mathbf{\Phi}_1$ based on the maximum biased downlink received signal power from either MBSs or aggregators.

A hybrid network of one-hop and two-hop uplink connections with MBSs is an effective topology to increase data rate and reduce power consumption.

Table 3.1: Mathematical notations used in Chapter 3

| **Notation** | **Description** |
|---|---|
| $\boldsymbol{\Phi}_1;\boldsymbol{\Phi}_2;\boldsymbol{\Phi}_{\mathcal{D}}$ | PPP of MBSs; aggregators; devices. |
| $\lambda_1;\lambda_2;\lambda_{\mathcal{D}}$ | Densities of tier-1 MBSs;tier-2 aggregators; devices. |
| $P_1;P_2$ | Downlink transmit power of MBS-tier; aggregator-tier. |
| $P_{\mathcal{D}};P_A$ | Uplink transmit power of devices; aggregator-tier. |
| $\epsilon_1;\epsilon_2$ | Power control fraction for devices; aggregator-tier. |
| $B_1;B_2$ | Association bias for MBS-tier;aggregator-tier. |
| $\eta$ | Spectrum partition ratio between MBS-tier and aggregator-tier. |
| $\alpha$ | Path loss exponent. |
| $R_{\mathcal{D},1};R_{\mathcal{D},2};R_{2,1}$ | Data rate of Direct link;Indirect Link ($1^{st}$ hop); Indirect Link ($2^{nd}$ hop). |
| $\mathcal{A}_1;\mathcal{A}_2$ | Typical device association probability to tier-1;tier-2. |
| $\zeta_{\mathcal{D},1};\zeta_{\mathcal{D},2};\zeta_{2,1}$ | Spectrum allocated to a device associated to tagged MBS;a device associated to tagged aggregator; to aggregator associated to tagged MBS. |
| $h(\mathbf{x},\mathbf{y})$ | Rayleigh fading channel gain between two locations $\mathbf{x}$, $\mathbf{y}$. |
| $U$ | Uplink mean data rate utility function. |
| $\tau_1;\tau_2$ | Target SIR at MBSs;aggregators. |
| $\Theta(\alpha,\epsilon_1);\Theta(\alpha,\epsilon_2)$ | $\frac{1}{2}\Gamma\left[1+\frac{(1-\epsilon_1)\alpha}{2}\right];\frac{1}{2}\Gamma\left[1+\frac{(1-\epsilon_2)\alpha}{2}\right]$ |
| $G(\alpha,\epsilon_1);G(\alpha,\epsilon_2)$ | $\frac{1}{2(\alpha-2)}\Gamma\left[\frac{\alpha}{2}(\epsilon_1-1)+2\right];\frac{1}{2(\alpha-2)}\Gamma\left[\frac{\alpha}{2}(\epsilon_2-1)+2\right]$ |
| $Q(\alpha,\epsilon_1);Q(\alpha,\epsilon_2)$ | $G(\alpha,\epsilon_1)\Theta(\alpha,\epsilon_1);G(\alpha,\epsilon_2)\Theta(\alpha,\epsilon_2)$ |
| $\ddot{\boldsymbol{\alpha}};\ddot{\boldsymbol{\beta}}$ | Backtracking line search parameters |
| $\nu$ | Gradient ascent stopping parameter |

- *One-hop connection*: Devices associate with tier-1 MBSs directly using one-hop connection based on the maximum downlink received power from MBSs and measured at the devices. Let $L_{\mathcal{D},1}$ denote the one-hop connection between a device and a MBS. Let $R_{\mathcal{D},1}$ denote the uplink data rate of the one-hop link for the scheduled device.

- *Two-hop connection*: Devices connect to a tier-2 aggregator based on the maximum biased received power from the aggregators and measured at the devices. Let $L_{\mathcal{D},2}$ denote the *first hop* of the two-hop connection, from devices to aggregators. Then, aggregators send their aggregated data to MBSs. Aggregators associate with MBSs based on the maximum received power from MBSs and measured at the aggregators. Let $L_{2,1}$ denote the *second hop* of the two-hop connection, from devices to aggregators. Note that the uplink traffic goes through two consecutive links $L_{\mathcal{D},2}$ and $L_{2,1}$. The link with the minimum data rate becomes the bottleneck link and determines the end-to-end throughput of the indirect uplink connection. We assume no buffering capability at aggregators. Thus, the data rate for the scheduled device in the indirect uplink connection is $R = min(R_{\mathcal{D},2}, R_{2,1})$.

### 3.2.2 Association Criteria

Device associations (downlink and uplink) are determined based on the maximum biased downlink received power from aggregators or MBSs, which is measured at devices. A device located at location $\mathbf{x}$ associates with a tier-1 MBS or a tier-2 aggregator if it provides the maximum biased received power [3]:

$$P_k B_k (\min_i \|\mathbf{y}_{k,i} - \mathbf{x}\|)^{-\alpha} \geq P_j B_j (\min_{i'} \|\mathbf{y}_{j,i'} - \mathbf{x}\|)^{-\alpha}, \forall j \tag{3.1}$$

where $\|.\|$ denotes the Euclidean distance, and $B_1$ and $B_2$ are the association bias for MBSs and aggregators, respectively. The association bias $B_2$ artificially encourages/discourages devices to associate with the aggregator tier [3]. Note that we do not consider association bias between aggregators and MBSs. Therefore, aggregator associations with MBSs are determined based on the maximum downlink received power from MBSs, which is measured at aggregators, i.e., $B_1 = 1$. In the uplink direction, the association is the same as the downlink, i.e., a device or aggregator associates with the same serving node (given by Eq. (4.2)), which is termed ***tagged node*** (tagged aggregator or tagged macro base station). We assume that both network tiers have the same path loss exponent $\alpha_1 = \alpha_2 = \alpha$. For the sake of clarity of exposition, we define $\hat{P}_{jk} \triangleq \frac{P_j}{P_k}$, $\hat{B}_{jk} \triangleq \frac{B_j}{B_k}$, $\hat{\lambda}_{jk} \triangleq \frac{\lambda_j}{\lambda_k}$.

Let $\mathcal{A}_k$ denote the probability that a device associates itself with a MBS (when $k = 1$) or with an aggregator (when $k = 2$). As derived in [113], the association probability of the devices to tier $k$ ($k = 1, 2$) is as follows:

$$\mathcal{A}_k = \frac{\lambda_k (P_k B_k)^{\frac{2}{\alpha}}}{\sum_{j=1}^{2} \lambda_j (P_j B_j)^{\frac{2}{\alpha}}} = \left( \sum_{j=1}^{2} \hat{\lambda}_{jk} (\hat{P}_{jk} \hat{B}_{jk})^{\frac{2}{\alpha}} \right)^{-1}. \tag{3.2}$$

The probability density function (PDF) $f_{d_{\mathcal{D},2}}$ of the distance $d_{\mathcal{D},2}$ between a typical device and its tagged aggregator located at the origin (or the PDF $f_{d_{\mathcal{D},1}}$ of the distance $d_{\mathcal{D},1}$ between a typical device to its tagged MBS located at the origin) under the association criteria given in [3] is as follows:

$$\begin{aligned} f_{d_{\mathcal{D},k}}(r) &= \frac{2\pi r \lambda_k}{\mathcal{A}_k} \exp\left( -\pi r^2 \sum_{j=1}^{2} \lambda_j (\hat{P}_{jk} \hat{B}_{jk})^{\frac{2}{\alpha}} \right) \\ &\overset{(a)}{=} \frac{2\pi r \lambda_k}{\mathcal{A}_k} \exp\left( \frac{-\pi r^2 \lambda_k}{\mathcal{A}_k} \right), r \geq 0, \end{aligned} \tag{3.3}$$

where $(a)$ follows Eq. (3.2).

### 3.2.3 Pathloss Model, Power Control, and Transmission Model

A general power law path loss model is considered in which the signal power decays at rate $d^{-\alpha}$ with the distance $d$, where $\alpha$ is the path loss exponent ($\alpha > 2$). Let $h(\mathbf{x}, \mathbf{y})$ denote the channel gain (fast fading term) between two generic locations $\mathbf{x}$, $\mathbf{y} \in \mathbb{R}$. The channel gain $h(\mathbf{x}, \mathbf{y}) \sim \exp(1)$ is independently exponentially distributed with unit mean (Rayleigh fading with power normalization). We ignore shadowing[2] in the analysis for tractability. Every aggregator or MBS of the $k^{th}$ tier transmits with the same transmit power $P_k$ in the downlink. In the uplink direction, we assume that devices ($\mathbf{\Phi}_{\mathcal{D}}$) and tier-2 aggregators ($\mathbf{\Phi}_2$) use fractional power control [77] that partially compensates for path loss. Let a device be located at $\mathbf{x}$ and associated with a tagged node (aggregator or MBS) at location $\mathbf{y}$. The

---

[2] Note that more general fading/shadowing distributions can be taken into consideration as in [54], but it comes at the expense of tractability and without much change to the results.

received power at the tagged node is $P_{\mathcal{D}}\|\mathbf{y}-\mathbf{x}\|^{(\epsilon_1-1)\alpha}h(\mathbf{x},\mathbf{y})$, where $0 \leq \epsilon_1 \leq 1$ is the PCF for devices. Let $P_{\mathcal{A}}$ be the aggregator transmit power in the uplink direction before performing fractional power control. Let an aggregator be located at $\mathbf{x}'$ and associated with a MBS at location $y$. Therefore, the received power at the serving MBS is $P_{\mathcal{A}}\|\mathbf{y}-\mathbf{x}'\|^{(\epsilon_2-1)\alpha}h(\mathbf{x}',\mathbf{y})$.

### 3.2.4 Spectrum Allocation

We focus on uplink transmission analysis. We assume that uplink and downlink transmissions in our model are separated via FDD or TDD and they are treated independently. As a result, downlink interference and capacity have no influence on uplink analysis. There is no spectrum sharing or dynamic spectrum partitioning between the uplink and downlink. Both FSR and OSP are considered among tier 1 and tier 2. Let $W$, $W_1$, and $W_2$ denote the total available spectrum bandwidth for the network, the spectrum allocated to MBSs, and the spectrum allocated to aggregators, respectively.

There are two spectrum partitioning schemes available for two-tier cellular networks: *full spectrum reuse* (FSR) and *orthogonal spectrum partition* (OSP). We consider both schemes in our model. In the *FSR scheme*, all aggregators and all MBSs in the network share the entire spectrum band, i.e., $W_1 = W_2 = W$. In the *OSP scheme* each tier is allocated a non-overlapping frequency band, i.e., $W_1 = \eta W$ and $W_2 = (1-\eta)W$, where $\eta$ is the spectrum partition ratio between tier 1 and tier 2 and $W = W_1 + W_2$.

We assume a fully loaded network, i.e., each aggregator and MBS has an active uplink transmission from a scheduled device or aggregator for each time-frequency resource block. We assume that the available spectrum at a node (MBS or aggregator) is shared equally among the associated devices or aggregators. Similarly, all aggregators associated with a MBS are assigned the same amount of bandwidth. This is can be achieved by using round robin scheduling which results in such an equipartition of resources [94].

### 3.2.5 Uplink SIR Coverage Probability

The uplink coverage probability is defined as the complementary cumulative distribution function (CCDF) of SIR:

$$C_k = \mathbb{P}[SIR > \tau_k], \tag{3.4}$$

where $\tau_k$ denotes the predefined threshold for correct signal reception at a tagged MBS ($k = 1$) or tagged aggregator ($k = 2$). We assume that the network under consideration is interference limited and the background noise is negligible. Following [114], in each resource block we assume that devices and aggregators do not get positive data rate in the uplink direction unless the $SIR$ is higher than the predefined $\tau_k$. We assume a fixed modulation and coding scheme where the data rate is constant when the SIR is greater than $\tau_k$. Therefore, the average spectral efficiency ($\mathcal{SE}$) measured in nats/sec/Hz for a randomly chosen device or aggregator is as follows:

$$\mathcal{SE}_k = \log(1 + \tau_k)\mathbb{1}(SIR_k > \tau_k), \tag{3.5}$$

where $\mathbb{1}(.)$ is the indicator function. The device or aggregator data rate is calculated by summing the above spectral efficiencies across the spectrum $\zeta_k$ assigned to this device or aggregator. The mean of device or aggregator uplink data rate is as follows:

$$R_k = \zeta_k \mathbb{E}(\mathcal{SE}_k) = \zeta_k C_k \log(1 + \tau_k). \tag{3.6}$$

## 3.3 Proposed Analytical Model: Device Uplink Mean Data Rate Utility Function

In this section, we characterize the uplink mean DRUF of a typical device. We use the law of total probability for a typical device, which is connected to the core network via either one-hop or two-hop communication. By calculating the uplink mean data rate of a typical device and a typical aggregator, we obtain the mean performance of the entire network under study. In this chapter, we adopt a notion of the coverage-rate-based proportionally fair utility, defined as the logarithm of the user coverage rate. Using assumptions made in Section 3.2.1, let $U$ denote the mean DRUF which is given by the following equation:

$$\begin{aligned}
U &= \underbrace{\mathcal{A}_1 U_{\mathcal{D},1}}_{\text{One-hop data rate utility}} + \underbrace{\mathcal{A}_2 \min\left(U_{\mathcal{D},2}, U_{2,1}\right)}_{\text{Two-hop data rate utility}}, \\
U &= \mathcal{A}_1 U_{\mathcal{D},1} + \mathcal{A}_2 \mathbb{E}_{\mathbf{\Phi}_1,\mathbf{\Phi}_2,\mathbf{\Phi}_{\mathcal{D}}}\left[\mathbb{E}_h\left[\log[R]\right]\right], \\
U &= \mathcal{A}_1 U_{\mathcal{D},1} + \mathcal{A}_2 \mathbb{E}_{\mathbf{\Phi}_1,\mathbf{\Phi}_2,\mathbf{\Phi}_{\mathcal{D}}}\left[\mathbb{E}_h\left[\log[\min(R_{\mathcal{D},2}, R_{2,1})]\right]\right]. \qquad (3.7)
\end{aligned}$$

The proportionally fair utility (logarithm of the device coverage rate) captures a tradeoff between opportunism and device fairness, by encouraging low rate users to improve their rates while saturating the utility gain of high-rate users. We now compute the first term (one-hop data rate utility) and the second term (two-hop data rate utility) of Eq. (3.7) in Sections 3.3.1 and 3.3.2, respectively. In Section 3.3.3, we discuss the computation of the sum of first and second terms of Eq. (3.7) to obtain $U$.

### 3.3.1 One-hop Connection Data Rate

In this section, we compute the first term of Eq. (3.7), which is the expected average logarithm of the data rate of the devices that have one-hop connections to MBSs. The DRUF $U_{\mathcal{D},1}$ is given by:

$$\begin{aligned}
U_{\mathcal{D},1} &= \mathbb{E}[\log(R_{\mathcal{D},1})], \\
&= \mathbb{E}[\log(\zeta_{\mathcal{D},1})] + \mathbb{E}[\log(C_{\mathcal{D},1})] + \log[\log(1+\tau_1)], \qquad (3.8)
\end{aligned}$$

where $\zeta_{\mathcal{D},k}$ is the spectrum allocated to a device associated with a tagged MBS when $k = 1$ or a tagged aggregator when $k = 2$, and $\zeta_{2,1}$ is the spectrum allocated to an aggregator associated with the tagged MBS. We now compute the first and the second terms of Eq. (3.8), namely, the mean logarithm of allocated spectrum per device $\mathbb{E}[\log(\zeta_{\mathcal{D},1})]$ and the mean logarithm of uplink coverage probability for devices $\mathbb{E}[\log(C_{\mathcal{D},1})]$.

### Mean Logarithm of Allocated Spectrum Per Device $\mathbb{E}[\log(\zeta_{\mathcal{D},1})]$

We assume that all devices associated with MBSs or aggregators are assigned an equal amount of spectrum. Similarly, all aggregators associated with a MBS are assigned the same amount of spectrum. This is achieved by round-robin scheduling. Let $\mathcal{N}_{\mathcal{D},1}$ denote the average number of devices associated with a tagged MBS in tier 1 and sharing resources with a typical device. Then $\mathcal{N}_{\mathcal{D},1}$ is given by the following Eq. [31]:

$$\mathcal{N}_{\mathcal{D},1} = \mathbb{E}[\hat{\mathcal{N}}_{\mathcal{D},1}] = \frac{1.28\lambda_{\mathcal{D}}\mathcal{A}_1}{\lambda_1} + 1, \tag{3.9}$$

where $\hat{\mathcal{N}}_{\mathcal{D},1}$ is the total load of devices at the tagged MBS. Therefore, the mean logarithm of allocated spectrum per device based on the association criteria is as follows:

$$\mathbb{E}[\log(\zeta_{\mathcal{D},1})] \overset{(a)}{\leq} \log[\mathbb{E}(\zeta_{\mathcal{D},1})] = \log\left(\frac{W}{\mathcal{N}_{\mathcal{D},1}}\right) = \log\left(\frac{W\lambda_1}{1.28\lambda_{\mathcal{D}}\mathcal{A}_1 + \lambda_1}\right), \tag{3.10}$$

where (a) follows from Jensen's inequality [115] since log(.) is a monotonically increasing function and it is concave. We derived its upper bound $\log[\mathbb{E}(\zeta_{\mathcal{D},1})]$ to approximate $\mathbb{E}[\log(\zeta_{\mathcal{D},1})]$. Our simulation results in Section 3.5.1 show that the upper bound is quite tight.

### Mean Logarithm of Uplink Coverage Probability for Devices $\mathbb{E}[\log(C_{\mathcal{D},k})]$

Note that the derivation for $\mathbb{E}[\log(C_{\mathcal{D},k})]$ in this section can be used for the calculations of both the one-hop connection data rate when $k = 1$ and the two-hop connection date rate when $k = 2$. We now compute $\mathbb{E}[\log(C_{\mathcal{D},k})]$ for two spectrum allocation schemes: FSR and OSP.

### Full Spectrum Reuse Scheme

In the case of full spectrum reuse scheme, The mean logarithm of uplink coverage probability for devices $\mathbb{E}[\log(C_{\mathcal{D},k})]$ can be obtained as in the following lemma.

**Lemma 1.** *The mean logarithm of uplink coverage probability for devices* $\mathbb{E}[\log(C_{\mathcal{D},k})]$ *is as follows:*

$$\mathbb{E}_{\mathbf{\Phi}_1^0,\mathbf{\Phi}_2^0,\mathbf{\Phi}_{\mathcal{D}}^0,\Psi,d_{\mathcal{D},k},h}[\log(C_{\mathcal{D},k})] \approx -8\tau_k Q(\alpha,\epsilon_1)\sum_{j=1}^{2}\mathcal{A}_j(\hat{P}_{jk}\hat{B}_{jk})^{\epsilon_1-\frac{2}{\alpha}}. \tag{3.11}$$

*Proof.* See **Appendix A.1**. ■

**Orthogonal Spectrum Partition Scheme**

Let $I_{\Psi_k}$ denote the total interference from the set of devices $\mathbf{\Phi}_{\mathcal{D}}^k$ scheduled by the $k^{th}$ tier excluding the typical device. Then $I_{\Psi_k}$ is calculated as follows:

$$I_{\Psi_k} = \sum_{i:\mathbf{x}_{j,i}\in\mathbf{\Phi}_{\mathcal{D}}^j\setminus\mathbf{x}_{k,0}} P_{\mathcal{D}}R_{j,i}^{\epsilon_1\alpha}D_{j,i}^{-\alpha}h(\mathbf{x}_{j,i},0). \tag{3.12}$$

Therefore, the $SIR_{\mathcal{D},k}$ of a typical device associated with the $k^{th}$ tier is

$$SIR_{\mathcal{D},k} = \frac{P_{\mathcal{D}}d_{\mathcal{D},k}^{(\epsilon_1-1)\alpha}h(d_{\mathcal{D},k},0)}{I_{\Psi_k}}. \tag{3.13}$$

**Corollary 1.** *Therefore, the mean logarithm of the uplink coverage probability for devices in the case of no inter-tier interference can be obtained in the same way as in the case of the FSR scheme and is as follows:*

$$\mathbb{E}_{\mathbf{\Phi}_1^0,\mathbf{\Phi}_2^0,\mathbf{\Phi}_{\mathcal{D}}^0,\Psi,d_{\mathcal{D},k},h}[\log(C_{\mathcal{D},k})] = -8\tau_k Q(\alpha,\epsilon_1)\mathcal{A}_k. \tag{3.14}$$

*Proof.* See **Appendix A.1**. ■

### 3.3.2 Two-hop Connection Data Rate

In this section, we compute the second term in Eq. (3.7), $\mathcal{A}_2\mathbb{E}_{\mathbf{\Phi}_1,\mathbf{\Phi}_2,\mathbf{\Phi}_{\mathcal{D}}}\left[\mathbb{E}_h\left[\log[\min(R_{\mathcal{D},2},R_{2,1})]\right]\right]$, which is the average expected data rate of devices that have two-hop connections to MBSs through aggregators (i.e., the expected average of data rate of the two-hop links).

$$
\begin{aligned}
&\mathbb{E}_{\boldsymbol{\Phi}_1,\boldsymbol{\Phi}_2,\boldsymbol{\Phi}_\mathcal{D}}\left[\mathbb{E}_h[\log\{R\}]\right]\\
=&\mathbb{E}_{\boldsymbol{\Phi}_1^0,\boldsymbol{\Phi}_2^0,\boldsymbol{\Phi}_\mathcal{D}^0,d_{\mathcal{D},2},d_{2,1}}\left[\mathbb{E}_h[\log\{\min(R_{\mathcal{D},2},R_{2,1})\}]\right],\\
=&\mathbb{E}_{\boldsymbol{\Phi}_1^0,\boldsymbol{\Phi}_2^0,\boldsymbol{\Phi}_\mathcal{D}^0,d_{\mathcal{D},2},d_{2,1}}\Bigg[\log\Bigg\{\mathbb{P}\left(SIR_{\mathcal{D},2}>\tau_2\right)\mathbb{P}\left(SIR_{2,1}>\tau_1\right)\times\\
&\qquad\qquad\min\left[\zeta_{\mathcal{D},2}\log(1+\tau_2),\zeta_{2,1}\log(1+\tau_1)\right]\Bigg\}\Bigg],\\
\overset{(a)}{=}&\mathbb{E}_{\boldsymbol{\Phi}_1^0,\boldsymbol{\Phi}_2^0,\boldsymbol{\Phi}_\mathcal{D}^0,d_{\mathcal{D},2},d_{2,1}}\Bigg[\log\Bigg\{\mathbb{P}\left(SIR_{\mathcal{D},2}>\tau_2\right)\Bigg\}+\log\Bigg\{\mathbb{P}\left(SIR_{2,1}>\tau_1\right)\Bigg\}+\\
&\qquad\qquad\log\Bigg\{\min\left[\zeta_{\mathcal{D},2}\log(1+\tau_2),\zeta_{2,1}\log(1+\tau_1)\right]\Bigg\}\Bigg],\\
=&\mathbb{E}_{\boldsymbol{\Phi}_1^0,\boldsymbol{\Phi}_2^0,\boldsymbol{\Phi}_\mathcal{D}^0,d_{\mathcal{D},2},d_{2,1}}\Bigg[\log\Bigg\{\mathbb{P}\left(SIR_{\mathcal{D},2}>\tau_2\right)\Bigg\}\Bigg]+\mathbb{E}_{\boldsymbol{\Phi}_1^0,\boldsymbol{\Phi}_2^0,\boldsymbol{\Phi}_\mathcal{D}^0,d_{\mathcal{D},2},d_{2,1}}\Bigg[\log\Bigg\{\mathbb{P}\left(SIR_{2,1}>\tau_1\right)\Bigg\}\Bigg]+\\
&\qquad\qquad\mathbb{E}_{\boldsymbol{\Phi}_1^0,\boldsymbol{\Phi}_2^0,\boldsymbol{\Phi}_\mathcal{D}^0,d_{\mathcal{D},2},d_{2,1}}\Bigg[\log\Bigg\{\min\left[\zeta_{\mathcal{D},2}\log(1+\tau_2),\zeta_{2,1}\log(1+\tau_1)\right]\Bigg\}\Bigg],\\
\overset{(b)}{\leq}&\mathbb{E}_{\boldsymbol{\Phi}_1^0,\boldsymbol{\Phi}_2^0,\boldsymbol{\Phi}_\mathcal{D}^0,d_{\mathcal{D},2},d_{2,1}}\Bigg[\log\Bigg\{\mathbb{P}\left(SIR_{\mathcal{D},2}>\tau_2\right)\Bigg\}\Bigg]+\mathbb{E}_{\boldsymbol{\Phi}_1^0,\boldsymbol{\Phi}_2^0,\boldsymbol{\Phi}_\mathcal{D}^0,d_{\mathcal{D},2},d_{2,1}}\Bigg[\log\Bigg\{\mathbb{P}\left(SIR_{2,1}>\tau_1\right)\Bigg\}\Bigg]+\\
&\qquad\qquad\log\Bigg\{\mathbb{E}_{\boldsymbol{\Phi}_1^0,\boldsymbol{\Phi}_2^0,\boldsymbol{\Phi}_\mathcal{D}^0,d_{\mathcal{D},2},d_{2,1}}\left[\min\left[\zeta_{\mathcal{D},2}\log(1+\tau_2),\zeta_{2,1}\log(1+\tau_1)\right]\right]\Bigg\},
\end{aligned}
\tag{3.15}
$$

where $\boldsymbol{\Phi}_1^0$, $\boldsymbol{\Phi}_2^0$, $\boldsymbol{\Phi}_\mathcal{D}^0$ are Palm point processes for $\boldsymbol{\Phi}_1$, $\boldsymbol{\Phi}_2$, $\boldsymbol{\Phi}_\mathcal{D}$, respectively, and (a) follows from breaking the dependency between $SIR_{\mathcal{D},2}$ and $SIR_{2,1}$ for tractability [12, 10] and the accuracy of this assumption is verified later in Section 3.5.1, (b) follows from Jensen's inequality [115] since log(.) is a monotonically increasing function and concave. We approximate the following term: $\mathbb{E}_{\boldsymbol{\Phi}_1^0,\boldsymbol{\Phi}_2^0,\boldsymbol{\Phi}_\mathcal{D}^0,d_{\mathcal{D},2},d_{2,1}}\Bigg[\log\Bigg\{\min\left[\zeta_{\mathcal{D},2}\log(1+\tau_2),\zeta_{2,1}\log(1+\tau_1)\right]\Bigg\}\Bigg]$ with its upper bound as follows: $\log\Bigg\{\mathbb{E}_{\boldsymbol{\Phi}_1^0,\boldsymbol{\Phi}_2^0,\boldsymbol{\Phi}_\mathcal{D}^0,d_{\mathcal{D},2},d_{2,1}}\left[\min\left[\zeta_{\mathcal{D},2}\log(1+\tau_2),\zeta_{2,1}\log(1+\tau_1)\right]\right]\Bigg\}$. Our simulation results in Section 3.5.1 show that the upper bound is quite tight.

### Mean Logarithm of the Coverage Probability in the Uplink Direction for Aggregators $\mathbb{E}[\log(C_{2,1})]$

We compute $\mathbb{E}[\log(C_{2,1})]$, i.e., the second term in Eq. (3.15), under the two spectrum allocation schemes FSR and OSP.

#### Full Spectrum Reuse Scheme

The mean logarithm of the uplink coverage probability of a typical aggregator $\mathbb{E}[\log(C_{2,1})]$ can be obtained by the following lemma.

**Lemma 2.** *The mean logarithm of the uplink coverage probability of a typical aggregator* $\mathbb{E}[\log(C_{2,1})]$ *in the case of FSR scheme is as follows:*

$$\begin{aligned}\mathbb{E}_{\mathbf{\Phi}_1^0,\mathbf{\Phi}_2^0,\mathbf{\Phi}_{\mathcal{D}}^0,\Psi,d_{2,1},h}[\log(C_{2,1})] &\approx -8\tau_1 Q(\alpha,\epsilon_2)- \\ &8\pi P_{\mathcal{D}}\tau_1 P_{\mathcal{A}}^{-1}\lambda_1\left(\pi\lambda_1\right)^{(\epsilon_2-1)\frac{\alpha}{2}}\left(\frac{\mathcal{A}_1}{\pi\lambda_1}\right)^{1+\frac{\alpha}{2}(\epsilon_1-1)}\Theta(\alpha,\epsilon_2)G(\alpha,\epsilon_1). \quad (3.16)\end{aligned}$$

*Proof.* See **Appendix A.2**. ■

#### Orthogonal Spectrum Partition Scheme

In a given allocated spectrum resource block, the total interference received at the tagged MBS and generated by the set of aggregators $\mathbf{\Phi}_{\mathcal{A}}$ scheduled in tier 1, excluding the typical aggregator, is denoted by $I_{2,1}$. Therefore, $SIR_{2,1}$ is calculated as follows:

$$SIR_{2,1} = \frac{P_{\mathcal{A}} d_{2,1}^{(\epsilon_2-1)\alpha} h(\mathbf{y}'_{2,0},0)}{I_{2,1}}. \quad (3.17)$$

**Corollary 2.** *Therefore, the mean logarithm of the uplink coverage probability of an aggregator can be derived as in the case of the FSR scheme without inter-tier interference and is as follows:*

$$\begin{aligned}\mathbb{E}_{\mathbf{\Phi}_1^0,\mathbf{\Phi}_2^0,\mathbf{\Phi}_{\mathcal{D}}^0,\Psi,d_{2,1},h}[\log(C_{2,1})] &\approx -\tau_1 P_{\mathcal{A}}^{-1}\left(2\left(\pi\lambda_1\right)^{(\epsilon_2-1)\frac{\alpha}{2}}\Theta(\alpha,\epsilon_2)\right)\left(4(\pi\lambda_1)^{\frac{\alpha}{2}(1-\epsilon_2)}P_{\mathcal{A}}G(\alpha,\epsilon_2)\right), \\ &\approx -8\tau_1\Theta(\alpha,\epsilon_2)G(\alpha,\epsilon_2), \\ &\approx -8\tau_1 Q(\alpha,\epsilon_2). \quad (3.18)\end{aligned}$$

*Proof.* See **Appendix A.2**. ■

### Logarithm Mean of Minimum Data Rate Capacity of Two-Hop Connections

The logarithm mean of the minimum capacity of the two-hop data rate, i.e, the last term in Eq. (3.15), $\log\left\{\mathbb{E}_{\mathbf{\Phi}_1^0,\mathbf{\Phi}_2^0,\mathbf{\Phi}_{\mathcal{D}}^0,d_{\mathcal{D},2},d_{2,1}}\left[\min\left[\zeta_{\mathcal{D},2}\log(1+\tau_2),\zeta_{2,1}\log(1+\tau_1)\right]\right]\right\}$, is characterized by the following lemma.

**Lemma 3.** *The logarithm mean of the minimum capacity of the two-hop data rate is as follows:*

$$\log\left[\mathbb{E}_{\mathbf{\Phi}_1^0,\mathbf{\Phi}_2^0,\mathbf{\Phi}_{\mathcal{D}}^0,d_{\mathcal{D},2},d_{2,1}}\left[\min\left[\zeta_{\mathcal{D},2}\log(1+\tau_2),\zeta_{2,1}\log(1+\tau_1)\right]\right]\right] = \varphi(v,n,\mathcal{N}_{\mathcal{D},2},\mathcal{N}_{2,1},\zeta_{\mathcal{D},2},\zeta_{2,1},\tau_1,\tau_2), \tag{3.19}$$

*where* $\varphi(v,n,\mathcal{N}_{\mathcal{D},2},\mathcal{N}_{2,1},\zeta_{\mathcal{D},2},\zeta_{2,1},\tau_1,\tau_2) \triangleq \log\left[\int_0^\infty\left(\sum_{n=0}^{S_X(v)} g_X(n)\right)\left(\sum_{n=0}^{S_Z(v)} g_Z(n)\right)dv\right]$, $g_X(n) \triangleq \frac{3.5^{3.5}\Gamma(n+4.5)(\lambda_{\mathcal{D}}\mathcal{A}_2/\lambda_2)^n}{\Gamma(3.5)n!(3.5+\lambda_{\mathcal{D}}\mathcal{A}_2/\lambda_2)^{(n+4.5)}}$, $g_Z(n) \triangleq \frac{3.5^{3.5}\Gamma(n+4.5)(\lambda_2\mathcal{A}_1/\lambda_1)^n}{\Gamma(3.5)n!(3.5+\lambda_2\mathcal{A}_1/\lambda_1)^{(n+4.5)}}$, *and that* $\sum_{n=0}^\infty g_X(n) = 1$ *and* $\sum_{n=0}^\infty g_Z(n) = 1$. *Therefore,* $S_X(v) \triangleq \left\lfloor \frac{W_2\log(1+\tau_2)}{v} - 1\right\rfloor$ *and* $S_Z(v) \triangleq \left\lfloor \frac{W_1\log(1+\tau_1)}{v} - 1\right\rfloor$.

*Proof.* See **Appendix A.3**. ■

## 3.3.3 Device Uplink Total Average Data Rate

In this section, we derive the total uplink mean DRUF of devices for both the FSR scheme and OSP scheme as follows:

### Full Spectrum Reuse

The uplink mean data rate utility is computed by the following lemma.

**Lemma 4.** *In the case of FSR scheme, the uplink mean data rate utility is as follows.*

$$U = \mathcal{A}_1 \left( \log \left( \frac{W \lambda_1 \log(1+\tau_1)}{1.28 \lambda_{\mathcal{D}} \mathcal{A}_1 + \lambda_1} \right) - 8\tau_1 Q(\alpha, \epsilon_1) \sum_{j=1}^{2} \mathcal{A}_j (\hat{P}_{jk} \hat{B}_{jk})^{\epsilon_1 - \frac{2}{\alpha}} \right) - \mathcal{A}_2 8\tau_2 Q(\alpha, \epsilon_1) \sum_{j=1}^{2} \mathcal{A}_j (\hat{P}_{jk} \hat{B}_{jk})^{\epsilon_1 - \frac{2}{\alpha}}$$
$$- \frac{\mathcal{A}_2 \tau_1}{P_{\mathcal{A}}} \left( 2 \, (\pi\lambda_1)^{(\epsilon_2 - 1)\frac{\alpha}{2}} \, \Theta(\alpha, \epsilon_2) \right) \times \left( 4(\pi\lambda_1)^{\frac{\alpha}{2}(1-\epsilon_2)} P_{\mathcal{A}} G(\alpha, \epsilon_2) + 4\pi P_{\mathcal{D}} \left( \frac{\mathcal{A}_1}{\pi \lambda_1} \right)^{1 + \frac{\alpha}{2}(\epsilon_1 - 1)} \lambda_1 G(\alpha, \epsilon_1) \right) +$$
$$\mathcal{A}_2 \varphi(v, n, \mathcal{N}_{\mathcal{D},2}, \mathcal{N}_{2,1}, \zeta_{\mathcal{D},2}, \zeta_{2,1}, \tau_1, \tau_2). \tag{3.20}$$

*Proof.* See **Appendix A.4**. ■

### Orthogonal Spectrum Partition

The uplink mean data rate utility is computed by the following lemma.

**Lemma 5.** *In the case of OSP scheme, the uplink mean data rate utility is as follows:*

$$U = \mathcal{A}_1 \left( \log \left( \frac{W_1 \lambda_1 \log(1+\tau_1)}{1.28 \lambda_{\mathcal{D}} \mathcal{A}_1 + \lambda_1} \right) - 8\tau_1 Q(\alpha, \epsilon_1) \mathcal{A}_1 \right) +$$
$$\mathcal{A}_2 \Big( - 8\tau_2 Q(\alpha, \epsilon_1) \mathcal{A}_2 - 8\tau_1 Q(\alpha, \epsilon_2) + \varphi(v, n, \mathcal{N}_{\mathcal{D},2}, \mathcal{N}_{2,1}, \zeta_{\mathcal{D},2}, \zeta_{2,1}, \tau_1, \tau_2) \Big). \tag{3.21}$$

*Proof.* See **Appendix A.5**. ■

Since the DRUF expressions, Eq. (3.20) and (3.21), are not in closed form, optimal solutions in closed form are not attainable for the optimal aggregator association bias (for the FSR scheme) or the optimal joint spectrum partition ratio and aggregator association bias (for the OSP scheme). Therefore, in the following section, we use constraint gradient ascent optimization algorithms to obtain the optimal aggregator association bias (for the FSR scheme) and the optimal joint spectrum partition ratio and aggregator association bias (for the OSP scheme).

## 3.4 Computing the Optimal Aggregator Association Biases and the Optimal Spectrum Partition Ratio

In this section, we develop constraint gradient ascent optimization algorithms to obtain the optimal aggregator association bias (for the FSR scheme) and the optimal joint spectrum partition ratio and aggregator association bias (for the OSP scheme) in Section 3.4.1. Then we validate the accuracy of the optimal values in Section 3.4.2 using simulations.

### 3.4.1 Optimization Algorithms

The log utility of the uplink data rate function $U$ (i.e., the objective function) for the FSR and OSP schemes computed by Eq. (3.20) and (3.21), respectively, is complex. Part of Eq. (3.20) and (3.21), the term $\varphi(v, n, \mathcal{N}_{\mathcal{D},2}, \mathcal{N}_{2,1}, \zeta_{\mathcal{D},2}, \zeta_{2,1}, \tau_1, \tau_2)$, is in non-closed form. [This term is defined in Lemma A.3, Eq. (A.35)]. Therefore, an optimal solution in closed form is not attainable for the optimal aggregator association bias (for the FSR scheme) or the optimal joint spectrum partition ratio and optimal aggregator association bias (for the OSP scheme).

Thus we resort to the constraint gradient ascent optimization method to find the aforementioned optimal values, which generates local optimal solutions rapidly and accurately. The constraint gradient ascent optimization method determines the local maximum, which can also be considered as the global maximum for function $U$ for the following reason.

In all our simulations described in Section 3.4.2, we have noticed that there is only one single maximum point in each experiment; see the graphs in Fig. 3.2, 3.4 and 3.6. As a result, the local maximum point given by the optimization algorithm in each graph can be considered as the global maximum as shown in Fig. 3.2, 3.4 and 3.6. In this case, the constraint gradient ascent optimization algorithm will generate global maximum solutions [116]. We now discuss the optimization algorithms in detail.

**Algorithm 1** Constraint gradient ascent optimization algorithm for the OSP scheme

```
Input: $\mathbf{\Phi}_1, \mathbf{\Phi}_2, \mathbf{\Phi}_{\mathcal{D}}, \lambda_1, \lambda_2, \lambda_{\mathcal{D}}$   /*Locations and densities of MBSs, aggregators, and devices, respectively*/
    $P_1, P_2, P_{\mathcal{D}}, P_A, \epsilon_1, \epsilon_2, B_1, \alpha, \tau_1, \tau_2$ /*Network configuration (see Section 3.5 for values)*/
    $\mathbf{Q}^{(0)} = [\eta^{(0)} = 0.5; B_2^{(0)} = 15]$   /*Gradient ascent optimization initial guess $\boldsymbol{Q}^{(0)} \in$ dom $U$*/
    $\Delta\eta = 0.0001, \Delta B_2 = 0.001$   /*Finite difference parameters to calculate the Gradient*/
    $\nu = 10^{-3}$   /*Gradient ascent stopping parameter*/
    /*The gradient ascent optimization algorithm for U which is given by Eq. (21).*/
while $\|\nabla U(\mathbf{Q}^{(k)})\| > \nu$ do
    $\mathbf{Q}^{(0)}$, $k = 0$
    $\nabla U(\eta^{(k)}) = \left(U(\eta^{(0)} + \frac{\Delta\eta}{2}, B_2^{(0)}) - U(\eta^{(0)} - \frac{\Delta\eta}{2}, B_2^{(0)})\right) / \Delta\eta$   /*Gradient in $\eta$ direction*/
    $\nabla U(B_2^{(k)}) = \left(U(\eta^{(0)}, B_2^{(0)} + \frac{\Delta B_2}{2}) - U(\eta^{(0)}, B_2^{(0)} - \frac{\Delta B_2}{2})\right) / \Delta B_2$   /*Gradient in $B_2$ direction*/
    $\nabla U(\mathbf{Q}^{(k)}) = [\nabla U(\eta^{(k)}); \nabla U(B_2^{(k)})]$
    $\mathbf{t}^{(k)} = [t_\eta = 1; t_{B_2} = 1], \ddot{\boldsymbol{\alpha}} = [0.2; 0.2], \ddot{\boldsymbol{\beta}} = [0.5; 0.5]$   /*Initializing backtracking line search algorithm*/
    while $U(\mathbf{Q}^{(k)} + \mathbf{t}^{(k)} \nabla U(\mathbf{Q}^{(k)})) > U(\mathbf{Q}^{(k)}) + \ddot{\boldsymbol{\alpha}} \mathbf{t}^{(k)} \|\nabla U(\mathbf{Q}^{(k)})\|^2$ do
        $\mathbf{t}^{(k)} = \ddot{\boldsymbol{\beta}} \mathbf{t}^{(k)}$   /*Update step size using backtracking line search*/
    end while
    $\mathbf{Q}^{(k+1)} = \mathbf{Q}^{(k)} + \mathbf{t}^{(k)} \nabla U(\mathbf{Q}^{(k)})$   /*Update position of guess*/
    $k = k + 1$
end while
Output: $\mathbf{Q}^{(k)} = [B_2^*; \eta^*]$ /*Optimal joint aggregator association bias and spectrum partition ratio.*/
```

### Optimization Algorithm for the OSP Scheme

Algorithm 1 on the previous page summarizes the optimization method. At the beginning of Algorithm 1, the network configuration parameters are initialized. (Their values are given at the beginning of Section 3.4.2.) Then we define the gradient ascent optimization initial guess $\mathbf{Q}^{(0)} \in \mathbf{dom}\ U$. Since the function $U$ is not in closed form, we use the finite difference method with parameters $\Delta\eta = 0.0001$ and $\Delta B_2 = 0.001$ to calculate the gradient in two directions, $\eta$ and $B_2$, respectively, as shown in steps 3, 4, and 5 of Algorithm 1.

Note that we use the backtracking line search (BLS) algorithm with BLS control parameters $0 < \ddot{\boldsymbol{\alpha}} < 0.5$ and $0 < \ddot{\boldsymbol{\beta}} < 1$ to update the step size of the optimization [116] as shown in steps 6 to 9 in Algorithm 1. The BLS algorithm starts with a unit step size and then reduces it by the factor $\ddot{\boldsymbol{\beta}} = [0.5; 0.5]$ until the stopping condition in step 7 is satisfied. We assume that $\ddot{\boldsymbol{\alpha}} = [0.2; 0.2]$ which is the fraction of the increase in $U$ predicted by linear extrapolation that we will accept. Then, we update the guess position in step 10 in Algorithm 1. We repeat steps 1 to 12 until the stopping condition in step 1, $\|\nabla U(\mathbf{Q}^{(k)})\| > \nu$, is satisfied, where $\nu = 10^{-3}$ is the gradient ascent stopping parameter.

Following is a discussion about the convergence of the developed constraint gradient ascent optimization algorithm. Based on the recommendations made in the book [116] and on multiple runs of the optimization algorithm for different values of $\ddot{\boldsymbol{\beta}}$ and $\ddot{\boldsymbol{\alpha}}$, we find that the optimization with $\ddot{\boldsymbol{\beta}} = [0.5; 0.5]$ and $\ddot{\boldsymbol{\alpha}} = [0.2; 0.2]$ converges fairly quickly to the optimal results after a small number of iterations (e.g., typically fewer than 14 iterations).

### Optimization Algorithm for the FSR Scheme

The optimization algorithm for the FSR scheme is similar to Algorithm 1, but runs only in one dimension (aggregator association bias $B_2$). We do not present the FSR optimization algorithm here to avoid repetition.

In the following sub-section, we validate the accuracy of the above optimization algorithms using simulations.

### 3.4.2 Validation of Optimal Values Obtained via the Developed Optimization Algorithms

Unless otherwise stated, we use the following parameters in our simulations and analysis. The transmission power of tier 1 and tier 2 in the downlink direction are $P_1 = 50$ watts and $P_2 = 5$ watts, respectively. The transmission power of tier-2 aggregators in the uplink direction before power control is $P_{\mathcal{A}} = 5$ watts. The uplink transmission power of devices before power control is $P_{\mathcal{D}} = 1$ watt. The network size is 40km × 40km. The pathloss exponent is set to $\alpha = 4$. We assume that the density of MBSs is $\lambda_1 = 2$ MBS/km$^2$, and the density of devices is $\lambda_{\mathcal{D}} = 70$ devices/km$^2$. The association bias for the MBS tier is $B_1 = 1$. The network uplink bandwidth is 10 MHz, which is divided into 1024 subcarriers. We averaged the coverage probability over 20 time slots in each network configuration. The Rayleigh fading channel gain is generated over both the frequency subcarrier and the time slots. Devices and aggregators are scheduled in a round-robin fashion in the uplink direction. A typical device or typical aggregator can be scheduled on multiple subcarriers. Therefore, the coverage rate of either a device or an aggregator is proportional to the number of subcarriers that offer non-zero rates. A device or aggregator can offer a zero rate in the uplink direction if all of its subcarriers are below the SIR threshold. We assume that the threshold for correct signal reception at MBSs and aggregators are $\tau_1 = -4$ dB and $\tau_2 = -4$ dB, respectively.

#### Validation of Optimal Device Association Bias for the FSR Scheme

We examine the mean data rate utility ($\log_2$(Mbps)) as a function of the aggregator bias association $B_2$ by varying device PCF $\epsilon_1$ and aggregator PCF $\epsilon_2$. We determine the optimal aggregator association bias $B_2^*$ in order to achieve the maximum mean data rate utility ($\log_2$(Mbps)) for the FSR scheme in the uplink direction.

Fig. 3.2 depicts the variation of the mean data rate utility ($\log_2$(Mbps)) as a function of aggregator bias association $B_2$ under the uplink FSR scheme for several values of device

PCF $\epsilon_1$ and aggregator PCF $\epsilon_2$, namely, $\epsilon_1 = \epsilon_2 = u$, where $u = \{0, 0.1, 0.2, ..., 0.9, 1\}$.

In Fig. 3.2, we show the variation of the mean data rate utility for only four values of $u$ due to space limitation: $\epsilon_1 = \epsilon_2 = u = \{0.1, 0.5, 0.75, 1\}$. We use these graphs to determine the optimal aggregator association bias $B_2^*$ in order to achieve the maximum mean data rate utility for the uplink FSR scheme. For example, when $\epsilon_1 = \epsilon_2 = 0.1$ (Fig. 3.2(a)), the maximum mean data rate utility $-9.0159$ ($\log_2$(Mbps)) is achieved when $B_2^* = 8.5$. Similarly, the maximum mean data rate and the corresponding optimal $B_2^*$ for the other cases are listed in Table 3.2.

We can observe from Fig. 3.2 and Table 3.2 that the mean data rate utility ($\log_2$(Mbps)) for the uplink FSR scheme increases then decreases with increasing PCFs for both devices and aggregators.

Table 3.2: Maximum mean data rate utility and corresponding optimal $B_2^*$.

| PCFs ($\epsilon_1 = \epsilon_2$) | U (Max. Utility) | Optimal $B_2^*$ |
|---|---|---|
| 0.1 | -9.0159 | 8.5 |
| 0.5 | -2.4335 | 2.5 |
| 0.75 | -2.2 | 2.5 |
| 1 | -2.2626 | 2 |

Table 3.3: Maximum data rate utility and its joint optimal $\eta^*$ and $B_2^*$ when $\lambda_1 = 2$.

| Aggregator density | U (Max. Utility) | Optimal $\eta^*$ | Optimal $B_2^*$ |
|---|---|---|---|
| $\lambda_2 = \lambda_1$ | -3.7957 | 0.6 | 1 |
| $\lambda_2 = 2\lambda_1$ | -3.3088 | 0.4 | 4 |
| $\lambda_2 = 4\lambda_1$ | -2.4679 | 0.4 | 28 |
| $\lambda_2 = 8\lambda_1$ | -1.7310 | 0.3 | 30 |

We use the graphs in Fig. 3.2 to determine the optimal aggregator association bias $B_2^*$ in order to achieve the maximum mean data rate utility for the uplink FSR scheme.

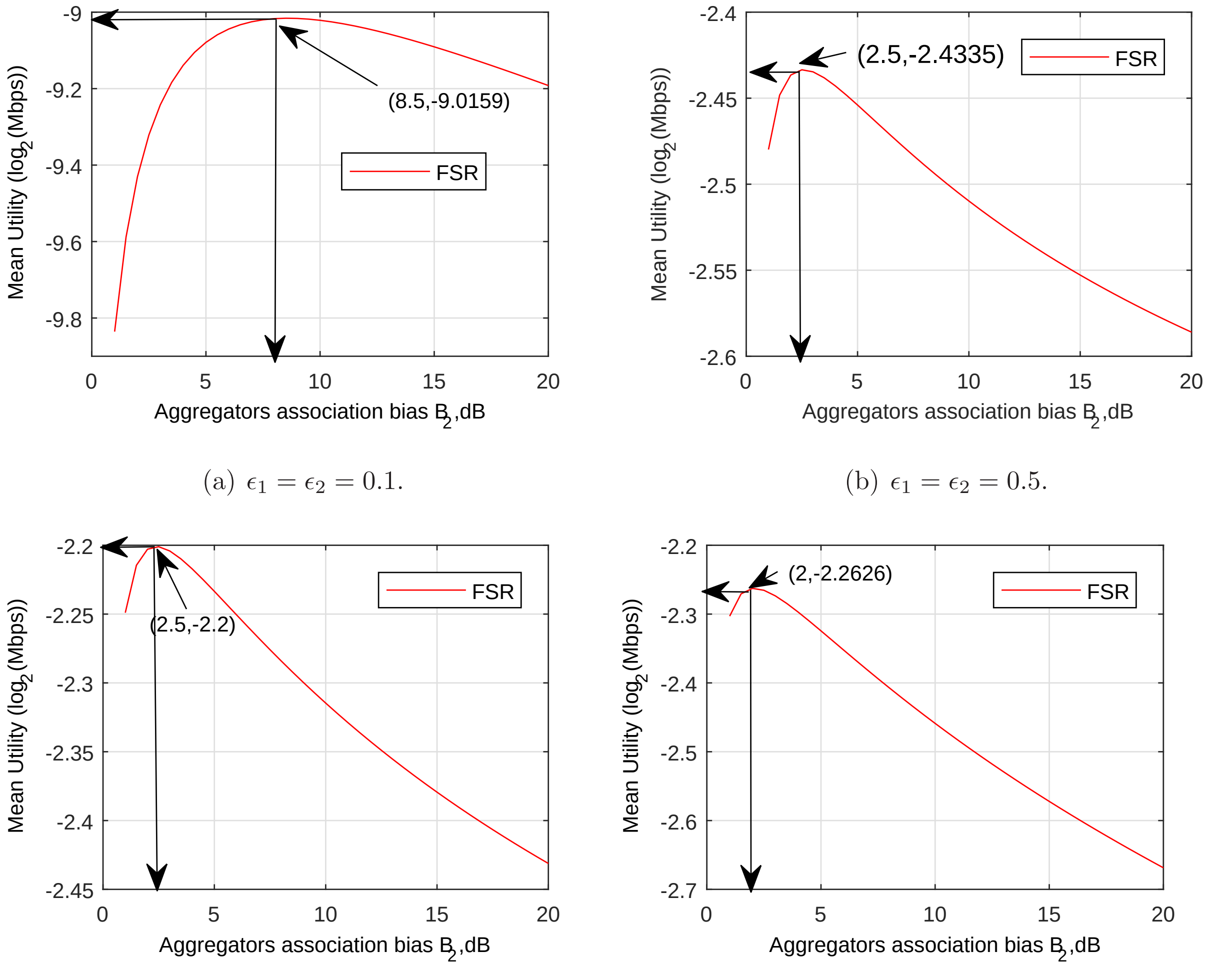

(a) $\epsilon_1 = \epsilon_2 = 0.1$.

(b) $\epsilon_1 = \epsilon_2 = 0.5$.

(c) $\epsilon_1 = \epsilon_2 = 0.75$.

(d) $\epsilon_1 = \epsilon_2 = 1$.

Figure 3.2: Mean data rate utility ($\log_2$(Mbps)) as a function of aggregator association bias $B_2$ when $B_1 = 1$, $\lambda_{\mathcal{D}} = 70$ devices/km$^2$, $\lambda_1 = 2$ MBS/km$^2$, and $\lambda_2 = 4\lambda_1$.

Fig. 3.3 illustrates the optimal uplink aggregator association bias $B_2^*$ as a function of device and aggregator PCFs $\epsilon_1 = \epsilon_2 = \{0, 0.1, 0.2, ..., 0.9, 1\}$. The graph shows that by increasing device and aggregator PCFs $\epsilon_1$ and $\epsilon_2$, the optimal aggregator association bias $B_2^*$ increases until it reaches 8.5 dB at $\epsilon_1 = \epsilon_2 = 0.1$. It then decreases gradually until it reaches 2 dB at $\epsilon_1 = \epsilon_2 = 1$. This result can be intuitively explained as follows. Due to the long distances between the devices and their tagged MBSs in tier 1, low PCFs (i.e, $\epsilon_1 = \epsilon_2 = 0$) force these devices to transmit at lower power, causing less interference to devices associated with tier 2, hence a lower value of $B_2^* = 7.5$ dB. However, when the PCFs increase, this forces these devices to transmit at higher power, which causes higher interference. Therefore, a subset of these devices, especially strong interferers, must be offloaded to tier 2. This leads to an increase in the optimal aggregator association bias $B_2^*$. The maximum $B_2^* = 8.5$ dB is achieved when $\epsilon_1 = \epsilon_2 = 0.1$. When most of the strong interferers have been offloaded to tier 2, as PCFs $\epsilon_1$ and $\epsilon_2$ increase, the optimal aggregator association bias $B_2^*$ then decreases due to the increased interference caused by the devices that were offloaded to tier 2. This leads to a decrease in the optimal aggregator association bias $B_2^*$ as the PCFs $\epsilon_1$ and $\epsilon_2$ increase. $B_2^*$ is reduced to 2 dB when $\epsilon_1 = \epsilon_2 = 1$.

The optimal values we obtained from the FSR optimization algorithm closely match the results in Fig. 3.3.

#### Validation of the Optimal Joint Bias and Spectrum Partition Ratio for the OSP Scheme

We examine the mean data rate utility ($\log_2$(Mbps)) as a function of the spectrum partition ratio $\eta$ and aggregator association bias $B_2$ by varying the following parameters: a) aggregator density $\lambda_2$, where $\lambda_2 = T\lambda_1$ and $T$ ranges from 1 to 65 (Fig. 3.5); b) device and aggregator PCFs $\epsilon_1$ and $\epsilon_2$, respectively, where $\epsilon_1 = \epsilon_2 = \{0, 0.1, \ldots 0.9, 1\}$ (Fig. 3.7).

#### Varying Aggregator Density $\lambda_2$

Fig. 3.4 depicts the mean data rate utility ($\log_2$(Mbps)) as a function of the spectrum

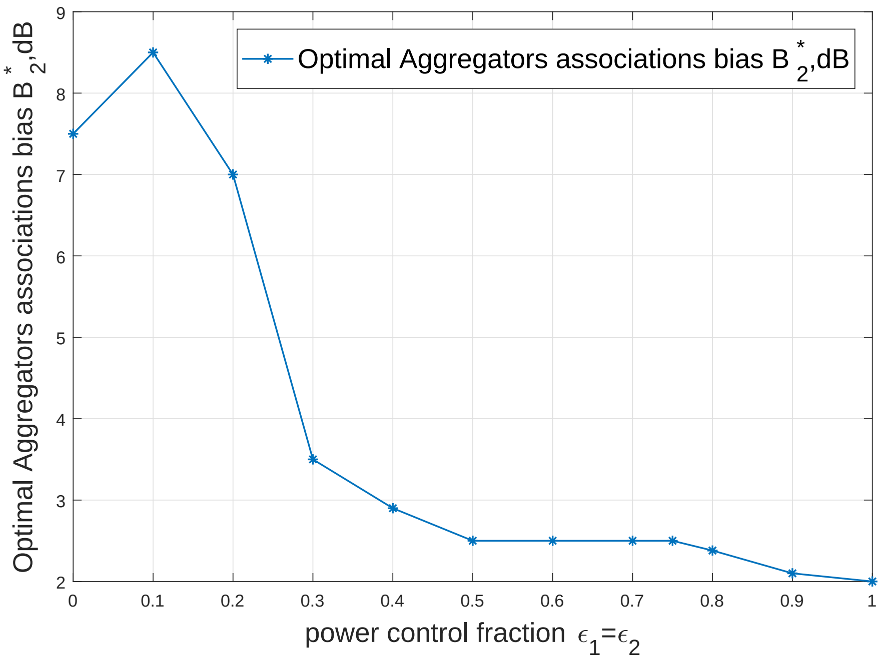

Figure 3.3: Optimal aggregator association bias $B_2^*$ vs. device and aggregator PCFs $\epsilon_1 = \epsilon_2$ when $B_1 = 1$, $\lambda_{\mathcal{D}} = 70$ devices/km$^2$, $\lambda_1 = 2$ MBS/km$^2$, and $\lambda_2 = 4\lambda_1$.

partition ratio $\eta$ and the aggregator association bias $B_2$ for four different aggregator densities, $\lambda_2 = T\lambda_1$ and $T = \{1, 2, 4, 8\}$. We use these graphs to determine the optimal joint spectrum partition ratio $\eta^*$ and aggregators association bias $B_2^*$ for achieving the maximum mean data rate utility. When $\lambda_2 = \lambda_1$, as shown in Fig. 3.4(a), the maximum mean data rate utility $-3.7957$ ($\log_2$(Mbps)) is achieved at joint optimal $\eta^* = 0.6$ and $B_2^* = 1$. Similarly, the maximum mean data rate and the corresponding joint optimal $\eta^*$ and $B_2^*$ values for the other cases are listed in Table 3.3. In general, the mean data rate utility increases as the density of aggregators increases.

We use the graphs in Fig. 3.4 to determine the optimal joint spectrum partition ratio $\eta^*$ and aggregators association bias $B_2^*$ for achieving the maximum mean data rate utility.

Fig. 3.5 illustrates the optimal spectrum partition ratio $\eta^*$ and aggregator association bias $B_2^*$ as functions of the *density ratio* $\lambda_2/\lambda_1$. The graph shows that the optimal aggregator

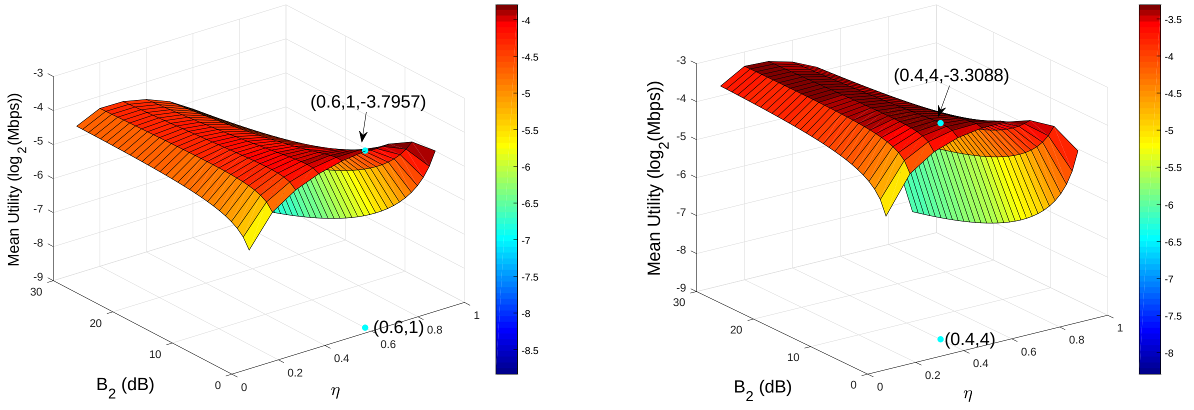

(a) $\lambda_2 = \lambda_1$. (b) $\lambda_2 = 2\lambda_1$.

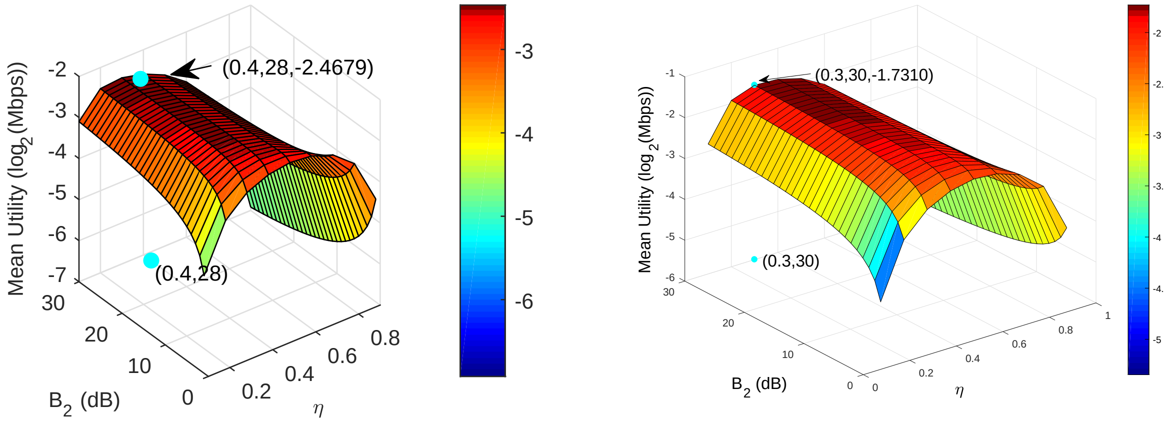

(c) $\lambda_2 = 4\lambda_1$. (d) $\lambda_2 = 8\lambda_1$.

Figure 3.4: Mean data rate utility ($\log_2$(Mbps)) as a function of spectrum partition ratio $\eta$ and aggregator association bias $B_2$ for different aggregators densities when $B_1 = 1$, $\epsilon_1 = \epsilon_2 = 1$, $\lambda_{\mathcal{D}} = 70$ devices/km$^2$, and $\lambda_1 = 2$ MBS/km$^2$.

association bias $B_2^*$ increases rapidly as the density ratio increases from 1 to 9 (the blue curve in Fig. 3.5), then stays constant at $B_2^* = 30$ dB. Fig. 3.5 also shows that by adding more aggregators to the network, the optimal spectrum partition ratio decreases until $\eta^* = 0.3$ at $\lambda_2 = 7\lambda_1$ and then increases until $\eta^* = 0.5$ at $\lambda_2 = 32\lambda_1$. After that $\eta^*$ stays constant at $\eta^* = 0.5$.

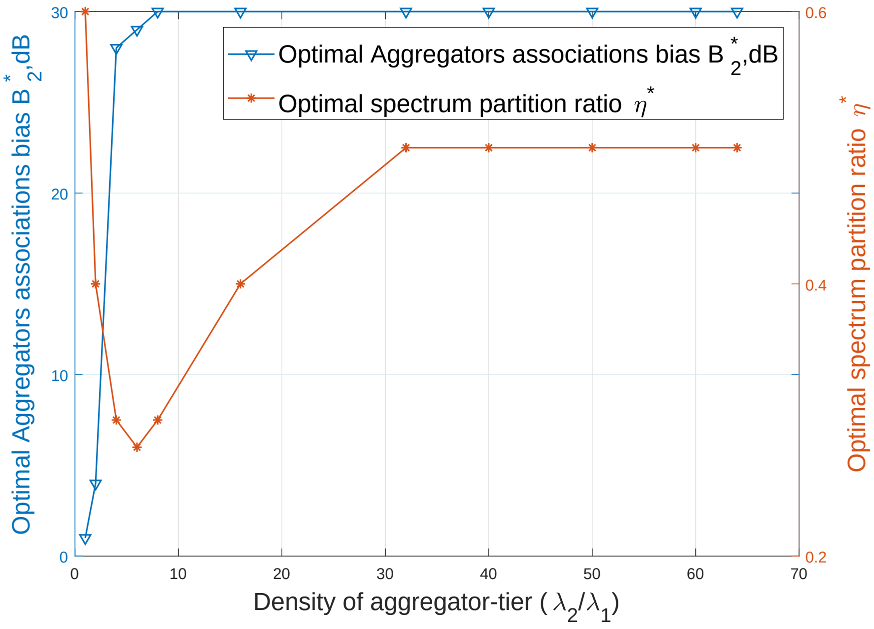

Figure 3.5: Optimal uplink spectrum partition ratio $\eta^*$ and aggregator association bias $B_2^*$ as a function of density of aggregators $(\lambda_2/\lambda_1)$ when $B_1 = 1$, $\epsilon_1 = \epsilon_2 = 1$, $\lambda_{\mathcal{D}} = 70$ devices/km$^2$, and $\lambda_1 = 2$ MBS/km$^2$.

### Varying Device and Aggregator PCFs

We vary the device and aggregator PCFs $\epsilon_1$ and $\epsilon_2$, where $\epsilon_1 = \epsilon_2 = \{0, 0.1, \ldots 0.9, 1\}$. Fig. 3.6 illustrates the variation of the mean data rate utility ($\log_2$(Mbps)) as a function of the aggregator association bias $B_2$ and spectrum partition ratio $\eta$ for four different devices and agregators PCFs $\epsilon_1 = \epsilon_2 = \{0.1, 0.5, 0.75, 1\}$. These graphs allow us to determine the optimal joint spectrum partition ratio $\eta^*$ and aggregators association bias $B_2^*$ for achieving the maximum mean data rate utility. When $\epsilon_1 = \epsilon_2 = 0.1$ (Fig. 3.6(a)), the maximum mean data rate utility $-5.5795$ ($\log_2$(Mbps)) is achieved at the optimal joint $\eta^* = 0.6$ and $B_2^* = 1$. Similarly, the maximum mean data rate and the corresponding joint optimal values $\eta^*$ and $B_2^*$ for the other cases are listed in Table 3.4. The graphs show that the mean data rate utility increases then decreases as $\epsilon_1$ and $\epsilon_2$ increase.

Table 3.4: Maximum mean data rate utility and its joint optimal $\eta^*$ and $B_2^*$.

| PCFs ($\epsilon_1 = \epsilon_2$) | U (Max. Utility) | Optimal $\eta^*$ | Optimal $B_2^*$ |
|---|---|---|---|
| 0.1 | -5.5795 | 0.6 | 1 |
| 0.5 | -2.4679 | 0.3 | 27 |
| 0.75 | -2.3266 | 0.3 | 30 |
| 1 | -2.4679 | 0.4 | 28 |

The graphs in Fig. 3.6 allow us to determine the optimal joint spectrum partition ratio $\eta^*$ and aggregator association bias $B_2^*$ for achieving the maximum mean data rate utility. Fig. 3.7 illustrates the optimal joint spectrum partition ratio $\eta^*$ and aggregator association bias $B_2^*$ as a function of device and agregator PCFs $\epsilon_1 = \epsilon_2$. The graphs show that by increasing the device and aggregator PCFs $\epsilon_1 = \epsilon_2$, the optimal spectrum partition ratio (the orange curve in Fig. 3.7) decreases until $\eta^* = 0.3$ at $\epsilon_1 = \epsilon_2 = 0.6$. Then, it increases after that until $\eta^* = 0.4$ at $\epsilon_1 = \epsilon_2 = 1$. The optimal aggregator association bias (the blue curve in Fig. 3.7) corresponding to the optimal spectrum allocation first increases rapidly until $B_2^* = 30$ dB at $\epsilon_1 = \epsilon_2 = .75$. It then decreases slowly until it reaches $B_2^* = 28$ dB at $\epsilon_1 = \epsilon_2 = 1$.

The optimal values we obtained from the OSP optimization algorithm closely match the results in Fig. 3.5 and 3.7.

## 3.5 Model Validation and Performance Analysis

In this section, we validate the accuracy of the developed analytical model for estimating the uplink mean data rate utility under the FSR and OSP schemes (Section 3.5.1). Then,

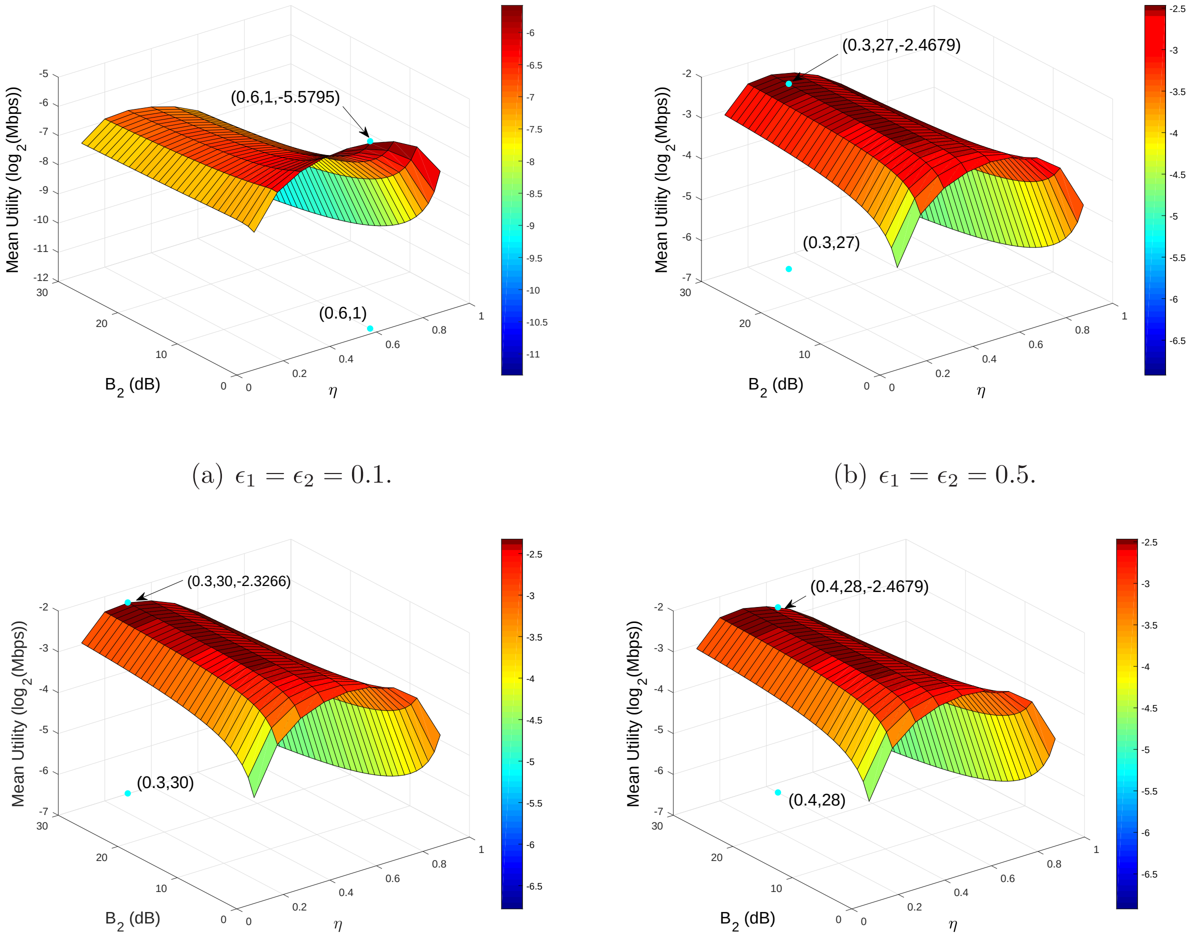

(a) $\epsilon_1 = \epsilon_2 = 0.1$.

(b) $\epsilon_1 = \epsilon_2 = 0.5$.

(c) $\epsilon_1 = \epsilon_2 = 0.75$.

(d) $\epsilon_1 = \epsilon_2 = 1$.

Figure 3.6: Mean data rate utility ($\log_2$(Mbps)) as a function of spectrum partition ratio $\eta$ and aggregator association bias $B_2$ when $B_1 = 1$, $\lambda_{\mathcal{D}} = 70$ devices/km$^2$, $\lambda_2 = 4\lambda_1$, and $\lambda_1 = 2$ per km$^2$.

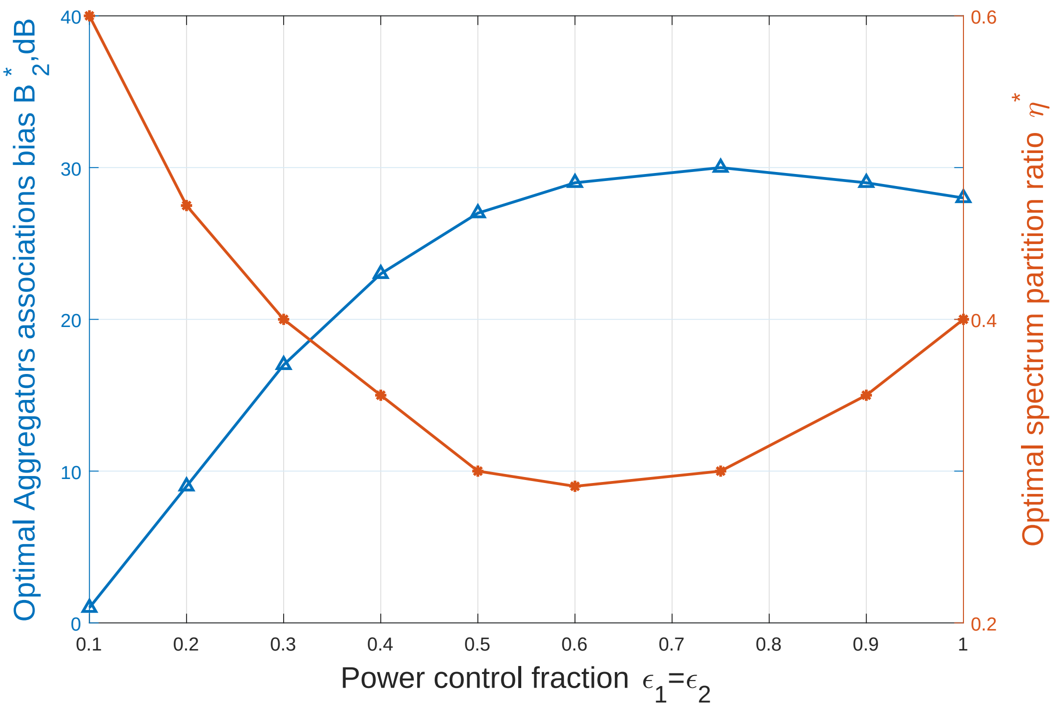

Figure 3.7: Optimal aggregator association bias $B_2^*$ (dB) and optimal spectrum partition ratio $\eta^*$ as a functions of $\epsilon_1 = \epsilon_2$ when $B_1 = 1$, $\lambda_{\mathcal{D}} = 70$ devices/km$^2$, $\lambda_2 = 4\lambda_1$, and $\lambda_1 = 2$ MBS/km$^2$.

we compare the performance of the optimized OSP and FSR schemes with the benchmark maximum- SIR based association scheme and the minimum-distance association scheme in terms of the device uplink data rate (Section 3.5.2). *The network parameters and assumptions used in this section are the same as those described at the beginning of Section 3.4.2.*

### 3.5.1 Model Validation

The proposed analytical model is validated using Monte Carlo simulation implemented in MATLAB. We performed Monte Carlo simulations over $40,000$ network configurations with different spatial topologies using three independent homogenous PPPs with densities $\lambda_1$, $\lambda_2$, and $\lambda_{\mathcal{D}}$ in order to calculate the average DRUF. Fig. 3.8 illustrates the uplink mean data rate utility (expressed in $\log_2$(Mbps)) as a function of aggregators bias association $B_2$ under both FSR and OSP schemes, when $\eta = 0.42$, $\epsilon_1 = \epsilon_2 = 1$, $\lambda_2 = 4\lambda_1 = 8$ aggregators/km$^2$. The data points were obtained from the analytical model, Eq. (3.20) and Eq. (3.21), and the Monte Carlo simulations. (Note that the uplink mean data rate utility (expressed in $\log_2$(Mbps)) in this chapter has negative values. The exponential form can be used to convert mean data rate utility to Mbps value. For example, a mean data rate utility value of $-9$ is equivalent to $2^{-9} = 0.001953$ Mbps.)

As can be seen in Fig. 3.8, the analytical results of the derived uplink mean DRUF under both resource allocation schemes match the simulation results. This confirms the accuracy of the analytical expressions derived above for our model. As observed from Fig. 3.8, as $B_2$ increases, the DRUF of the FSR scheme decays much faster than that of the OSP scheme. The reason is higher interference generated by devices offloaded from tier 1 to tier 2 in the FSR scheme. Therefore, in this particular network configurations, it is recommended that cellular operators use the FSR scheme when $B_2 < 16$ and the OSP scheme for $B_2 \geq 16$.

### 3.5.2 Performance Evaluation of the Optimized Resource Allocation Schemes

From the results in Section 3.4.2, we obtain the optimal association bias $B_2^* = 2$ dB (from Fig. 3.2(d)), which gives us the optimized FSR scheme for $\epsilon_1 = \epsilon_2 = 1$. Similarly, from the results in Section 3.4.2, we obtain the optimal joint spectrum partition ratio $\eta^* = 0.4$ and aggregator association bias $B_2^* = 28$ (from Fig. 3.6(d)), which give us the optimized OSP scheme for $\epsilon_1 = \epsilon_2 = 1$. In this section, we compare the performance of the optimized FSR and OSP schemes with that of two benchmark schemes: (a) maximum-SIR based association scheme (achieved when $B_1 = B_2 = 1$), and (b) minimum-distance based association scheme (achieved when $B_1 = 1/P_1$ and $B_2 = 1/P_2$).

Fig. 3.9 illustrates the CDF of the uplink device data rate (Mbps) for the different association schemes. The red curves show the results of the optimized FSR scheme, maximum-SIR

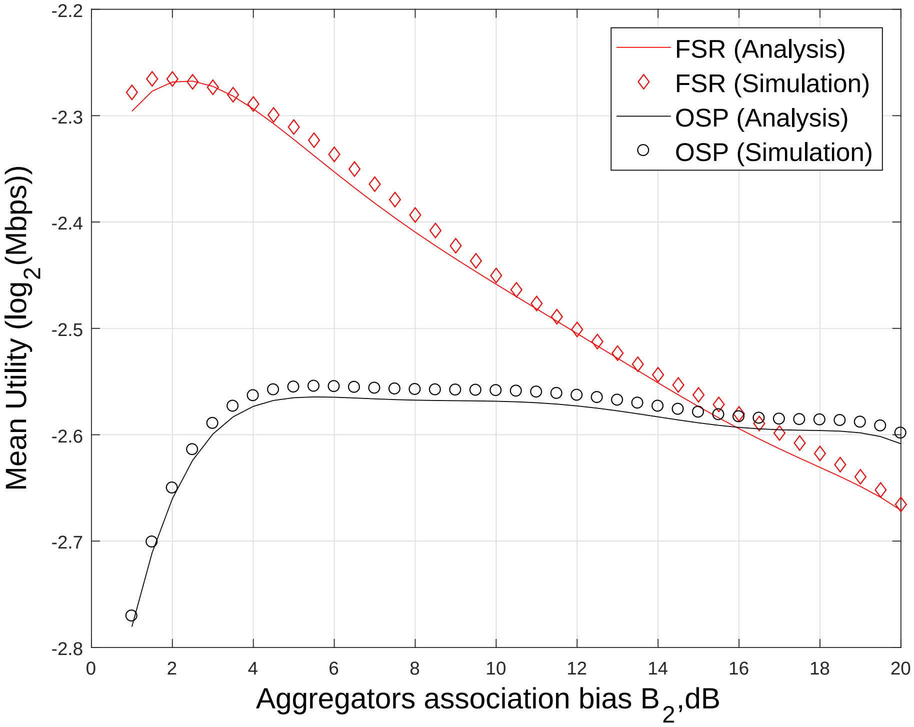

Figure 3.8: Mean data rate utility ($\log_2$(Mbps)) as a function of aggregator association bias $B_2$ when $B_1 = 1$, $\eta = 0.42$, $\epsilon_1 = \epsilon_2 = 1$,$\lambda_{\mathcal{D}} = 70$ devices/km$^2$, $\lambda_1 = 2$ MBS/km$^2$, and $\lambda_2 = 4\lambda_1$.

based association scheme, and minimum-distance association scheme under the FSR spectrum allocation scheme. We observe that the optimized FSR scheme always outperforms both benchmark schemes in terms of the CDF of the uplink device data rate for both cell-edge and cell-center devices. This indicates that our proposed optimization method mitigates interference and enhances the uplink mean per-device data rate. Fig. 3.9(a) and Fig. 3.9(b) also show that such an optimization is crucial to cell-edge devices (see the lower left portion of the figures when the CDF varies from 0.1 to 0.3). The optimization noticeably enhances the data rate of those cell-edge devices that suffer from high interference in the cases of $\epsilon_1 = \epsilon_2 = 0.1$ (Fig. 3.9(a)) and $\epsilon_1 = \epsilon_2 = 0.5$ (Fig. 3.9(b)).

The black curves in Fig. 3.9 illustrate the results of the optimized OSP scheme, maximum-

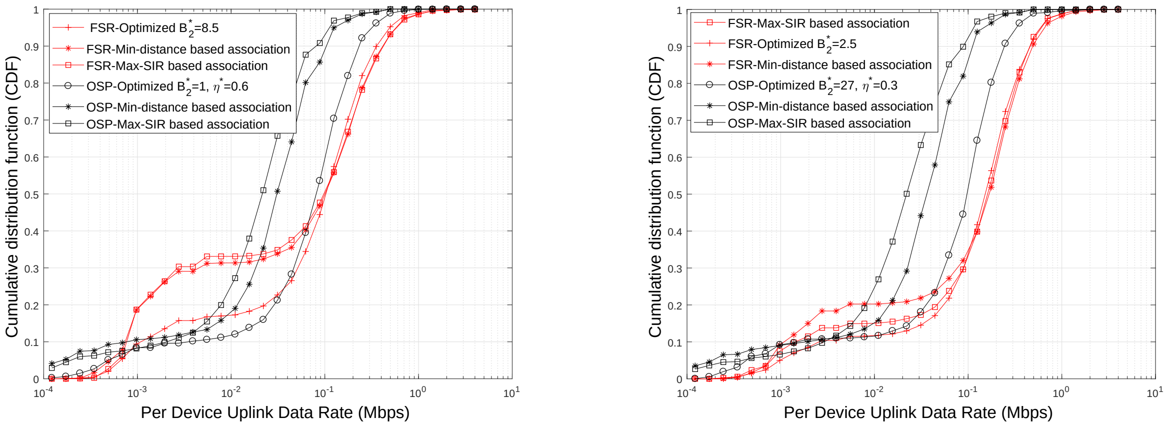

(a) $\epsilon_1 = \epsilon_2 = 0.1$.

(b) $\epsilon_1 = \epsilon_2 = 0.5$.

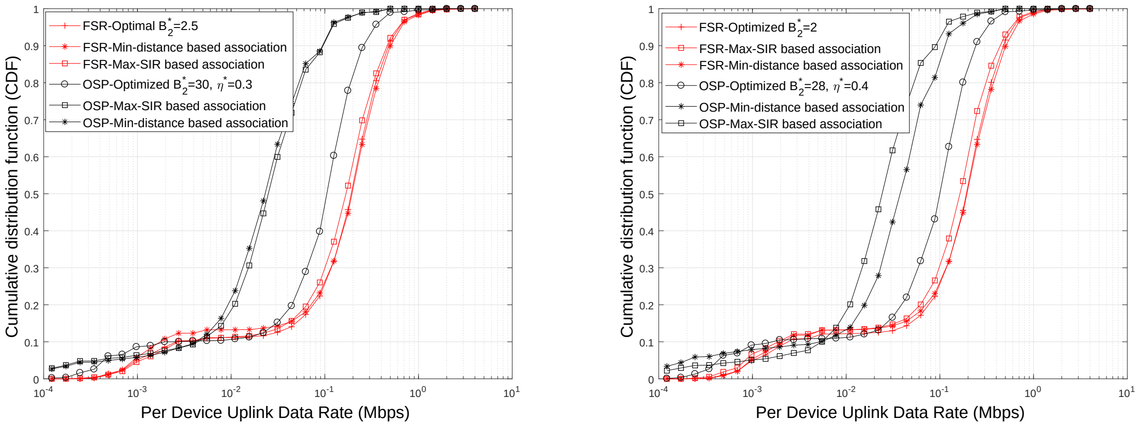

(c) $\epsilon_1 = \epsilon_2 = 0.75$.

(d) $\epsilon_1 = \epsilon_2 = 1$.

Figure 3.9: CDF of uplink per-device data rate (Mbps) when $\lambda_2 = 4\lambda_1$, $\lambda_{\mathcal{D}} = 70$ devices/km$^2$, $\lambda_2 = 4\lambda_1$, $\lambda_1 = 2$ MBS/km$^2$.

SIR based association scheme, and minimum-distance association scheme under the OSP scheme. The results show that the optimized OSP scheme always outperforms both benchmark schemes in terms of the CDF of the uplink device data rate for cell-center devices, thanks to the proposed optimization method. Fig. 3.9(a) also shows that such an optimization is very important to both cell-edge devices (when the CDF varies from 0.1 to 0.3) and cell-center devices (when the CDF is greater than 0.3). The optimization noticeably improves the data rate of the devices that suffer from high interference in the case of $\epsilon_1 = \epsilon_2 = 0.1$.

## 3.6 Chapter Summary

We present a novel analytical model to estimate the mean uplink device DRUF under both the FSR and OSP spectrum allocation schemes using stochastic geometry. The model takes into account the aggregator spatial density, aggregator association bias and spectrum partition ratio across the MBS tier and the aggregator tier, and device and aggregator PCFs. We developed constraint gradient ascent optimization algorithms to obtain the optimal aggregator association bias (for the FSR scheme) and the optimal joint spectrum partition ratio and optimal aggregator association bias (for the OSP scheme). Then, we confirm the accuracy of the computed optimal values using simulations. We then use the proposed model and obtained optimal values to quantify the performance gains offered by the proposed optimized FSR and OSP schemes, in comparison with benchmark schemes such as the minimum-distance based association scheme and the maximum-SIR based association scheme.

The optimized FSR and OSP schemes always outperform the benchmark schemes in terms of the CDF of the uplink device data rate. The optimized schemes reduce interference from devices by controlling two critical network parameters: the aggregator association bias and the spectrum partition ratio across the MBS tier and the aggregator tier. The former parameter controls the offloading of devices from being served by MBSs to being served by aggregators situated closer to their locations. The offloading allows devices to lower their transmission power, which reduces interference and thus improves the overall uplink data rate. The latter parameter serves as a load balancing mechanism between the MBS tier and the aggregator tier, which enhances the uplink data rate.

# Chapter 4

# The Meta Distributions of the SIR/SNR and Data Rate in Coexisting Sub-6GHz and Millimeter-wave Cellular Networks

## 4.1 Motivations and Contributions

Internet of things (IoT) networks are widely adopted across the globe to build smart cities and connected societies. IoT cellular networks can be classified into four types [5]: 1) massive IoT networks, which provide cellular connectivity to IoT devices with narrow-band IoT (NB-IoT) or LTE-M technologies and support applications such as low-cost sensors, wearables and trackers that infrequently send or receive messages; 2) broadband IoT networks, which use mobile broadband connectivity for applications such as advanced wearables and aerial and ground vehicles; 3) critical IoT networks, which require extremely low latencies and ultra-high reliability such as smart grids, intelligent transportation systems, and health-care; and 4) industrial automation IoT networks. Our work in this chapter is most applicable and beneficial to broadband and industrial IoT networks, which can potentially be enabled by the 5G technology [117, 118, 8].

As the sub-6GHz spectrum is running out of bandwidth to support a huge number of devices in the IoT, operators of the upcoming 5G networks will tap into the millimeter-wave (mm-wave) spectrum. The mm-wave spectrum has wider bandwidths that can meet higher traffic demands and support data rates into the order of gigabits per second [5]. However, mm-wave transmissions are highly susceptible to blockages and penetration losses; therefore the mm-wave spectrum will complement and coexist with the sub-6GHz spectrum in 5G networks [7, 8]. In this chapter, we term the sub-6GHz spectrum as *microwave spectrum* for the sake of brevity, although different sources may define different frequency ranges as microwaves.

We assume a two-tier network architecture as illustrated in Fig. 4.1. Tier 1 consists of macro base stations (MBSs) and tier 2 is composed of small base stations (SBSs). A MBS communicates with SBSs on *backhaul links* in the microwave spectrum. SBSs communicate with devices on *access links* in the mm-wave spectrum. This scenario supports dual-hop communications between MBSs and devices. Devices can also communicate with MBSs via *direct links* in the microwave spectrum, as shown in Fig. 4.1.

Given the above *hybrid spectrum network* architecture, it is crucial to develop new theoretic frameworks to characterize the performance of such networks. Within this context, we consider the use of *meta distributions* to study the performance of such hybrid spectrum networks.

The meta distribution is first introduced by M. Haenggi [119] to provide a fine-grained *reliability and latency* analysis of 5G wireless networks with ultra-reliable and low latency communication requirements [120, 121]. Meta distribution is defined as the distribution of the conditional success probability (CSP) of the transmission link (also termed as *link reliability*), conditioned on the locations of the wireless transmitters. The meta distribution provides answers to questions such as "*What fraction of devices can achieve x% transmission success probability?*" whereas the conventional success probability answers questions such as *“What fraction of devices experience transmission success?”* [119]. In addition to the standard coverage (or success) probability which is equivalent to the mean of CSP, the meta distribution can capture important network performance measures such as the mean of the local transmission delay, the variance of the local transmission delay (referred to as *network jitter*), and the variance of the CSP which depicts the variation of the devices’ performance from the mean coverage probability. Evidently, the standard coverage probability provides limited information about the performance of a typical wireless network [122, 123, 124].

To illustrate the significance of the meta distribution, assume that 50% of the devices achieve 10% reliability and the other 50% achieve 99% reliability. Then, the standard mean coverage probability is 54.5%. On the other hand, if 100% of the devices achieve 54.5% reliability, the standard mean coverage probability is also 54.5%. However, the two scenarios are very different in terms of user experience. Meta distributions, on the other hand, can distinguish the above two scenarios. Furthermore, cellular operators are typically interested in the performance of the “5% device percentile”, which is the performance level that 95% of the devices achieve. The meta distribution reveals this information, while the standard coverage probability does not reveal any information about it.

In this chapter, we develop a novel stochastic geometry framework based on meta distributions to estimate and analyze the communication latency and reliability of IoT devices in a coexisting sub-6GHz and mm-wave IoT cellular network.

To the best of our knowledge, our work is the first to characterize the meta distributions of SIR/SNR and data rate for coexisting $\mu$wave and mm-wave networks. Different from previous research in [25, 29, 28, 30], we develop a stochastic geometry framework that takes in consideration (i) coexistence of two different network tiers with completely different channel propagation, interference, and fading models, (ii) dual-hop transmissions enabled by two different spectrums, one in each network tier, and (iii) Nakagami-m fading model with shape parameter $m$ for LOS mm-wave channels. Nakagami-m fading is a generic and versatile distribution that includes Rayleigh distribution (typically used for non-LOS fading) as its special case when $m = 1$ and can well approximate the Rician fading distribution for $1 \leq$

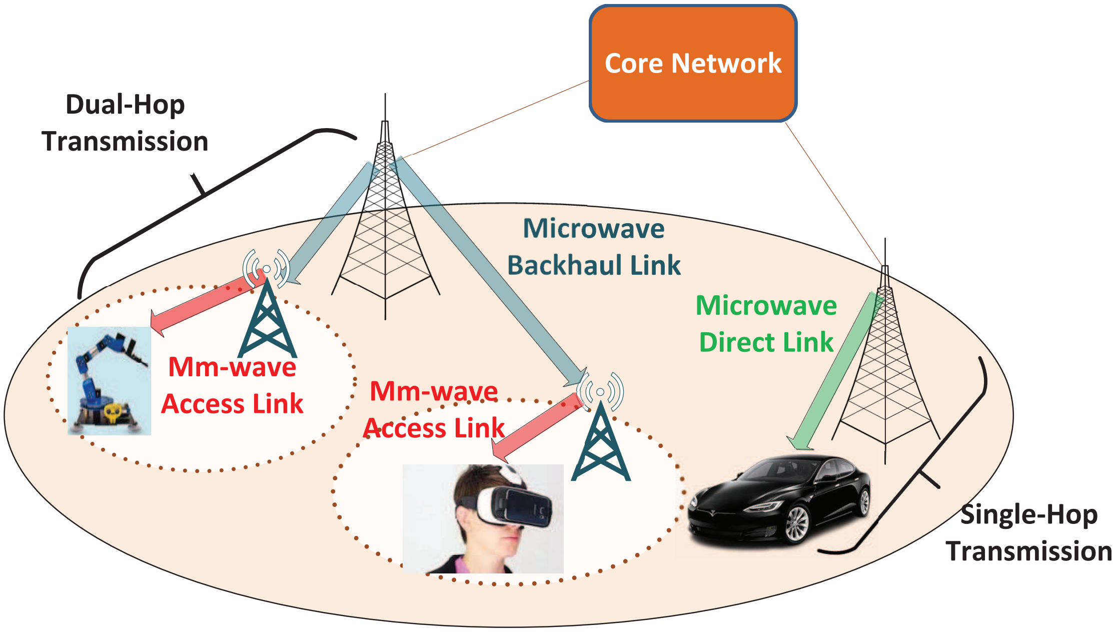

Figure 4.1: Coexisting sub-6GHz and mm-wave IoT cellular networks.

$m \leq \infty$ (typically used for LOS fading).

We assume a hybrid spectrum network architecture described above and illustrated in Fig. 1. Since microwave transmissions are interference limited and mm-wave transmission are noise limited[1], we study the meta distributions of the SIR and SNR in $\mu$wave and mm-wave channels, respectively. We also characterize the meta distrubusiton of data rates. Our contributions and methodology include the following:

- Different from existing works, we characterize the CSP (which is equivalent to reliability) of a typical device and its $b^{\text{th}}$ moment when the device either associates to (1) $\mu$wave MBS for direct transmission or (2) mm-wave SBS for dual-hop transmission (access and backhaul transmission). Using the novel moment expressions in the two scenarios, we derive a novel expression for the cumulative moment $M_{b,\mathrm{T}}$ of the considered hybrid spectrum IoT network.

---

[1] Given highly directional beams and high sensitivity to blockage, recent studies showed that mm-wave networks can be considered as noise limited rather than interference limited [125, 27, 126].

- Using the cumulative moment $M_{b,\mathrm{T}}$, we characterize the exact and approximate meta distributions of the data rate and downlink SIR/SNR of a typical device. Since the expression of $M_{b,\mathrm{T}}$ relies on a Binomial expansion of power $b$, the results for the meta-distribution requiring complex values of $b$ are obtained by applying Newton's Generalized Binomial Theorem.
- We characterize important network performance metrics such as coverage probability, mean local delay (which is equivalent to latency), and variance of the local delay (network jitter), using the derived cumulative moment $M_{b,\mathrm{T}}$. For metrics with negative values of $b$, we apply the binomial theorem for negative integers.
- To model the LOS nature of mm-wave, we consider the versatile *Nakagami-$m$* fading channel model. To the best of our knowledge, the meta distribution for the Nakagami-$m$ fading channel has not been investigated yet.
- We demonstrate the application of this framework to other specialized network scenarios where (i) SBSs are connected to MBSs via a mm-wave wireless backhaul and (ii) a network where all transmissions are conducted in $\mu$wave spectrum. Closed-form results are provided for special cases and asymptotic scenarios.

We validate analytical results using Monte-Carlo simulations. Numerical results give valuable insights related to the reliability, mean local delay, variance of CSP, and standard success probability of a device. For example, the mean local delay increases with the increasing density of SBSs in a $\mu$wave-only network; however, it stays constant in a hybrid spectrum network. Moreover, the data rate reliability, i.e., the fraction of devices achieving a required data rate, increases as the number of antenna elements increases. We also note that as the number of antenna elements in a hybrid spectrum network increases, the reduction in the variance of reliability is noticeable, which shows the importance of analyzing the higher moments of the CSP using the meta distribution. These insights would help IoT cellular network operators to find the most efficient operating antenna configurations for ultra-reliable and low latency applications.

The remainder of the chapter is organized as follows. In Section 4.2, we describe the system model and assumptions. In Section 4.3, we provide mathematical preliminaries of the meta distribution. In Section 4.4, we characterize the association probabilities of a typical device and formulate the meta distribution of the SIR/SNR of a device in the hybrid spectrum IoT network. In Section 4.5, we characterize the CSP and its $b^{\text{th}}$ moment for direct, access, and backhaul transmissions. Finally, we derive the exact and approximate meta distributions of the SIR/SNR and data rate in a hybrid spectrum IoT network as well as $\mu$wave-only IoT network in Section VI. Finally, Section 4.8 presents numerical results and Section 4.9 concludes the chapter.

## 4.2 System Model and Assumptions

In this section, we describe the network deployment model (Section 4.2.1), antenna model (Section 4.2.2), channel model (Section 4.2.3), device association criteria (Section 4.2.4), and SNR/SIR models for access and backhaul transmissions (Section 4.2.5).

### 4.2.1 Network Deployment and Spectrum Allocation Model

We assume a two-tier IoT network architecture as shown in Fig. 4.1 in which the locations of the MBSs and SBSs are modeled as a two-dimensional (2D) homogeneous Poisson point process (PPP) $\mathbf{\Phi}_k = \{\mathbf{y}_{k,1}, \mathbf{y}_{k,2}, ...\}$ of density $\lambda_k$, where $\mathbf{y}_{k,i}$ is the location of $i^{\text{th}}$ MBS (when $k = 1$) or the $i^{\text{th}}$ SBS (when $k = 2$). Let the MBS tier be tier 1 ($k = 1$) and the SBSs constitute tier 2 ($k = 2$). Let $\mathcal{D}$ denotes the set of devices. The locations of devices in the network are modeled as independent homogeneous PPP $\mathbf{\Phi}_{\mathcal{D}} = \{\mathbf{x}_1, \mathbf{x}_2, ....\}$ with density $\lambda_{\mathcal{D}}$, where $\mathbf{x}_i$ is the location of the $i^{\text{th}}$ device. We assume that $\lambda_{\mathcal{D}} \gg \lambda_2 > \lambda_1$ as in [40,127,101]. We consider a typical outdoor device which is located at the origin and is denoted by 0 and its tagged BS is denoted by $\mathbf{y}_{k,0}$, i.e., tagged MBS (when $k = 1$) or tagged SBS (when $k = 2$). All BSs in the $k^{\text{th}}$ tier transmit with the same transmit power $P_k$ in the downlink. A list of the key mathematical notations is given in Table 4.1.

We assume that a portion $\eta W_1$ of the frequency band $W_1$ is reserved for the access transmission and the rest $(1-\eta)W_1$ is reserved for the backhaul transmission, where $W_1$, and $W_2$ denote the total available $\mu$wave spectrum and mm-wave spectrum, respectively, and $0 \leq \eta \leq 1$. Determining the optimal spectrum allocation ratio $\eta$ will be studied in our future work.

Table 4.1: Mathematical notations in Chapter 4

| **Notation** | **Description** | **Notation** | **Description** |
|---|---|---|---|
| $\mathbf{\Phi}_k$;$\mathbf{\Phi}_{\mathcal{D}}$ | PPP of BSs of $k^{\text{th}}$ tier; PPP of devices | $\lambda_k$;$\lambda_{\mathcal{D}}$ | Density of BSs of $k^{\text{th}}$ tier; density of devices |
| $P_k$ | Transmit power of BSs in $k^{\text{th}}$ tier | $B_k$ | Association bias for BSs of $k^{\text{th}}$ tier |
| $\alpha_1, \alpha_{2,L}, \alpha_{2,N}$ | Path loss exponent of MBS tier;<br>LOS SBS; NLOS SBS | $G_1^o$ | omnidirectional antenna gain of $\mu$wave MBSs |
| $G_2^{max}$;$G_2^{min}$;$\theta_a$ | Main lobe gain; side lobe gain; and<br>3 dB beamwidth for mm-wave SBS | $h_l$ | Gamma fading channel gain for mm-wave SBSs |
| $g$ | Rayleigh fading channel gain | $m_l$ | Nakagami-m fading parameter where $l \in \{L, N\}$<br>denotes LOS and NLOS transmission links |
| $p_L$;$p_N$ | Mm-wave blockage LOS probability; NLOS probability | $\theta$ | Predefined SIR/SNR threshold |
| $\bar{F}_{P_s}(x)$ | Meta distribution of SIR/SNR | $P_s(\theta)$ | Conditional success probability (CSP) |
| $M_b(\theta)$ | The $b^{th}$ moment of $P_s(\theta)$ | $\mathcal{A}_2$;$\mathcal{A}_{2,L}$;$\mathcal{A}_{2,N}$ | Association Probability with $\mu$wave MBS;<br>LOS mm-wave SBS; NLOS mm-wave SBS |

### 4.2.2 Antenna Model

We assume that all MBSs are equipped with omnidirectional antennas with gain denoted by $G_1^{\text{o}}$ dB. We consider SBSs and devices are equipped with directional antennas with sectorized gain patterns as in [126, 23, 30] to approximate the actual antenna pattern. The sectorized gain pattern is given by:

$$G_a(\theta) = \begin{cases} G_a^{\max} & \text{if } |\theta| \leq \frac{\theta_a}{2} \\ G_a^{\min} & \text{otherwise} \end{cases}, \tag{4.1}$$

where subscript $a \in \{2, \mathcal{D}\}$ denotes for SBSs and devices, respectively. Considering a $\sqrt{\mathcal{N}} \times \sqrt{\mathcal{N}}$ uniform planar square antenna array with $\mathcal{N}$ elements, the antenna parameters of a uniform planar square antenna array can be given as in [30], i.e., $G_a^{\max} = \mathcal{N}$ is the main lobe antenna gain, $G_a^{\min} = 1/\sin^2\left(\frac{3\pi}{2\sqrt{\mathcal{N}}}\right)$ is the side lobe antenna gain, $\theta \in [-\pi, \pi)$ is the angle of the boresight direction, and $\theta_a = \frac{\sqrt{3}}{\sqrt{\mathcal{N}}}$ is the main lobe beam width. A perfect beam alignment is assumed between a device and its serving SBS [28] [29]. The antenna beams of the desired access links are assumed to be perfectly aligned, i.e., the direction of arrival (DoA) between the transmitter and receiver is known a priori at the BS and the effective gain on the intended access link can thus be denoted as $G_2^{\max} G_{\mathcal{D}}^{\max}$. This can be done by assuming that the serving mm-wave SBS and device can adjust their antenna steering orientation using the estimated angles of arrivals. The analysis of the alignment errors on the desired link is beyond the scope of this work.

### 4.2.3 Channel Model

#### Path-Loss Model

The signal power decay is modeled as $L(r) = r^{\alpha}$, where $L(r)$ is the path loss for a typical receiver located at a distance $r$ from the transmitter and $\alpha$ is the path loss exponent (PLE). Let $L_1(r) = \|r_{1,\mathcal{D}}\|^{\alpha_1}$ denotes the path loss of a typical device associated with the MBS tier, where $\alpha_1$ is the PLE. Similarly, $L_2(r) = \|r_{2,\mathcal{D}}\|^{\alpha_{2,l}}$ denotes the path loss of a typical device associated with the SBS tier where $\alpha_{2,l} = \alpha_{2,L}$ is the PLE in the case of LOS and $\alpha_{2,l} = \alpha_{2,N}$ is the PLE in the case of NLOS. It has been shown that mm-wave LOS and NLOS conditions have markedly different PLEs [128]. Also, we consider the near-field path loss factor $\zeta = (\frac{\text{carrier wavelength}}{4\pi})^2$ at 1 m [28], i.e., different path loss for different frequencies at the reference distance.

#### Fading Model

For outdoor mm-wave channels, we consider a versatile Nakagami-m fading channel model due to its analytical tractability and following the previous line of research studies [29, 25, 129, 130, 26]. Nakagami-$m$ fading is a general and tractable model to characterize mm-wave channels. Also, in several scenarios, Nakagami-m can approximate the Rician fading which is commonly used to model the LOS transmissions but not tractable for meta distribution modeling [131, 132]. The fading parameter $m_l \in [1, 2, ..., \infty)$ where $l \in \{L, N\}$ denotes LOS and NLOS transmission links, respectively, and the mean fading power is denoted by $\Omega_l$. The fading channel power $h_l$ follows a gamma distribution given as $f_{h_l}(x) = \frac{m_l^{m_l} x^{m_l - 1}}{\Omega_l^{m_l} \Gamma(m_l)} \exp(\frac{-m_l x}{\Omega_l})$, $x > 0$, where $\Gamma(.)$ is the Gamma function, $m_l$ is the shape (or fading) parameter, and $\frac{m_l}{\Omega_l}$ is the scale parameter. That is, we consider $h_l \sim \Gamma(m_L, 1/m_L)$ for the LOS links and $h_l \sim \Gamma(m_N, 1/m_N)$ for the NLOS links. Rayleigh fading is a special case of Nakagami-$m$ for $m_L = m_N = 1$. Due to the NLOS nature of $\mu$wave channels, we assume Rayleigh fading with power normalization, i.e., the channel gain $g(\mathbf{x}, \mathbf{y}) \sim \exp(1)$, is independently distributed with the unit mean.

**Blockage Model for Millimeter-wave Access Links**

For mm-wave channels, LOS transmissions are vulnerable to significant penetration losses [128]; thus LOS transmissions can be blocked with a certain probability. Following [29, 133, 129, 134], we consider the actual LOS region of a device as a fixed LOS ball referred to as "equivalent LOS ball". For the sake of mathematical tractability, we consider a distance dependent blockage probability $p(r)$ that a mm-wave link of length $r$ observes, i.e., the LOS probability $p_L(r)$ if the mm-wave desired link length is less than $d$ and $p_N(r)$ otherwise. That is, SBSs within a LOS ball of radius $d$ are marked LOS with probability $p_L(r)$, while the SBSs outside that LOS ball are marked as NLOS with probability $p_N(r)$. Note that we will drop the notation $(r)$ in both $p_L(r)$ and $p_N(r)$ from this point onwards and we will use only $p_L$ and $p_N$, respectively.

### 4.2.4 Association Mechanism

Each device associates with either a MBS or a SBS depending on the maximum biased received power in the downlink. The association criterion at the typical device can be written mathematically as follows:

$$P_k B_k G_k \zeta_k L_k(r)^{-1} \geq P_j B_j G_j \zeta_j L_{\min,j}(r)^{-1}, \forall j \in \{1, 2\}, j \neq k \tag{4.2}$$

where $P_{(\cdot)}$, $B_{(\cdot)}$, $G_{(\cdot)}$, and $\zeta_{(\cdot)}$ denote the transmission power, biasing factor, effective antenna gain, and near-field path loss at 1 m of the intended link, respectively, in the corresponding tier (which is determined by the index in the subscript). Let $L_{\min,j}(r)^{-1}$ be the minimum path loss of a typical device from a BS in the $j^{\text{th}}$ tier. When a device associates with a mm-wave SBS in tier-2, i.e., $k = 2$, the antenna gain of the intended link is $G_2 = G_2^{\max} G_{\mathcal{D}}^{\max}$, otherwise $G_1 = G_1^{\text{o}} G_{\mathcal{D}}$, where $G_1^{\text{o}}$ is defined as the omnidirectional antenna gain of MBSs and $G_{\mathcal{D}}$ is the device antenna gain while operating in $\mu$wave spectrum. On the other hand, the SBS associates with a MBS offering the maximum received power in the downlink.

### 4.2.5 SNR/SIR Models for Access and Backhaul Transmissions

The device associates to either a MBS for direct transmission or a SBS for dual-hop transmission. The first link (backhaul link) transmissions occur on the $\mu$wave spectrum between MBSs and SBSs and the second link (access link) transmissions take place in the mm-wave spectrum between SBSs and devices. Let $\theta_2$ denotes the predefined SIR threshold for SBSs in the backhaul link and $\theta_{\mathcal{D}}$ denotes the predefined SIR/SNR threshold for devices. Throughout this chapter, we use subscripts "$1, 2$", "$2, \mathcal{D}$", "$1, \mathcal{D}$", "$\mathcal{D}$", "BH" to denote backhaul link, access link, direct link, device, and backhaul, respectively.

#### Backhaul Transmission

The SIR of a typical SBS associated with a MBS can be modeled as:

$$\text{SIR}_{1,2} = \frac{P_1 r_{1,2}^{-\alpha_1} g(0, \mathbf{y}_{1,0})}{\mathcal{I}_{1,2}}, \tag{4.3}$$

where $\mathcal{I}_{1,2}$ denotes the backhaul interference received at a SBS from MBSs that are scheduled to transmit on the same resource block excluding the tagged MBS. Then, $\mathcal{I}_{1,2} = P_1 \sum_{i:\mathbf{y}_{1,i} \in \mathbf{\Phi}_1 \setminus \{\mathbf{y}_{1,0}\}} \|\mathbf{y}_{1,i}\|^{-\alpha_1} g(0, \mathbf{y}_{1,i})$.

### Direct Transmission

The SIR of a typical device associated directly with a MBS is modeled as:

$$\mathrm{SIR}_{1,\mathcal{D}} = \frac{P_1 r_{1,\mathcal{D}}^{-\alpha_1} g(0, \mathbf{y}_{1,0})}{\mathcal{I}_{1,\mathcal{D}}}, \tag{4.4}$$

where $\mathcal{I}_{1,\mathcal{D}}$ denotes the interference received at a typical device from MBSs excluding the tagged MBS. Then $\mathcal{I}_{1,\mathcal{D}}$ can be calculated as: $\mathcal{I}_{1,\mathcal{D}} = P_1 \sum_{i:\mathbf{y}_{1,i}\in\mathbf{\Phi}_1\setminus\{\mathbf{y}_{1,0}\}} \|\mathbf{y}_{1,i}\|^{-\alpha_1} g(0, \mathbf{y}_{1,i})$.

### Access Transmission

The SNR of a typical device associated with a mm-wave SBS is modeled as:

$$\mathrm{SNR}_{2,\mathcal{D}} = \frac{P_2 G_2 \zeta_2 \|r_{2,\mathcal{D}}\|^{-\alpha_{2,l}} h_l(0, \mathbf{y}_{2,0})}{\sigma_2^2}, \tag{4.5}$$

where $\zeta_2$ is the near-field path loss at 1 m for mm-wave channels, and $\sigma_2^2$ is the variance of the additive white Gaussian noise at the device receiver. Given highly directional beams and high sensitivity to blockage, recent studies showed that mm-wave networks are typically noise limited [125, 27, 126].

## 4.3 The Meta Distribution: Mathematical Preliminaries

In this section, we define the meta distribution of the SIR of a typical device and highlight exact and approximate methods to evaluate the meta distribution.

**Definition 1** (Meta Distribution of the SIR and CSP)**.** *The meta distribution $\bar{F}_{P_s}(x)$ is the complementary cumulative distribution function (CCDF) of the CSP (or reliability) $P_s(\theta)$ and given by [119]:*

$$\bar{F}_{P_s}(x) \stackrel{\Delta}{=} \mathbb{P}(P_s(\theta) > x), \qquad x \in [0, 1], \tag{4.6}$$

*where, conditioned on the locations of the transmitters and that the desired transmitter is active, the CSP* $P_s(\theta)$ *of a typical device [119] can be given as* $P_s(\theta) \triangleq \mathbb{P}(\mathrm{SIR} > \theta|\mathbf{\Phi}, tx)$ *where* $\theta$ *is the desired* SIR*.*

Physically, the meta distribution provides the fraction of the active links whose CSP (or reliability) is greater than the reliability threshold $x$. Given $M_b(\theta)$ denotes the $b^{\mathrm{th}}$ moment of $P_s(\theta)$, i.e., $M_b(\theta) \triangleq \mathbb{E}^0(P_s(\theta)^b)$, $b \in \mathbb{C}$, the exact meta distribution can be given using the Gil-Pelaez theorem [135] as [119]:

$$\bar{F}_{P_s}(x) = \frac{1}{2} + \frac{1}{\pi}\int_0^{\infty} \frac{\Im\left(e^{-jt\log x} M_{jt}(\theta)\right)}{t}\mathrm{d}t, \tag{4.7}$$

where $\Im(w)$ is imaginary part of $w \in \mathbb{C}$ and $M_{jt}(\theta)$ denotes the imaginary moments of $P_s(\theta)$, i.e., , $j \triangleq \sqrt{-1}$. Using moment matching techniques and taking $\beta \triangleq \frac{(M_1(\theta)-M_2(\theta))(1-M_1(\theta))}{M_2(\theta)-M_1(\theta)^2}$, the meta distribution of the CSP can be approximated using the Beta distribution as follows:

$$\bar{F}_{P_s}(x) \approx 1 - I_x\left(\frac{\beta M_1(\theta)}{1-M_1(\theta)}, \beta\right), \qquad x \in [0,1], \tag{4.8}$$

where $M_1(\theta)$ and $M_2(\theta)$ are the first and the second moments, respectively; $I_x(a,b)$ is the regularized incomplete Beta function $I_x(a,b) \triangleq \frac{\int_0^x t^{a-1}(1-t)^{b-1}dt}{B(a,b)}$ and $B(a,b)$ is the Beta function.

## 4.4 The Meta Distribution of the SIR/SNR in Hybrid Spectrum Networks

To characterize the meta distribution of the SIR/SNR of a typical device that can associate with either a $\mu$wave MBS with probability $\mathcal{A}_1$ or with a wireless backhauled mm-wave SBS with probability $\mathcal{A}_2$, the methodology of analysis is listed as follows:

1. Derive the probability of a typical device associating with $\mu$wave MBSs $\mathcal{A}_1$, LOS mm-wave SBSs $\mathcal{A}_{2,\mathrm{L}}$, and NLOS mm-wave SBSs $\mathcal{A}_{2,\mathrm{N}}$ where $\mathcal{A}_2 = \mathcal{A}_{2,\mathrm{L}} + \mathcal{A}_{2,\mathrm{N}}$ (**Section 4.4.1**).

2. Formulate the meta distribution of the SIR/SNR of a device in the hybrid network ($\bar{F}^{b}_{P_{s,\mathrm{T}}}(x)$) considering the direct link and dual-hop link with wireless backhaul transmission (**Section 4.4.2**).

3. Formulate the CSP ($P_{s,\mathrm{T}}(\theta)$) and its $b^{\text{th}}$ moment ($M_{b,\mathrm{T}}$) (**Section 4.4.2**).

4. Derive the CSP at backhaul link $P_{s,\mathrm{BH}}(\theta_2)$, CSP at access link $P_{s,2}(\theta_{\mathcal{D}})$, and CSP at direct link $P_{s,1}(\theta_{\mathcal{D}})$. Derive the $b^{\text{th}}$ moments of CSPs, i.e., $M_{b,\mathrm{BH}}(\theta_2)$, $M_{b,2}(\theta_{\mathcal{D}})$, and $M_{b,1}(\theta_{\mathcal{D}})$ for backhaul link, access link, and direct link transmissions, respectively (**Section 4.5**).

5. Obtain the meta distributions of SIR/SNR and data rate in hybrid spectrum IoT network using Gil-Pelaez inversion and the Beta approximation (**Section 4.6**).

### 4.4.1 Association Probabilities in Hybrid Spectrum Networks

In this subsection, we characterize the probabilities with which a typical device associates with $\mu$wave MBSs ($\mathcal{A}_1$) or mm-wave SBSs ($\mathcal{A}_2$). The results are presented in the following.

**Lemma 6** (The Probability of Associating with mm-wave SBSs)**.** *The probability of a typical device to associate with a mm-wave SBS, using the association scheme in Eq.* (4.2)*, can be expressed as:*

$$\mathcal{A}_2 = 1 - \frac{2\pi\lambda_1}{\hat{a}\alpha_1}\Bigg(\int_0^{d^{\alpha_{2,L}}} H(l_1)e^{-\pi\lambda_2 p_L l_1^{\frac{2}{\alpha_{2,L}}}}\,dl_1 + \int_{d^{\alpha_{2,L}}}^{d^{\alpha_{2,N}}} H(l_1)e^{-\pi\lambda_2 p_L d^2}\,dl_1 + \int_{d^{\alpha_{2,N}}}^{\infty} H(l_1)e^{-\pi\lambda_2\left[(p_L-p_N)d^2+p_N l_1^{\frac{2}{\alpha_{2,N}}}\right]}\,dl_1\Bigg), \tag{4.9}$$

*where* $\hat{a} \triangleq \frac{P_2B_2G_2\zeta_2}{P_1B_1G_1\zeta_1}$ *and* $H(l_1) \triangleq \left(\frac{l_1}{\hat{a}}\right)^{\frac{2}{\alpha_1}-1}\exp\left(-\pi\lambda_1\left(\frac{l_1}{\hat{a}}\right)^{\frac{2}{\alpha_1}}\right)$*. Subsequently, the probability of a device to associate with a $\mu$wave MBS can be given as $\mathcal{A}_1 = 1-\mathcal{A}_2$. The conditional* *association probability for a typical device to associate with SBS is as follows:*

$$\bar{\mathcal{A}}_2(l_1) = 1 - \frac{2\pi\lambda_1}{\hat{a}\alpha_1}\Bigg( H(l_1)e^{-\pi\lambda_2 p_L l_1^{\frac{2}{\alpha_{2,L}}}} + H(l_1)e^{-\pi\lambda_2 p_L d^2} + H(l_1)e^{-\pi\lambda_2\left[(p_L - p_N)d^2 + p_N l_1^{\frac{2}{\alpha_{2,N}}}\right]}\Bigg), \quad (4.10)$$

*subsequently,* $\bar{\mathcal{A}}_1(l_1) = 1 - \bar{\mathcal{A}}_2(l_1)$.

*Proof.* See **Appendix B.1**. ■

A closed-form expression of $\mathcal{A}_1$ can be derived for a case of practical interest as follows.

**Corollary 3.** *When* $\alpha_1 = 4$, $\alpha_{2,L} = 2$, *and* $\alpha_{2,N} = 4$, *then* $\mathcal{A}_1$ *can be given in closed-form as follows:*

$$\mathcal{A}_1 = \frac{e^{C}(\Phi[\sqrt{C} + \sqrt{\pi\lambda_2 p_L d^2}] - \Phi[\sqrt{C}])}{\sqrt{p_L\lambda_2/\hat{a}}} + \frac{e^{-d^2\pi p_L\lambda_2}(e^{-\pi\lambda_1\sqrt{d^2/\hat{a}}} - e^{-\pi\lambda_1\sqrt{d^4/\hat{a}}})}{\pi\lambda_1/2\hat{a}} + \frac{e^{d^2\pi(p_N - p_L)\lambda_2 - C_1\sqrt{d^4/\hat{a}}})}{C_1/2\hat{a}}, \quad (4.11)$$

*where* $\Phi(\cdot)$ *is the error function,* $C = \frac{\pi\lambda_1^2}{4\hat{a}p_L\lambda_2}$ *and* $C_1 = \pi(\lambda_1 + \sqrt{\hat{a}}p_N\lambda_2)$ *and* $\mathcal{A}_2 = 1 - \mathcal{A}_1$.

It can be seen from **Corollary 1** that when the number of antenna elements $\mathcal{N}$ goes to infinity, i.e., $G_2 \rightarrow \infty$, $\hat{a} \rightarrow \infty$, then $\mathcal{A}_1$ can be simplified as $\mathcal{A}_1 = \frac{\Phi[\sqrt{\pi\lambda_2 p_L d^2}]}{\sqrt{p_L\lambda_2/\hat{a}}} + \frac{e^{d^2\pi(p_N - p_L)\lambda_2}}{C_1/2\hat{a}}$, which shows that association probability to MBS will be very small. Similar insights can be extracted for other parameters.

In order to derive the $b^{\text{th}}$ moment of CSP $P_{s,2}(\theta_{\mathcal{D}})$ on an access link when a device associates with a SBS (the CSP will be discussed later in Lemma 9), we have to derive the probability of a device to associate with LOS SBS $\mathcal{A}_{2,L}$ and NLOS SBS $\mathcal{A}_{2,N}$ which are defined as follows.

**Lemma 7** (The Probability of Associating with LOS and NLOS mm-wave SBSs)**.** *When a typical device associates with the mm-wave SBS tier, this typical device has two possibilities* *to connect to (a) a LOS mm-wave SBS with association probability $\mathcal{A}_{2,L}$ and (b) a NLOS mm-wave SBS with association probability $\mathcal{A}_{2,N}$ which are characterized, respectively, as follows:*

$$\mathcal{A}_{2,L} = \int_{0}^{d^{\alpha_{2,L}}} \bar{\mathcal{A}}_{2,L}(l_{2,L}) dl_{2,L}, \quad \mathcal{A}_{2,N} = \int_{d^{\alpha_{2,N}}}^{\infty} \bar{\mathcal{A}}_{2,N}(l_{2,N}) dl_{2,N}, \tag{4.12}$$

*where $\bar{\mathcal{A}}_{2,L}(l_{2,L})$ and $\bar{\mathcal{A}}_{2,N}(l_{2,N})$ are the conditional probabilities with which a typical device may associate to the LOS and NLOS mm-wave SBSs, respectively, and are defined as follows:*

$$\begin{aligned}
\bar{\mathcal{A}}_{2,L}(l_{2,L}) &\triangleq \frac{2\pi\lambda_2 p_L}{\alpha_{2,L}} l_{2,L}^{\frac{2}{\alpha_{2,L}}-1} e^{\left(-\pi\lambda_1(\bar{a}l_{2,L})^{\frac{2}{\alpha_1}} - \pi\lambda_2 p_L l_{2,L}^{\frac{2}{\alpha_{2,L}}}\right)}, \\
\bar{\mathcal{A}}_{2,N}(l_{2,N}) &\triangleq \frac{2\pi\lambda_2 p_N}{\alpha_{2,N}} l_{2,N}^{\frac{2}{\alpha_{2,N}}-1} \exp\Big(-\pi\lambda_1 \left(\bar{a}l_{2,N}\right)^{\frac{2}{\alpha_1}} - \\
&\qquad \pi\lambda_2 \big[p_L d^2 + p_N(l_{2,N}^{\frac{2}{\alpha_{2,N}}} - d^2)\big]\Big) dl_{2,N},
\end{aligned}$$

*where $\bar{a} \triangleq \frac{P_1 B_1 G_1 \zeta_1}{P_2 B_2 G_2 \zeta_2}$, $\bar{\mathcal{A}}_2(l_2) = \bar{\mathcal{A}}_{2,L}(l_{2,N}) + \bar{\mathcal{A}}_{2,N}(l_{2,N})$ and $\mathcal{A}_2 = \mathcal{A}_{2,L} + \mathcal{A}_{2,N}$.*

*Proof.* See **Appendix B.2**. ∎

A case of interest is when the number of antenna elements at mm-wave SBSs increases asymptotically. In such a case, the LOS and NLOS association probabilities can be simplified as follows:

**Corollary 4.** *When the number of antenna elements at mm-wave SBSs increases, i.e., $\mathcal{N} \to \infty$, $\alpha_1 = 4$, $\alpha_{2,L} = 2$, and $\alpha_{2,N} = 4$, then $\bar{a} \to 0$. The association probabilities can be given in closed-form as follows:*

$$\begin{aligned}
\mathcal{A}_{2,L} &= 1 - e^{-\pi p_L d^2 \lambda_2}, \\
\mathcal{A}_{2,N} &= e^{d^2\pi(-p_L+p_N)\lambda_2}(1 - \pi p_N d^2 \lambda_2 \, {}_1F_1[1; 2; \pi p_N d^2 \lambda_2]),
\end{aligned}$$

*where ${}_1F_1[a; b; z]$ is the Kummer Confluent Hypergeometric function.*

An interesting insight from **Corollary 2** can be seen when the intensity of SBSs $\lambda_2 \to \infty$ or $d$ is large, the probability of association to LOS SBSs $\mathcal{A}_{2,L}$ becomes almost 1. On the other hand, when $\lambda_2 \to 0$ or $d$ is small, ${}_1F_1[a; b; 0] = 1$ thus $\mathcal{A}_{2,N}$ becomes almost 1.

### 4.4.2 Formulation of the Meta distribution, CSP and its $b^{\text{th}}$ Moment in the Hybrid Network

When a device associates with a mm-wave SBS, the overall CSP depends on the CSPs of the SIR and SNR on both the backhaul link and the access link, respectively. On the other hand, when a device associates to MBS the CSP depends on the SIR of the direct link. It is thus necessary to formulate the relationship between the meta distribution, CSP, and its $b^{\text{th}}$ moment in the considered hybrid network as follows.

**Lemma 8** (Meta Distribution of a Typical Device in the Hybrid Network)**.** *The combined meta distribution of the SIR/SNR in the hybrid spectrum IoT network can be characterized as follows:*

$$\bar{F}_{P_{s,T}}(x) = \frac{1}{2} + \frac{1}{\pi}\int_0^\infty \frac{\Im\left(e^{-jt\log x} M_{jt,T}(\cdot)\right)}{t}dt, \tag{4.13}$$

*where $M_{jt,T}(\theta)$ can be characterized by deriving the $b^{\text{th}}$ moment of the $P_{s,T}(\cdot)$*[2]*.*

$$\begin{aligned} M_{b,T}(\cdot) &= M_{b,\text{Dual-Hop}} + M_{b,\text{Single-Hop}}, \\ &\overset{(a)}{=} \mathbb{E}_\Phi[\bar{\mathcal{A}}_2(l_2)P^b_{s,\text{Dual-Hop}}(\theta_2)] + \mathbb{E}_\Phi[\bar{\mathcal{A}}_1(l_1)P^b_{s,1}(\theta_\mathcal{D})], \\ &\overset{(b)}{=} \mathbb{E}_\Phi\left[\bar{\mathcal{A}}_2(l_2)(P_{s,\text{BH}}(\theta_2)P_{s,2}(\theta_\mathcal{D}))^b\right] + \mathbb{E}_\Phi\left[\bar{\mathcal{A}}_1(l_1)P^b_{s,1}(\theta_\mathcal{D})\right], \\ &\overset{(c)}{=} \mathbb{E}_\Phi\left[P_{s,\text{BH}}(\theta_2)^b\right]\mathbb{E}_\Phi\left[\bar{\mathcal{A}}_2(l_2)P_{s,2}(\theta_\mathcal{D})^b\right] + \mathbb{E}_\Phi\left[\bar{\mathcal{A}}_1(l_1)P^b_{s,1}(\theta_\mathcal{D})\right], \\ &\overset{(d)}{=} \mathbb{E}_\Phi\left[P_{s,\text{BH}}(\theta_2)^b\right]\mathbb{E}_\Phi\left[(\bar{\mathcal{A}}_{2,L}(l_{2,L}) + \bar{\mathcal{A}}_{2,N}(l_{2,N}))P_{s,2}(\theta_\mathcal{D})^b\right] + \mathbb{E}_\Phi\left[\bar{\mathcal{A}}_1(l_1)P^b_{s,1}(\theta_\mathcal{D})\right], \\ &\overset{(e)}{=} \underbrace{M_{b,\text{BH}}(\theta_2)M_{b,2}(\theta_\mathcal{D})}_{\textit{Device Associated with SBS}} + \underbrace{M_{b,1}(\theta_\mathcal{D})}_{\textit{Device Associated with MBS}}, \end{aligned} \tag{4.14}$$

*where $M_{b,\text{Dual-Hop}}$ is the $b^{\text{th}}$ moment of the SIR/SNR when a device associates to mm-wave SBS for dual-hop transmission and $M_{b,\text{Single-Hop}}$ is the $b^{\text{th}}$ moment of the SIR when a device associates to MBS for direct transmission. After reformulation, we define $M_{b,\text{BH}}(\theta_2)$ as the unconditional $b^{\text{th}}$ moment of the backhaul SIR, $M_{b,2}(\theta_\mathcal{D})$ as the unconditional $b^{\text{th}}$ moment of the SNR at access link when a device associates to mm-wave SBS, and $M_{b,1}(\theta_\mathcal{D})$*

---

[2] The $b^{\text{th}}$ moment of a random variable $X$ is the expected value of random variable to the power $b$, i.e., $\mathbb{E}[X^b]$.

*as the unconditional $b^{\text{th}}$ moment of the SIR at direct link when a device associates to $\mu$wave BS. Note that $P_{s,1}(\theta_{\mathcal{D}}) \overset{\Delta}{=} \mathbb{P}(\mathrm{SIR}_{1,\mathcal{D}} > \theta_{\mathcal{D}}|\mathbf{\Phi}_1, tx)$ denotes the CSP of device over the direct link, $P_{s,\mathrm{BH}}(\theta_2) \overset{\Delta}{=} \mathbb{P}(\mathrm{SIR}_{1,2} > \theta_2|\mathbf{\Phi_1}, tx)$ denotes the CSP at backhaul link, and $P_{s,2}(\theta_{\mathcal{D}}) \overset{\Delta}{=} \mathbb{P}(\mathrm{SNR}_{2,\mathcal{D}} > \theta_{\mathcal{D}}|\mathbf{\Phi}_2, tx)$ denotes the CSP for the access link transmission.*

*Proof.* Step (a) follows from the fact that the $b^{\text{th}}$ moment of the SIR or SNR of a device associated to tier $i$ can be defined as $M_b^{(i)} = \mathbb{E}[\bar{\mathcal{A}}_i M_{b|i}]$ where $\bar{\mathcal{A}}_i$ is the conditional association probability to tier $i$ and $M_{b|i} = P_{s,i}^b$ is the conditional $b^{\text{th}}$ moment of the SIR or SNR in tier $i$. In our case, we have $\bar{\mathcal{A}}_2(l_2)$ which is the conditional association probability to mm-wave SBS where $l_2 \in \{L, N\}$ since a device can associate to either LOS or NLOS mm-wave SBS. The step (b) follows from the fact that the CSP of the dual-hop transmission depends on the CSP of access and backhaul link; therefore, we have a product of the access and backhaul CSPs, i.e., $P_{s,\mathrm{BH}}(\theta_2)P_{s,2}(\theta_{\mathcal{D}})$ that are independent random variables. There is no correlation since $\mu$wave backhaul does not interfere with mm-wave transmissions. The step (c) follows from the fact if $X$ and $Y$ are independent then $\mathbb{E}[(XY)^b] = \mathbb{E}[X^b]\mathbb{E}[Y^b]$. Finally, the step (d) follows from the definition of $\bar{\mathcal{A}}_2(l_2)$ in **Lemma 2** and the step (e) follows by applying the definition of moments. ■

In the next section, we derive the CSP of access, backhaul, and direct links along with their respective $b^{\text{th}}$ moments, as needed in **Lemma 4** to characterize the overall moment as well as the meta distribution.

## 4.5 Characterization of the CSPs and Moments

In this section, we derive the CSPs $P_{s,\mathrm{BH}}(\theta_2)$, $P_{s,2}(\theta_{\mathcal{D}})$, $P_{s,1}(\theta_{\mathcal{D}})$ and the $b^{\text{th}}$ moments $M_{b,\mathrm{BH}}(\theta_2)$, $M_{b,2}(\theta_{\mathcal{D}})$, and $M_{b,1}(\theta_{\mathcal{D}})$ for backhaul link, access link, and direct link, respectively.

### 4.5.1 CSP and the $b^{\text{th}}$ Moment - Access Link

We condition on having a device at the origin which becomes a typical device. The CSP of a typical device at the origin associating with the mm-wave SBS-tier (when $k=2$) can be described as follows:

$$P_{s,2}(\theta_{\mathcal{D}}) = p_L P_{s,2,L}(\theta_{\mathcal{D}}) + p_N P_{s,2,N}(\theta_{\mathcal{D}}). \tag{4.15}$$

The CSP of the SNR of a device on the access link with LOS can be defined by substituting $\text{SNR}_{2,\mathcal{D}}$ defined in Eq. (4.5) into Definition 1 as follows:

$$\begin{aligned} P_{s,2,L}(\theta_{\mathcal{D}}) &= \mathbb{P}\left( h_L(0, \mathbf{y}_{2,0}) > \frac{\theta_{\mathcal{D}} r_{2,\mathcal{D}}^{\alpha_{2,L}} \sigma_2^2}{P_2 G_2} | \mathbf{\Phi}_1, \mathbf{\Phi}_2, \text{tx} \right), \\ &\overset{(a)}{=} 1 - \frac{\gamma\left(m_L, \frac{m_L}{\Omega_L}\nu_L\right)}{\Gamma(m_L)} \overset{(b)}{=} \frac{\Gamma\left(m_L, \frac{m_L}{\Omega_L}\nu_L\right)}{\Gamma(m_L)}, \end{aligned} \tag{4.16}$$

where (a) follows from the definition of $\nu_L \overset{\Delta}{=} \frac{\theta_{\mathcal{D}} r_{2,\mathcal{D}}^{\alpha_{2,L}} \sigma_2^2}{P_2 G_2}$ and the fact that the channel gain $h_L(0, \mathbf{y}_{2,0})$ is a normalized gamma random variable and $\gamma(.,.)$ is the lower incomplete gamma function and $\Gamma(s) = \gamma(s,x) + \Gamma(s,x)$, where $\Gamma(.,.)$ is the upper incomplete gamma function. Similarly, CSP of the SNR on the access link for NLOS case can be given as follows:

$$P_{s,2,N}(\theta_{\mathcal{D}}) = \frac{\Gamma\left(m_N, \frac{m_N}{\Omega_N}\nu_N\right)}{\Gamma(m_N)}, \tag{4.17}$$

where $\nu_N \overset{\Delta}{=} \frac{\theta_{\mathcal{D}} r_{2,\mathcal{D}}^{\alpha_{2,N}} \sigma_2^2}{P_2 G_2}$. As such, the $\boldsymbol{b^{th}}$ moment of the CSP on the access link for the typical device when it is served by the mm-wave SBS tier is given by the following:

**Lemma 9.** *The $b^{\text{th}}$ moment of the SNR at an "access link" when a device associates with a mm-wave SBS can be characterized in Eq. (4.18) as follows:*

$$\begin{aligned} M_{b,2}(\theta_{\mathcal{D}}) = \sum_{k=0}^{b} \binom{b}{k} (-1)^k \Bigg( & p_L^b \sum_{\ddot{k}=0}^{m_L k} \binom{m_L k}{\ddot{k}} (-1)^{\ddot{k}} \int_0^{d^{\alpha_{2,L}}} e^{-\zeta_L \ddot{k} \ddot{\nu}_L l_{2,L}} \bar{\mathcal{A}}_{2,L}(l_{2,L}) + \\ & p_N^b \sum_{\ddot{k}=0}^{m_N k} \binom{m_N k}{\ddot{k}} (-1)^{\ddot{k}} \int_{d^{\alpha_{2,N}}}^{\infty} e^{-\zeta_N \ddot{k} \ddot{\nu}_N l_{2,N}} \bar{\mathcal{A}}_{2,N}(l_{2,N}) \Bigg), \end{aligned} \tag{4.18}$$

*where* $\bar{\mathcal{A}}_{2,L}(l_{2,L})$ *and* $\bar{\mathcal{A}}_{2,N}(l_{2,N})$ *are given in* **Lemma 2**, $\zeta_L \triangleq m_L(m_L!)^{-1/m_L}$, $\nu_L \triangleq \frac{\theta_{\mathcal{D}} r_{2,\mathcal{D}}^{\alpha_{2,L}} \sigma_2^2}{P_2 G_2}$, $\zeta_N \triangleq m_N(m_N!)^{-1/m_N}$, *and* $\nu_N \triangleq \frac{\theta_{\mathcal{D}} r_{2,\mathcal{D}}^{\alpha_{2,N}} \sigma_2^2}{P_2 G_2}$, $\ddot{\nu}_L \triangleq \frac{\nu_L}{r^{\alpha_{2,L}}} = \frac{\nu_L}{l_{2,L}} = \frac{\theta_{\mathcal{D}}\sigma_2^2}{P_2 G_2}$ *and* $\ddot{\nu}_N \triangleq \frac{\nu_N}{r^{\alpha_{2,N}}} = \frac{\nu_N}{l_{2,N}} = \frac{\theta_{\mathcal{D}}\sigma_2^2}{P_2 G_2}$.

*Proof.* See **Appendix B.3**. ■

For $\alpha_1 = 4$, $\alpha_{2,L} = 2$, and $\alpha_{2,N} = 4$, we can get $M_{b,2}(\theta_{\mathcal{D}})$ in closed-form using **Corollary 1**. Also, for scenarios where $\mathcal{N} \to \infty$, $\alpha_1 = 4$, $\alpha_{2,L} = 2$, and $\alpha_{2,N} = 4$, then $\bar{a} \to 0$. Also, $\ddot{v}_L \to 0$ and $\ddot{v}_N \to 0$, we can get $M_{b,2}(\theta_{\mathcal{D}})$ in closed-form using **Corollary 2**.

### 4.5.2 CSP and $b^{\text{th}}$ Moment - Backhaul Link

For the backhaul link, we condition on having a SBS at the origin which becomes the typical SBS. Using the expression of $\text{SIR}_{1,2}$ in Eq. (4.3) the CSP of the backhaul link $P_{s,\text{BH}}(\theta_2)$ can be given as:

$$\begin{aligned}
P_{s,\text{BH}}(\theta_2) &= \mathbb{P}\left(g(0,\mathbf{y}_{1,0}) > \frac{\theta_2 r_{1,2}^{\alpha_1}}{P_1}\mathcal{I}_{1,2}|\mathbf{\Phi}_1,\mathbf{\Phi}_2,\text{tx}\right),\\
&\overset{(a)}{=} \mathbb{E}\Bigg[\exp(-\theta_2 r_{1,2}^{\alpha_1}\sum_{i:\mathbf{y}_{1,i}\in\mathbf{\Phi}_1\setminus\{\mathbf{y}_{1,0}\}}\|\mathbf{y}_{1,i}\|^{-\alpha_1} g(0,\mathbf{y}_{1,i}))\Bigg],\\
&= \prod_{\mathbf{y}_{1,i}\in\mathbf{\Phi}_1\setminus\{\mathbf{y}_{1,0}\}}\mathbb{E}\Bigg[\exp\left(-\theta_2 r_{1,2}^{\alpha_1}\|\mathbf{y}_{1,i}\|^{-\alpha_1} g(0,\mathbf{y}_{1,i})\right)\Bigg],\\
&\overset{(b)}{=} \prod_{\mathbf{y}_{1,i}\in\mathbf{\Phi}_1\setminus\{\mathbf{y}_{1,0}\}}\frac{1}{1+\theta_2\left(\frac{r_{1,2}}{\|\mathbf{y}_{1,i}\|}\right)^{\alpha_1}}.
\end{aligned} \tag{4.19}$$

where (a) follows from the Rayleigh fading channel gain $g(0,\mathbf{y}_{1,0}) \sim \exp(1)$ and (b) is found by taking the expectation with respect to $g(0,\mathbf{y}_{2,i})$. The $\boldsymbol{b^{th}}$ moment of the CSP on the backhaul link is given as:

$$\begin{aligned}
M_{b,\text{BH}}(\theta_2) &= \mathbb{E}\Big[P_{s,\text{BH}}(\theta_2)^b\Big],\\
&= \mathbb{E}\Bigg[\prod_{\mathbf{y}_{1,i}\in\mathbf{\Phi}_1\setminus\{\mathbf{y}_{1,0}\}}\frac{1}{\left(1+\theta_2\left(\frac{r_{1,2}}{\|\mathbf{y}_{1,i}\|}\right)^{\alpha_1}\right)^b}\Bigg],
\end{aligned}$$

$$\overset{(a)}{=}\left(1+2\int_0^1\left(1-\frac{1}{(1+\theta_2 r^{\alpha_1})^b}\right)r^{-3}dr\right)^{-1},$$
$$=\frac{1}{{}_2F_1(b,-\frac{2}{\alpha_1};1-\frac{2}{\alpha_1};-\theta_2)}, \tag{4.20}$$

where (a) follows from the probability generating functional (PGFL) of PPP, i.e., $G_{\mathcal{R}}[f] \overset{\Delta}{=} \mathbb{E}\prod_{x\in\mathcal{R}} f(x) = \frac{1}{1+2\int_0^1(1-f(x))x^{-3}dx}$. [136, lemma 1] and ${}_2F_1(.,.;.;.)$ represents Gauss' Hypergeometric function.

### 4.5.3 CSP and $b^{\text{th}}$ Moment - Direct Link

Using the expression of $\text{SIR}_{1,\mathcal{D}}$ in Eq. (4.4), we calculate the CSP of the direct link $P_{s,1}(\theta_{\mathcal{D}})$ as follows:

$$\begin{aligned}
P_{s,1}(\theta_{\mathcal{D}}) &= \mathbb{P}\left(g(0,\mathbf{y}_{1,0}) > \frac{\theta_{\mathcal{D}} r_{1,\mathcal{D}}^{\alpha_1}}{P_1}\mathcal{I}_{1,\mathcal{D}}|\mathbf{\Phi}_1,\mathbf{\Phi}_2,\text{tx}\right),\\
&\overset{(a)}{=}\mathbb{E}\left[\exp\left(-\theta_{\mathcal{D}} r_{1,\mathcal{D}}^{\alpha_1}\sum_{i:\mathbf{y}_{1,i}\in\mathbf{\Phi}_1\setminus\{\mathbf{y}_{1,0}\}}\|\mathbf{y}_{1,i}\|^{-\alpha_1}g(0,\mathbf{y}_{1,i})\right)\right],\\
&=\prod_{\mathbf{y}_{1,i}\in\mathbf{\Phi}_1\setminus\{\mathbf{y}_{1,0}\}}\mathbb{E}\left[\exp\left(-\theta_{\mathcal{D}} r_{1,\mathcal{D}}^{\alpha_1}\|\mathbf{y}_{1,i}\|^{-\alpha_1}g(0,\mathbf{y}_{1,i})\right)\right],\\
&\overset{(b)}{=}\prod_{\mathbf{y}_{1,i}\in\mathbf{\Phi}_1\setminus\{\mathbf{y}_{1,0}\}}\frac{1}{1+\theta_{\mathcal{D}}\left(\frac{r_{1,\mathcal{D}}}{\|\mathbf{y}_{1,i}\|}\right)^{\alpha_1}}.
\end{aligned} \tag{4.21}$$

where (a) follows from the channel gain $g(0,\mathbf{y}_{1,0}) \sim \exp(1)$ and is independently exponentially distributed with unit mean and (b) is obtained by taking the expectation with respect to $g(0,\mathbf{y}_{1,i})$. While taking the association probabilities into consideration, the $\boldsymbol{b^{th}}$ moment of the CSP $P_{s,1}(\theta_{\mathcal{D}})$ of the typical device when it is served by a $\mu$wave MBS is characterized in the following lemma.

**Lemma 10** (The $b^{\text{th}}$ moment of the CSP ($P_{s,1}(\theta_{\mathcal{D}})$) when a device associates with a MBS)**.** *The $b^{\text{th}}$ moment of the CSP experienced by a device, when the device associates with a MBS, can be characterized in Eq. (4.22) as follows:*

$$M_{b,1}(\theta_{\mathcal{D}}) = \frac{2\pi\lambda_1}{\hat{a}\alpha_1}\left\{\int_0^{d^{\alpha_{2,L}}} H(l_1)\exp\left(-\pi\lambda_2 p_L l_1^{\frac{2}{\alpha_{2,L}}}\right)dl_1 + \int_{d^{\alpha_{2,L}}}^{d^{\alpha_{2,N}}} H(l_1)\exp\left(-\pi\lambda_2 p_L d^2\right)dl_1 + \right.$$

$$\int_{d^{\alpha_{2,N}}}^{\infty} H(l_1) \exp\left(-\pi\lambda_2[p_L d^2 + p_N \left(l_1^{\frac{2}{\alpha_{2,N}}} - d^2\right)\right) dl_1 \Bigg\} \times \exp\left(\frac{-2\lambda_1 \pi l_1^{\frac{2}{\alpha_1}}}{\alpha_1} \int_0^1 \left[1 - \frac{1}{(1+\theta_{\mathcal{D}} v)^b}\right] \frac{1}{v^{\frac{2}{\alpha_1}+1}} dv\right), \tag{4.22}$$

*Proof.* See **Appendix B.4**. ■

Note that $\int_0^1 \left[1 - \frac{1}{(1+\theta_{\mathcal{D}} v)^b}\right] \frac{1}{v^{\frac{2}{\alpha_1}+1}} \mathrm{d}v$ is independent of $l_1$, thus where $\mathcal{N} \to \infty$ or $\alpha_1 = 4$, $\alpha_{2,L} = 2$, and $\alpha_{2,N} = 4$, then we can get a closed-form for the three integral over $l_1$ using **Corollary 1** and **Corollary 2**.

### 4.5.4 Combined $b^{\text{th}}$ Moment of the CSP in Hybrid Networks

After substituting the values of $M_{b,\text{BH}}(\theta_2)$, $M_{b,2}(\theta_{\mathcal{D}})$, and $M_{b,1}(\theta_{\mathcal{D}})$ in Eq. (4.20), Eq. (4.18), and Eq. (4.22), respectively into the total meta distribution for the entire network in Eq. (4.14), we get the $b^{\text{th}}$ moment of the CSP at a typical device as shown in Eq. (4.23) as follows:

$$M_{b,\text{T}} =$$

$$\frac{1}{{}_2F_1(b, -\frac{2}{\alpha_1}; 1 - \frac{2}{\alpha_1}; -\theta_2)} \times \Bigg\{ \sum_{k=0}^{b} \binom{b}{k} (-1)^k \Bigg( p_L^b \sum_{\ddot{k}=0}^{m_L k} \binom{m_L k}{\ddot{k}} (-1)^{\ddot{k}} \int_0^{d^{\alpha_{2,L}}} e^{-\zeta_L \ddot{k} \ddot{\nu}_L l_{2,\mathrm{L}}} \bar{\mathcal{A}}_{2,L}(l_{2,L}) +$$

$$p_N^b \sum_{\ddot{k}=0}^{m_N k} \binom{m_N k}{\ddot{k}} (-1)^{\ddot{k}} \int_{d^{\alpha_{2,N}}}^{\infty} e^{-\zeta_N \ddot{k} \ddot{\nu}_N l_{2,\mathrm{N}}} \bar{\mathcal{A}}_{2,N}(l_{2,N}) \Bigg) \Bigg\} + M_{b,1}(\theta_{\mathcal{D}}), \tag{4.23}$$

In the next section, we use the combined $b^{\text{th}}$ moment in (4.23) to compute the meta distributions of SIR/SNR and data rate using Gil-Pelaez inversion and the Beta approximation.

## 4.6 Computing the Meta Distributions and Special Cases

In this section, we compute the meta distribution of SIR/SNR using Gil-Pelaez inversion and beta approximation by applying the derived result of $M_{b,\text{T}}$. Special cases where $b = 1$ provides the standard coverage probability and $b = -1$ provides the mean local delay are discussed. Further, we show how to evaluate the data rate meta distribution from the derived framework.

### 4.6.1 Computing the Meta Distribution of the SIR/SNR

Technically, substituting $b = jt$ in (4.23), we should obtain the imaginary moments $M_{jt,\mathrm{T}}$. However, since the expression of $M_{jt,\mathrm{T}}$ relies on a Binomial expansion of power $b$, the results cannot be obtained directly through substitution. Therefore, we apply Newton's generalized binomial theorem given as follows.

**Definition 2.** *Isaac Newton's generalized binomial theorem is to allow real exponents other than non-negative integers, i.e., imaginary exponent* $r$*, as* $\binom{r}{k} = \frac{r(r-1)\ldots(r-k+1)}{k!} = \frac{(r)_k}{k!}$*, where* $(.)_k$ *is the Pochhammer symbol, which stands here for a falling factorial.*

Applying **Definition 2** in step (e) of **Appendix B.3**, we then obtain the expression for $M_{jt,\mathrm{T}}$ as shown in Eq. (4.24) as follows:

$$M_{jt,\mathrm{T}} =$$

$$\frac{1}{{}_2F_1(jt, -\frac{2}{\alpha_1}; 1-\frac{2}{\alpha_1}; -\theta_2)} \times \Bigg\{ p_L^{jt} \sum_{k=0}^{\infty} \frac{(jt)_k}{k!} (-1)^k \sum_{\ddot{k}=0}^{m_L k} \binom{m_L k}{\ddot{k}} (-1)^{\ddot{k}} \int_0^{d^{\alpha_{2,L}}} e^{-\zeta_L \ddot{k} \ddot{\nu}_L l_{2,\mathrm{L}}} \bar{\mathcal{A}}_{2,L}(l_{2,L}) + p_N^{jt} \sum_{k=0}^{\infty} \frac{(jt)_k}{k!} (-1)^k \sum_{\ddot{k}=0}^{m_N k} \binom{m_N k}{\ddot{k}} (-1)^{\ddot{k}} \int_{d^{\alpha_{2,N}}}^{\infty} e^{-\zeta_N \ddot{k} \ddot{\nu}_N l_{2,\mathrm{N}}} \bar{\mathcal{A}}_{2,N}(l_{2,N}) \Bigg\} + M_{jt,1}(\theta_{\mathcal{D}}), \tag{4.24}$$

The imaginary moments can be substituted in the Gil-Pelaez inversion theorem as in **Definition 1** to obtain $\bar{F}_{P_s,\mathrm{T}}$. Furthermore, we follow [119, 123, 137] to approximate the meta distribution by a Beta distribution by matching the first and second moments, which are easily obtained from the general result in Eq. (4.23) by substituting $b = 1$ and $b = 2$ to get $M_{1,\mathrm{T}}$ and $M_{2,\mathrm{T}}$, respectively. Taking $\beta \triangleq \frac{(M_{1,\mathrm{T}} - M_{2,\mathrm{T}})(1-M_{1,\mathrm{T}})}{M_{2,\mathrm{T}} - M_{1,\mathrm{T}}^2}$, the meta distribution using beta approximation can be given as follows:

$$\bar{F}_{P_{s,\mathrm{T}}}(x) \approx 1 - I_x\left(\frac{\beta M_{1,\mathrm{T}}}{1 - M_{1,\mathrm{T}}}, \beta\right), \tag{4.25}$$

where $x \in [0, 1]$.

### 4.6.2 The Mean and Variance of the Local Delay

The mean local delay is the mean number of transmission attempts, i.e., re-transmissions, needed to successfully transmit a packet to the target receiver. The mean local delay $M_{-1,\mathrm{T}}$ which is the $-1^{\mathrm{st}}$ moment of the CSP of a typical device should be calculated by substituting $b = -1$ in Eq. (4.23). However, since the expression of $M_{b,\mathrm{T}}$ relies on a Binomial expansion of power $b$, the results cannot be obtained directly through substitution. Therefore, we apply the Binomial theorem for the negative integers as follows.

**Definition 3.** *The Binomial theorem for a negative integer power $n$ can be given [138] as* $(x+y)^n = \sum_{k=0}^{\infty}(-1)^k\binom{-n+k-1}{k}y^{n-k}x^k$,

Applying **Definition 3** in step (e) of **Appendix B.3**, we then obtain the expression for $M_{-1,\mathrm{T}}$ in Eq. (4.26) as follows:

$$
\begin{aligned}
&M_{-1,\mathrm{T}} = \\
&\frac{1}{{}_2F_1(-1,-\frac{2}{\alpha_1};1-\frac{2}{\alpha_1};-\theta_2)} \times \Bigg\{p_L^{-1}\sum_{k=0}^{\infty}\sum_{\ddot{k}=0}^{m_L k}\binom{m_L k}{\ddot{k}}(-1)^{\ddot{k}}\int_0^{d^{\alpha_{2,L}}} e^{-\zeta_L \ddot{k}\ddot{\nu}_L l_{2,\mathrm{L}}}\bar{\mathcal{A}}_{2,L}(l_{2,L})+ \\
&\qquad p_N^{-1}\sum_{k=0}^{\infty}\sum_{\ddot{k}=0}^{m_N k}\binom{m_N k}{\ddot{k}}(-1)^{\ddot{k}}\int_{d^{\alpha_{2,N}}}^{\infty} e^{-\zeta_N \ddot{k}\ddot{\nu}_N l_{2,\mathrm{N}}}\bar{\mathcal{A}}_{2,N}(l_{2,N})dl_{2,N}\Bigg\} + M_{-1,1}(\theta_{\mathcal{D}}),
\end{aligned}
\tag{4.26}
$$

**Remark:** In order to better characterize the fluctuation of the local delay, the variance of the local delay (also referred to as network jitter) can be given by $NJ = M_{-2,\mathrm{T}} - M_{-1,\mathrm{T}}^2$.

### 4.6.3 The Meta Distribution of the Data Rate in Hybrid Spectrum Networks

Let $\mathcal{T}$ denotes the data rate (in bits per sec) of the typical device on a specific transmission link which is a random variable and is defined as $\mathcal{R} = W\log_2(1+\mathrm{SIR})$ using Shannon capacity. Using the meta distribution of the SIR, the meta distribution of the data rate can be derived to present the fraction of active devices in each realization of the point process that have a data rate $\mathcal{R}$ greater than $\mathcal{T}$ with probability at least $x$, i.e., devices data rate reliability threshold. That is, first deriving the CSP of the data rate as follows:

$$\begin{aligned}\mathbb{P}[\mathcal{R} > \mathcal{T} | \mathbf{\Phi}, \mathrm{tx}] &= \mathbb{P}[W \log_2(1 + \mathrm{SIR}) > \mathcal{T} | \mathbf{\Phi}, \mathrm{tx}], \\ &= \mathbb{P}[\mathrm{SIR} > 2^{\frac{\mathcal{T}}{W}} - 1 | \mathbf{\Phi}, \mathrm{tx}]. \end{aligned} \tag{4.27}$$

where $P_s(2^{\frac{\mathcal{T}}{W}} - 1) \triangleq \mathbb{P}(\mathrm{SIR} > 2^{\frac{\mathcal{T}}{W}} - 1 | \mathbf{\Phi}_1, \mathrm{tx})$ denote the CSP of the device data rate over single link. Finally, deriving the $b^{\mathrm{th}}$ moment of the CSP of the data rate and applying Gil-Pelaez inversion we can obtain the meta distribution of the data rate.

**Corollary 5.** *Similar to the meta distribution of the SIR/SNR derived in Lemma 8 and conditioned on the location of the point process, we derive the meta distribution of the data rate in hybrid IoT cellular networks, using the moment $\mathcal{Q}_b$ of the conditional data rate as follows:*

$$\begin{aligned}\mathcal{Q}_b(\mathcal{T}) &= \mathbb{E}[\bar{\mathcal{A}}_2(l_2)\mathbb{P}^0\left(P_{s,\mathrm{BH}}(2^{\frac{\mathcal{T}_{\mathrm{BH}}}{(1-\eta)W_1}} - 1) P_{s,2}(2^{\frac{\mathcal{T}_2}{W_2}} - 1) > x\right)] + \mathbb{E}[\bar{\mathcal{A}}_1(l_1)\mathbb{P}^0(P_{s,1}(2^{\frac{\mathcal{T}_1}{\eta W_1}} - 1) > x)], \\ &= M_{b,\mathrm{BH}}\left(2^{\frac{\mathcal{T}_{\mathrm{BH}}}{(1-\eta)W_1}} - 1\right) M_{b,2}\left(2^{\frac{\mathcal{T}_2}{W_2}} - 1\right) + M_{b,1}\left(2^{\frac{\mathcal{T}_1}{\eta W_1}} - 1\right), \end{aligned} \tag{4.28}$$

*where $P_{s,1}(2^{\frac{\mathcal{T}_1}{\eta W_1}} - 1) \triangleq \mathbb{P}(\mathrm{SIR}_{1,\mathcal{D}} > 2^{\frac{\mathcal{T}_1}{\eta W_1}} - 1 | \mathbf{\Phi}_1, tx)$, $P_{s,\mathrm{BH}}(2^{\frac{\mathcal{T}_{\mathrm{BH}}}{(1-\eta)W_1}} - 1) \triangleq \mathbb{P}(\mathrm{SIR}_{1,2} > 2^{\frac{\mathcal{T}_{\mathrm{BH}}}{(1-\eta)W_1}} - 1 | \mathbf{\Phi_1}, tx)$, and $P_{s,2}(2^{\frac{\mathcal{T}_2}{W_2}} - 1) \triangleq \mathbb{P}(\mathrm{SNR}_{2,\mathcal{D}} > 2^{\frac{\mathcal{T}_2}{W_2}} - 1 | \mathbf{\Phi}_2, tx)$ denote the CSP of the device data rate on the direct, backhaul, and access link, respectively.*

In the following section, we discuss the application of this framework to two scenarios (i) $\mu$wave only network and (ii) mm-wave backhauls and microwave access links.

## 4.7 Extensions of The Model to Other Network Architectures

The framework discussed above can be flexibly applied to different network architectures. In this section we discuss how to extend the framework to two other network architectures:

1) both tiers operating in the sub-6GHz (microwave) spectrum as in traditional cellular networks; and 2) the two tiers operating in two millimeter-wave spectrums that are orthogonal to each other. We provide only general directions of how to extend the earlier framework to these two other network architectures.

### 4.7.1 The Meta Distribution of the SIR in Microwave-only Networks

We characterize the meta distribution of the downlink SIR attained at a typical device in a $\mu$wave-only IoT network, i.e., the access and backhaul links of SBSs operate in the $\mu$wave frequency. A device associates with either a serving MBS for direct transmissions (when $k = 1$) or a SBS for dual-hop transmissions (when $k = 2$), depending on the biased received signal power criterion. MBSs and SBSs are assumed to operate on orthogonal spectrums; thus, there is no inter-tier interference. On the other hand, each SBS associates with a MBS based on the maximum received power at the SBS. The association criterion for a typical device can be described as follows [3]:

$$P_k B_k (\min_i \|\mathbf{y}_{k,i} - \mathbf{x}\|)^{-\alpha_k} \geq P_j B_j (\min_{i'} \|\mathbf{y}_{j,i'} - \mathbf{x}\|)^{-\alpha_j}, \forall j \tag{4.29}$$

where $\|.\|$ denotes the Euclidean distance. A typical device associates with a serving node (given by Eq. (4.29))), which is termed the tagged SBS. For the sake of clarity, we define $\hat{P}_{jk} \triangleq \frac{P_j}{P_k}$, $\hat{B}_{jk} \triangleq \frac{B_j}{B_k}$, $\hat{\lambda}_{jk} \triangleq \frac{\lambda_j}{\lambda_k}$. As derived in [3], the conditional association probability for the typical device connecting to the $k^{\text{th}}$ tier (conditional over the desired link distance $r_{\mathcal{D},k}$) is as follows:

$$\mathbb{P}(n = k | r_{\mathcal{D},k}) = \prod_{j \neq k} e^{-\pi \lambda_j (\hat{P}_{jk} \hat{B}_{jk})^{2/\alpha_j} r^2}, \tag{4.30}$$

where $n$ denotes the index of the tier associating with the typical device. We calculate the CSP $P_{s,2'}(\theta_{\mathcal{D}})$ (when $k = 2$) of the access link operating in the $\mu$wave band as follows:

$$P_{s,2'}(\theta_{\mathcal{D}}) = \mathbb{P}\left( g(0, \mathbf{y}_{2,0}) > \frac{\theta_{\mathcal{D}} r_{2,\mathcal{D}}^{\alpha_2}}{P_2} \mathcal{I}_{2,\mathcal{D}} | \mathbf{\Phi}_1, \mathbf{\Phi}_2, \text{tx} \right),$$

$$\overset{(a)}{=} \mathbb{E}\left[ \exp\left( -\theta_{\mathcal{D}} r_{2,\mathcal{D}}^{\alpha_2} \sum_{i:\mathbf{y}_{2,i}\in\mathbf{\Phi}_2\setminus\{\mathbf{y}_{2,0}\}} \|\mathbf{y}_{2,i}\|^{-\alpha_2} g(0,\mathbf{y}_{2,i}) \right) \right],$$

$$\overset{(b)}{=} \prod_{\mathbf{y}_{2,i}\in\mathbf{\Phi}_2\setminus\{\mathbf{y}_{2,0}\}} \frac{1}{1+\theta_{\mathcal{D}}\left(\frac{r_{2,\mathcal{D}}}{\|\mathbf{y}_{2,i}\|}\right)^{\alpha_2}}. \tag{4.31}$$

where (a) follows from the channel gain $g(0,\mathbf{y}_{2,0}) \sim \exp(1)$ and is independently exponentially distributed with unit mean and (b) is obtained by taking the expectation with respect to $g(0,\mathbf{y}_{2,i})$.

**Lemma 11.** *Using Eq. (4.21) and Eq. (4.31), we calculate a general expression for the* $\boldsymbol{b}^{\mathbf{th}}$ *moment of the CSP on direct link* $M_{b,k'}$ *(when* $k=2$*) and the* $\boldsymbol{b}^{\boldsymbol{th}}$ *moment of the CSP at access link (when* $k=1$*) as:*

$$M_{b,k'} = \frac{1}{\sum\limits_{j\neq k} \hat{\lambda}_{jk}(\hat{P}_{jk}\hat{B}_{jk})^{2/\alpha_j} + {}_2F_1(b,-\frac{2}{\alpha_k};1-\frac{2}{\alpha_k};-\theta_{\mathcal{D}})}. \tag{4.32}$$

*Proof.* See **Appendix B.5**. ■

Note that Lemma 11 is novel and different from [139] where we derive the $b^{\text{th}}$ moment of CSP for orthogonal spectrum two tier IoT network while the work in [139] is done for shared spectrum tiers.

Similarly, the moment of the CSP of a typical device with offloading biases is defined as follows:

$$M_{b,\mathrm{T}} = \underbrace{M_{b,\text{dual-hop}}}_{\text{Dual-hop transmission}} + \underbrace{M_{b,1'}(\theta_{\mathcal{D}})}_{\text{Direct transmission}},$$

$$\overset{(a)}{=} M_{b,\mathrm{BH}}(\theta_2)M_{b,2'}(\theta_{\mathcal{D}}) + M_{b,1'}(\theta_{\mathcal{D}}), \tag{4.33}$$

where $M_{b,\mathrm{BH}}(\theta_2)$, $M_{b,2'}(\theta_{\mathcal{D}})$, and $M_{b,1'}(\theta_{\mathcal{D}})$ are defined in Eq. (4.20), Eq. (4.32) (when $k=2$), and Eq. (4.32) (when $k=1$), respectively. The step (a) follows from the similar approach as taken in **Lemma 4**.

$$M_{b,\text{dual-hop}} = \mathbb{E}\left[ P_{s,\mathrm{BH}}(\theta_2)^b \times \prod_{j\neq k} e^{-\pi\lambda_j(\hat{P}_{jk}\hat{B}_{jk})^{2/\alpha_j}r^2} P_{s,2'}(\theta_{\mathcal{D}})^b \right]$$

$$
\begin{aligned}
&\overset{(a)}{=} \underbrace{\mathbb{E}\Big[P_{s,\mathrm{BH}}(\theta_2)^b\Big]}_{M_{b,\mathrm{BH}}(\theta_2)(\text{Backhaul link })} \underbrace{\mathbb{E}\Big[\prod_{j\neq k} e^{-\pi\lambda_j(\hat{P}_{jk}\hat{B}_{jk})^{2/\alpha_j}r^2} P_{s,2'}(\theta_{\mathcal{D}})^b\Big]}_{M_{b,2}(\theta_{\mathcal{D}})(\text{access link})}, \\
&\overset{(b)}{=} \frac{1}{{}_2F_1(b,-\frac{2}{\alpha_1};1-\frac{2}{\alpha_1};-\theta_2)} \times \frac{1}{\hat{\lambda}_{12}(\hat{P}_{12}\hat{B}_{12})^{2/\alpha_1} + {}_2F_1(b,-\frac{2}{\alpha_2};1-\frac{2}{\alpha_2};-\theta_{\mathcal{D}})}, \qquad (4.34)
\end{aligned}
$$

where (a) follows from the independence between the location of the MBSs and SBSs. In step (b) we substitute $M_{b,\mathrm{BH}}(\theta_2)$ from Eq. (4.20) and $M_{b,2'}(\theta_{\mathcal{D}})$ into Eq. (4.32) when $k = 2$. By substituting Eq. (4.34) and Eq. (4.32) (when $k = 1$) in Eq. (4.33), we get the $b^{\text{th}}$ moment $M_{b,\mathrm{T}}$. Finally, by substituting $M_{b,\mathrm{T}}$ in Eq. (4.33) into either Eq. (4.13) or Eq. (4.8), we get the meta distribution of the SIR.

### 4.7.2 Other Network Architecture Scenarios

The proposed framework can be extended to a scenario where the backhaul and access transmissions are conducted on orthogonal mm-wave spectrum. Note that Eq. (4.3) will be changed similar to Eq. (4.5). Then, only the first term, $M_{b,\mathrm{BH}}(\theta_2)$ in the main Eq. (4.14) of our model that characterizes the moment of the CSP in the backhaul will be re-defined as $M_{b,\mathrm{BH}}(\theta_2) = \mathbb{E}[P^b_{s,2}(\theta_2)]$.

The framework can also be extended to a scenario where the backhaul transmissions are conducted on the mm-wave spectrum and the access links of SBSs operate on $\mu$-wave. In this case, we will need to use the results in Section VII.A while redefining the term $M_{b,\mathrm{BH}}(\theta_2)$ as $M_{b,\mathrm{BH}}(\theta_2) = \mathbb{E}[P^b_{s,2}(\theta_2)]$ in (4.34).

## 4.8 Numerical Results and Discussions

We present the simulation parameters in Section 4.8.1. Then, we validate our numerical results using Monte-Carlo simulations in Section 4.8.2. Also in Section 4.8.2, we use the developed analytical models to obtain insights related to the meta distribution of the SIR/SNR of a typical device, mean and variance of the success probability, transmission delay, and the reliability of a typical device in the downlink direction.

### 4.8.1 Simulation Parameters

Unless otherwise stated, we use the following simulation parameters throughout our numerical results. The transmission powers of MBSs and SBSs in the downlink are $P_1 = 50$ Watts and $P_2 = 5$ Watts, respectively. The size of the simulated network is 90km × 90km. We assume that the density of MBSs is $\lambda_1 = 2$ MBSs/km$^2$ and the density of SBSs is $\lambda_2 = 70$ SBSs/km$^2$. The offloading biases for the MBSs and the SBSs are $B_1 = B_2 = 1$, respectively. The PLE for MBSs is set to $\alpha_1 = 4$ and for mm-wave SBSs, $\alpha_{2,L} = 2$ in the case of LOS and $\alpha_{2,N} = 4$ in the case of NLOS. The network downlink bandwidth is 100 MHz for $\mu$wave MBSs and 1 GHz for mm-wave SBSs with channel frequency 28 GHz. The LOS (NLOS) states are modeled by large (small) values of $m$, i.e., $m_L = 2$ and $m_N = 1$ [25]. SBSs number of antenna elements is $\mathcal{N} = 10$. The receiver noise is calculated as [27] $\sigma_2^2 = -174$ dBm/Hz $+ 10\log_{10}(W_2) + 10$ dB, where $W_2 = 1$ GHz is bandwidth allocated to the mm-wave SBSs. The antenna gains of MBSs are $G_1^{\mathrm{o}} = 0$ dB and devices directional antenna gain is $G_{\mathcal{D}}^{\max} = 10$ dB.

### 4.8.2 Discussions

#### Association Probability

Fig. 4.2 illustrates the accuracy of association probabilities in a hybrid spectrum network, derived in **Lemma 6** and **Lemma 7**, as a function of $\lambda_2$ by showing a comparison with Monte-Carlo simulations. We notice from Fig. 4.2 that by increasing the density of the mm-wave SBSs $\lambda_2$, the probability of association with mm-wave LOS SBSs $\mathcal{A}_{2,L}$ increases which confirms the insights from **Corollary 1** and **Corollary 2**. The reason is the increasing number of SBSs per unit area within the LOS ball will favour the device association towards LOS SBSs and reduces the chances of associating with NLOS SBSs. The addition of $\mathcal{A}_1 +$

$\mathcal{A}_{2,L}+\mathcal{A}_{2,N}=1$ is equal to unity for different densities of SBSs $\lambda_2$. Note that the probability of associating with $\mu$wave MBSs is minimal due to a higher path-loss exponent and NLOS omnidirectional transmissions from MBSs.

### The Meta Distribution of the SIR/SNR

In Fig. 4.3, we validate our analytical results for the meta distribution of the SIR/SNR of a typical device in a hybrid spectrum IoT network through simulations. Fig. 4.3 also depicts the probability of achieving reliability $x$, i.e., $x$% fraction of devices can achieve their quality of service for $\theta \in \{10, 1, 0.1\}$ dB. From Fig. 4.3, we note that about 18% of the devices (when $\theta = 10$), 51% of devices (when $\theta = 1$), and 96% of devices (when $\theta = 0.1$) have success probabilities equal to 0.3.

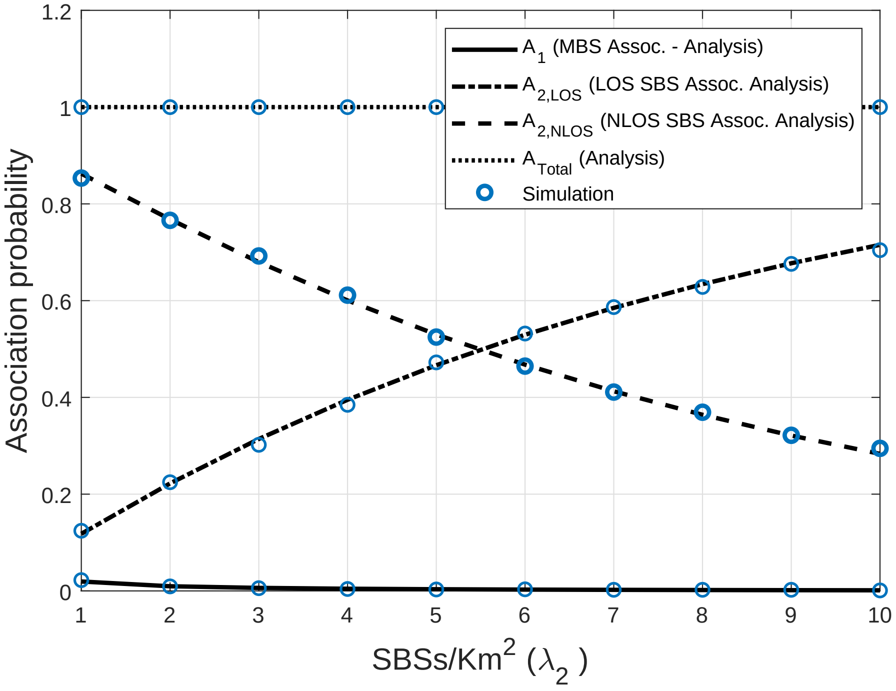

Figure 4.2: Association probabilities as a function of $\lambda_2$ for the hybrid spectrum IoT network when $\lambda_1 = 2$ MBSs/km$^2$, $B_1 = B_2 = 1$, and $d = 200$m.

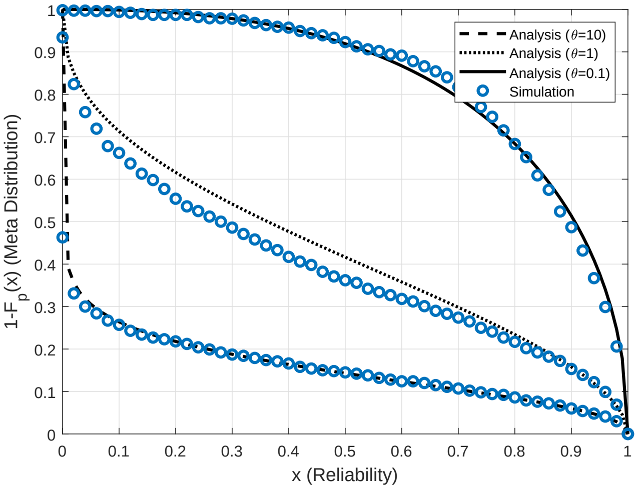

Figure 4.3: The meta distribution vs. reliability threshold $x$ for $\theta = \theta_{\mathcal{D}} = \theta_2 =$10, 1, and 0.1 for the hybrid spectrum IoT network when $B_1 = B_2 = 1$, and $d = 200$m.

**The Coverage and Variance as Functions of the SIR/SNR Threshold in Hybrid Spectrum Networks**

Fig. 4.4 illustrates the standard success probability $M_{1,\mathrm{T}}$ and its variance $M_{2,\mathrm{T}} - M_{1,\mathrm{T}}^2$ as a function of target SIR/SNR threshold $\theta$ of devices in a hybrid spectrum IoT network. As we can see in Fig. 4.4 that the simulation results match the analytical results, however the slight gap is due to the Alzer's inequality considered in **Appendix B.3**. This gap will be zero when Nakagami fading turns into Rayleigh fading as shown in the next figure. By examining Fig. 4.4, a numerical evaluation shows that the variance is maximized at $\theta = -3$ dB where the success is $M_{1,\mathrm{T}} = 0.49$. For moderate values of $\theta$, there is a trade-off between maximizing coverage or reducing variance because the variance first increases and then decreases while the coverage probability is monotonically decreasing. For higher values of $\theta$, lower coverage probabilities have lower variance so its a low-reliability regime where more devices' performances are spread around low coverage probability. As such, the low values of $\theta$ provides a higher reliability regime.

Fig. 4.5 illustrates the standard success probability $M_{1,\mathrm{T}}$ and the variance as a function of $\theta$ with Rayleigh fading (i.e., $m_L = m_N = 1$). As we can see in Fig. 4.5 that the simulation results closely match the analytical results. The reason is that the approximation of the incomplete Gamma function (also referred to as Alzer's inequality) becomes exact when $m_L$ becomes equal to unity. Subsequently, this figure explains the reason for the gap between the simulation and the analytical curves in Fig. 4.4.

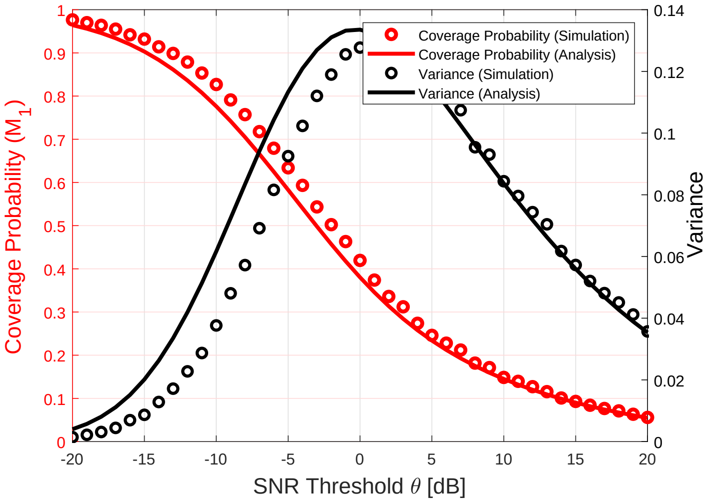

Figure 4.4: Coverage probability $M_{1,\mathrm{T}}$ and variance $M_{2,\mathrm{T}} - M_{1,\mathrm{T}}^2$ as a function of $\theta$ considering Nakagami-m fading when $B_1 = B_2 = 1$ and $d = 200$m.

### The Coverage and Variance as Functions of the Number of Antenna Array Elements in Hybrid Spectrum Networks

Fig. 4.6 depicts the coverage probability and variance as a function of $\theta$ considering the number of antenna array elements as $\mathcal{N} = 10$, 20, and 30 to show the effect of higher directional antenna gains. The general trends for the coverage probability and its variance are found to be the same as in previous figures. The main observation is that although the coverage enhancement is not significant with increasing antenna elements, the reduction in the variance is noticeable which supports higher directional antenna gains and the importance of analyzing the higher moments of the CSP.

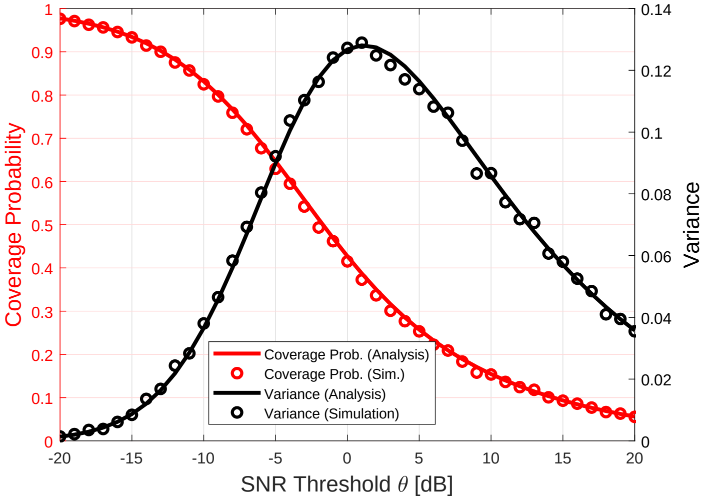

Figure 4.5: Coverage probability $M_{1,\mathrm{T}}$ and variance $M_{2,\mathrm{T}} - M_{1,\mathrm{T}}^2$ as a function of $\theta$ considering Rayleigh fading (i.e., $m_L = m_N = 1$, when $B_1 = B_2 = 1$ and $d = 200$m.

**The Coverage and Variance as Functions of $B_2$ in Microwave-only Networks**

In Fig. 4.7, we study the effect of offloading devices from the MBS tier to the SBSs tier in terms of the coverage probability (which is the mean reliability) and the variance of the CSP (or reliability). By offloading devices from the MBS tier to the SBSs tier when $B_2 = 30$, the coverage probability $M_{1,\mathrm{T}}$ suffers due to the dual-hop transmission effect in wireless backhauled SBSs; however the variance of the results reduces which is a novel and positive insight. Another observation is that the variance of the CSP in $\mu$wave-only IoT network is high compared to the hybrid IoT network. This can be shown by comparing points $V_1 = (1, 0.1)$ in Fig. 4.6 and $V_2 = (4, 0.19)$ in Fig. 4.7, for the case of $B_1 = B_2 = 1$. We noticed that the variance has decreased from 0.19 to 0.1 when the SBS antenna array size is increased to $\mathcal{N} = 20$. This implies that the hybrid spectrum IoT network outperforms the $\mu$wave-only IoT network due to the directional antenna gains.

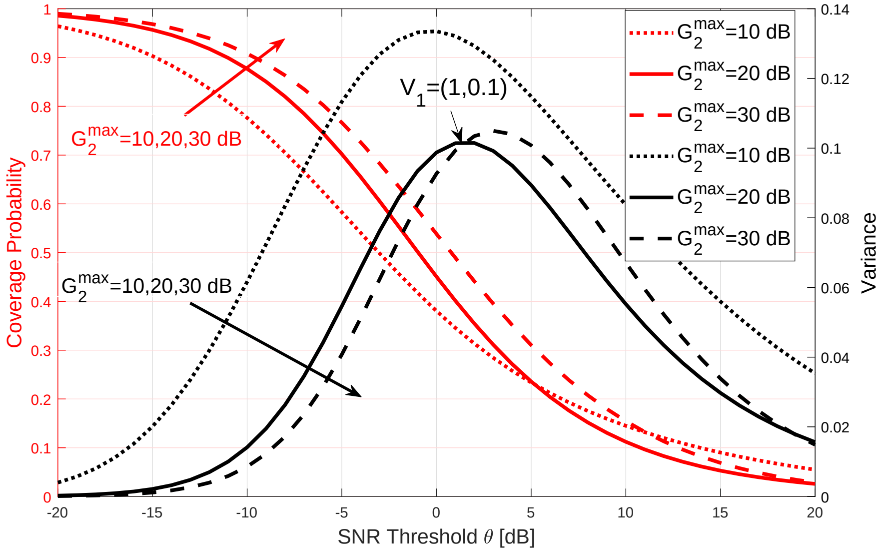

Figure 4.6: Coverage probability $M_{1,\mathrm{T}}$ and variance $M_{2,\mathrm{T}} - M_{1,\mathrm{T}}^2$ as a function of $\mathcal{N}$ for hybrid spectrum IoT network when $B_1 = B_2 = 1$, and $d = 200$m.

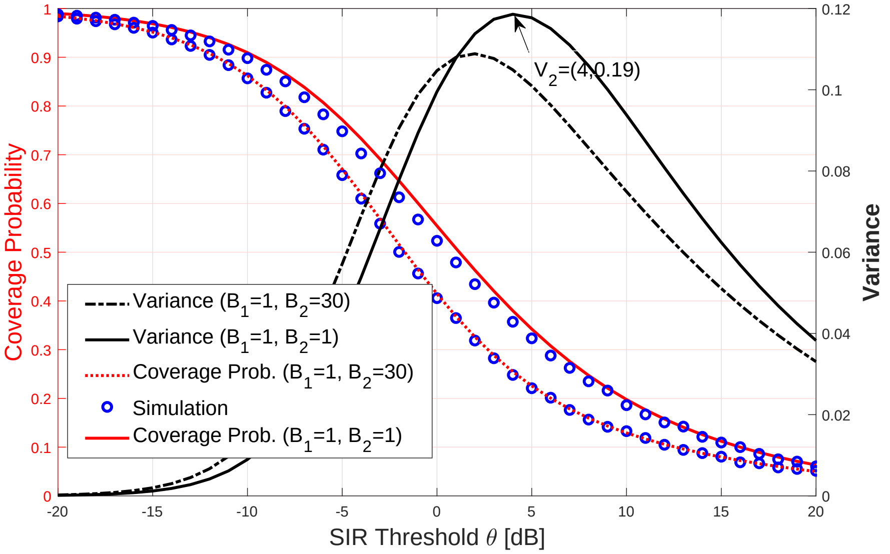

Figure 4.7: Coverage probability $M_{1,\mathrm{T}}$ and variance $M_{2,\mathrm{T}} - M_{1,\mathrm{T}}^2$ as a function of $\theta$ for $\mu$wave-only IoT network when $\alpha_1 = \alpha_2 = 4$, $B_1 = 1$, and $B_2 = 1$ and 30.

### The Mean Local Delay

Fig. 4.8 depicts the mean local delay experienced by a typical device as a function of the SBSs density $\lambda_2$ in a hybrid spectrum IoT network. The mean local delay is the mean number of transmission attempts to successfully transmit a packet. The mean local delay increases by increasing $\lambda_2$. After the SBS density reaches $\lambda_2 = 20$ SBSs/km$^2$, the mean local delay stays constant at value 1.11. This result can be intuitively explained as follows. When the mm-wave SBS density is low, the typical device has a higher probability to connect to a MBS, i.e., the mean local delay of the network results from only one hop communication (from the MBS to the device). However, when the $\lambda_2$ increases, the typical device has a higher probability to connect to a mm-wave SBS, i.e., the network local delay results from two hops communication (from the MBS to the SBS then from the SBS to the device). Furthermore, the beamforming high directional gain steerable antennas will push more devices to associate with SBSs thus a higher network delay is observed. Fig. 4.9 shows that, all else being equal, the mean local delay of the hybrid spectrum network is lower than that of the $\mu$wave-only network.

Fig. 4.9 depicts the mean local delay for a $\mu$wave-only network as a function of $\lambda_2$. When $\lambda_2$ increases the mean local delay of the total network increases again due to the increase in interference which is not the case in the hybrid spectrum network. The network mean local delay in the case of $\alpha_1 = \alpha_2 = 3$ is higher than that in the case of $\alpha_1 = \alpha_2 = 4$ due to higher path loss degradation for higher PLEs.

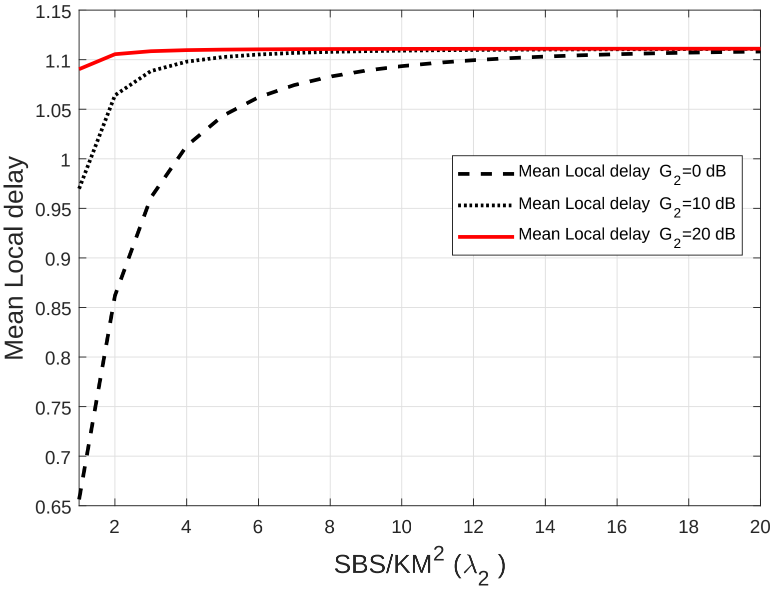

Figure 4.8: Mean local delay $M_{-1,\mathrm{T}}$ as a function of $\lambda_2$ for the hybrid spectrum IoT network when $\lambda_1 = 2$ MBS/Km$^2$, $B_1 = 1$, $B_2 = 10$, $\alpha_1 = 4$, $d = 200$m, and $\theta = \theta_{\mathcal{D}} = \theta_2$ =-10 dB.

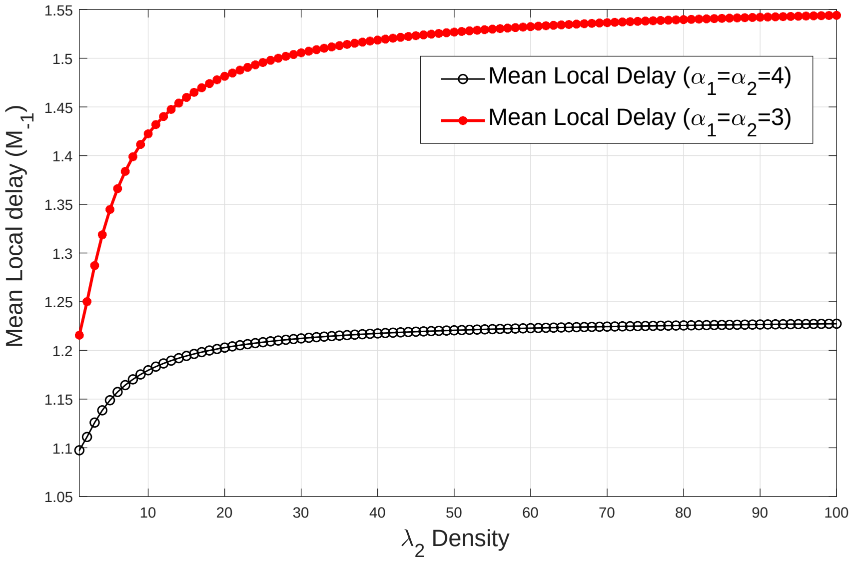

Figure 4.9: Mean local delay $M_{-1,\mathrm{T}}$ as a function of $\lambda_2$ for the $\mu$wave-only IoT network when $\lambda_1 = 2$ MBS/KM$^2$, $B_1 = 1$ and $B_2 = 10$, $\alpha_1 = \alpha_2 = 3$ and 4, and $\theta = \theta_{\mathcal{D}} = \theta_2$ =-10 dB.

### The Meta Distribution of the Achievable Data Rate in Hybrid Spectrum Networks

Fig. 4.10 depicts the meta distribution of the data rate in hybrid spectrum IoT networks as a function of reliability $x$ for different number of antenna elements $\mathcal{N} = 10$, 20, 40, and 50 with rate threshold $\mathcal{T} = 1$ Gbps. As shown in Fig. 4.10, the fraction of devices achieving a required rate increases as the number of antennas elements increases. In other words, increasing the number of antenna elements of SBSs has a positive effect on the achievable rate and its meta distribution. This insight helps IoT cellular network operators to find the most efficient operating antenna configuration to achieve certain reliability for certain IoT applications.

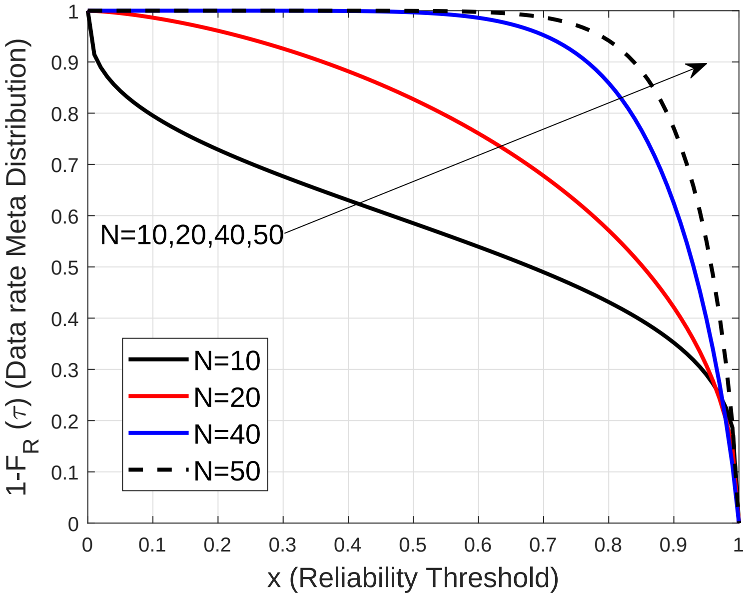

Figure 4.10: Meta distribution of the achievable data rate as a function of reliability $x$ for different number of antenna elements $\mathcal{N}$ with rate threshold $\mathcal{T} = 1$ Gbps.

### The Meta Distribution of SIR in a Microwave-only Network

In Fig. 4.11, we validate our analysis by depicting the exact (Gil-Pelaez) meta distribution in a $\mu$wave-only IoT network defined in Eq. (4.13), and the beta approximation for the meta distribution defined in Eq. (4.8). Our simulation result provides an excellent match for a wide range of $\theta$ values and this validates the correctness of our analytical model. Fig. 4.11 also serves as an illustration of the meta distribution of the SIR of a typical device in a $\mu$wave-only IoT network. We note that about 23% of devices (when $\theta = 10$), 72% of devices (when $\theta = 1$), and 98% of devices (when $\theta = 0.1$) have reliability, i.e., success probability, equal to 0.3.

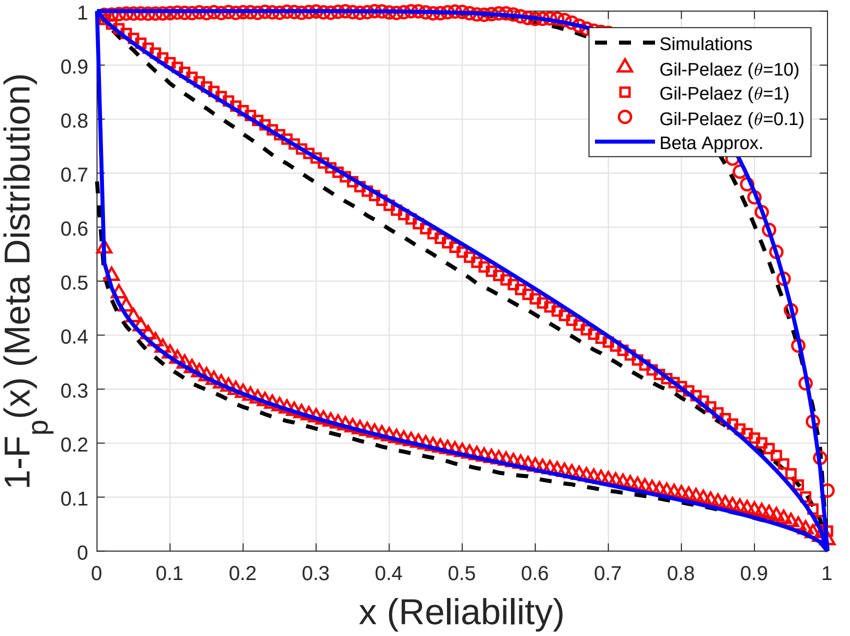

Figure 4.11: The meta distribution as a function of reliability $x$ for $\theta = \theta_{\mathcal{D}} = \theta_2$ =10, 1, and 0.1 for SBSs in a $\mu$wave-only IoT network when $B_1 = B_2 = 1$ and $\alpha_1 = \alpha_2 = 4$.

## 4.9 Chapter Summary

This chapter characterizes the meta distributions of the SIR/SNR and data rate of a typical device in a hybrid spectrum network and $\mu$wave-only network. The meta distribution is evaluated first by formulating and then characterizing the moments of the CSP of a typical device in the hybrid network. Important performance metrics such as the mean local delay, coverage probability, network jitter, and variance of the CSP (or reliability) are studied.

Numerical results demonstrate the significance of evaluating the meta distribution. Evaluating the meta distribution requires a systematic evaluation of the generalized moment of order $b$ that helps in evaluating network metric such as coverage probability when $b = 1$, mean local delay when $b = -1$, network jitter using $b = -2$ and $b = -1$, etc. Numerical results provide valuable insights related to the reliability and latency of the hybrid spectrum network, $\mu$wave-only network, and mm-wave only network. These insights will help cellular network operators to find the most efficient operating antenna configuration to achieve required level of reliability for certain applications.

# Chapter 5

# Mobility-Aware Modeling and Analysis of Dense Cellular Networks with C-plane/U-plane Split Architecture

## 5.1 Motivations and Contributions

The fifth generation (5G) of cellular networks is challenged to enhance devices' experience, support new services, and satisfy the ever-increasing mobile users and devices population and their traffic demands. Compared to the state-of-the-art 4G cellular systems, 5G networks are expected to achieve thousandfold capacity improvement with at least hundredfold increase in the peak data rate and one order of magnitude delay reduction [2]. Researchers in both academia and industry almost agree that network densification, via base station deployment, is among the key solutions to achieve this ambitious performance goal [2]. Therefore, it is expected that cellular network operators will significantly densify their networks infrastructures to fulfill the 5G performance requirements. In this case, network densification via deployments of small base stations (SBSs) is preferred over deployments of macro base stations (MBSs) due to lower cost and faster deployment.

Deploying more SBSs within the same geographical region reduces the footprint of each BS, and thus, decreases the number of devices served by each BS. Reduced BS footprints shorten device-to-serving-BS distances and improve the spatial frequency reuse. Therefore, network densification is foreseen to improve spatial spectral efficiency and thus network capacity. However, narrowing BS footprints leads to higher handover rates and control overhead per unit area. The increased handover rate imposes a major challenge that may negate the foreseen densification gain if conventional network operation is preserved. In extreme cases, where high mobility exists in urban areas (e.g., monorails in city downtowns or the Shinkansen network of high-speed railway in Tokyo), a densely deployed cellular network may fail to support very fast moving users and devices or cars due to excessive handover rates. Particularly, the network cannot support devices with a cell dwell time that is comparable or less than the handover delay. Consequently, the undesirable effect of narrowing the BSs footprints requires solutions that reduce handover rate and control overhead in order to harvest the foreseen network densification gain.

Decoupling control plane (C-plane) and user plane (U-plane)[1] for cellular networks, under a cloud radio access network (C-RAN) umbrella, is proposed as a potential solution to reduce handover rate and control burden [141]. Cellular network architecture with C-plane/U-plane (CP/UP) split is also referred to as "*Lean Carrier*" for LTE [142]. Fig. 5.1 illustrates cellular network architecture with CP/UP split. In this architecture, devices can receive data packets from a nearby SBS while being controlled via a farther MBS. It is shown in [142,141] that implementing the control plane at the macro cell level and the data plane at the small cell level incurs less control overhead compared to the conventional architecture (i.e.,

---

[1] The data and control splitting in the CP/UP split architecture is implemented at the radio access network level. This implementation is different from the network services and control splitting enabled by software defined networking (SDN), which is implemented at the core network side. However, both implementations are considered fundamental building blocks for 5G networks [140].

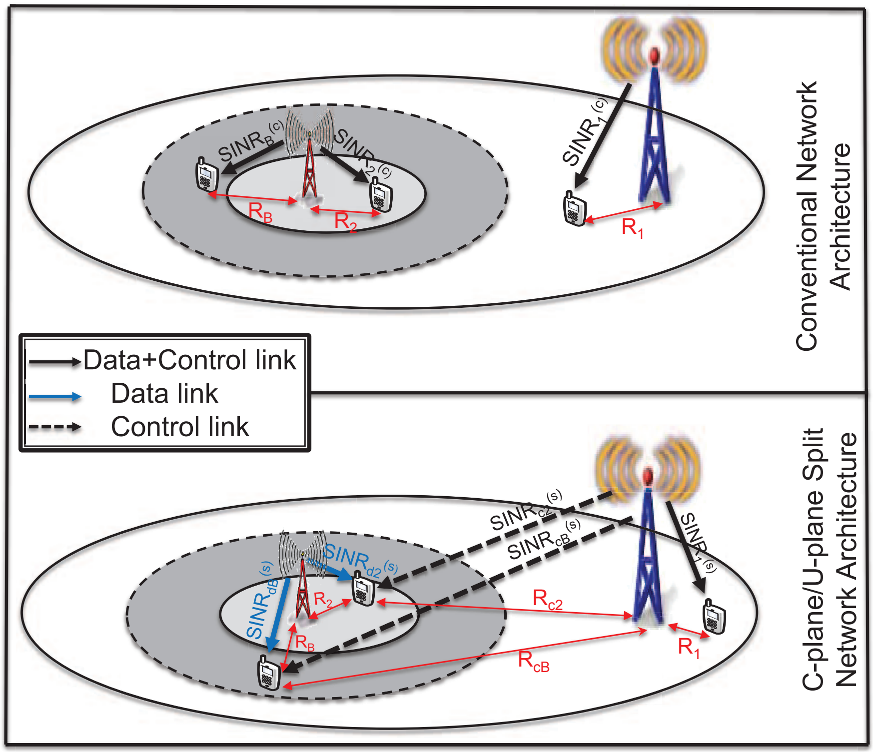

Figure 5.1: Conventional vs. CP/UP split network architecture: There are three types of links in the conventional network with three corresponding SINR values: $\mathrm{SINR}_1^{(C)}$ for macrocell devices, $\mathrm{SINR}_2^{(C)}$ for non-biased devices, and $\mathrm{SINR}_B^{(C)}$ for biased devices. There are five types of links in the CP/UP split network with five corresponding SINR values: $\mathrm{SINR}_1^{(s)}$ for macrocell devices, $\mathrm{SINR}_{d2}^{(s)}$ for non-biased devices' data, $\mathrm{SINR}_{c2}^{(s)}$ for non-biased devices' control, $\mathrm{SINR}_{dB}^{(s)}$ for biased devices' data and $\mathrm{SINR}_{cB}^{(s)}$ for biased devices' control and service distances.

both C-plane and U-plane are jointly served from each BS). The CP/UP split architecture imposes less control overhead because the cell specific control signals/channels for SBSs, which identify each SBS, are not broadcast.[2] Consequently, the SBSs become transparent to the devices and the MBSs take charge of managing the radio resource control (RRC)

---

[2] Examples of cell specific control signals/channels are primary/secondary synchronization signals [PSS/SSS], cell-specific reference signals [CRS], master information blocks [MIB] and system information blocks [SIB] (see [141, 142] for details).

procedures between mobile devices and SBSs, such as session establishment and release. In the CP/UP split network, the SBSs are referred to as *phantom BSs* because their identities are hidden from the devices.[3]

In addition to reducing the control overhead, the CP/UP split architecture can also be exploited to mitigate handover delays in dense cellular environments. Since the MBSs are in charge of the control signaling for the phantom cells including SBS selection, the MBSs can act as handover anchors and mange the handovers between underlying SBSs. In this case, the core network is only informed about inter-MBSs handovers. Compared to the conventional network architecture which informs the core network about MBSs and SBSs handovers. Hence, the CP/UP split architecture can significantly reduce handover delay by only reporting the less frequent inter-MBSs handovers, thanks to the larger coverage of macro cells. It is ought to be mentioned that the relative performance between the conventional and CP/UP split architectures highly depends on the availability of the direct X2 interfaces between the BSs. This is because the X2 interface also enables core network transparent handover procedure. However, the X2 interface does not provide signaling overhead reduction as in the CP/UP split case.

In this chapter, we use stochastic geometry to develop a tractable mobility-aware model that characterizes the performance of cellular networks with and without CP/UP split. In particular, we model downlink transmission in two-tier cellular networks with flexible cell association, in which the model takes into account the impact of the handover rate and control overhead on devices throughput. Tractable expressions for per-device throughput in terms of the BSs intensity, devices velocity, and handover delay are obtained to study the effect of mobility on throughput in dense cellular environments, in which the performances of conventional and CP/UP split architectures are compared. To this end, we shed light on the handover delay problem in dense cellular environments and show the potential delay mitigation via the CP/UP split architecture. The developed model is also used to quantify the expected performance gain for the CP/UP split architecture, obtain design insights, and

---

[3] The abbreviation SBS in this chapter refers to both a small BS and a phantom BS.

discuss the performance limits of the conventional and CP/UP split architectures. To the best of our knowledge, this chapter is the first to develop a theoretical and tractable mobility-aware modeling paradigm to study the handover problem in dense cellular environments and evaluate the performance of the CP/UP split network architecture. Based on the developed model, potential scenarios where CP/UP split is essential to support device mobility are highlighted and the feasibility of CP/UP split is also discussed. This architecture has been considered as a promising solution to increase the overall performance and quality of service of 5G cellular networks [2].

The remainder of the chapter is organized as follows. In Section 5.2, we provide the system model and assumptions. Section 5.3 presents the conventional and CP/UP split transmission rate models. Section 5.4 characterizes the coverage probability and spectral efficiencies of the conventional and CP/UP split architectures. Section 5.5 presents mobility analysis and evaluate the handover costs incurred by mobile devices. We validate the proposed model and discuss numerical results in Section 5.6. Finally, Section 3.6 summarizes and concludes the chapter.

## 5.2 System Model and Assumptions

In this section, we describe the network and mobility models and assumptions.

### 5.2.1 Network Model

We consider a two-tier downlink cellular network with BSs in each tier modeled via an independent two dimensional homogeneous Poisson point process (PPP) $\mathbf{\Phi}_k$ of density $\lambda_k$, where $k \in \{1, 2\}$. The macro cell tier and small cell (phantom cell) tier are denoted by $k = 1$ and $k = 2$, respectively. Devices are spatially distributed according to an independent PPP $\mathbf{\Phi}_u$ with density $\lambda^{(u)}$. All BSs in the $k^{th}$ tier are equipped with single antennas, transmit with the same power $P_k$, and always have packets to transmit. We consider a general power law path loss model, with path loss exponent $\alpha_k$, for both desired and interference downlink signal powers. Furthermore, signal attenuation due to multi-path fading is modeled using an independent Rayleigh distribution such that the channel power gain $H_x \sim \exp(1)$. A list of the key mathematical notations used in this chapter is given in Table 5.1.

Due to the transmission power disparity between the two tiers, the BSs footprints are represented by a weighted Poisson Voronoi diagram [143] as depicted in Fig. 5.2. To enable flexible cell association and fine-grained control of BS loads, we follow the model in [3] and introduce the bias factor $B$ to artificially encourages/discourages devices to associate with the small cell tier.

Let $r_k$ denote the distance between an arbitrary mobile device and the nearest BS in the $k^{th}$ tier, then the biased association rule assigns a mobile device to the macro tier if $P_1 r_1^{-\alpha_1} > P_2 B r_2^{-\alpha_2}$, and to a small (phantom) cell otherwise. Based on the aforementioned association criterion and following the notation in [31], the complete set of devices is divided into the following three non-overlapping sets:

$$u \in \begin{cases} \mathcal{U}_1 & \text{if } P_1 r_1^{-\alpha_1} \geq P_2 B r_2^{-\alpha_2} \\ \mathcal{U}_2 & \text{if } P_2 r_2^{-\alpha_2} > P_1 r_1^{-\alpha_1} \\ \mathcal{U}_B & \text{if } P_2 r_2^{-\alpha_2} \leq P_1 r_1^{-\alpha_1} < P_2 B r_2^{-\alpha_2} \end{cases} \tag{5.1}$$

where $\mathcal{U}_1$ denotes the set of macrocell devices, $\mathcal{U}_2$ denotes the set of non-biased small cell devices, and $\mathcal{U}_B$ is the set of biased small cell devices, where $\mathcal{U}_1 \cup \mathcal{U}_2 \cup \mathcal{U}_B = \mathbf{\Phi}_u$ and $\mathcal{U}_1 \cap \mathcal{U}_2 \cap \mathcal{U}_B = \phi$.

We consider two modes of operation, namely the conventional and CP/UP split, as shown in Fig. 5.1. In the conventional network architecture, we assume that the control overhead consumes $\mu_c$ of the data rate and that each device gets the control and data from the same BS. We also assume universal frequency reuse scheme with almost blank sub-frames (ABS) interference management between macro cells and biased small cells [31].[4] That

---

[4] Universal frequency reuse is considered for the conventional network architecture because it always

Table 5.1: Mathematical notations in Chapter 5

| **Notation** | **Description** |
|---|---|
| $\mathbf{\Phi}_k$;$\mathbf{\Phi}_u$ | PPP of BSs of $k^{th}$ tier; PPP of mobile devices. |
| $\lambda_k$;$\lambda^{(u)}$ | Density of BSs of $k^{th}$ tier; density of mobile devices. |
| $P_k$ | Transmit power of BSs of $k^{th}$ tier. |
| B | Association bias for $2^{nd}$ tier. |
| $\alpha_k$ | Path loss exponent of $k^{th}$ tier. |
| $\mathcal{V}$ | Mobile device velocity. |
| $HO_{ij}^{(c)}$ | Mean number of handovers per unit length from tier $i$ to $j$, for conventional network. |
| $MHO^{(s)}$ | Mean number of inter-anchor handovers per unit length for CP/UP split network. |
| $VHO^{(s)}$ | Mean number of intra-anchor handovers per unit length for CP/UP split network. |
| $\eta$ | Fraction of time dedicated to serve biased mobile devices with no interference from the macro tier. |
| $\mu_{\mathbf{C}}$ | Control data overhead fraction in overall network capacity. |
| $\theta$ | Predefined threshold for correct signal reception. |
| $D_{HO}^{(c)}$ | Handover cost in conventional network. |
| $D_{HO}^{(s)}$ | Handover cost in CP/UP split network. |
| $\mathcal{X}$; $\mathcal{Z}$ | Probability of having X2 interface in conventional; and CP/UP split architecture handovers. |
| $d^{(c)}$; $\tilde{d}^{(c)}$ | Delay per non X2 handover;delay per X2 handover in conventional network. |
| $d_m^{(s)}$; $\tilde{d}_m^{(s)}$ | Inter-anchor handover delay without X2 interface;Inter-anchor handover delay with X2 handover in CP/UP split network. |
| $d_v^{(s)}$ | Intra-anchor handover delay for CP/UP split network. |
| $\mathcal{U}_j$ | Macro cell devices $j = 1$, small cell devices $j$ =2, biased small cell devices $j$ = B . |
| $\gamma$ | Control signaling reduction factor |
| $AT^{(c)}$ | Average per-device throughput in the conventional network. |
| $AT^{(s)}$ | Average per-device throughput in CP/UP split network. |
| $\mathcal{A}_j$ | Association probability of a typical device $\mathcal{U}_j$ . |
| $\mathcal{T}_j^{(c)}$ | BS throughput in each association state category for conventional network. |
| $\mathcal{T}_j^{(s)}$ | BS throughput in each association state category for CP/UP split network. |
| $\mathcal{SE}^{(c)}$ | Spectral efficiency for conventional network. |
| $\mathcal{SE}^{(s)}$ | Spectral efficiency for CP/UP split network. |
| $P_{12}$;$P_{21}$ | $P_{12} = \frac{P_1}{P_2}$; $P_{21} = \frac{1}{P_{12}}$. |
| $\tilde{P}_{12}$;$\tilde{P}_{21}$ | $\tilde{P}_{12} = \frac{P_1}{BP_2}$; $\tilde{P}_{21} = \frac{1}{\tilde{P}_{12}}$. |
| $\rho(a,b)$ | $\rho(a,b) = a + \sqrt{b}\arctan(\sqrt{b})$. |
| $\tilde{\lambda}_k$ | $\tilde{\lambda}_k = \frac{2\pi\lambda_k}{\alpha_k - 2}$. |
| ${}_2F_1(\cdot,\cdot;\cdot;\cdot)$ | The hypergeometric function. |

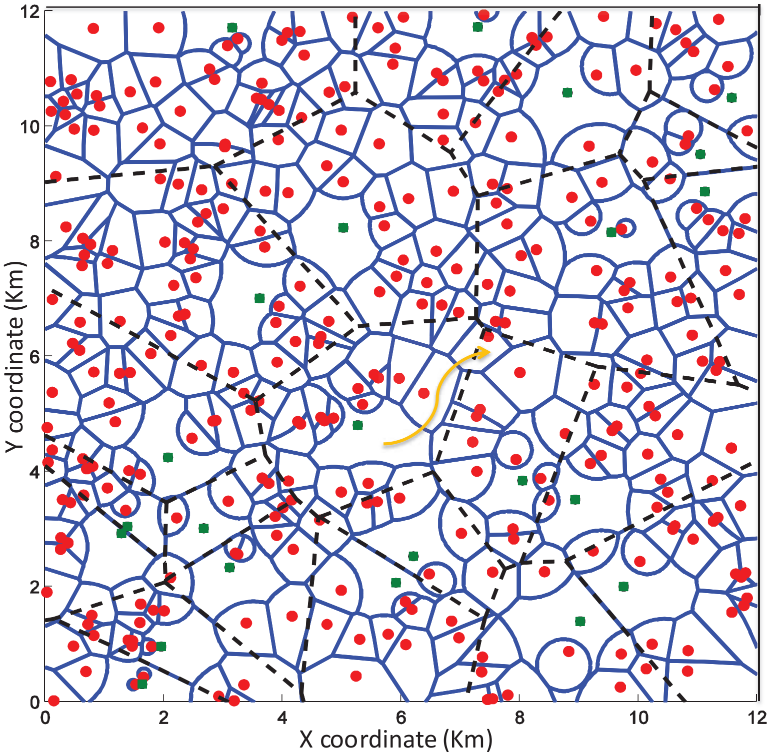

Figure 5.2: Two-tier weighted Possion Voronoi diagram representing a cellular network. The green squares and the red circles represent macro BSs and small BSs, respectively. The figure shows a device's trajectory (highlighted in orange), intra-anchor handover boundaries (in blue) and inter-anchor handover boundaries (in dotted black) for the CP/UP split architecture.

is, a fraction $\eta$ of time is dedicated to serving biased mobile devices (i.e., $\mathcal{U}_B$) with no interference from the macro tier (i.e., MBSs do not send or send with very low power during the ABSs interval). In the CP/UP split network architecture, each small cell device (i.e., each device in $\mathcal{U}_2$ and $\mathcal{U}_B$) has double association in which the SBS transmit data only and the control signaling overhead is communicated via the MBS. Note that the control overhead for small cell devices in the CP/UP split case consumes $\mu_c/\gamma$ of the data rate, where $\gamma \geq 1$ is offered control reduction factor [142, 141]. It is worth noting that the decoupled, but simultaneous, data and control association of the CP/UP split architecture necessitates a

---

results in higher device throughput than dedicated spectrum access as shown in [40].

dedicated spectrum assignment for each tier. To conduct a fair comparison, we assume both the conventional and CP/UP split architectures have the same available spectrum of $W$, however, the CP/UP architecture split $W$ into $W_1$ and $W_2 = W - W_1$ for the macro and small-cell tiers, respectively.

### 5.2.2 Device Mobility

We assume that each device moves with an arbitrary trajectory and velocity, in which a handover occurs when a device crosses over a cell boundary. However, we assume that the overall devices mobility model preserves the spatial uniformity of devices across the network. We define a vertical handover as one made between two BSs in two different tiers, and a horizontal handover as one made between two BSs in the same tier.

Fig. 5.2 shows the handover boundaries for the conventional and CP/UP split network architectures. In the CP/UP split network architecture, the black dotted Voronoi tessellation represents control handover boundaries and the blue weighted Voronoi tessellation represents the data handover boundaries. In the conventional network architecture, the blue weighted Voronoi tessellation represents both the data and control handover boundaries.

In the conventional network architecture, devices change their association (i.e., control and data) upon each handover. All handovers are managed through mobility management entity (MME) in the core network if direct X2 interface is not available between the serving and target BSs. Otherwise, the handover signalling is performed via the X2 interface without involving the core network, which highly reduces the handover delay. The handovers that occurs in the conventional network architecture can be categorized into the following cases: (1) vertical handover from a MBS to a SBS, (2) vertical handover from a SBS to a MBS, (3) horizontal handover between two MBSs, and (4) horizontal handover between two SBSs. In the conventional network architecture, the mean number of handovers, from tier $i$ to tier $j$, that occurs per unit length of a device trajectory is denoted by $HO_{ij}^{(c)}$, where $i, j \in \{1, 2\}$ and the superscript $(c)$ denotes the conventional network architecture.

In the CP/UP split network architecture, the MBSs function as mobility anchors for data handovers within macro-to-macro Voronoi tessellation (black dotted tessellation in Fig. 5.2). That is, the weighted Voronoi tessellation constructed w.r.t. all BSs in all tiers determines the data plane association and the Voronoi tessellation constructed w.r.t. MBSs only determines the control signaling and handover support association as shown in Fig. 5.2. Consequently, only two types of handover occurs in the CP/UP split architecture, namely, (1) intra-anchor handover, and (2) inter-anchor handover. An inter-anchor handover occurs when a device crosses the boundary between two MBSs, and the handover is managed via the MME in the core network when there is no X2 interface between the engaged MBSs. In contrast, an intra-anchor handover is always transparent to the MME and is managed via the anchor BS, which reduces the handover delay because the MME is not notified. In the CP/UP split network architecture, we denote the mean number of inter-anchor and intra-anchor handovers per unit length of the device trajectory as $MHO^{(s)}$ and $VHO^{(s)}$, respectively, where the superscript (s) denotes the CP/UP split network. It is worth noting that s change their control association without changing their data association when crossing over a macro-boundary within the coverage of a SBS. This type of handover is treated as an inter-anchor handover because the MME is informed.

For tractability, we assume that devices' trajectories are long enough to go through all three association states $j \in 1, 2, B$. We also use the spatially averaged signal-to-interference-plus-noise-ratio (SINR) for stationary devices provided by a given tier to infer the average SINR experienced by a mobile device during the journey through that tier. This assumption is validated later in Section 5.6. In other words, we compute $\text{SINR}_j$ provided by tier $j$ for a randomly selected stationary device and assume that mobile devices will experience an average $\text{SINR}_j$ during their trajectories in the $j^{th}$ tier.

It is worth noting that the average stationary SINR assumption is needed for model tractability and was used in [43,45,44]. This assumption only ignores the spatial correlations between the SINR values along each trajectory. However, averages over all trajectories and all devices under all network realization are still captured by the analysis.

## 5.3 Conventional and CP/UP Split Transmission Rate Models

Using Shannon's formula to define the ergodic rate, the average throughput delivered by a MBS and SBS for non-biased and biased devices in the conventional architecture can be expressed as follows:

$$\mathcal{T}_1^{(c)} = (1-\mu_C)(1-\eta)W\mathbb{E}[\ln(1+\mathrm{SINR}_1^{(c)})], \tag{5.2}$$

$$\mathcal{T}_2^{(c)} = (1-\mu_C)(1-\eta)W\mathbb{E}[\ln(1+\mathrm{SINR}_2^{(c)})], \tag{5.3}$$

$$\mathcal{T}_B^{(c)} = (1-\mu_C)\eta W\mathbb{E}[\ln(1+\mathrm{SINR}_B^{(c)})]. \tag{5.4}$$

Note that MBSs are active only for $1-\eta$ fraction of the time due to the ABS interference management. On the other hand, small BSs are active all the time in which $1-\eta$ fraction of the time is dedicated for non-biased devices $\mathcal{U}_2$ and $\eta$ fraction of the time is dedicated for biased devices $\mathcal{U}_B$.

The decoupled data and control associations and dedicated spectrum access eliminate the inter-tier interference in the CP/UP split operation and changes the statistical nature of the SINR in the CP/UP split network architecture when compared to the conventional network architecture. In particular, in the CP/UP split network architecture as shown in Fig. 5.1, we have five different SINRs to consider, namely, $\mathrm{SINR}_1^{(s)}$ for macrocell devices, $\mathrm{SINR}_{d2}^{(s)}$ for non-biased devices' data, $\mathrm{SINR}_{c2}^{(s)}$ for non-biased devices' control signaling, $\mathrm{SINR}_{dB}^{(s)}$ for biased devices' data and $\mathrm{SINR}_{cB}^{(s)}$ for biased devices' control signaling. Let $W_1$ be the spectrum assigned to the macro tier and $W_2 = W - W_1$ be the spectrum assigned to the phantom cell tier. In this case, the average throughput of a small (phantom) cell s is given by:

$$\mathcal{T}_2^{(s)} = (1-\eta)W_2\mathbb{E}[\ln(1+\mathrm{SINR}_{d2}^{(s)})], \tag{5.5}$$

$$\mathcal{T}_B^{(s)} = \eta W_2\mathbb{E}[\ln(1+\mathrm{SINR}_{dB}^{(s)})]. \tag{5.6}$$

Although there is no cross-tier interference in the CP/UP split network architecture due to spectrum splitting, time sharing still exists in (5.5) and (5.6) because the phantom BSs dedicate a fraction $\eta$ of time to serve biased devices. Note that the control overhead $\mu_c$ does not appear in the above throughput expressions because all control overhead is offloaded to the macro cells. The average throughput delivered to the macrocell devices, after reserving the resources for phantom cell control signaling, is characterized via the following lemma:

**Lemma 12.** *Consider a two-tier cellular network with the CP/UP split architecture, PPP macro BSs with density* $\lambda_1$*, PPP phantom BSs with density* $\lambda_2$*, and a control reduction factor* $\gamma$*. Then the average throughput delivered to the macrocell devices after resources for control signaling for phantom cell devices have been reserved is expressed as:*

$$\mathcal{T}_1^{(s)} = (1-\mu_C)\mathcal{R}_1^{(s)}\left(1-\frac{\lambda_2\mu_C}{\lambda_1\gamma}\left(\frac{\mathcal{T}_2^{(s)}}{\mathcal{R}_{c2}}+\frac{\mathcal{T}_B^{(s)}}{\mathcal{R}_{cB}}\right)\right), \tag{5.7}$$

*where* $\mathcal{R}_1^{(s)} = W_1\mathbb{E}[\ln(1+\mathrm{SINR}_1^{(s)})]$ *is the ergodic rate for macrocell devices,* $\mathcal{R}_{c2} = W_1\mathbb{E}[\ln(1+\mathrm{SINR}_{c2}^{(s)})]$ *is the average rate at which the control data is delivered to non-biased phantom cell devices,* $\mathcal{R}_{cB} = W_1\mathbb{E}[\ln(1+\mathrm{SINR}_{cB}^{(s)})]$ *is the average rate at which the control data is delivered to biased phantom cell devices, and* $\mathcal{T}_2^{(s)}$ *and* $\mathcal{T}_B^{(s)}$ *are the throughputs of non-biased and biased phantom cell devices given in* (5.5) *and* (5.6)*, respectively.*

*Proof.* See **Appendix C.1** ■

It is worth mentioning that (5.7) implicitly assumes that the control overhead is always a fraction $\mu_c$ of the available data rate and is only reduced by a factor of $\gamma$ for phantom cell devices. Eq. (5.7) also assumes that the device population is sufficiently dense so that each phantom BS always has non-biased and biased small cell devices to serve.

A CP/UP split network is said to be *feasible* if the MBSs have sufficient bandwidth to serve macrocell devices and to provide control signaling to phantom cell devices. From Lemma 12, the feasibility of the CP/UP split architecture is given in the following corollary

**Corollary 6.** *The CP/UP split architecture is feasible if and only if*

$$\frac{\mathcal{T}_2^{(s)}}{\mathcal{R}_{c2}} + \frac{\mathcal{T}_B^{(s)}}{\mathcal{R}_{cB}} \leq \frac{\lambda_1 \gamma}{\lambda_2 \mu_C}, \tag{5.8}$$

*or equivalently*

$$(1-\eta)\frac{\mathbb{E}[\ln(1+\mathrm{SINR}_{d2}^{(s)})]}{\mathbb{E}[\ln(1+\mathrm{SINR}_{c2}^{(s)})]} + \eta\frac{\mathbb{E}[\ln(1+\mathrm{SINR}_{dB}^{(s)})]}{\mathbb{E}[\ln(1+\mathrm{SINR}_{cB}^{(s)})]} \leq \frac{W_1 \lambda_1 \gamma}{W_2 \lambda_2 \mu_C}. \tag{5.9}$$

According to Corollary 6, the feasibility of the CP/UP split architecture is mainly limited by the average SINR experienced by the phantom cell devices in MBSs. Corollary 6 also suggests possible factors that can be manipulated to ensure the feasibility of the CP/UP split architecture are bandwidth assignment, relative BS densities, and/or control reduction factors.

### 5.3.1 Per-device Mobility-aware Throughput Model

The above expressions give the expected throughput for a typical device without capturing the main effects of network densifications. To have a realistic assessment to the densification gains, both throughput gains and the handover effects should be incorporated into the analysis. On one hand, network densification shrinks the BSs footprint, which reduces the number of devices served by each BS and increases the share each device gets from his serving BS's throughput. On the other hand, network densification shrinks the BSs footprint, which increases the handover rate and overhead. During handover execution, the device releases the serving BS session and establishes a new session with the target BS. We assume that no data is delivered during handover execution and only handover-related signaling is communicated to the device. To incorporate the handover delay into the throughput expressions, we first compute the handover cost[5] for the conventional and CP/UP split architectures, which is the average duration consumed in handovers per unit time. Then we eliminate

---

[5] The handover cost is a dimensionless unit which is computed as delay $\left(\frac{sec}{handover}\right)$ × velocity $\left(\frac{meter}{sec}\right)$ × handover rate $\left(\frac{handovers}{meter}\right)$.

the handover duration from the throughput expressions (5.2)-(5.7). For the conventional network architecture, the handover cost is expressed as:

$$D_{HO}^{(c)} = \left( (1 - \mathcal{X})\, d^{(c)} + \mathcal{X} \tilde{d}^{(c)} \right) \mathcal{V} \sum_{i} \sum_{j} HO_{ij}^{(c)}, \tag{5.10}$$

where $d^{(c)}$ and $\tilde{d}^{(c)}$ are the delays incurred by non X2 interface handover and X2 interface handover, respectively. $\mathcal{X}$ is the probability that an X2 interface is available between the serving and target BSs. In the CP/UP split network architecture, the delay incurred by an inter-anchor handover is different from the delay incurred by an intra-anchor handover, because the intra-anchor handover is always transparent to the core network.[6] On the other hand, all inter-anchor handovers are managed through the MME in the core network unless an X2 interface is available. Therefore, the handover cost for the CP/UP split architecture is given by:

$$D_{HO}^{(s)} = \mathcal{V} \left( MHO^{(s)} \left( (1 - \mathcal{Z})\, d_{m}^{(s)} + \mathcal{Z} \tilde{d}_{m}^{(s)} \right) + VHO^{(s)} d_{v}^{(s)} \right), \tag{5.11}$$

where $d_m^{(s)}$, $\tilde{d}_m^{(s)}$, and $d_v^{(s)}$ are the delays incurred by an inter-anchor handover without X2 interface, an inter-anchor handover with X2 interface, and an intra-anchor handover, respectively. $\mathcal{Z}$ is the probability that a direct X2 connectivity is available between the serving and target MBSs.

Incorporating the handover delay in to the throughput analysis, assuming that each BS uniformly distributes the resources across the devices it serves, and using the law of total probability, the average per-device throughput along his trajectory for the conventional and CP/UP split architectures are, respectively, expressed as:

---

[6] It is expected that removing the core network delay from a handover in the CP/UP split network (intra-anchor handover) reduces the handover delay by 50% compared to a handover in the conventional network [144].

$$AT^{(c)} = \left( \frac{\mathcal{A}_1 \mathcal{T}_1^{(c)}}{\mathcal{N}_1} + \frac{\mathcal{A}_2 \mathcal{T}_2^{(c)}}{\mathcal{N}_2} + \frac{\mathcal{A}_B \mathcal{T}_B^{(c)}}{\mathcal{N}_B} \right) \left(1 - \min\left(1, D_{HO}^{(c)}\right)\right), \tag{5.12}$$

$$AT^{(s)} = \left( \frac{\mathcal{A}_1 \mathcal{T}_1^{(s)}}{\mathcal{N}_1} + \frac{\mathcal{A}_2 \mathcal{T}_2^{(s)}}{\mathcal{N}_2} + \frac{\mathcal{A}_B \mathcal{T}_B^{(s)}}{\mathcal{N}_B} \right) \left(1 - \min\left(1, D_{HO}^{(s)}\right)\right), \tag{5.13}$$

where $\mathcal{A}_j$ is the probability of being served by a BSs in $j \in \{1, 2, B\}$ case and $\mathcal{N}_j$ is the expected number of devices sharing the BS resources with the typical device in the $j \in \{1, 2, B\}$ case. Note that $\mathcal{A}_j$ and $\mathcal{N}_j$ in (5.12) and (5.13) are independent from the network architecture and are calculated according to the association rule (5.1). The effect of control signaling offloaded to the MBSs in the CP/UP split is already captured by $\mathcal{T}_j^{(s)}$.

Eqs. (5.12) and (5.13) are the main performance metrics in this chapter, which are the mobility aware per-device average throughput in the conventional and CP/UP split architectures. It is worth re-emphasizing that (5.12) and (5.13) assume that the devices have long trajectories, that each device passes through all association states during their trajectories, and that the mobility model preserves the devices spatial uniformity across the network. It is worth mentioning that when the average cell dwell time becomes less than the handover delay, the handover costs in (5.10) and (5.11) are greater than unity. Consequently, the network fails to support devices and the average throughputs in (5.12) and (5.13) are nullified.

Exploiting the long trajectories and devices spatial uniformity, the association probabilities and BS loads can be obtained by following [31] and [3], respectively. In particular, the association probabilities $\mathcal{A}_1$, $\mathcal{A}_2$ and $\mathcal{A}_B$ can be viewed as the percentages of the $\mathbb{R}^2$ domain served by the MBSs, the unbiased SBS, and the biased SBS, respectively. Consequently, the association probabilities are given by [31]:

$$\mathcal{A}_1 = 2\pi\lambda_1 \int_0^{\infty} r \exp\left(-\pi\left(\lambda_1 r^2 + \lambda_2 \tilde{P}_{21}^{\frac{2}{\alpha_2}} r^{\frac{2\alpha_1}{\alpha_2}}\right)\right) \mathrm{d}r, \tag{5.14}$$

$$\mathcal{A}_2 = 2\pi\lambda_2 \int_0^{\infty} r \exp\left(-\pi\left(\lambda_2 r^2 + \lambda_1 P_{12}^{\frac{2}{\alpha_1}} r^{\frac{2\alpha_2}{\alpha_1}}\right)\right) \mathrm{d}r, \tag{5.15}$$

$$\mathcal{A}_B = 2\pi\lambda_2 \int_0^\infty r\Bigg\{ \exp\left[-\pi\left(\lambda_1\left(\tilde{P}_{12}^{\frac{2}{\alpha_1}} r^{\frac{2\alpha_2}{\alpha_1}} + \lambda_2 r^2\right)\right)\right] - \exp\left[-\pi\left(\lambda_1\left(P_{12}^{\frac{2}{\alpha_1}} r^{\frac{2\alpha_2}{\alpha_1}} + \lambda_2 r^2\right)\right)\right]\Bigg\}\mathrm{d}r, \quad (5.16)$$

where $P_{12} = \frac{P_1}{P_2}$, $P_{21} = \frac{1}{P_{12}}$, $\tilde{P}_{12} = \frac{P_1}{BP_2}$, and $\tilde{P}_{21} = \frac{1}{\tilde{P}_{12}}$.

Since the device spatial uniformity is preserved, the average number of devices sharing the resources with the typical device for each of the association cases is computed as follows [31]:

$$\mathcal{N}_j = \frac{1.28\lambda^{(u)}\mathcal{A}_j}{\lambda_{J(j)}} + 1,$$

where $J(j)$ is a map from device set association index $j \in \{1, 2, B\}$ to serving tier index $k \in \{1, 2\}$ as follows: $J(1) = 1$, $J(2) = J(B) = 2$. Therefore,

$$\mathcal{N}_1 = 1.28\left(2\pi\lambda^{(u)}\int_0^\infty r\ \exp\left\{-\pi\left[\lambda_1 r^2 + \lambda_2\tilde{P}_{21}^{\frac{2}{\alpha_2}} r^{\frac{2\alpha_1}{\alpha_2}}\right]\right\}\mathrm{d}r\right) + 1,$$

$$\mathcal{N}_2 = 1.28\left(2\pi\lambda^{(u)}\int_0^\infty r\ \exp\left\{-\pi\left[\lambda_1 P_{12}^{\frac{2}{\alpha_1}} r^{\frac{2\alpha_2}{\alpha_1}} + \lambda_2 r^2\right]\right\}\mathrm{d}r\right) + 1,$$

$$\mathcal{N}_B = 1.28\Bigg(2\pi\lambda^{(u)}\int_0^\infty r\Bigg[\exp\left(-\pi\left(\lambda_1 P_{12}^{\frac{2}{\alpha_1}} r^{\frac{2\alpha_2}{\alpha_1}} + \lambda_2 r^2\right)\right) - \exp\left(-\pi\left(\lambda_1 \tilde{P}_{12}^{\frac{2}{\alpha_1}} r^{\frac{2\alpha_2}{\alpha_1}} + \lambda_2 r^2\right)\right)\Bigg]\mathrm{d}r\Bigg) + 1.$$

An important scenario of interest is the case of equal path-loss exponents ($\alpha_1 = \alpha_2 = 4$), which not only simplifies the analysis but also a practical value for outdoor cellular communications in urban environments [63, 31, 32, 3, 33, 34, 35, 36, 37, 38, 39, 40]. In this case, the association probabilities and BS loads reduce to:

$$\mathcal{A}_1 = \frac{\lambda_1}{\lambda_1 + \lambda_2\sqrt{\tilde{P}_{21}}}, \mathcal{A}_2 = \frac{\lambda_2}{\lambda_1\sqrt{P_{12}} + \lambda_2}, \mathcal{A}_B = \frac{\lambda_2}{\lambda_1\sqrt{\tilde{P}_{12}} + \lambda_2} - \frac{\lambda_2}{\lambda_1\sqrt{P_{12}} + \lambda_2}, \quad (5.17)$$

and

$$\mathcal{N}_1 = \frac{1.28\lambda^{(u)}}{\lambda_1+\lambda_2\sqrt{\tilde{P}_{21}}} + 1,\ \mathcal{N}_2 = \frac{1.28\lambda^{(u)}}{\lambda_1\sqrt{P_{12}}+\lambda_2} + 1,\ \mathcal{N}_B = 1.28\left(\frac{\lambda^{(u)}}{\lambda_1\sqrt{\tilde{P}_{12}}+\lambda_2} - \frac{\lambda^{(u)}}{\lambda_1\sqrt{P_{12}}+\lambda_2}\right) + 1.$$

The missing components to calculate (5.12) and (5.13) are the spectral efficiencies (i.e., $\mathcal{SE} = \mathbb{E}[\ln(1+\text{SINR})]$) and handover cost (i.e., $D_{HO}$), which are characterized in Section 5.4 and Section 5.5, respectively.

## 5.4 SINR and Spectral Efficiency Characterization

As mentioned earlier, for tractability, we use the spatially averaged spectral efficiency for stationary devices to infer the average spectral efficiency for mobile devices. This assumption is validated later in Section 5.6 and shown to give accurate approximation for the SINR distribution.

To characterize the SINR, and hence the spectral efficiency, we first characterize the service distance distribution. Then, we characterize the SINR and spectral efficiency for both the conventional and CP/UP split network architectures.

### 5.4.1 Service Distances

As shown in Fig. 5.1, we need to characterize five service distances, namely $R_1$, $R_2$, $R_B$, $R_{c2}$, and $R_{cB}$. The conventional service distances $R_1$, $R_2$, $R_B$, which are for devices in $\mathcal{U}_1$, $\mathcal{U}_2$, and $\mathcal{U}_B$ respectively, are characterized in [31]. Conditioned on the association, the probability density functions (PDFs) of the $R_1$, $R_2$, and $R_B$ are given by

$$\mathbf{f}_{R_1}(r) = \frac{2\pi\lambda_1}{\mathcal{A}_1} r e^{-\pi\left(\lambda_1 r^2 + \lambda_2 \tilde{P}_{21}^{\frac{2}{\alpha_2}} r^{\frac{2\alpha_1}{\alpha_2}}\right)}, r \geq 0, \tag{5.18}$$

$$\mathbf{f}_{R_2}(r) = \frac{2\pi\lambda_2}{\mathcal{A}_2} r e^{-\pi\left(\lambda_2 r^2 + \lambda_1 P_{12}^{\frac{2}{\alpha_1}} r^{\frac{2\alpha_2}{\alpha_1}}\right)}, r \geq 0, \tag{5.19}$$

$$\mathbf{f}_{R_B}(r) = \frac{-2\pi\lambda_2}{\mathcal{A}_B} r \left[ e^{-\pi\left(\lambda_1 P_{12}^{\frac{2}{\alpha_1}} r^{\frac{2\alpha_2}{\alpha_1}} + \lambda_2 r^2\right)} - e^{-\pi\left(\lambda_1 \tilde{P}_{12}^{\frac{2}{\alpha_1}} r^{\frac{2\alpha_2}{\alpha_1}} + \lambda_2 r^2\right)} \right], r \geq 0. \quad (5.20)$$

As shown in Fig. 5.1, the association for $\mathcal{U}_1$, and the data association for $\mathcal{U}_2$ and $\mathcal{U}_B$ in the CP/UP split case have similar distribution to $R_1$, $R_2$, and $R_B$ given in (5.18), (5.19), and (5.20), respectively. The distributions for control link distances of the CP/UP split architecture are given by the following lemma

**Lemma 13.** *Let $R_{c2}$ and $R_{cB}$ denote the distances from the MBS that provides the control signaling to $\mathcal{U}_2$ and $\mathcal{U}_B$, respectively, in a cellular network with the CP/UP split architecture. Then the distributions of $R_{c2}$ and $R_{cB}$ are given by*

$$\mathbf{f}_{R_{c2}}(r) = \frac{2\pi\lambda_1 r}{\mathcal{A}_2} \left( e^{-\pi\lambda_1 r^2} - e^{-\pi\left(\lambda_1 r^2 + \lambda_2 P_{21}^{\frac{2}{\alpha_1}} r^{\frac{2\alpha_2}{\alpha_1}}\right)} \right), r \geq 0, \quad (5.21)$$

$$\mathbf{f}_{R_{cB}}(r) = \frac{2\pi\lambda_1 r}{\mathcal{A}_B} \left( e^{-\pi\left(\lambda_1 r^2 + \lambda_2 P_{21}^{\frac{2}{\alpha_1}} r^{\frac{2\alpha_2}{\alpha_1}}\right)} - e^{-\pi\left(\lambda_1 r^2 + \lambda_2 \tilde{P}_{21}^{\frac{2}{\alpha_1}} r^{\frac{2\alpha_2}{\alpha_1}}\right)} \right), r \geq 0. \quad (5.22)$$

*Proof.* See **Appendix C.2**. ■

### 5.4.2 Coverage Probability Analysis

The coverage probability is defined by the complementary cumulative distribution function (CCDF) of the SINR (i.e, $\mathbb{P}[\mathrm{SINR} > \theta]$, where $\theta$ denotes the predefined threshold for correct signal reception). Without loss of generality, the SINR analysis is performed for a test mobile device located at the origin. According to Slivnyak's theorem, all other devices have statistical SINR properties equivalent to that of the test device located at the origin [60]. Therefore, the analysis holds for an arbitrary mobile device located at any other location.

For the sake of exposition, we define four types of interferences caused by the BSs in $\Phi_1$ and $\Phi_2$ with respect to the origin, which are

- the interference from all MBSs $\mathcal{I}_1 = \sum_{x \in \boldsymbol{\Phi_1}} P_1 H_x x^{-\alpha_1}$.

- the interference from all MBSs excluding the one nearest to the origin $\mathcal{I}_1^o = \sum_{x \in \boldsymbol{\Phi_1} \setminus x_o} P_1 H_x x^{-\alpha_1}$.
- the interference from all SBSs $\mathcal{I}_2 = \sum_{x \in \boldsymbol{\Phi_2}} P_2 H_x x^{-\alpha_2}$.
- the interference from all SBSs excluding the one nearest to the origin $\mathcal{I}_2^o = \sum_{x \in \boldsymbol{\Phi_2} \setminus x_o} P_2 H_x x^{-\alpha_2}$.

The SINR at the test device's location, the origin, can be defined as

$$\text{SINR} = \frac{P_{BS} H r_0^{-\alpha}}{\mathcal{I}_{agg} + \sigma^2}, \tag{5.23}$$

where $P_{BS}$ is the serving BS transmit power, $H$ is the random channel power gain, $r_o$ is the distance between the test device and the serving BS, $\mathcal{I}_{agg}$ is the aggregate interference, and $\sigma^2$ is the noise power. The parameters in (5.23) to compute the SINR experienced by the devices in $\mathcal{U}_k$, $k \in \{1, 2, B\}$ for the conventional and CP/UP split architectures are given in Table 5.2.

Table 5.2: SINR parameters

| k | Conventional | | | | CP/UP split | | | |
|---|---|---|---|---|---|---|---|---|
| | **SINR** | $P_{BS}$ | $r_o$ | $\mathcal{I}_{agg}$ | **SINR** | $P_{BS}$ | $r_o$ | $\mathcal{I}_{agg}$ |
| 1 | $\text{SINR}_1^{(c)}$ | $P_1$ | $R_1$ | $\mathcal{I}_1^o + \mathcal{I}_2$ | $\text{SINR}_1^{(s)}$ | $P_1$ | $R_1$ | $\mathcal{I}_1^o$ |
| 2 | $\text{SINR}_2^{(c)}$ | $P_2$ | $R_2$ | $\mathcal{I}_1 + \mathcal{I}_2^o$ | $\text{SINR}_{d2}^{(s)}$ | $P_2$ | $R_2$ | $\mathcal{I}_2^o$ |
| | | | | | $\text{SINR}_{c2}^{(s)}$ | $P_1$ | $R_{c2}$ | $\mathcal{I}_1^o$ |
| B | $\text{SINR}_B^{(c)}$ | $P_2$ | $R_B$ | $\mathcal{I}_2^o$ | $\text{SINR}_{dB}^{(s)}$ | $P_2$ | $R_B$ | $\mathcal{I}_2^o$ |
| | | | | | $\text{SINR}_{cB}^{(s)}$ | $P_1$ | $R_{cB}$ | $\mathcal{I}_1^o$ |

As shown in Table 5.2, in the conventional network architecture, the macro and non-biased small cells devices experience inter-tier interference, which is due to the employed universal frequency reuse scheme. In contrast, the dedicated spectrum accesses employed by the CP/UP split architecture eliminates the inter-tier interference. Note that the biased devices do not experience inter-tier interference in the conventional network architecture due to the ABS interference coordination employed by the MBSs. Table 5.2 also shows the different SINR experienced by the data and control links in the CP/UP split architecture, which is due to the employed decoupled data and control associations.

For a predefined threshold reception $\theta$, the coverage probability $\mathcal{C} = \mathbb{P}[\text{SINR} > \theta]$ of all devices are characterized by the following lemma.

**Lemma 14.** *The* SINR *coverage for the conventional network is given by*

$$\mathcal{C}_1^{(c)} = \int_0^\infty \exp\Bigg( - \tilde{\lambda}_1 r^2 \theta \; {}_2F_1\left(1, 1 - \frac{2}{\alpha_1}; 2 - \frac{2}{\alpha_1}; -\theta\right) - \frac{\tilde{\lambda}_2}{B} r^2 \theta \tilde{P}_{21}^{\frac{2}{\alpha_2}} \; {}_2F_1\left(1, 1 - \frac{2}{\alpha_2}; 2 - \frac{2}{\alpha_2}; \frac{-\theta}{B}\right) \Bigg) \mathbf{f}_{R_1}(r) dr, \tag{5.24}$$

$$\mathcal{C}_2^{(c)} = \int_0^\infty \exp\left( - \tilde{\lambda}_1 r^2 \theta P_{12}^{\frac{2}{\alpha_1}} \; {}_2F_1\left(1, 1 - \frac{2}{\alpha_1}; 2 - \frac{2}{\alpha_1}; -\theta\right) - \tilde{\lambda}_2 r^2 \theta \; {}_2F_1\left(1, 1 - \frac{2}{\alpha_2}; 2 - \frac{2}{\alpha_2}; -\theta\right) \right) \mathbf{f}_{R_2}(r) dr, \tag{5.25}$$

$$\mathcal{C}_B^{(c)} = \int_0^\infty exp\left( - \tilde{\lambda}_2 r^2 \theta \; {}_2F_1\left(1, 1 - \frac{2}{\alpha_2}; 2 - \frac{2}{\alpha_2}; -\theta\right) \right) \mathbf{f}_{R_B}(r) dr. \tag{5.26}$$

*The* SINR *coverage for macrocell devices in the CP/UP split network architecture is given by*

$$\mathcal{C}_1^{(s)} = \int_0^\infty \exp\left( - \tilde{\lambda}_1 r^2 \theta \; {}_2F_1\left(1, 1 - \frac{2}{\alpha_1}; 2 - \frac{2}{\alpha_1}; -\theta\right) \right) \mathbf{f}_{R_1}(r) dr. \tag{5.27}$$

*The* SINR *coverage for the data connections for non-biased phantom cell devices is given by*

$$\mathcal{C}_{d2}^{(s)} = \int_0^\infty \exp\left( - \tilde{\lambda}_2 r^2 \theta \; {}_2F_1\left(1, 1 - \frac{2}{\alpha_2}; 2 - \frac{2}{\alpha_2}; -\theta\right) \right) \mathbf{f}_{R_2}(r) dr, \tag{5.28}$$

*and the biased small cell devices $\mathcal{C}_{dB}^{(s)} = \mathcal{C}_B^{(c)}$ given in* (5.26)*. The SINR coverage probabilities for the control links of the non-biased and biased phantom cell devices are given by*

$$\mathcal{C}_{c2}^{(s)} = \int_0^\infty \exp\left( - \tilde{\lambda}_1 r^2 \theta \; {}_2F_1\left(1, 1 - \frac{2}{\alpha_1}; 2 - \frac{2}{\alpha_1}; -\theta\right) \right) \mathbf{f}_{R_{c2}}(r) dr, \tag{5.29}$$

$$\mathcal{C}_{cB}^{(c)} = \int_0^\infty exp\left(-\tilde{\lambda}_1 r^2 \theta \; {}_2F_1\left(1, 1 - \frac{2}{\alpha_1}; 2 - \frac{2}{\alpha_1}; -\theta\right)\right) \mathbf{f}_{R_{cB}}(r)\, dr, \tag{5.30}$$

*where* $\tilde{\lambda}_k = \frac{2\pi\lambda_k}{\alpha_k - 2}$, ${}_2F_1(\cdot, \cdot; \cdot; \cdot)$ *is the hypergeometric function, and* $\mathbf{f}_{R_1}(r)$, $\mathbf{f}_{R_2}(r)$, $\mathbf{f}_{R_B}(r)$, $\mathbf{f}_{R_{c2}}(r)$, *and* $\mathbf{f}_{R_{cB}}(r)$ *are given in Section 5.4.1.*

*Proof.* See **Appendix C.3**. ■

For the special case of equal path-loss exponents $\alpha_1 = \alpha_2 = 4$, the coverage probabilities reduce to the simple closed-form expressions shown below:

$$\mathcal{C}_1^{(c)} = \frac{\lambda_1 + \lambda_2 \sqrt{\tilde{P}_{21}}}{\lambda_1 \rho(1, \theta) + \lambda_2 \sqrt{\tilde{P}_{21}} \rho(1, \frac{\theta}{B})}, \tag{5.31}$$

$$\mathcal{C}_2^{(c)} = \frac{1}{\rho(1, \theta)}, \tag{5.32}$$

$$\mathcal{C}_1^{(s)} = \frac{\lambda_1 + \lambda_2 \sqrt{\tilde{P}_{21}}}{\lambda_1 \rho(1, \theta) + \lambda_2 \sqrt{\tilde{P}_{21}}}, \tag{5.33}$$

$$\mathcal{C}_{d2}^{(s)} = \frac{\lambda_2 + \lambda_1 \sqrt{P_{12}}}{\lambda_2 \rho(1, \theta) + \lambda_1 \sqrt{P_{12}}}, \tag{5.34}$$

$$\mathcal{C}_{c2}^{(s)} = \frac{\left(1 + \frac{\lambda_1}{\lambda_2} \sqrt{P_{12}}\right)\left(1 - \frac{1}{1 + \frac{\lambda_2}{\lambda_1} \sqrt{P_{21}} \rho(1, \theta)^{-1}}\right)}{\rho(1, \theta)}, \tag{5.35}$$

$$\mathcal{C}_{dB}^{(s)} = \mathcal{C}_B^{(c)} = \frac{\lambda_2}{\mathcal{A}_B} \left( \frac{\lambda_1 \left(\sqrt{P_{12}} - \sqrt{\tilde{P}_{12}}\right)}{\left(\lambda_2 \rho(1, \theta) + \lambda_1 \sqrt{\tilde{P}_{12}}\right) \left(\lambda_2 \rho(1, \theta) + \lambda_1 \sqrt{P_{12}}\right)} \right), \tag{5.36}$$

$$\mathcal{C}_{cB}^{(s)} = \frac{\lambda_1}{\mathcal{A}_B} \left( \frac{\lambda_2 \left(\sqrt{\tilde{P}_{21}} - \sqrt{P_{21}}\right)}{\left(\lambda_1 \rho(1, \theta) + \lambda_2 \sqrt{P_{21}}\right) \left(\lambda_1 \rho(1, \theta) + \lambda_2 \sqrt{\tilde{P}_{21}}\right)} \right), \tag{5.37}$$

where $\rho(a, b) = a + \sqrt{b} \arctan\left(\sqrt{b}\right)$.

### 5.4.3 Spectral Efficiency Analysis

The spectral efficiency is one of the main parameters to calculate the throughput of the conventional and CP/UP split devices throughputs as shown in Section 5.3. The spectral efficiency ($\mathcal{SE} = \mathbb{E}[\ln(1+\mathrm{SINR})]$) can be directly derived from the coverage probability as follows:

$$\begin{aligned}\mathcal{SE} = \mathbb{E}[\ln(1+\mathrm{SINR})] &\overset{(a)}{=} \int_0^\infty \mathbb{P}[\ln(1+\mathrm{SINR}) > \zeta]\mathrm{d}\zeta \\ &= \int_0^\infty \mathbb{P}[\mathrm{SINR} > (e^{\zeta}-1)]\mathrm{d}\zeta \\ &\overset{(b)}{=} \int_0^\infty \frac{\mathbb{P}[\mathrm{SINR} > t]}{t+1}\mathrm{d}t, \qquad (5.38)\end{aligned}$$

where (a) follows because $\ln(1+\mathrm{SINR})$ is a strictly positive random variable, and (b) follows by substituting variable $t = e^{\zeta}-1$. For general path loss exponent, the spectral efficiencies for macro-cell and small-cell devices in the shared spectrum access scheme in the conventional network are given by (5.39) and (5.40), respectively. For the dedicated spectrum access scheme in the CP/UP split RAN, the spectral efficiencies are given by:

$$\mathcal{SE}_1^{(c)} = \int_0^\infty\int_0^\infty \frac{\exp\Big( -\tilde{\lambda}_1 r^2 t\ {}_2F_1\left(1,1-\frac{2}{\alpha_1};2-\frac{2}{\alpha_1};-t\right) - \tilde{\lambda}_2 r^2 t P_{21}^{\frac{2}{\alpha_2}} B^{\frac{2}{\alpha_2}-1}\ {}_2F_1\left(1,1-\frac{2}{\alpha_2};2-\frac{2}{\alpha_2};\frac{-t}{B}\right)\Big)}{t+1}\mathbf{f}_{R_1}(r)\mathrm{d}r\mathrm{d}t, \qquad (5.39)$$

$$\mathcal{SE}_2^{(c)} = \int_0^\infty\int_0^\infty \frac{\exp\left(-\tilde{\lambda}_1 r^2 t P_{12}^{\frac{2}{\alpha_1}}\ {}_2F_1\left(1,1-\frac{2}{\alpha_1};2-\frac{2}{\alpha_1};-t\right) - \tilde{\lambda}_2 r^2 t\ {}_2F_1\left(1,1-\frac{2}{\alpha_2};2-\frac{2}{\alpha_2};-t\right)\right)}{t+1}\mathbf{f}_{R_2}(r)\mathrm{d}r\mathrm{d}t. \qquad (5.40)$$

$$\mathcal{SE}_1^{(s)} = \int_0^\infty\int_0^\infty \frac{\exp\left(-\tilde{\lambda}_1 r^2 t\ {}_2F_1\left(1,1-\frac{2}{\alpha_1};2-\frac{2}{\alpha_1};-t\right)\right)}{t+1}\mathbf{f}_{R_1}(r)\mathrm{d}r\mathrm{d}t, \qquad (5.41)$$

$$\mathcal{SE}_{d2}^{(s)} = \int_0^\infty\int_0^\infty \frac{\exp\left(-\tilde{\lambda}_2 r^2 t\ {}_2F_1\left(1,1-\frac{2}{\alpha_2};2-\frac{2}{\alpha_2};-t\right)\right)}{t+1}\mathbf{f}_{R_2}(r)\mathrm{d}r\mathrm{d}t, \qquad (5.42)$$

$$\mathcal{SE}_{c2}^{(s)} = \int\limits_0^\infty \int\limits_0^\infty \frac{\exp\left(-\tilde{\lambda}_1 r^2 t \ {}_2F_1\left(1, 1-\frac{2}{\alpha_1}; 2-\frac{2}{\alpha_1}; -t\right)\right)}{t+1} \mathbf{f}_{R_{c2}}(r) \mathrm{d}r \mathrm{d}t, \tag{5.43}$$

$$\mathcal{SE}_{B}^{(c)} = \mathcal{SE}_{dB}^{(s)} = \int\limits_0^\infty \int\limits_0^\infty \frac{\exp\left(-\tilde{\lambda}_2 r^2 t \ {}_2F_1\left(1, 1-\frac{2}{\alpha_2}; 2-\frac{2}{\alpha_2}; -t\right)\right)}{t+1} \mathbf{f}_{R_B}(r) \mathrm{d}r \mathrm{d}t, \tag{5.44}$$

$$\mathcal{SE}_{cB}^{(s)} = \int\limits_0^\infty \int\limits_0^\infty \frac{\exp\left(-\tilde{\lambda}_1 r^2 t \ {}_2F_1\left(1, 1-\frac{2}{\alpha_1}; 2-\frac{2}{\alpha_1}; -t\right)\right)}{t+1} \mathbf{f}_{R_{cB}}(r) \mathrm{d}r \mathrm{d}t. \tag{5.45}$$

As shown in equations (5.39)-(5.45), two fold integrals are required to obtain the spectral efficiency for general path loss exponents, which is numerically complex to evaluate. For the special case of path loss exponents $\alpha_1 = \alpha_2 = 4$, the spectral efficiency for all types of devices can be evaluated via single integral as follows:

$$\mathcal{SE}_{1}^{(c)} = \int_0^\infty \frac{1}{t+1} \frac{\lambda_1 + \lambda_2 \sqrt{\tilde{P}_{21}}}{\lambda_1 \rho(1,t) + \lambda_2 \sqrt{\tilde{P}_{21}} \rho(1, \frac{t}{B})} \mathrm{d}t, \tag{5.46}$$

$$\mathcal{SE}_{2}^{(c)} = \int_0^\infty \frac{1}{t+1} \frac{1}{\rho(1,t)} \mathrm{d}t, \tag{5.47}$$

$$\mathcal{SE}_{B}^{(c)} = \mathcal{SE}_{dB}^{(s)} = \int_0^\infty \frac{1}{t+1} \left( \frac{(\lambda_1 \sqrt{\tilde{P}_{12}} + \lambda_2)(\lambda_1 \sqrt{P_{12}} + \lambda_2)}{\lambda_1 \left(\sqrt{P_{12}} - \sqrt{\tilde{P}_{12}}\right)} \right) \left( \frac{\lambda_1 \left(\sqrt{P_{12}} - \sqrt{\tilde{P}_{12}}\right)}{(\lambda_2 \rho(1,t) + \lambda_1 \sqrt{\tilde{P}_{12}})(\lambda_2 \rho(1,t) + \lambda_1 \sqrt{P_{12}})} \right) \mathrm{d}t, \tag{5.48}$$

$$\mathcal{SE}_{1}^{(s)} = \int_0^\infty \frac{1}{t+1} \frac{\lambda_1 + \lambda_2 \sqrt{\tilde{P}_{21}}}{\lambda_1 \rho(1,t) + \lambda_2 \sqrt{\tilde{P}_{21}}} \mathrm{d}t, \tag{5.49}$$

$$\mathcal{SE}_{d2}^{(s)} = \int_0^\infty \frac{1}{t+1} \frac{\lambda_2 + \lambda_1 \sqrt{P_{12}}}{\lambda_2 \rho(1,t) + \lambda_1 \sqrt{P_{12}}} \mathrm{d}t, \tag{5.50}$$

$$\mathcal{SE}_{c2}^{(s)} = \int\limits_0^\infty \frac{\left(1 + \frac{\lambda_1}{\lambda_2} \sqrt{P_{12}}\right) \left(1 - \frac{1}{1 + \frac{\lambda_2}{\lambda_1} \sqrt{P_{21}} \rho(1,t)^{-1}}\right)}{(t+1)\rho(1,t)} dt, \tag{5.51}$$

$$\mathcal{SE}_{cB}^{(s)} = \int_0^\infty \frac{1}{t+1} \left( \frac{(\lambda_1\sqrt{\tilde{P}_{12}}+\lambda_2)(\lambda_1\sqrt{P_{12}}+\lambda_2)}{\lambda_1\left(\sqrt{P_{12}}-\sqrt{\tilde{P}_{12}}\right)} \right) \left( \frac{\lambda_2\left(\sqrt{\tilde{P}_{21}}-\sqrt{P_{21}}\right)}{\left(\lambda_1\rho(\sqrt{t},t)+\lambda_2\sqrt{P_{21}}\right)\left(\lambda_1\rho(\sqrt{t},t)+\lambda_2\sqrt{\tilde{P}_{21}}\right)} \right) \mathrm{d}t. \quad (5.52)$$

## 5.5 Handover Analysis

In this section, we take into account the effect of mobility on the system performance. In order to compute the average throughputs in Eq. (5.12) and (5.13), we need to compute the handover cost for both the CP/UP split network and conventional network architectures. The handover cost is a function of the handover rate per unit length of devices trajectories, which is calculated in this section.

We assume that devices move according to an arbitrary mobility pattern with velocity $\mathcal{V}$. The handover rate is determined based on the model obtained by Bao and Liang [42], which gives the handover rate per unit length for arbitrary trajectories in a PPP multi-tier network. Hence, the handover rate is independent of the underlying mobility pattern. Following [42], the tier-$i$-to-tier-$j$ handover rate per unit length of an arbitrary trajectory is given by

$$HO_{ij}^{(c)} = \frac{\lambda_i\lambda_j\mathcal{F}(x_{ij})}{\pi\left(\lambda_i+\lambda_j x_{ij}^2\right)^{\frac{3}{2}}}, \quad (5.53)$$

where $x_{12} = \left(\tilde{P}_{12}\right)^{\frac{1}{\alpha}}$, $x_{21} = \frac{1}{x_{12}}$, $x_{11} = x_{22} = 1$, and

$$\mathcal{F}(x) = \frac{1}{x^2}\int_0^\pi \sqrt{(x^2+1)-2x\cos(\theta)}d\theta. \quad (5.54)$$

From Eq. (5.10), the total handover cost per unit time in the conventional network is given by:

$$D_{HO}^{(c)} = \left(d^{(c)}\left(1-\mathcal{X}\right)+\tilde{d}^{(c)}\mathcal{X}\right)\frac{\mathcal{V}}{\pi}\sum_{i=1}^{2}\sum_{j=1}^{2}\frac{\lambda_i\lambda_j\mathcal{F}(x_{ij})}{\left(\lambda_i+\lambda_j x_{ij}^2\right)^{\frac{3}{2}}}. \quad (5.55)$$

In the CP/UP split network, an inter-anchor handover takes place when crossing a MBS-to-MBS cell boundary (see Fig. 5.2); thus the inter-anchor handover rate is equivalent to the handover rate in the single-tier MBS case with density $\lambda_1$. Following [42], we calculate the inter-anchor handover rate per unit length in the CP/UP split architecture network as follows:

$$MHO^{(s)} = \frac{4\sqrt{\lambda_1}}{\pi}. \tag{5.56}$$

As discussed earlier, intra-anchor handovers are defined as all types of handovers that do not require changing the anchor BS. Hence, the intra-anchor handover rate per unit length is given by:

$$VHO^{(s)} = \frac{2}{\pi}\left(\sum_{i=1}^{2}\sum_{j=1}^{2}\frac{\lambda_i\lambda_j\mathcal{F}(x_{ij})}{2\left(\lambda_i+\lambda_j x_{ij}^2\right)^{\frac{3}{2}}} - 2\sqrt{\lambda_1}\right). \tag{5.57}$$

From Eq. (5.11), the total handover cost per unit time in the CP/UP split network is given by:

$$\begin{aligned} D_{HO}^{(s)} &= \frac{2\mathcal{V}d_v^{(s)}}{\pi}\left(\sum_{i=1}^{2}\sum_{j=1}^{2}\frac{\lambda_i\lambda_j\mathcal{F}(x_{ij})}{2\left(\lambda_i+\lambda_j x_{ij}^2\right)^{\frac{3}{2}}} - 2\sqrt{\lambda_1}\right) + \left(\left(1-\mathcal{Z}\right)d_m^{(s)} + \mathcal{Z}\tilde{d}_m^{(s)}\right)\mathcal{V}\frac{4\sqrt{\lambda_1}}{\pi} \\ &= \frac{\mathcal{V}}{\pi}\left(d_v^{(s)}\sum_{i=1}^{2}\sum_{j=1}^{2}\frac{\lambda_i\lambda_j\mathcal{F}(x_{ij})}{\left(\lambda_i+\lambda_j x_{ij}^2\right)^{\frac{3}{2}}} + 4\sqrt{\lambda_1}\left(\left(1-\mathcal{Z}\right)d_m^{(s)} + \mathcal{Z}\tilde{d}_m^{(s)} - d_v^{(s)}\right)\right). \end{aligned} \tag{5.58}$$

Note that the inter-anchor handover delay is equal to the conventional handover delay (i.e., $d_m^{(s)} = d^{(c)}$ and $\tilde{d}_m^{(s)} = \tilde{d}^{(c)}$) because the handover procedure is the same. Thus we can infer from Eq. (5.55) and (5.58) that the handover cost depends on the relative values of $d^{(c)}$, $d_v^{(s)}$, $\lambda_2$, and $\lambda_1$. In fact, in an ultra dense small cell network with $\lambda_2 >> \lambda_1$, we can obtain a bound on the maximum gain in terms of the handover cost that the CP/UP split architecture can offer when $\mathcal{X} = \mathcal{Z} = 0$ as follows:

$$\mathcal{G} = \lim_{\lambda_2\to\infty}\frac{D_{HO}^{(c)} - D_{HO}^{(s)}}{D_{HO}^{(c)}} = 1 - \frac{d_v^{(s)}}{d^{(c)}}. \tag{5.59}$$

Note that the core network is mainly wired and the core network elements may be located far away from the network edge, and hence, core network signaling travels farther distances with lower speed[7]. Hence, the core network signaling may add significant delay to the handover procedure. For instance, if $d^{(c)} = 5d_v^{(s)}$, Eq. (5.59) shows that the CP/UP split architecture can offer 80% reduction in the handover delay.

## 5.6 Model Validation and Numerical Results

In this section, we first validate our results via simulations using MATLAB. We then use the developed analytical model to compare the performance of the conventional and CP/UP split RAN architectures and obtain design insights.

Unless otherwise stated, we use the following parameters in our simulations and analysis. The transmission powers are $P_1 = 50$ Watt and $P_2 = 5$ Watt. The bandwidth is $W = 10$ MHz. The ABS factor is $\eta = 0.3$. The percentage of control data in the available time/frequency resources is $\mu_C = 0.3$ based on 3GPP Release 11 [142]. The biasing factor for the small BSs tier is $B = 30$. The available air interface bandwidth for macro cells resource allocation is $W_1 = 2$ MHz, and for small cells resource allocation is $W_2 = 8$ MHz. We assume that the density of MBSs is $\lambda_1 = 2$ BS/km$^2$ and the density of mobile devices is $\lambda^u = 50$ devices/km$^2$. The path loss exponent is $\alpha_1 = \alpha_2 = 4$.

### 5.6.1 Model Validation

In each simulation run, the network is realized in $90 \times 90\text{km}^2$ via two independent homogenous PPPs with densities $\lambda_1$ and $\lambda_2$. A test device is then generated at the origin and moves along five consecutive straight trajectories, each with a random length (Rayleigh distributed with parameter $1/\sqrt{2\pi\lambda_1}$) and random angle (uniformly distributed on $[0, 2\pi]$). The trajectories are then partitioned with a 100-point resolution and the device's association and SINR are recorded at each point. The association type is determined based on Eq. (5.1). According

---

[7] Wave propagation within any medium is less than the speed of electromagnetic waves in the air, which travels with the speed of light.

to the association, the SINR value at each point of the test device trajectory is saved in one of the eight cumulative vectors corresponding to the 8 link types listed in Fig. 5.1. Then, the above process is repeated 1000 times. The empirical CCDF of the values recorded in the eight cumulative vectors are then compared to the respective CCDF in Eq. (5.31) to (5.37).

Fig. 5.3 plots the SINR CCDF obtained from the analysis (for stationary devices) and the simulation (for mobile devices). The figure shows that the analysis (for stationary devices) closely captures the simulation result (for mobile devices), confirming the validity of the proposed model for both stationary and mobile devices. While the simulation result (for mobile devices) considers the spatial correlation between SINR values across devices' trajectories, the close match between the analysis and simulation result can be explained by the rapid spatial decay of the spatial correlation between the interference signal and the distance [145]. Hence, we can deduce that averaging over all locations in all network configurations closely captures the averaging over all trajectories in all network configurations. Fig. 5.3(a) shows that the CP/UP split architecture offers higher coverage probability, for tier-1 and tier-2 devices data links, than the conventional RAN architecture due to the absence of cross-tier interference. Fig. 5.3(b) shows that SINR coverage probability for the control signaling of the biased SBS devices is better than that of the unbiased SBSs devices. This is because the biased SBSs devices are closer on average to the MBSs than the unbiased SBSs devices.

### 5.6.2 Handover Rate and Throughput

Fig 4. illustrates the handover cost imposed by device mobility. In particular, Fig. 5.4(a) shows the handover rates per unit length of an arbitrary trajectory as a function of the density of SBS in the conventional and CP/UP split networks. The graph shows that small cell densification linearly increases the total number of handovers in the conventional network architecture. Looking into the explicit handover types, we notice that $HO_{11}^{(c)}$ (handovers between MBSs) decreases as the density of small cells increases.

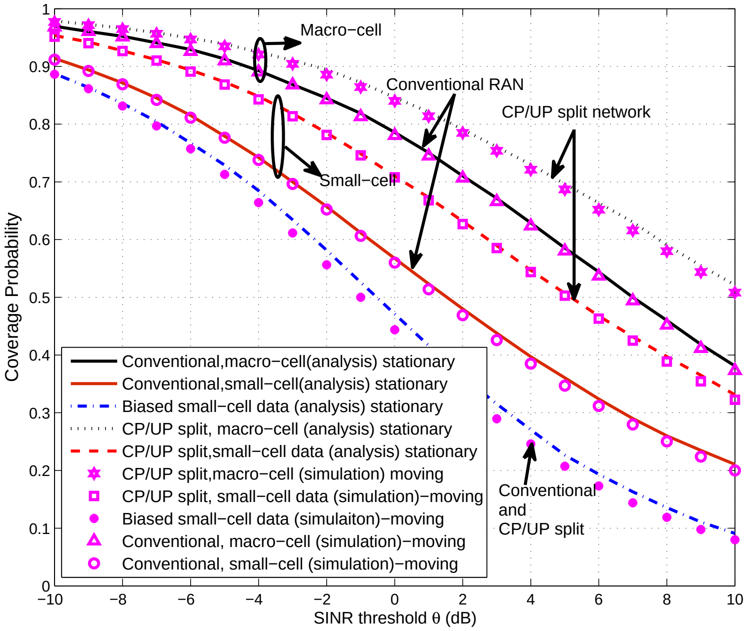

(a) Conventional association & CP/UP split data association.

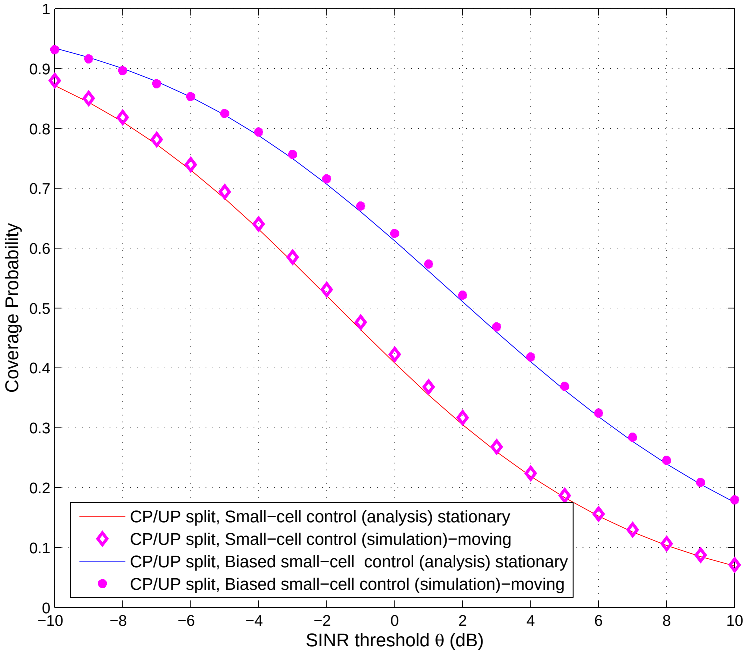

(b) CP/UP split control association.

Figure 5.3: Coverage probability as a function of the SINR threshold $\theta$ for stationary users (analysis) and mobile users (simulation).

The reason is that the boundaries of MBSs become more populated by SBSs when $\lambda_2$ increases. Hence, a MBS-to-MBS handover is replaced by MBS-to-SBS followed by SBS-to-MBS handover and possibly several SBS-to-SBS handovers inbetween. Also, $HO_{22}^{(c)}$ linearly increases and $HO_{12}^{(c)} = HO_{21}^{(c)}$ saturates. Hence, with high SBS densities, the handover rate is dominated by $HO_{22}^{(c)}$, which motivates the anchoring solution via CP/UP splitting to reduce the handover delay. As shown in the graph, in the CP/UP split network architecture, the inter-anchor handover rate is kept constant due to the constant density of the MBSs. However, the intra-anchor handover rate increases linearly with $\lambda_2$. Fig. 5.4(b) depicts the handover cost for the conventional architecture given in Eq. (5.10) and the handover cost for the CP/UP split architecture given in Eq. (5.11) as functions of the mobile device velocity. The graphs show a significant reduction in the handover delay provided by the CP/UP architecture, in which MBSs act as handover anchors that manage handovers between underlying SBSs. Note that the handover cost reduction provided by the CP/UP splitting does not necessarily lead to a throughput increase. The reason is that the handover cost reduction is obtained at the expense of degraded SINR association for the control signalling, which imposes a tradeoff between the conventional and CP/UP split that is discussed in Fig. 5.5. It is worth noting that the infeasibility region shown in Fig. 5.4(b) occurs when the average cell dwell time becomes shorter than the average handover delay, which may happen due to high mobility and/or high BSs density. In this case, the handover costs given by Eq. (5.10) and (5.11) are corrected to one in order to make the throughput become zero. That is, the network fails to support mobile devices whose very high mobility speeds fall in the infeasibility region.

The next set of simulation results show the effect of mobility, control signaling reduction factor $\gamma$, the availability of X2 interface between BSs, and SBS density on the average device throughput. Unless otherwise stated, we assume that $d^{(c)} = 0.7$ seconds and that $d_v^{(s)} = \tilde{d}^{(c)} = \tilde{d}_m^{(s)} = 0.5 d^{(c)}$ [144]. Fig. 5.5 shows the effect of the handover delay on the average device throughput in the conventional and CP/UP split architectures for different mobility profiles: (a) stationary $\mathcal{V} = 0$ $km/h$, (b) low velocity $\mathcal{V} = 50$ $km/h$ (e.g., driving in

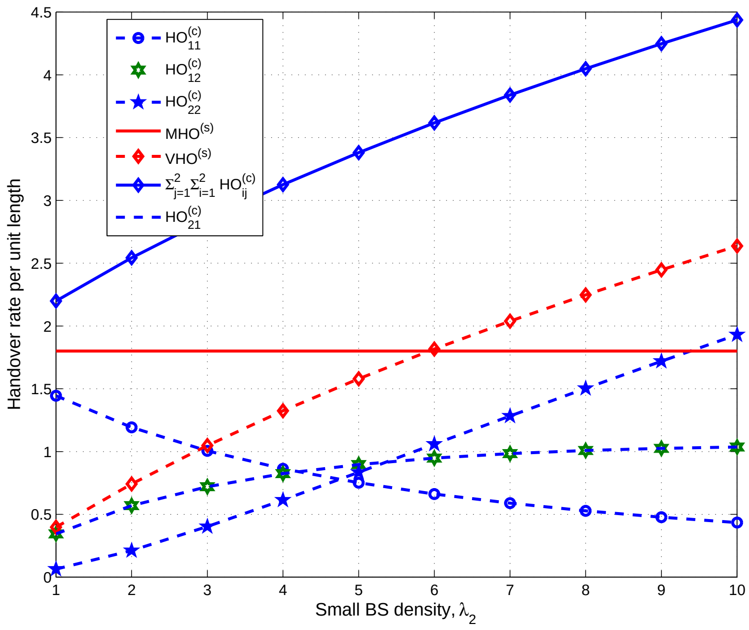

(a) Handover rate per unit length.

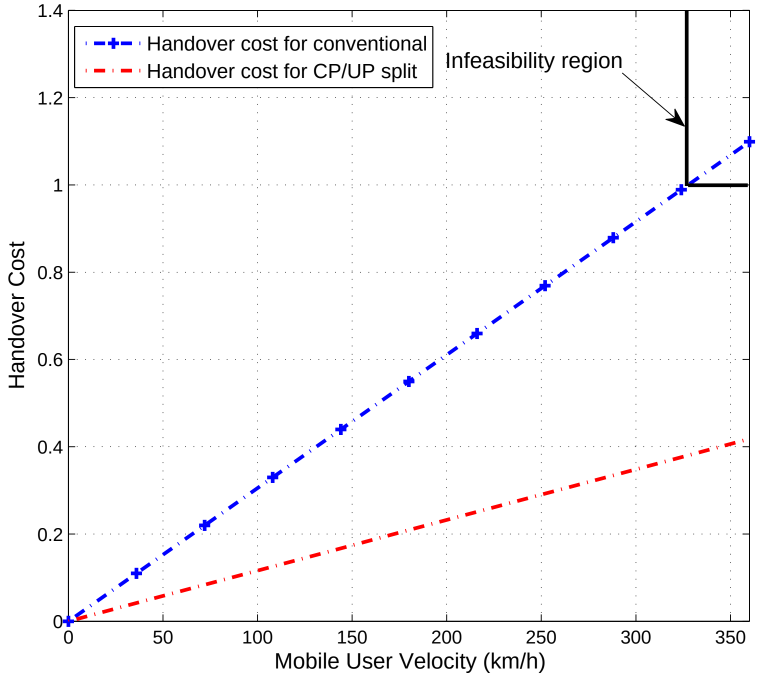

(b) Handover cost when $\lambda_2 = 150$ BS/km$^2$, $d_v^{(s)} = 0.5d^{(c)}$, and $\mathcal{X} = \mathcal{Z} = 0$.

Figure 5.4: Handover costs in terms of (a) handover rate per unit length of the user trajectory and (b) handover cost given in Eq. (5.10) and (5.11).

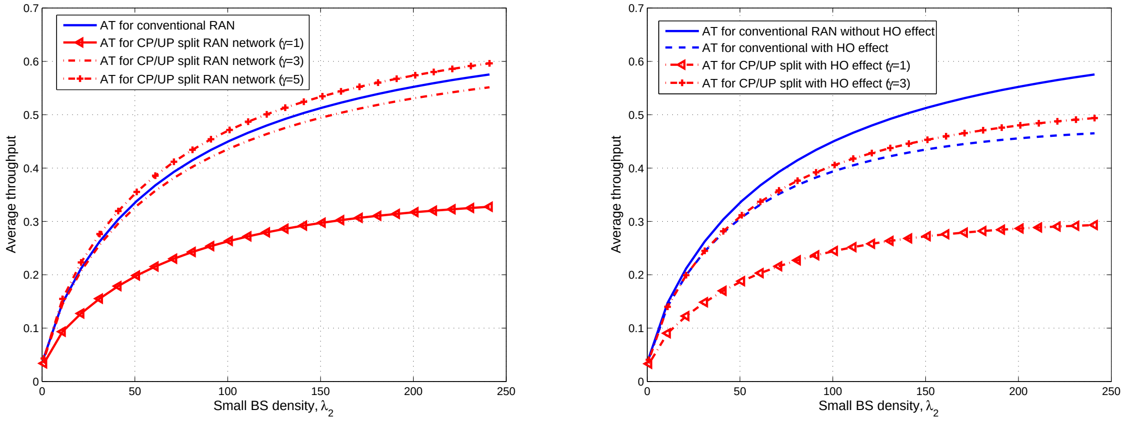

(a) Stationary $\mathcal{V} = 0\ km/h$.

(b) Low speed $\mathcal{V} = 50\ km/h$.

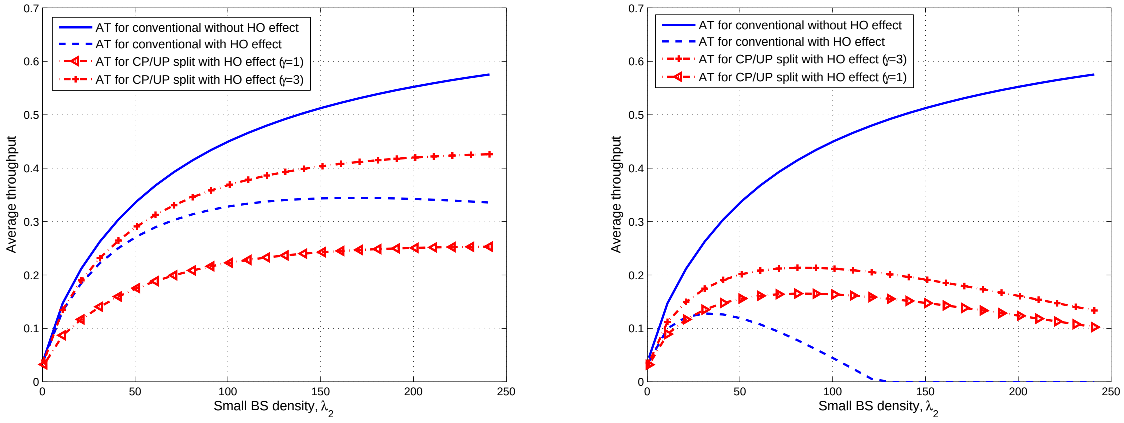

(c) Medium speed $\mathcal{V} = 108\ km/h$.

(d) High speed $\mathcal{V} = 360\ km/h$.

Figure 5.5: Average throughput with and without handover cost for mobile device with different velocities for $\gamma \in \{1, 3, 5\}$ and $\mathcal{X} = \mathcal{Z} = 0$.

the city), (c) medium velocity $\mathcal{V} = 108\ km/h$ (e.g., traveling on highways or in monorails in city downtowns), and (d) high velocity $\mathcal{V} = 360\ km/h$. (e.g., traveling on a high speed train such as Shinkansen when passing through downtown Tokyo, Japan).

In the case of stationary devices, Fig. 5.5(a) shows that a high control reduction factor $\gamma$ is required for the CP/UP split architecture to achieve an equivalent average throughout to the conventional network architecture. This result can be interpreted by the poor control rate provided by MBSs to the unbiased phantom cell devices when compared to the rate they get from the SBSs (cf. Fig. 5.3(b)). Hence, offloading the control signaling to the MBSs requires a high control reduction factor to compensate for such rate loss. Note that the per device rate for unbiased devices of the SBSs increases with $\lambda_2$, and hence, offloading control to the MBSs incurs higher rate loss. Consequently, the CP/UP split architecture is not beneficial to networks with stationary devices unless a high control reduction factor can be achieved.

For mobile devices, Figs. 5.5(b), 5.5(c) and 5.5(d) show that the CP/UP split architecture is beneficial especially for high speeds and $\mathcal{X} = \mathcal{Z} = 0$; i.e., there is no X2 interface handovers on both conventional and CP/UP split architectures. Note that we show the ideal case; i.e, AT for stationary devices, to clearly visualize the effect of mobility on the average throughput. Figs. 5.5(b) and 5.5(c) show that a control reduction factor of $\gamma = 3$ is sufficient for the CP/UP split architecture to outperform the conventional network architecture when devices move at low or medium speeds. When the mobility speed is high (Fig. 5.5(d)), the CP/UP split network outperforms the conventional network even without control reduction (i.e., $\gamma = 1$). More importantly, only the CP/UP split network can support devices moving at such high speeds while the conventional network cannot.

It is important to note that Fig. 5.5 is plotted for $d_v^{(s)} = 0.5d^{(c)}$. The CP/UP split architecture can offer even higher throughput gains if the intra-anchor delay is lowered. Fig. 5.6 shows the additional gain that the CP/UP split network offers when $d_v^{(s)} = 0.3d^{(c)}$ versus the case where $d_v^{(s)} = 0.5d^{(c)}$. The graph demonstrates the importance of lowering the intra-anchor delay and minimizing the involvement of the core network during handovers.

Therefore, the CP/UP split architecture can be used to increase the throughput of mobile devices in dense small cell deployments by making the MBSs act as handover anchors instead of involving the core network in handovers.

Fig. 5.7 shows the effect of the direct X2 interface availability between BSs on the average throughput in the conventional and CP/UP splitting architectures. The figure shows that the X2 interfaces have more prominent effect on the conventional network architecture because it reduces the delay for all handover types. On the other hand, the X2 interference does not have a noticeable effect on in CP/UP split architecture because it only reduces the inter-anchor handover delay, which is considered a rare handover event. The figure also shows that the relative performance gains between the conventional and CP/UP splitting architectures highly depends on the X2 interface availability. Particularly, there are critical points at which the conventional network with sufficient X2 interface deployment outperforms the CP/UP split architecture in terms of average throughput. Such critical points are depicted in Fig. 5.7 at $\mathcal{X} = \mathcal{Z} = 0.5$, $\mathcal{X} = \mathcal{Z} = 0.8$, and $\mathcal{X} = \mathcal{Z} = 0.95$ for $\mathcal{V} = 50\ km/h$, $\mathcal{V} = 108\ km/h$. and $\mathcal{V} = 360\ km/h$, respectively.

### 5.6.3 Feasibility of the CP/UP Split Architecture

To examine the feasibility of the CP/UP split architecture as stated in Corollary 6, we plot Fig. 5.8, which shows the average throughputs for all types of devices as functions of the SBS density, assuming $\mathcal{V} = 0$, $\gamma = 3$, and $B = 30$. Note that we assume saturation conditions such that newly added SBSs always have devices to serve. The graph shows the breaking point (point A in Fig. 5.8) at which the MBSs fail to provide the control signaling required by phantom cell devices. Point A is the point at which the inequality (5.8) is violated. Note that the CP/UP split architecture can still be made feasible by allocating more spectrum to the MBSs or enhancing the control reduction factor $\gamma$ as shown in Corollary 6.

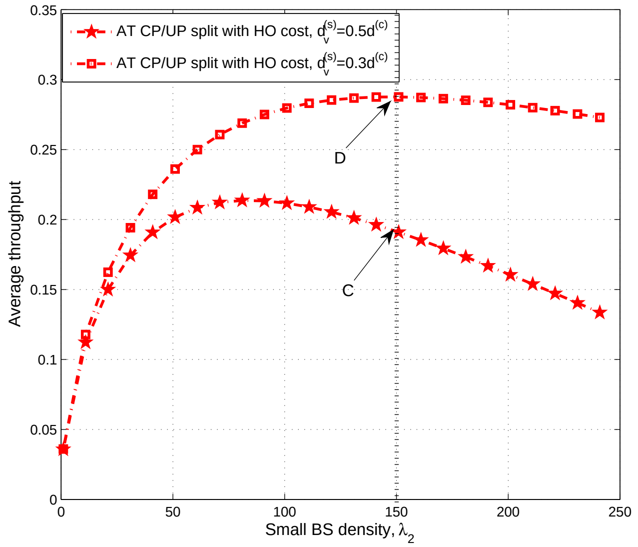

Figure 5.6: Average throughput with handover cost and intra-anchor handover delay values $d_v^{(s)} = 0.5d^{(c)}$ and $d_v^{(s)} = 0.3d^{(c)}$ ($\mathcal{V} = 360\ km/h$, $\gamma = 3$, and $\mathcal{X} = \mathcal{Z} = 0$).

### 5.6.4 Design Insights

From the above numerical results, several design insights can be drawn for the CP/UP split network architecture. First, the CP/UP architecture becomes more appealing for higher mobility profiles when the availability of direct X2 interface between the BSs is low, in which the control signaling reduction factor plays a key role in the throughput gains when compared to the conventional architecture. The amount of delay reduction provided by the intra-anchor handover also has a significant impact on the throughput gains provided by the CP/UP split networks. For instance, Fig. 5.6 shows a 60% throughput improvement when the intra-anchor handover delay $d_v^{(s)}$ is reduced from $0.5d^{(c)}$ (point C in Fig. 5.6) to $0.3d^{(c)}$ (point D in Fig. 5.6).

Cellular operators can solve the excess handover problem, which is coupled with network densification, either by deploying more X2 interfaces between adjacent BSs or applying CP/UP splitting. While the former reduces the handover delay only, the latter reduces both

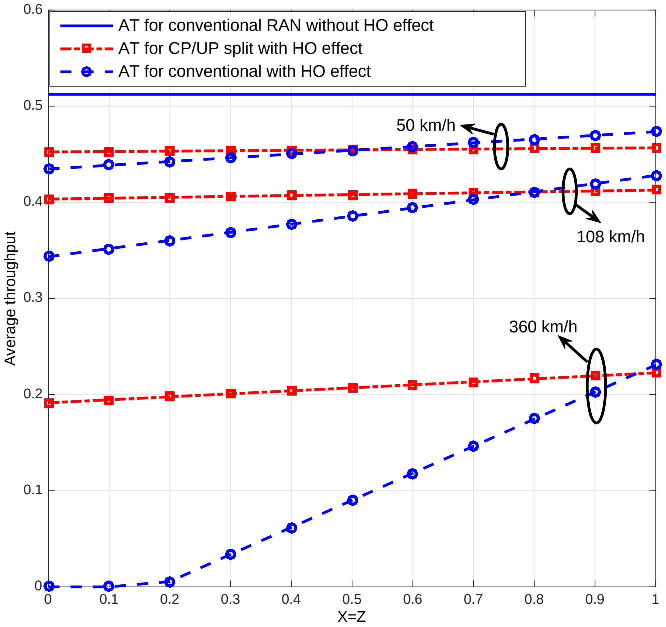

Figure 5.7: Average throughput with and without handover cost when $\gamma = 3$, $\lambda_2 = 150$ BS/km$^2$, and $d_v^{(s)} = \tilde{d}^{(c)} = \tilde{d}_m^{(s)} = 0.5d^{(c)}$.

the handover delay as well as the signaling overhead. Note that at higher SBSs densities and/or control reduction factors, the conventional network may not achieve the CP/UP split throughput even with 100% X2 deployment. Consequently, the CP/UP split architecture is more appealing in ultra dense environments with high mobility profiles.

Another noteworthy insight is that there is a tradeoff between traffic offloading via biasing and control offloading via the CP/UP architecture on macrocell devices rate. As shown in Fig. 5.8, there is a turning point for the average throughput of macro cell devices at $\lambda_2 = 22$ (point B in Fig. 5.8). For the given network configuration, prior to point B, the positive impact of offloading devices traffic to phantom cells (i.e., decreasing $\mathcal{N}_1$) dominates the negative impact of offloading control signaling from the phantom cells to MBSs. Then, the situation is reversed after point B and the negative impact of the control burden dominates the positive impact of traffic offloading until the infeasibility point is reached (point A). Such

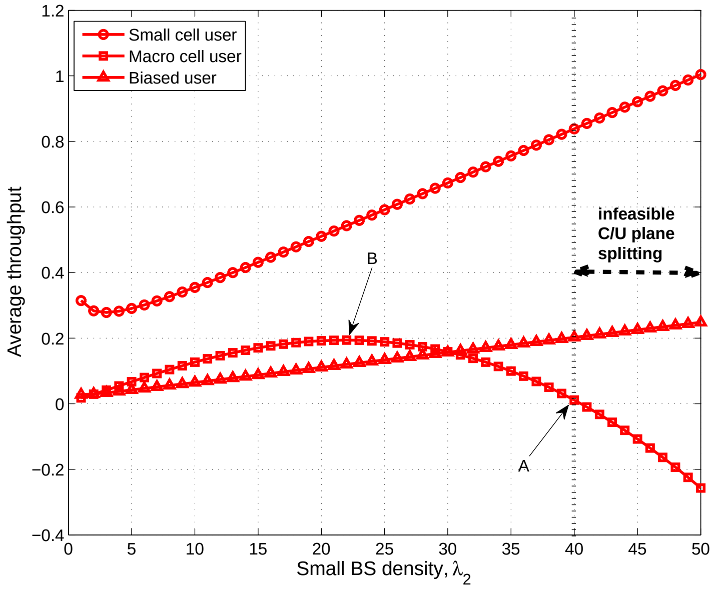

Figure 5.8: Average throughput of small cell, macro cell and biased devices as a function of small cell density ($\mathcal{V} = 0$, $\gamma = 3$ and $B = 30$)

tradeoff can be used to optimize the biasing factor such that the macrocell devices rate is maximized.

## 5.7 Chapter Summary

We present a novel mobility-aware analytical paradigm for CP/UP split RAN network architecture with flexible device association. We derive tractable mathematical expressions for coverage probability and device throughput, which can be reduced to closed-form expressions in special cases. The analysis takes into account the control signaling overhead, spectrum allocation schemes, interference coordination via almost blank subframes, the availability of X2 interface between BSs, and delay incurred by handovers. We then use the developed model to quantify the performance gains offered by the CP/UP split RAN network architecture. In particular, we quantify the impacts of handover delay and mobility speed on the device throughput. We also examine the effects of small cell density, control reduction factor, and core network delay on the device throughput.

The developed model shows that the handovers impose a fundamental limit on the performance gain that can be obtained via densification. In moderate and high mobility profiles, the CP/UP split network architecture offers a potential solution to reduce the control overload and mitigate the handover delay, and hence, improve the network densification gain in networks with low availability of direct X2 interface between BSs. It is also crucial to know the optimal small cell density for a specific network configuration in order to balance the trade-off between the offloading of device data traffic away from MBSs and control signaling towards MBSs in order to maximize the network throughput.

# Chapter 6

# Conclusion and Future Research Directions

## 6.1 Conclusion

Providing large-scale IoT networks with reliable, scalable, and reduced delay is the key requirement for realizing a widely connected networked society. The objective of this dissertation is to model and analyze the performance of large-scale heterogeneous two-tier IoT cellular networks, and offer design insights to maximize their performance. Our research in this dissertation contributes towards that goal. Following are summaries of our contributions.

### 6.1.1 Data Rate Utility Analysis for Uplink Two-Tier IoT Networks

Our first contribution is the design, implementation, and evaluation of a novel analytical model to estimate the mean uplink device data rate utility function under both spectrum allocation schemes, full spectrum reuse (FSR) and orthogonal spectrum partition (OSP), for uplink two-hop IoT networks. The model takes into account the aggregator spatial density, aggregator association bias and spectrum partition ratio across the MBS tier and the aggregator tier, and device and aggregator power control fractionals (PCFs). We develop constraint gradient ascent optimization algorithms to obtain the optimal aggregator association bias (for the FSR scheme) and the optimal joint spectrum partition ratio and optimal aggregator association bias (for the OSP scheme). Then, we confirm the accuracy of the computed optimal values using simulations. We then use the propose model and obtain optimal values to quantify the performance gains offered by the proposed optimized FSR and OSP schemes, in comparison with benchmark schemes such as the minimum-distance based association scheme and the maximum-SIR based association scheme.

The optimized FSR and OSP schemes always outperform the benchmark schemes in terms of the cumulative distribution function (CDF) of the uplink device data rate. The optimized schemes reduce interference from devices by controlling two critical network parameters: the aggregator association bias and the spectrum partition ratio across the MBS tier and the aggregator tier. The former parameter controls the offloading of devices from being served by MBSs to being served by aggregators situated closer to their locations. The offloading allows devices to lower their transmission power, which reduces interference and thus improves the overall uplink data rate. The latter parameter serves as a load balancing mechanism between the MBS tier and the aggregator tier, which enhances the uplink data rate.

### 6.1.2 The Meta Distributions of the SIR/SNR and Data Rate in Coexisting Sub-6GHz and Millimeter-wave IoT Cellular Networks

Our second contribution is the characterization of the meta distributions of the SIR/SNR and data rate of a typical device in a hybrid spectrum IoT network and $\mu$wave-only IoT network. The meta distributions are evaluated first by formulating and then characterizing the moments of the CSP of a typical device in the hybrid IoT network. Important performance metrics such as the mean local delay, coverage probability, network jitter, and variance of the CSP (or reliability) are studied. Numerical results demonstrate the significance of the meta distribution, which needs a systematic evaluation of the generalized moment of order $b$ that helps in evaluating network metrics such as coverage probability when $b = 1$, mean local delay when $b = -1$, and network jitter using $b = -2$ and $b = -1$. Numerical results provide valuable insights related to the reliability and latency of hybrid spectrum IoT networks and $\mu$wave-only IoT networks. These insights help IoT cellular network operators to find the most efficient operating antenna configurations to achieve specific reliability for specific IoT applications.

### 6.1.3 Mobility-Aware Modeling and Analysis of Dense Cellular Networks with C-plane/U-plane Split Architecture

The third contribution is the design, implementation, and evaluation of a novel tractable mobility-aware model for a two-tier downlink cellular network with high-density deployments of small cells and a C-plane/U-plane split architecture. We propose to split the control plane (C-plane) and user plane (U- plane) as a potential solution to harvest densification gain in heterogeneous two-tier networks while minimizing the handover rate and network control overhead. We derive tractable mathematical expressions for coverage probability and device throughput, which can be reduced to closed-form expressions in special cases. The analysis takes into account the control signaling overhead, spectrum allocation schemes, interference coordination via almost blank subframes, the availability of X2 interface between BSs, and delay incurred by handovers. We then use the developed model to quantify the performance gains offered by the CP/UP split RAN network architecture. In particular, we quantify the impacts of the handover delay and mobility speed on the device throughput. We also examine the effects of the small cell density, control reduction factor, and core network delay on the device throughput.

The developed model shows that the handovers impose a fundamental limit on the performance gain that can be obtained via densification. In moderate and high mobility profiles, the CP/UP split network architecture offers a potential solution to reduce the control overload and mitigate the handover delay, and hence, improve the network densification gain in networks with low availability of direct X2 interface between BSs. It is also crucial to know the optimal small cell density for a specific network configuration in order to balance the trade-off between the offloading of device data traffic away from MBSs and the amount of control signaling towards MBSs in order to maximize the network throughput.

## 6.2 Future Research Directions

In this thesis, we have addressed several key challenges for heterogenous cellular networks in serving IoT communications. In order to successfully deploy IoT networks on a global scale, several other aspects and research topics have to be investigated. We plan to study the following open research problems:

1. Millimeter wave and massive multiple-input and multiple-output communication: 5G networks are also likely to include massive multiple-input and multiple-output (MIMO) and mm-wave technologies. Massive MIMO is expected to be incorporated in base stations, where each BS is equipped with a very large number of service antennas (e.g., hundreds or thousands) and utilizes these to communicate with single-antenna devices [146]. The mm-wave spectrum brings extremely high frequency spectrum bands which will be utilized for communication (i.e., 30 GHz to 300 GHz) [147] and it has potentially broader applications in heterogeneous networks. The consideration of these two technologies in conjunction with smart devices can be subjects of future work.

2. Consideration of other point processes: In this thesis, we used the Poisson point process to model the IoT networks, since the independence assumption for the location results in the analytical tractability. For other certain IoT networks, the node distribution is not exactly spatially random. Instead it can be either clustered or more regular distributed [148]. For example, when devices are concentrated around SBS, the clustered

point process is a better model [148]. Under the carrier sense multiple access type MAC scheme, since there is a minimum distance imposed between the transmitters, the hard-core process is more suitable [148]. Therefore, it is interesting to develop models to investigate the performance of future IoT networks with such clustered or regular point processes.

3. Device to device (D2D) in millimeter waves: Using millimeter waves for D2D communications is an interesting topic to research. The short range nature of mm-wave communication is very suitable for D2D communications. The narrow beams and beamforming characterizing mm-wave would reduce the interference effect between D2D and cellular communications. This interference reduction could result in networks where coordination between D2D and cellular communications is not necessary. A study using stochastic geometry tool on the advantages and disadvantages of using mm-wave for D2D communications would be valuable and intersting.

# Appendix A

# Derivations and Proofs in Chapter 3

## A.1 Proof of Lemma 1

We derive the mean logarithm of the uplink coverage probability $\mathbb{E}[\log(C_{\mathcal{D},k})]$ of a typical device located at $\mathbf{x}_{k,0}$ and measured at the tagged node. Let $(k,0)$ denote a tagged node (aggregator or MBS) or a typical device. In order to compute $C_{\mathcal{D},k}$, we have to compute $SIR_{\mathcal{D},k}$. We assume that the tagged node is located at the origin by redefining the coordinates. Let $d_{\mathcal{D},2}$ ($d_{\mathcal{D},1}$) denote the distance between a typical device to its tagged aggregator (MBS) in tier 2 (tier 1). Let $D_{j,i} = \|\mathbf{x}_{j,i} - 0\|$ denote the distance between an interfering device (located at $\mathbf{x}_{j,i}$) and the tagged node located at the origin (0,0). Let $I_\Psi$ denote the total interference from the set of devices $\mathbf{\Phi}_{\mathcal{D}}^{j}$ scheduled by the $j^{th}$ tier excluding the typical device. Then $I_\Psi$ is calculated as follows:

$$I_\Psi = \sum_{j=1}^{2} \sum_{i:\mathbf{x}_{j,i} \in \mathbf{\Phi}_{\mathcal{D}}^{j} \setminus \mathbf{x}_{k,0}} P_{\mathcal{D}} R_{j,i}^{\epsilon_1 \alpha} D_{j,i}^{-\alpha} h(\mathbf{x}_{j,i}, 0). \tag{A.1}$$

From Eq (1), given that a typical device is associated with the $k^{th}$ tier, the distance between the interferer devices and their serving nodes $R_{j,i}$ and the distance between interfering devices and the tagged MBS $D_{j,i}$ have the following inequality

$$R_{j,i} < (\hat{P}_{jk}\hat{B}_{jk})^{\frac{1}{\alpha}} D_{j,i}, \qquad \forall (j,i) \neq (k,0). \tag{A.2}$$

Therefore, the $SIR_{\mathcal{D},k}$ of a typical device associated with the $k^{th}$ tier is

$$SIR_{\mathcal{D},k} = \frac{P_{\mathcal{D}} d_{\mathcal{D},k}^{(\epsilon_1-1)\alpha} h(d_{\mathcal{D},k},0)}{I_{\Psi}}. \tag{A.3}$$

By averaging over the locations of the tagged aggregator (or MBS) and interfering devices, the locations of aggregators and MBSs, and the interference channel, we obtain the mean logarithm of the coverage probability as follows:

$$\begin{aligned}
\mathbb{E}_{\mathbf{\Phi}_1^0,\mathbf{\Phi}_2^0,\mathbf{\Phi}_{\mathcal{D}}^0,\Psi,d_{\mathcal{D},k},h}[\log(C_{\mathcal{D},k})] &= \mathbb{E}_{\mathbf{\Phi}_1^0,\mathbf{\Phi}_2^0,\mathbf{\Phi}_{\mathcal{D}}^0,\Psi,d_{\mathcal{D},k},h}[\log(\mathbb{P}[SIR_{\mathcal{D},k} > \tau_k])], \\
&= \mathbb{E}_{\mathbf{\Phi}_1^0,\mathbf{\Phi}_2^0,\mathbf{\Phi}_{\mathcal{D}}^0,\Psi,d_{\mathcal{D},k},h}[\log(\mathbb{P}[h(d_{\mathcal{D},k},0) > \tau_k P_{\mathcal{D}}^{-1} d_{\mathcal{D},k}^{(1-\epsilon_1)\alpha} I_{\Psi}])], \\
&\overset{(a)}{=} \mathbb{E}_{\mathbf{\Phi}_1^0,\mathbf{\Phi}_2^0,\mathbf{\Phi}_{\mathcal{D}}^0,\Psi,d_{\mathcal{D},k},h}[\log\left(\exp[-\tau_k P_{\mathcal{D}}^{-1} d_{\mathcal{D},k}^{(1-\epsilon_1)\alpha} I_{\Psi}]\right)], \\
&\overset{(b)}{\approx} -\tau_k P_{\mathcal{D}}^{-1} \mathbb{E}_{d_{\mathcal{D},k}}\left(d_{\mathcal{D},k}^{(1-\epsilon_1)\alpha}\right) \mathbb{E}_{\mathbf{\Phi}_1^0,\mathbf{\Phi}_2^0,\mathbf{\Phi}_{\mathcal{D}}^0,\Psi,h}\left(I_{\Psi}\right),
\end{aligned} \tag{A.4}$$

where $(a)$ follows from $h(d_{\mathcal{D},k},0) \sim \exp(1)$ and $(b)$ follows from ignoring the dependency between the distance $d_{\mathcal{D},k}$ between the typical device and the tagged aggregator or MBS and the uplink interference $I_{\Psi}$ for analytical tractability of the system model with minimal impact on the accuracy of the results [77]. This means that $\mathbb{E}_{\mathbf{\Phi}_1^0,\mathbf{\Phi}_2^0,\mathbf{\Phi}_{\mathcal{D}}^0,\Psi,d_{\mathcal{D},k},h}\left(d_{\mathcal{D},k}^{(1-\epsilon_1)\alpha} I_{\Psi}\right) \approx \mathbb{E}_{d_{\mathcal{D},k}}\left(d_{\mathcal{D},k}^{(1-\epsilon_1)\alpha}\right) \mathbb{E}_{\mathbf{\Phi}_1^0,\mathbf{\Phi}_2^0,\mathbf{\Phi}_{\mathcal{D}}^0,\Psi,h}\left(I_{\Psi}\right)$. Since the PDF of the distance $d_{\mathcal{D},k}$ between the typical device and its tagged node (aggregator or MBS) is given in Eq. (3.3), the first expectation in Eq. (A.4) can be evaluated as follows:

$$\begin{aligned}
\mathbb{E}_{d_{\mathcal{D},k}}\left(d_{\mathcal{D},k}^{(1-\epsilon_1)\alpha}\right) &= \frac{2\pi\lambda_k}{\mathcal{A}_k} \int_0^{\infty} r^{1+(1-\epsilon_1)\alpha} e^{\left(\frac{-\pi r^2 \lambda_k}{\mathcal{A}_k}\right)} dr \\
&\overset{(a)}{=} 2\left(\frac{\pi\lambda_k}{\mathcal{A}_k}\right)^{(\epsilon_1-1)\frac{\alpha}{2}} \int_0^{\infty} t^{1+(1-\epsilon_1)\alpha} e^{-t^2} dt, \\
&\overset{(b)}{=} 2\left(\frac{\pi\lambda_k}{\mathcal{A}_k}\right)^{(\epsilon_1-1)\frac{\alpha}{2}} \Theta(\alpha,\epsilon_1),
\end{aligned} \tag{A.5}$$

where $(a)$ follows by making changes to variable as follows. Let $t = r\sqrt{\frac{\pi\lambda_k}{\mathcal{A}_k}}$; then $dt = \sqrt{\frac{\pi\lambda_k}{\mathcal{A}_k}} dr$, $r = 0 \rightarrow t = 0, r = \infty \rightarrow t = \infty$ and $(b)$ follows from using the definition of the Gamma function $\Gamma(x) = 2\int_0^{\infty} t^{2x-1} e^{-t^2} dt$ and the assumption that $\Theta(\alpha,\epsilon_1) \triangleq \int_0^{\infty} t^{1+(1-\epsilon_1)\alpha} e^{-t^2} dt = \frac{1}{2}\Gamma\left[1 + \frac{(1-\epsilon_1)\alpha}{2}\right]$. The uplink mean interference for a typical device is as follows:

$$\begin{aligned}
\mathbb{E}_{\mathbf{\Phi}_1^0,\mathbf{\Phi}_2^0,\mathbf{\Phi}_{\mathcal{D}}^0,\Psi,h}\left(I_\Psi\right) &= P_{\mathcal{D}}\sum_{j=1}^{2}\mathbb{E}_{\mathbf{\Phi}_{\mathcal{D}}^j,\mathbf{\Phi_j}}\left(\sum_{i:\mathbf{x}_{j,i}\in\mathbf{\Phi}_{\mathcal{D}}^j\setminus\mathbf{x}_{k,0}} R_{j,i}^{\epsilon_1\alpha}D_{j,i}^{-\alpha}\right), \\
&= P_{\mathcal{D}}\sum_{j=1}^{2}\mathbb{E}_{\mathbf{\Phi}_{\mathcal{D}}^j,\mathbf{\Phi_j}}\left(\sum_{i:\mathbf{x}_{j,i}\in\mathbf{\Phi}_{\mathcal{D}}^j} R_{j,i}^{\epsilon_1\alpha}D_{j,i}^{-\alpha}\mathbb{1}(\mathbf{x}_{j,i}\neq\mathbf{x}_{k,0})\right), \\
&\overset{(a)}{=} P_{\mathcal{D}}\sum_{j=1}^{2}2\pi\lambda_j\int_0^\infty \mathbb{E}_{R_{j,i}}\left\{R_{j,i}^{\epsilon_1\alpha}\mathbb{1}(\mathbf{x}_{j,i}\neq\mathbf{x}_{k,0})\;\middle|\; D_{j,i}=x\right\}x^{-\alpha}xdx, \\
&\overset{(b)}{=} 2\pi P_{\mathcal{D}}\sum_{j=1}^{2}\lambda_j\int_0^\infty \mathbb{E}_{R_{j,i}}\left\{R_{j,i}^{\epsilon_1\alpha}\mathbb{1}\big[R_{j,i}<x(\hat{P}_{jk}\hat{B}_{jk})^{\frac{1}{\alpha}}\big]\right\}x^{1-\alpha}dx, \qquad \text{(A.6)}
\end{aligned}$$

where $(a)$ follows from Campbell's theorem[1] and that the density of $\mathbf{\Phi}_{\mathcal{D}}^j$ is the same as the density of the tagged node $\mathbf{\Phi}_j$, $(b)$ follows from the inequality in Eq. (A.2). It is worth mentioning that, the integral at $(a)$ starts from zero since the interfering device could be located close to the tagged node.

The PDF of $R_{j,i}$ follows the same distribution as $f_{d_{\mathcal{D},k}}$ as in Eq. (3.3) by changing the index from $k$ to $j$ as follows:

$$f_{R_{j,i}}(r) = \frac{2\pi r\lambda_j}{\mathcal{A}_j}\exp\left(\frac{-\pi r^2\lambda_j}{\mathcal{A}_j}\right), \quad r\geq 0. \qquad \text{(A.7)}$$

By substituting Eq. (A.7) into (A.6), we find that:

$$\begin{aligned}
\mathbb{E}_{\mathbf{\Phi}_1^0,\mathbf{\Phi}_2^0,\mathbf{\Phi}_{\mathcal{D}}^0,\Psi,h}\left(I_\Psi\right) &= 4\pi^2 P_{\mathcal{D}}\sum_{j=1}^{2}\left(\frac{\lambda_j^2}{\mathcal{A}_j}\int_0^\infty x^{1-\alpha}\int_0^{x(\hat{P}_{jk}\hat{B}_{jk})^{\frac{1}{\alpha}}} r^{1+\epsilon_1\alpha}e^{\left(\frac{-\pi r^2\lambda_j}{\mathcal{A}_j}\right)}drdx\right) \\
&\overset{(a)}{=} 4\pi P_{\mathcal{D}}\sum_{j=1}^{2}\left(\lambda_j\left(\frac{\mathcal{A}_j}{\pi\lambda_j}\right)^{\frac{\epsilon_1\alpha}{2}}\int_0^\infty x^{1-\alpha}\int_0^{x(\hat{P}_{jk}\hat{B}_{jk})^{\frac{1}{\alpha}}\sqrt{\frac{\pi\lambda_j}{\mathcal{A}_j}}} u^{1+\epsilon_1\alpha}e^{-u^2}dudx\right), \\
&\overset{(b)}{=} 4\pi P_{\mathcal{D}}\left(\frac{\mathcal{A}_k}{\pi\lambda_k}\right)^{\frac{\epsilon_1\alpha}{2}}\sum_{j=1}^{2}\left(\lambda_j(\hat{P}_{jk}\hat{B}_{jk})^{\epsilon_1}\int_0^\infty x^{1-\alpha}\int_0^{x\sqrt{\frac{\pi\lambda_k}{\mathcal{A}_k}}} u^{1+\epsilon_1\alpha}e^{-u^2}dudx\right), \\
&\overset{(c)}{=} 4\pi P_{\mathcal{D}}\left(\frac{\mathcal{A}_k}{\pi\lambda_k}\right)^{1+\frac{\alpha}{2}(\epsilon_1-1)}\sum_{j=1}^{2}\left(\lambda_j(\hat{P}_{jk}\hat{B}_{jk})^{\epsilon_1}\int_0^\infty v^{1-\alpha}\int_0^{v} u^{1+\epsilon_1\alpha}e^{-u^2}dudv\right),
\end{aligned}$$

---

[1] Campbell's theorem is used to compute the expectation of a sum of a function of random variables over a point process as an integral. It states that $\mathbb{E}[F]=\mathbb{E}\left[\sum_{X_i\in\phi}f(X_i)\right]=\int_{\mathbb{R}^d}\lambda f(x)dx$ [149].

$$\overset{(d)}{=} 4\pi P_{\mathcal{D}} \left(\frac{\mathcal{A}_k}{\pi\lambda_k}\right)^{1+\frac{\alpha}{2}(\epsilon_1-1)} G(\alpha,\epsilon_1) \sum_{j=1}^{2} \left(\lambda_j (\hat{P}_{jk}\hat{B}_{jk})^{\epsilon_1}\right), \tag{A.8}$$

where $(a)$ follows from the changes of variables as follows. Let $u = r\sqrt{\frac{\pi\lambda_j}{\mathcal{A}_j}}$; then $r = 0 \rightarrow u = 0, r = x(\hat{P}_{jk}\hat{B}_{jk})^{\frac{1}{\alpha}} \rightarrow u = x(\hat{P}_{jk}\hat{B}_{jk})^{\frac{1}{\alpha}}\sqrt{\frac{\pi\lambda_j}{\mathcal{A}_j}}$, and $(b)$ follows from Eq. (2) where $\hat{\mathcal{A}}_{jk} = \hat{\lambda}_{jk}(\hat{P}_{jk}\hat{B}_{jk})^{\frac{2}{\alpha}}$ can be represented as

$$\frac{\mathcal{A}_j}{\lambda_j} = \frac{\mathcal{A}_k}{\lambda_k}(\hat{P}_{jk}\hat{B}_{jk})^{2/\alpha}. \tag{A.9}$$

In Eq. (A.8), $(c)$ follows from a change of variables $v = x\sqrt{\frac{\pi\lambda_k}{\mathcal{A}_k}}$, and $(d)$ follows from the definition of $G(\alpha,\epsilon_1)$ as follows:

$$\begin{aligned} G(\alpha,\epsilon_1) &\triangleq \int_0^\infty v^{1-\alpha} \int_0^v u^{1+\epsilon_1\alpha} e^{-u^2} du dv, \\ &\overset{(a)}{=} \int_0^\infty u^{1+\epsilon_1\alpha} e^{-u^2} \int_u^\infty v^{1-\alpha} dv du = \frac{\int_0^\infty u^{\alpha(\epsilon_1-1)+3} e^{-u^2} du}{\alpha-2}, \\ &\overset{(b)}{=} \frac{\Gamma\left[\frac{\alpha}{2}(\epsilon_1-1)+2\right]}{2(\alpha-2)}, \end{aligned} \tag{A.10}$$

where $(a)$ follows from changing the order of integration and $(b)$ follows from the Gamma function definition $\Gamma(x) = 2\int_0^\infty t^{2x-1}e^{-t^2}dt$. Note that in order to have a converge integral for the uplink mean interference of a typical device, the parameter $\frac{\alpha}{2}(\epsilon_1-1)+2$ of the Gamma function has to be positive. Thus, the device PCF $\epsilon_1$ must satisfy this condition as follows $\epsilon_1 > \frac{\alpha-4}{\alpha}$ and $0 \leq \epsilon_1 \leq 1$: When $\epsilon_1 \leq \frac{\alpha-4}{\alpha}$, the uplink mean interference is unbounded, and this may happen if the interfering devices are arbitrarily close to the tagged MBS.

By substituting Eq. (A.5) and Eq. (A.8) into Eq. (A.4), we get

$$\begin{aligned} \mathbb{E}_{\mathbf{\Phi}_1^0,\mathbf{\Phi}_2^0,\mathbf{\Phi}_{\mathcal{D}}^0,\Psi,d_{\mathcal{D},k},h}[\log(C_{\mathcal{D},k})] &\approx -8\tau_k \frac{\mathcal{A}_k}{\lambda_k}\Theta(\alpha,\epsilon_1)G(\alpha,\epsilon_1)\sum_{j=1}^{2}\lambda_j(\hat{P}_{jk}\hat{B}_{jk})^{\epsilon_1}, \\ &\overset{(a)}{=} -8\tau_k Q(\alpha,\epsilon_1)\sum_{j=1}^{2}\mathcal{A}_j(\hat{P}_{jk}\hat{B}_{jk})^{\epsilon_1-\frac{2}{\alpha}}, \end{aligned} \tag{A.11}$$

where $(a)$ follows from Eq. (A.9) and by defining $Q(\alpha,\epsilon_1) \triangleq G(\alpha,\epsilon_1)\Theta(\alpha,\epsilon_1)$. ■

## A.2 Proof of Lemma 2

We derive the mean logarithm of the uplink coverage probability of a typical aggregator located at $\mathbf{y}'_{2,0}$. We assume that a typical aggregator is associated with its tagged MBS in tier-1 which is located at $\mathbf{y}_{1,0} = 0$. Let $d_{2,1} = \|\mathbf{y}'_{2,0} - \mathbf{y}_{1,0}\|$ denote the distance between a typical aggregator to its tagged MBS in tier-1. Let $I_{2,1}$ denote the interference received at the tagged MBS on a given allocated spectrum resource block from the set of aggregators $\mathbf{\Phi}_{\mathcal{A}}$ scheduled by tier-1 excluding the typical aggregator

$$I_{2,1} = \sum_{i:\mathbf{y}'_{2,i}\in\mathbf{\Phi}_{\mathcal{A}}\setminus\mathbf{y}'_{2,0}} P_{\mathcal{A}} R'^{\epsilon_2\alpha}_{2,i} D'^{-\alpha}_{2,i} h(\mathbf{y}'_{2,i}, 0). \tag{A.12}$$

Let $I_{\mathcal{D},1}$ denote the interference received at the tagged MBS of the typical aggregator in a given allocated spectrum resource block from the set of devices $\mathbf{\Phi}^1_{\mathcal{D}}$ scheduled by tier-1. Then $I_{\mathcal{D},1}$ is calculated as follows:

$$I_{\mathcal{D},1} = \sum_{i:\mathbf{x}_{1,i}\in\mathbf{\Phi}^1_{\mathcal{D}}\setminus\mathbf{x}_{1,0}} P_{\mathcal{D}} R^{\epsilon_1\alpha}_{1,i} D^{-\alpha}_{1,i} h(\mathbf{x}_{1,i}, 0), \tag{A.13}$$

where $D_{1,i} = \|\mathbf{x}_{1,i} - 0\|$ is the distance between an interfering device (located at $\mathbf{x}_{1,i}$) and the tagged MBS which is located at the origin $(0, 0)$, and $R_{1,i} = \|\mathbf{y}_{1,i} - \mathbf{x}_{1,i}\|$ is the distance between the interfering device located at $\mathbf{x}_{1,i}$ and its serving MBS located at $\mathbf{y}_{1,i}$. Let $I_{\Psi'} = I_{2,1} + I_{\mathcal{D},1}$ denote the total interference from the set of aggregators and devices scheduled by tier-1 MBSs excluding the typical aggregator. Therefore, the $SIR_{2,1}$ of a typical aggregator associated with the tagged MBS in tier-1 can be calculated as follows:

$$SIR_{2,1} = \frac{P_{\mathcal{A}} d_{2,1}^{(\epsilon_2-1)\alpha} h(\mathbf{y}'_{2,0}, 0)}{I_{\Psi'}}. \tag{A.14}$$

The mean logarithm of the coverage probability as follows:

$$\begin{aligned}
\mathbb{E}_{\mathbf{\Phi}^0_1,\mathbf{\Phi}^0_2,\mathbf{\Phi}^0_{\mathcal{D}},\Psi,d_{2,1},h}[\log(C_{2,1})] &= \mathbb{E}_{\mathbf{\Phi}^0_1,\mathbf{\Phi}^0_2,\mathbf{\Phi}^0_{\mathcal{D}},\Psi,d_{2,1},h}[\log(\mathbb{P}[SIR_{2,1} > \tau_1])],\\
&= \mathbb{E}_{\mathbf{\Phi}^0_1,\mathbf{\Phi}^0_2,\mathbf{\Phi}^0_{\mathcal{D}},\Psi,d_{2,1},h}[\log(\mathbb{P}[h(\mathbf{y}'_{2,0}, 0) > \tau_1 P_{\mathcal{A}}^{-1} d_{2,1}^{(1-\epsilon_2)\alpha} I_{\Psi'}])],\\
&\overset{(a)}{=} \mathbb{E}_{\mathbf{\Phi}^0_1,\mathbf{\Phi}^0_2,\mathbf{\Phi}^0_{\mathcal{D}},\Psi,d_{2,1},h}[\log\left(\exp[-\tau_1 P_{\mathcal{A}}^{-1} d_{2,1}^{(1-\epsilon_2)\alpha} I_{\Psi'}]\right)],
\end{aligned}$$

$$\overset{(b)}{\approx} -\tau_1 P_{\mathcal{A}}^{-1} \mathbb{E}_{d_{2,1}} \left( d_{2,1}^{(1-\epsilon_2)\alpha} \right) \mathbb{E}_{\boldsymbol{\Phi}_1^0,\boldsymbol{\Phi}_2^0,\boldsymbol{\Phi}_{\mathcal{D}}^0,\Psi,h} \left( I_{\Psi'} \right), \tag{A.15}$$

where $(a)$ follows from $h(\mathbf{y}'_{2,0}, 0) \sim \exp(1)$, and $(b)$ follows from ignoring the dependency between the distance between the typical aggregator and the tagged MBS $d_{2,1}$ and the uplink interference $I_{\Psi'}$ for analytical tractability [77]. This means that $\mathbb{E}_{\boldsymbol{\Phi}_1^0,\boldsymbol{\Phi}_2^0,\boldsymbol{\Phi}_{\mathcal{D}}^0,\Psi,d_{2,1},h} \left( d_{2,1}^{(1-\epsilon_2)\alpha} I_{\Psi'} \right) \approx \mathbb{E}_{d_{2,1}} \left( d_{2,1}^{(1-\epsilon_2)\alpha} \right) \mathbb{E}_{\boldsymbol{\Phi}_1^0,\boldsymbol{\Phi}_2^0,\boldsymbol{\Phi}_{\mathcal{D}}^0,\Psi,h} \left( I_{\Psi'} \right)$.Since the PDF of the distance $d_{2,1}$ between the typical aggregator and its tagged MBS in tier-1 [54] is

$$f_{d_{2,1}} = 2\pi\lambda_1 r e^{-\lambda_1 \pi r^2}, \tag{A.16}$$

the first expectation in Eq. (A.15) can be evaluated as follows:

$$\begin{aligned}
\mathbb{E}_{d_{2,1}} \left( d_{2,1}^{(1-\epsilon_2)\alpha} \right) &= 2\pi\lambda_1 \int_0^\infty r^{1+(1-\epsilon_2)\alpha} e^{-\pi r^2 \lambda_1} dr, \\
&\overset{(a)}{=} 2\left(\pi\lambda_1\right)^{(\epsilon_2-1)\frac{\alpha}{2}} \int_0^\infty t^{1+(1-\epsilon_2)\alpha} e^{-t^2} dt, \\
&\overset{(b)}{=} 2\left(\pi\lambda_1\right)^{(\epsilon_2-1)\frac{\alpha}{2}} \Theta(\alpha, \epsilon_2),
\end{aligned} \tag{A.17}$$

where $(a)$ follows by making changes to variables as follows. Let $t = r\sqrt{\pi\lambda_1}$ , then $dt = \sqrt{\pi\lambda_1} dr$, $r = 0 \rightarrow t = 0, r = \infty \rightarrow t = \infty$ and $(b)$ follows from using the definition of the Gamma function $\Gamma(x) = 2\int_0^\infty t^{2x-1} e^{-t^2} dt$ and the assumption of $\Theta(\alpha, \epsilon_2) \triangleq \int_0^\infty t^{1+(1-\epsilon_2)\alpha} e^{-t^2} dt = \frac{1}{2}\Gamma\left[1 + \frac{(1-\epsilon_2)\alpha}{2}\right]$.

The uplink mean interference for a typical aggregator is as follows:

$$\mathbb{E}_{\boldsymbol{\Phi}_1^0,\boldsymbol{\Phi}_2^0,\boldsymbol{\Phi}_{\mathcal{D}}^0,\Psi,h} \left( I_{\Psi'} \right) = \mathbb{E}_{\boldsymbol{\Phi}_1^0,\boldsymbol{\Phi}_2^0,\boldsymbol{\Phi}_{\mathcal{D}}^0,\Psi,h} \left( I_{2,1} + I_{\mathcal{D},1} \right) = \mathbb{E}_{\boldsymbol{\Phi}_1^0,\boldsymbol{\Phi}_2^0,\boldsymbol{\Phi}_{\mathcal{D}}^0,\Psi,h} \left( I_{2,1} \right) + \mathbb{E}_{\boldsymbol{\Phi}_1^0,\boldsymbol{\Phi}_2^0,\boldsymbol{\Phi}_{\mathcal{D}}^0,\Psi,h} \left( I_{\mathcal{D},1} \right). \tag{A.18}$$

The uplink mean interference received at the tagged MBS on a given allocated spectrum resource block for a typical aggregator from other scheduled interfering aggregators is as follows:

$$\mathbb{E}_{\boldsymbol{\Phi}_1^0,\boldsymbol{\Phi}_2^0,\boldsymbol{\Phi}_{\mathcal{D}}^0,\Psi,h}(I_{2,1}) = P_{\mathcal{A}} \mathbb{E}_{\boldsymbol{\Phi}_{\mathcal{A}},\boldsymbol{\Phi}_1^0} \left( \sum_{i:\mathbf{y}'_{2,i} \in \boldsymbol{\Phi}_{\mathcal{A}} \setminus \mathbf{y}'_{2,0}} R_{2,i}'^{\epsilon_2\alpha} D_{2,i}'^{-\alpha} \right)$$

$$
\begin{aligned}
&= P_{\mathcal{A}} \mathbb{E}_{\mathbf{\Phi}_{\mathcal{A}}, \mathbf{\Phi}_1^0} \left( \sum_{i: \mathbf{y}'_{2,i} \in \mathbf{\Phi}_{\mathcal{A}}} R'^{\epsilon_2 \alpha}_{2,i} D'^{-\alpha}_{2,i} \mathbb{1}(\mathbf{y}'_{2,i} \neq \mathbf{y}'_{2,0}) \right), \\
&\overset{(a)}{=} 2\pi \lambda_1 P_{\mathcal{A}} \int_0^\infty \mathbb{E}_{R_{2,i}} \left\{ R^{\epsilon_2 \alpha}_{2,i} \mathbb{1}(\mathbf{y}'_{2,i} \neq \mathbf{y}'_{2,0}) \;\middle|\; D'_{2,i} = y \right\} y^{-\alpha} y dy, \\
&\overset{(b)}{=} 2\pi \lambda_1 P_{\mathcal{A}} \int_0^\infty \mathbb{E}_{R_{2,i}} \left\{ R^{\epsilon_2 \alpha}_{2,i} \mathbb{1}\left[ R_{2,i} < y \right] \right\} y^{1-\alpha} dy, \qquad \text{(A.19)}
\end{aligned}
$$

where $(a)$ follows from Campbell's theorem and that the density of $\mathbf{\Phi}_{\mathcal{A}}$ is the same as the density of the MBS $\mathbf{\Phi}_1$, $(b)$ follows from inequality in Eq. (A.2) which is modified for single-tier case[2]. Note that, the integral at $(a)$ starts from zero since the interfering aggregator could be located close to the tagged MBS.

By substituting Eq. (A.16) into Eq. (A.19), we obtain:

$$
\begin{aligned}
\mathbb{E}_{\mathbf{\Phi}_1^0, \mathbf{\Phi}_2^0, \mathbf{\Phi}_{\mathcal{D}}^0, \Psi, h}(I_{2,1}) &= 4\pi^2 \lambda_1^2 P_{\mathcal{A}} \int_0^\infty y^{1-\alpha} \int_0^y r^{\epsilon_2 \alpha + 1} e^{-\lambda_1 \pi r^2} dr dy, \\
&\overset{(a)}{=} 4(\pi \lambda_1)^{1 - \frac{\epsilon_2 \alpha}{2}} P_{\mathcal{A}} \int_0^\infty y^{1-\alpha} \int_0^{y\sqrt{\pi \lambda_1}} u^{\epsilon_2 \alpha + 1} e^{-u^2} du dy, \\
&\overset{(b)}{=} 4(\pi \lambda_1)^{\frac{\alpha}{2}(1-\epsilon_2)} P_{\mathcal{A}} \int_0^\infty v^{1-\alpha} \int_0^v u^{\epsilon_2 \alpha + 1} e^{-u^2} du dv, \\
&\overset{(c)}{=} 4(\pi \lambda_1)^{\frac{\alpha}{2}(1-\epsilon_2)} P_{\mathcal{A}} G(\alpha, \epsilon_2), \qquad \text{(A.20)}
\end{aligned}
$$

where $(a)$ follows from making changes to variables as follows. Let $u = r\sqrt{\pi \lambda_1}$, then $r = 0 \rightarrow u = 0, r = y \rightarrow u = y\sqrt{\pi \lambda_1}$; $(b)$ follows also by making changes to variables $v = y\sqrt{\pi \lambda_1}$; and $(c)$ follows from a similar derivation as in Eq. (A.10).

Similar to the derivation in Eq. (A.8), the uplink mean interference received at the tagged MBS on a given allocated spectrum resource block for a typical aggregator from other scheduled interfering devices is as follows:

$$
\mathbb{E}_{\mathbf{\Phi}_1^0, \mathbf{\Phi}_2^0, \mathbf{\Phi}_{\mathcal{D}}^0, \Psi, h}\left(I_{\mathcal{D},1}\right) = 4\pi P_{\mathcal{D}} \left( \frac{\mathcal{A}_1}{\pi \lambda_1} \right)^{1 + \frac{\alpha}{2}(\epsilon_1 - 1)} \lambda_1 G(\alpha, \epsilon_1). \qquad \text{(A.21)}
$$

---

[2] The distance $R_{2,i}$ between an interfering aggregator and its serving MBS has to be smaller than the distance $D'_{2,i}$ between that interfering aggregator and the tagged MBS. If the opposite happens; i.e., $R_{2,i} > D'_{2,i}$, the tagged MBS will become the serving MBS for that interfering aggregator [149].

By substituting Eq.(A.20) and Eq. (A.21) into Eq. (A.18), we find that:

$$\mathbb{E}_{\mathbf{\Phi}_1^0,\mathbf{\Phi}_2^0,\mathbf{\Phi}_{\mathcal{D}}^0,\Psi,h}\left(I_{\Psi'}\right) = 4(\pi\lambda_1)^{\frac{\alpha}{2}(1-\epsilon_2)}P_{\mathcal{A}}G(\alpha,\epsilon_2)+ \\ 4\pi P_{\mathcal{D}}\left(\frac{\mathcal{A}_1}{\pi\lambda_1}\right)^{1+\frac{\alpha}{2}(\epsilon_1-1)}\lambda_1 G(\alpha,\epsilon_1). \tag{A.22}$$

By substituting Eq. (A.22) and Eq. (A.17) into Eq. (A.15), we obtain the mean logarithm of the coverage probability as follows:

$$\begin{aligned}\mathbb{E}_{\mathbf{\Phi}_1^0,\mathbf{\Phi}_2^0,\mathbf{\Phi}_{\mathcal{D}}^0,\Psi,d_{2,1},h}[\log(C_{2,1})] &\approx -\tau_1 P_{\mathcal{A}}^{-1}\left(2\left(\pi\lambda_1\right)^{(\epsilon_2-1)\frac{\alpha}{2}}\Theta(\alpha,\epsilon_2)\right)\times \\ &\quad \left(4(\pi\lambda_1)^{\frac{\alpha}{2}(1-\epsilon_2)}P_{\mathcal{A}}G(\alpha,\epsilon_2)+4\pi P_{\mathcal{D}}\left(\frac{\mathcal{A}_1}{\pi\lambda_1}\right)^{1+\frac{\alpha}{2}(\epsilon_1-1)}\lambda_1 G(\alpha,\epsilon_1)\right), \\ &\approx -8\tau_1\Theta(\alpha,\epsilon_2)G(\alpha,\epsilon_2)-\tau_1 P_{\mathcal{A}}^{-1}\left(2\left(\pi\lambda_1\right)^{(\epsilon_2-1)\frac{\alpha}{2}}\Theta(\alpha,\epsilon_2)\right)4\pi P_{\mathcal{D}}\left(\frac{\mathcal{A}_1}{\pi\lambda_1}\right)^{1+\frac{\alpha}{2}(\epsilon_1-1)}\lambda_1 G(\alpha,\epsilon_1), \\ &\approx -8\tau_1 Q(\alpha,\epsilon_2)-8\pi P_{\mathcal{D}}\tau_1 P_{\mathcal{A}}^{-1}\lambda_1\left(\pi\lambda_1\right)^{(\epsilon_2-1)\frac{\alpha}{2}}\left(\frac{\mathcal{A}_1}{\pi\lambda_1}\right)^{1+\frac{\alpha}{2}(\epsilon_1-1)}\Theta(\alpha,\epsilon_2)G(\alpha,\epsilon_1).\end{aligned} \tag{A.23}$$

■

## A.3 Proof of Lemma 3

Let $\mathcal{N}_{\mathcal{D},2}$ and $\mathcal{N}_{2,1}$ denote the random variables that represent the number of devices associated with tagged aggregator and the number of aggregators associated with the tagged MBS, respectively. Following [110], the probability mass function (PMF) of the number of devices (including typical device) associated with the tagged aggregator is

$$\mathbb{P}(\mathcal{N}_{\mathcal{D},2}=n+1) \triangleq \frac{3.5^{3.5}\Gamma(n+4.5)(\lambda_{\mathcal{D}}\mathcal{A}_2/\lambda_2)^n}{\Gamma(3.5)n!\left(3.5+\lambda_{\mathcal{D}}\mathcal{A}_2/\lambda_2\right)^{(n+4.5)}}, \tag{A.24}$$

and the PMF of the number of aggregators (including the typical aggregator) associated with the tagged MBS is

$$\mathbb{P}(\mathcal{N}_{2,1}=n+1) \triangleq \frac{3.5^{3.5}\Gamma(n+4.5)(\lambda_2\mathcal{A}_1/\lambda_1)^n}{\Gamma(3.5)n!\left(3.5+\lambda_2\mathcal{A}_1/\lambda_1\right)^{(n+4.5)}}. \tag{A.25}$$

Therefore, the spectrum allocated to a device associated with the tagged aggregator is $\zeta_{\mathcal{D},2}=\frac{W_2}{\mathcal{N}_{\mathcal{D},2}}$ and it is a random variable and a function of $\mathcal{N}_{\mathcal{D},2}$. Similarly, the spectrum allocated to an aggregator associated with the tagged MBS is $\zeta_{2,1} = \frac{W_1}{\mathcal{N}_{2,1}}$ and it is a random variable and a function of $\mathcal{N}_{2,1}$. Therefore, the range of random variable $\mathcal{N}_{\mathcal{D},2}$ is $R_{\mathcal{N}_{\mathcal{D},2}} = \{1, 2, 3, ....\}$ and the range of $\zeta_{\mathcal{D},2}$ is $R_{\zeta_{\mathcal{D},2}} = \{W_2, \frac{W_2}{2}, \frac{W_2}{3}, ....\}$. Thus, the range of $\zeta_{\mathcal{D},2}$ are as follows:

$$\begin{aligned}
\mathbb{P}_{\zeta_{\mathcal{D},2}}(W_2) &= \mathbb{P}(\zeta_{\mathcal{D},2} = W_2) = \mathbb{P}\left(\frac{W_2}{\mathcal{N}_{\mathcal{D},2}} = W_2\right) = \mathbb{P}\left(\mathcal{N}_{\mathcal{D},2} = 1\right), \\
\mathbb{P}_{\zeta_{\mathcal{D},2}}\left(\frac{W_2}{2}\right) &= \mathbb{P}\left(\zeta_{\mathcal{D},2} = \frac{W_2}{2}\right) = \mathbb{P}\left(\frac{W_2}{\mathcal{N}_{\mathcal{D},2}} = \frac{W_2}{2}\right) = \mathbb{P}\left(\mathcal{N}_{\mathcal{D},2} = 2\right), \\
\mathbb{P}_{\zeta_{\mathcal{D},2}}\left(\frac{W_2}{3}\right) &= \mathbb{P}\left(\zeta_{\mathcal{D},2} = \frac{W_2}{3}\right) = \mathbb{P}\left(\frac{W_2}{\mathcal{N}_{\mathcal{D},2}} = \frac{W_2}{3}\right) = \mathbb{P}\left(\mathcal{N}_{\mathcal{D},2} = 3\right), \qquad \text{(A.26)} \\
&\vdots
\end{aligned}$$

Therefore, the PMF of the random variable $\zeta_{\mathcal{D},2}$ is as follows:

$$\mathbb{P}\left(\zeta_{\mathcal{D},2} = \frac{W_2}{n+1}\right) = \frac{3.5^{3.5}\Gamma(n+4.5)(\lambda_{\mathcal{D}}\mathcal{A}_2/\lambda_2)^n}{\Gamma(3.5)n!\,(3.5 + \lambda_{\mathcal{D}}\mathcal{A}_2/\lambda_2)^{(n+4.5)}}. \qquad \text{(A.27)}$$

Similarly, the PMF of the random variable $\zeta_{2,1}$ is as follows:

$$\mathbb{P}\left(\zeta_{2,1} = \frac{W_1}{n+1}\right) = \frac{3.5^{3.5}\Gamma(n+4.5)(\lambda_2\mathcal{A}_1/\lambda_1)^n}{\Gamma(3.5)n!\,(3.5 + \lambda_2\mathcal{A}_1/\lambda_1)^{(n+4.5)}}. \qquad \text{(A.28)}$$

Let $X \triangleq \zeta_{\mathcal{D},2}\log(1+\tau_2)$ and $Z \triangleq \zeta_{2,1}\log(1+\tau_1)$ are random variables and functions of $\zeta_{\mathcal{D},2}$ and $\zeta_{2,1}$, respectively. The range of $\zeta_{\mathcal{D},2}$ is $R_{\zeta_{\mathcal{D},2}} = \{W_2, \frac{W_2}{2}, \frac{W_2}{3}, ....\}$ and the range of $X$ is $R_X = \{W_2\log(1+\tau_2), \frac{W_2}{2}\log(1+\tau_2), \frac{W_2}{3}\log(1+\tau_2), ....\}$. Thus, the range of $X$ are as follows:

$$\begin{aligned}
&\mathbb{P}_X\left(W_2\log(1+\tau_2)\right) = \mathbb{P}\left(X = W_2\log(1+\tau_2)\right) = \mathbb{P}(\zeta_{\mathcal{D},2}\log(1+\tau_2) \\
&= W_2\log(1+\tau_2)) = \mathbb{P}(\zeta_{\mathcal{D},2} = W_2), \\
&\mathbb{P}_X\left(\frac{W_2}{2}\log(1+\tau_2)\right) = \mathbb{P}\left(X = \frac{W_2}{2}\log(1+\tau_2)\right) = \\
&\mathbb{P}\left(\zeta_{\mathcal{D},2}\log(1+\tau_2) = \frac{W_2}{2}\log(1+\tau_2)\right) = \mathbb{P}\left(\zeta_{\mathcal{D},2} = \frac{W_2}{2}\right), \\
&\mathbb{P}_X\left(\frac{W_2}{3}\log(1+\tau_2)\right) = \mathbb{P}\left(X = \frac{W_2}{3}\log(1+\tau_2)\right) = \\
&\mathbb{P}\left(\zeta_{\mathcal{D},2}\log(1+\tau_2) = \frac{W_2}{3}\log(1+\tau_2)\right) = \mathbb{P}\left(\zeta_{\mathcal{D},2} = \frac{W_2}{3}\right), \qquad \text{(A.29)}
\end{aligned}$$

$$\vdots$$

Therefore, the PMF of the random variable $X$ is as follows:

$$\begin{aligned}\mathbb{P}\left(X = \frac{W_2 \log(1+\tau_2)}{n+1}\right) &= \mathbb{P}\left(\mathcal{N}_{\mathcal{D},2} = n+1\right) \\ &= \frac{3.5^{3.5}\Gamma(n+4.5)(\lambda_{\mathcal{D}}\mathcal{A}_2/\lambda_2)^n}{\Gamma(3.5)n!\,(3.5+\lambda_{\mathcal{D}}\mathcal{A}_2/\lambda_2)^{(n+4.5)}}. \end{aligned} \tag{A.30}$$

Similarly, the PMF of the random variable $Z$ is as follows:

$$\begin{aligned}\mathbb{P}\left(Z = \frac{W_1 \log(1+\tau_1)}{n+1}\right) &= \mathbb{P}\left(\mathcal{N}_{2,1} = n+1\right) \\ &= \frac{3.5^{3.5}\Gamma(n+4.5)(\lambda_2\mathcal{A}_1/\lambda_1)^n}{\Gamma(3.5)n!\,(3.5+\lambda_2\mathcal{A}_1/\lambda_1)^{(n+4.5)}}. \end{aligned} \tag{A.31}$$

We assume that $V \triangleq \min[X, Z]$ and $V$ is a random variable too. The CDF of random variable $V$ can be calculated as follows:

$$\begin{aligned}F_V(v) &= \mathbb{P}(V \le v) = \mathbb{P}(\min[X,Z] \le v) = 1 - \mathbb{P}(\min[X,Z] > v) \\ &= 1 - \mathbb{P}(X > v, Z > v) = 1 - (1 - F_X(v))(1 - F_Z(v)). \end{aligned} \tag{A.32}$$

The CDF of random variables $X$ and $Z$ are as follows:

$$\begin{aligned}F_X(v) &= \mathbb{P}\left(X < v\right) = \sum_{a \in R_X, a \le v}^{\infty} P_X(a) = \\ &= \sum_{n: \frac{W_2 \log(1+\tau_2)}{n+1} \le v}^{\infty} \frac{3.5^{3.5}\Gamma(n+4.5)(\lambda_{\mathcal{D}}\mathcal{A}_2/\lambda_2)^n}{\Gamma(3.5)n!\,(3.5+\lambda_{\mathcal{D}}\mathcal{A}_2/\lambda_2)^{(n+4.5)}} \\ &= \sum_{n+1 \ge \frac{W_2 \log(1+\tau_2)}{v}}^{\infty} \frac{3.5^{3.5}\Gamma(n+4.5)(\lambda_{\mathcal{D}}\mathcal{A}_2/\lambda_2)^n}{\Gamma(3.5)n!\,(3.5+\lambda_{\mathcal{D}}\mathcal{A}_2/\lambda_2)^{(n+4.5)}}, \end{aligned} \tag{A.33}$$

$$\begin{aligned}F_Z(v) &= \mathbb{P}\left(Z < v\right) = \sum_{b \in R_Z, b \le v}^{\infty} P_Z(b) = \\ &= \sum_{n: \frac{W_1 \log(1+\tau_1)}{n+1} \le v}^{\infty} \frac{3.5^{3.5}\Gamma(n+4.5)(\lambda_2\mathcal{A}_1/\lambda_1)^n}{\Gamma(3.5)n!\,(3.5+\lambda_2\mathcal{A}_1/\lambda_1)^{(n+4.5)}} \\ &= \sum_{n+1 \ge \frac{W_1 \log(1+\tau_1)}{v}}^{\infty} \frac{3.5^{3.5}\Gamma(n+4.5)(\lambda_2\mathcal{A}_1/\lambda_1)^n}{\Gamma(3.5)n!\,(3.5+\lambda_2\mathcal{A}_1/\lambda_1)^{(n+4.5)}}. \end{aligned} \tag{A.34}$$

Therefore, the logarithm mean of minimum data rate capacity of two-hop data rate is given by

$$\begin{aligned}
&\log\left[\mathbb{E}_{\mathbf{\Phi}_1^0,\mathbf{\Phi}_2^0,\mathbf{\Phi}_{\mathcal{D}}^0,d_{\mathcal{D},2},d_{2,1}}\left[\min\left[\zeta_{\mathcal{D},2}\log(1+\tau_2),\zeta_{2,1}\log(1+\tau_1)\right]\right]\right] \\
&= \log\left[\mathbb{E}_{\mathbf{\Phi}_1^0,\mathbf{\Phi}_2^0\mathbf{\Phi}_{\mathcal{D}}^0,d_{\mathcal{D},2},d_{2,1}}\left[V\right]\right], \\
&\overset{(a)}{=} \log\left[\int_0^{\infty}(1-F(v))dv\right], \\
&= \log\left[\int_0^{\infty}(1-[1-(1-F_X(v))(1-F_Z(v))])dv\right], \\
&= \log\left[\int_0^{\infty}((1-F_X(v))(1-F_Z(v)))dv\right], \\
&= \log\left[\int_0^{\infty}\left(1-\sum_{n\geq\frac{W_2\log(1+\tau_2)}{v}-1}^{\infty}\frac{3.5^{3.5}\Gamma(n+4.5)(\lambda_{\mathcal{D}}\mathcal{A}_2/\lambda_2)^n}{\Gamma(3.5)n!\,(3.5+\lambda_{\mathcal{D}}\mathcal{A}_2/\lambda_2)^{(n+4.5)}}\right)\times\right. \\
&\left.\left(1-\sum_{n\geq\frac{W_1\log(1+\tau_1)}{v}-1}^{\infty}\frac{3.5^{3.5}\Gamma(n+4.5)(\lambda_2\mathcal{A}_1/\lambda_1)^n}{\Gamma(3.5)n!\,(3.5+\lambda_2\mathcal{A}_1/\lambda_1)^{(n+4.5)}}\right)dv\right], \\
&\overset{(b)}{=} \log\left[\int_0^{\infty}\left(\sum_{n=0}^{S_X(v)}g_X(n)\right)\left(\sum_{n=0}^{S_Z(v)}g_Z(n)\right)dv\right] \\
&\triangleq \varphi(v,n,\mathcal{N}_{\mathcal{D},2},\mathcal{N}_{2,1},\zeta_{\mathcal{D},2},\zeta_{2,1},\tau_1,\tau_2),
\end{aligned} \tag{A.35}$$

where $(a)$ follows from finding the mean of a random variable $V$ in terms of its CDF using Fubini's theorem which is as follows:$\mathbb{E}[V]=\int_0^{\infty}(1-F(v))dv-\int_{-\infty}^{0}F(v)dv$ and $F(v)=0$ where $v<0$, (b) follows from the definitions of $g_X(n)\triangleq\frac{3.5^{3.5}\Gamma(n+4.5)(\lambda_{\mathcal{D}}\mathcal{A}_2/\lambda_2)^n}{\Gamma(3.5)n!(3.5+\lambda_{\mathcal{D}}\mathcal{A}_2/\lambda_2)^{(n+4.5)}}$, and $g_Z(n)\triangleq\frac{3.5^{3.5}\Gamma(n+4.5)(\lambda_2\mathcal{A}_1/\lambda_1)^n}{\Gamma(3.5)n!(3.5+\lambda_2\mathcal{A}_1/\lambda_1)^{(n+4.5)}}$, and that $\sum_{n=0}^{\infty}g_X(n)=1$ and $\sum_{n=0}^{\infty}g_Z(n)=1$. Therefore, $S_X(v)\triangleq\left\lfloor\frac{W_2\log(1+\tau_2)}{v}-1\right\rfloor$and $S_Z(v)\triangleq\left\lfloor\frac{W_1\log(1+\tau_1)}{v}-1\right\rfloor$.We define $\varphi(v,n,\mathcal{N}_{\mathcal{D},2},\mathcal{N}_{2,1},\zeta_{\mathcal{D},2},\zeta_{2,1},\tau_1,\tau_2)\triangleq\log\left[\int_0^{\infty}\left(\sum_{n=0}^{S_X(v)}g_X(n)\right)\left(\sum_{n=0}^{S_Z(v)}g_Z(n)\right)dv\right]$. ■

# A.4 Proof of Lemma 4

In this section, we derive the total uplink mean DRUF of devices for the FSR scheme as follows:

### Full Spectrum Reuse

By combining Eq. (3.10) and Eq. (A.11), we get:

$$\begin{aligned}\mathcal{A}_1 U_{\mathcal{D},1} &= \mathcal{A}_1(\mathbb{E}[\log(\zeta_{\mathcal{D},1})] + \mathbb{E}[\log(C_{\mathcal{D},1})] + \log[\log(1+\tau_1)]),\\ &\approx \mathcal{A}_1\left(\log\left(\frac{W\lambda_1}{1.28\lambda_{\mathcal{D}}\mathcal{A}_1+\lambda_1}\right) - 8\tau_1 Q(\alpha,\epsilon_1)\sum_{j=1}^{2}\mathcal{A}_j(\hat{P}_{jk}\hat{B}_{jk})^{\epsilon_1-\frac{2}{\alpha}} + \log[\log(1+\tau_1)]\right),\\ &\approx \mathcal{A}_1\left(\log\left(\frac{W\lambda_1\log(1+\tau_1)}{1.28\lambda_{\mathcal{D}}\mathcal{A}_1+\lambda_1}\right) - 8\tau_1 Q(\alpha,\epsilon_1)\sum_{j=1}^{2}\mathcal{A}_j(\hat{P}_{jk}\hat{B}_{jk})^{\epsilon_1-\frac{2}{\alpha}}\right).\end{aligned} \tag{A.36}$$

By combining Eq. (A.11), Eq. (A.23), and Eq. (A.35) we get:

$$\begin{aligned}&\mathcal{A}_2\min\left(U_{\mathcal{D},2},U_{2,1}\right) = \mathcal{A}_2\mathbb{E}_{\mathbf{\Phi}_1,\mathbf{\Phi}_2,\mathbf{\Phi}_{\mathcal{D}}}\left[\mathbb{E}_h\left[\log[\min(R_{\mathcal{D},2},R_{2,1})]\right]\right],\\ &=\mathcal{A}_2\Bigg(\mathbb{E}_{\mathbf{\Phi}_1^0,\mathbf{\Phi}_2^0,\mathbf{\Phi}_{\mathcal{D}}^0,d_{\mathcal{D},2},d_{2,1}}\left[\log\left\{\mathbb{P}\left(SIR_{\mathcal{D},2}>\tau_2\right)\right\}\right] + \mathbb{E}_{\mathbf{\Phi}_1^0,\mathbf{\Phi}_2^0,\mathbf{\Phi}_{\mathcal{D}}^0,d_{\mathcal{D},2},d_{2,1}}\left[\log\left\{\mathbb{P}\left(SIR_{2,1}>\tau_1\right)\right\}\right] +\\ &\qquad\qquad \log\left\{\mathbb{E}_{\mathbf{\Phi}_1^0,\mathbf{\Phi}_2^0,\mathbf{\Phi}_{\mathcal{D}}^0,d_{\mathcal{D},2},d_{2,1}}\left[\min\left[\zeta_{\mathcal{D},2}\log(1+\tau_2),\zeta_{2,1}\log(1+\tau_1)\right]\right]\right\}\Bigg),\\ &=\mathcal{A}_2\Bigg\{-8\tau_2 Q(\alpha,\epsilon_1)\sum_{j=1}^{2}\mathcal{A}_j(\hat{P}_{jk}\hat{B}_{jk})^{\epsilon_1-\frac{2}{\alpha}} -\\ &\quad \tau_1 P_{\mathcal{A}}^{-1}\left(2\left(\pi\lambda_1\right)^{(\epsilon_2-1)\frac{\alpha}{2}}\Theta(\alpha,\epsilon_2)\right)\times\left(4(\pi\lambda_1)^{\frac{\alpha}{2}(1-\epsilon_2)}P_{\mathcal{A}}G(\alpha,\epsilon_2) + 4\pi P_{\mathcal{D}}\left(\tfrac{\mathcal{A}_1}{\pi\lambda_1}\right)^{1+\frac{\alpha}{2}(\epsilon_1-1)}\lambda_1 G(\alpha,\epsilon_1)\right)\\ &\quad +\varphi(v,n,\mathcal{N}_{\mathcal{D},2},\mathcal{N}_{2,1},\zeta_{\mathcal{D},2},\zeta_{2,1},\tau_1,\tau_2)\Bigg\}.\end{aligned} \tag{A.37}$$

Then, by substituting Eq. (A.36) and Eq. (A.37) into Eq. (3.7), the uplink mean data rate utility is as follows:

$$U =$$

$$\mathcal{A}_1\left(\log\left(\frac{W\lambda_1\log(1+\tau_1)}{1.28\lambda_{\mathcal{D}}\mathcal{A}_1+\lambda_1}\right) - 8\tau_1 Q(\alpha,\epsilon_1)\textstyle\sum_{j=1}^{2}\mathcal{A}_j(\hat{P}_{jk}\hat{B}_{jk})^{\epsilon_1-\frac{2}{\alpha}}\right) - \mathcal{A}_2 8\tau_2 Q(\alpha,\epsilon_1)\displaystyle\sum_{j=1}^{2}\mathcal{A}_j(\hat{P}_{jk}\hat{B}_{jk})^{\epsilon_1-\frac{2}{\alpha}}$$

$$
\begin{aligned}
&- \mathcal{A}_2 \tau_1 P_{\mathcal{A}}^{-1} \left( 2 \left( \pi \lambda_1 \right)^{(\epsilon_2 - 1)\frac{\alpha}{2}} \Theta(\alpha, \epsilon_2) \right) \times \left( 4(\pi\lambda_1)^{\frac{\alpha}{2}(1-\epsilon_2)} P_{\mathcal{A}} G(\alpha, \epsilon_2) + 4\pi P_{\mathcal{D}} \left(\frac{\mathcal{A}_1}{\pi\lambda_1}\right)^{1+\frac{\alpha}{2}(\epsilon_1 - 1)} \lambda_1 G(\alpha, \epsilon_1) \right) \\
&+ \mathcal{A}_2 \varphi(v, n, \mathcal{N}_{\mathcal{D},2}, \mathcal{N}_{2,1}, \zeta_{\mathcal{D},2}, \zeta_{2,1}, \tau_1, \tau_2). \qquad \text{(A.38)}
\end{aligned}
$$

■

## A.5 Proof of Lemma 5

In this section, we derive the total uplink mean DRUF of devices for the OSP scheme as follows:

**Orthogonal Spectrum Partition**

By combining Eq. (3.10) and Eq. (3.14), we get:

$$
\begin{aligned}
\mathcal{A}_1 U_{\mathcal{D},1} &= \mathcal{A}_1 (\mathbb{E}[\log(\zeta_{\mathcal{D},1})] + \mathbb{E}[\log(C_{\mathcal{D},1})] + \log[\log(1+\tau_1)]) \\
&\approx \mathcal{A}_1 \left( \log\left( \frac{W_1 \lambda_1}{1.28 \lambda_{\mathcal{D}} \mathcal{A}_1 + \lambda_1} \right) - 8\tau_1 Q(\alpha, \epsilon_1) \mathcal{A}_1 + \log[\log(1+\tau_1)] \right) \\
&= \mathcal{A}_1 \left( \log\left( \frac{W_1 \lambda_1 \log(1+\tau_1)}{1.28 \lambda_{\mathcal{D}} \mathcal{A}_1 + \lambda_1} \right) - 8\tau_1 Q(\alpha, \epsilon_1) \mathcal{A}_1 \right), \qquad \text{(A.39)}
\end{aligned}
$$

By combining Eq. (3.14), Eq. (3.18) and Eq. (A.35), we get:

$$
\begin{aligned}
&\mathcal{A}_2 \min\left(U_{\mathcal{D},2}, U_{2,1}\right) = \mathcal{A}_2 \mathbb{E}_{\mathbf{\Phi}_1, \mathbf{\Phi}_2, \mathbf{\Phi}_{\mathcal{D}}} \left[ \mathbb{E}_h \left[ \log[\min(R_{\mathcal{D},2}, R_{2,1})] \right] \right] \\
&= \mathcal{A}_2 \Bigg( \mathbb{E}_{\mathbf{\Phi}_1^0, \mathbf{\Phi}_2^0, \mathbf{\Phi}_{\mathcal{D}}^0, d_{\mathcal{D},2}, d_{2,1}} \left[ \log\left\{ \mathbb{P}\left( SIR_{\mathcal{D},2} > \tau_2 \right) \right\} \right] + \mathbb{E}_{\mathbf{\Phi}_1^0, \mathbf{\Phi}_2^0, \mathbf{\Phi}_{\mathcal{D}}^0, d_{\mathcal{D},2}, d_{2,1}} \left[ \log\left\{ \mathbb{P}\left( SIR_{2,1} > \tau_1 \right) \right\} \right] + \\
&\log\left\{ \mathbb{E}_{\mathbf{\Phi}_1^0, \mathbf{\Phi}_2^0, \mathbf{\Phi}_{\mathcal{D}}^0, d_{\mathcal{D},2}, d_{2,1}} \left[ \min\left[ \zeta_{\mathcal{D},2} \log(1+\tau_2), \zeta_{2,1} \log(1+\tau_1) \right] \right] \right\} \Bigg) \\
&= \mathcal{A}_2 \Big( -8\tau_2 Q(\alpha, \epsilon_1) \mathcal{A}_2 - 8\tau_1 Q(\alpha, \epsilon_2) + \varphi(v, n, \mathcal{N}_{\mathcal{D},2}, \mathcal{N}_{2,1}, \zeta_{\mathcal{D},2}, \zeta_{2,1}, \tau_1, \tau_2) \Big) \qquad \text{(A.40)}
\end{aligned}
$$

Then, by substituting Eq. (A.39) and Eq. (A.40) into Eq. (3.7), we get:

$$\begin{aligned}U = \mathcal{A}_1 \left( \log\left( \frac{W_1 \lambda_1 \log(1+\tau_1)}{1.28\lambda_{\mathcal{D}}\mathcal{A}_1 + \lambda_1} \right) - 8\tau_1 Q(\alpha, \epsilon_1)\mathcal{A}_1 \right) + \mathcal{A}_2 \times \\ \left( -8\tau_2 Q(\alpha, \epsilon_1)\mathcal{A}_2 - 8\tau_1 Q(\alpha, \epsilon_2) + \varphi(v, n, \mathcal{N}_{\mathcal{D},2}, \mathcal{N}_{2,1}, \zeta_{\mathcal{D},2}, \zeta_{2,1}, \tau_1, \tau_2) \right).\end{aligned} \tag{A.41}$$

■

# Appendix B

# Derivations and Proofs in Chapter 4

## B.1 Proof of Lemma 6

The intensity measure of the path loss process for a mm-wave SBS is as follows [28]:

$$
\begin{aligned}
&\Lambda_2([0,x)) \overset{(a)}{=} \int_{\mathbb{R}^2} \mathbb{P}(L_2(r) < x)\mathrm{d}r, \\
&= 2\pi\lambda_2 \int_0^\infty \mathbb{P}(r^{\alpha_2(r)} < x) r\mathrm{d}r, \\
&\overset{(b)}{=} 2\pi\lambda_2 \left( p_L \int_0^d r\mathbb{1}(r^{\alpha_{2,L}} < x)\mathrm{d}r + p_N \int_d^\infty r\mathbb{1}(r^{\alpha_{2,N}} < x)\mathrm{d}r \right), \\
&= 2\pi\lambda_2 \left( p_L \int_0^d r\mathbb{1}(r < x^{\frac{1}{\alpha_{2,L}}})\mathrm{d}r + p_N \int_d^\infty r\mathbb{1}(r < x^{\frac{1}{\alpha_{2,N}}})\mathrm{d}r \right), \\
&= 2\pi\lambda_2 \left( p_L \int_0^{\min(d, x^{\frac{1}{\alpha_{2,L}}})} r\mathrm{d}r + p_N \int_d^{x^{\frac{1}{\alpha_{2,N}}}} r\mathbb{1}(x^{\frac{1}{\alpha_{2,N}}} > d)\mathrm{d}r \right), \\
&= 2\pi\lambda_2 \left( p_L \frac{r^2}{2}\bigg|_0^{\min(d, x^{\frac{1}{\alpha_{2,L}}})} + p_N \frac{r^2}{2}\bigg|_d^{x^{\frac{1}{\alpha_{2,N}}}} \right), \\
&= \pi\lambda_2 \left[ p_L \left( d^2\mathbb{1}(x^{\frac{1}{\alpha_{2,L}}} > d) + x^{\frac{2}{\alpha_{2,L}}}\mathbb{1}(d > x^{\frac{1}{\alpha_{2,L}}}) \right) + p_N \left( x^{\frac{2}{\alpha_{2,N}}} - d^2 \right) \mathbb{1}(x > d^{\alpha_{2,N}}) \right], \\
&= \pi\lambda_2 \left[ p_L \left( d^2\mathbb{1}(x > d^{\alpha_{2,L}}) + x^{\frac{2}{\alpha_{2,L}}}\mathbb{1}(x < d^{\alpha_{2,L}}) \right) + p_N \left( x^{\frac{2}{\alpha_{2,N}}} - d^2 \right) \mathbb{1}(x > d^{\alpha_{2,N}}) \right],
\end{aligned}
$$

$$\overset{(c)}{=} \pi\lambda_2 \big[p_L x^{\frac{2}{\alpha_{2,L}}} \mathbb{1}(x < d^{\alpha_{2,L}}) + p_L d^2 \mathbb{1}(d^{\alpha_{2,L}} \leq x < d^{\alpha_{2,N}}) + p_L d^2 + p_N \left(x^{\frac{2}{\alpha_{2,N}}} - d^2\right) \mathbb{1}(x > d^{\alpha_{2,N}})\big], \tag{B.1}$$

where (a) follows from the definition of the intensity function for the point process of the path loss $\mathcal{N}_2 = \{L_2(r) = \|r\|^{\alpha_2(r)}\}_{r\in\mathbf{\Phi}_2}$ and (b) follows based on the fixed LOS ball blockage model mentioned in Section 4.2.3 where $\alpha_2(r) = \alpha_{2,L}$ when $r \leq d$ and $\alpha_2(r) = \alpha_{2,N}$ when $r > d$. In step (c), we rearrange the terms to get the final expression for the path loss process intensity. Therefore, the CCDF of the path loss from a typical user device to the SBS can be formulated as follows:

$$\begin{aligned}
\bar{F}_2(x) &= \mathbb{P}(L_2(r) > x) = \exp(-\Lambda_2([0, x))),\\
&= \exp\Bigg( - \pi\lambda_2 \big[p_L x^{\frac{2}{\alpha_{2,L}}} \mathbb{1}(x < d^{\alpha_{2,L}}) + p_L d^2 \mathbb{1}(d^{\alpha_{2,L}} \leq x < d^{\alpha_{2,N}}) + p_L d^2 + p_N \left(x^{\frac{2}{\alpha_{2,N}}} - d^2\right) \mathbb{1}(x > d^{\alpha_{2,N}})\big]\Bigg).
\end{aligned} \tag{B.2}$$

Similarly, the CCDF of the path loss from a typical user device to the MBS can be formulated as follows:

$$\bar{F}_1(x) = \exp(-\pi\lambda_1 x^{2/\alpha_1}), \tag{B.3}$$

and the corresponding PDF is as follows:

$$\bar{f}_1(x) = \frac{2\pi\lambda_1}{\alpha_1} x^{\frac{2}{\alpha_1}-1} \exp(-\pi\lambda_1 x^{\frac{2}{\alpha_1}}). \tag{B.4}$$

Therefore, the association probability of a typical user device to MBS is as follows:

$$\begin{aligned}
\mathcal{A}_1 &= \mathbb{P}(P_1 B_1 G_1 L_{1,min}(d)^{-1} > P_2 B_2 G_2 L_{2,min}(d)^{-1}),\\
&\overset{(a)}{=} \mathbb{P}(L_{2,min} > \hat{a} L_{1,min}(d)),\\
&\overset{(b)}{=} \int_0^\infty \bar{F}_2(\hat{a} l_1) \bar{f}_1(l_1) d\mathrm{l}_1 \overset{(c)}{=} \frac{1}{\hat{a}} \int_0^\infty \bar{F}_2(l) \bar{f}_1\left(\frac{l}{\hat{a}}\right) d\mathrm{l},\\
&= \frac{1}{\hat{a}} \int_0^\infty \frac{2\pi\lambda_1}{\alpha_1} \left(\frac{l}{\hat{a}}\right)^{\frac{2}{\alpha_1}-1} \exp\left(-\pi\lambda_1 \left(\frac{l}{\hat{a}}\right)^{\frac{2}{\alpha_1}}\right) \Bigg\{ \exp\left(-\pi\lambda_2 P_L l^{\frac{2}{\alpha_{2,L}}}\right) \mathbb{1}(l < d^{\alpha_{2,L}}) +\\
&\qquad \exp\left(-\pi\lambda_2 P_L d^2\right) \mathbb{1}(d^{\alpha_{2,L}} \leq l < d^{\alpha_{2,N}}) + \exp\left(-\pi\lambda_2 \left[p_l d^2 + p_N \left(l^{\frac{2}{\alpha_{2,N}}} - d^2\right)\right]\right) \mathbb{1}(l > d^{\alpha_{2,N}}) \Bigg\} d\mathrm{l},\\
&\overset{(d)}{=} \frac{2\pi\lambda_1}{\hat{a}\alpha_1} \Bigg\{ \int_0^{d^{\alpha_{2,L}}} H(l) \exp\left(-\pi\lambda_2 p_L l^{\frac{2}{\alpha_{2,L}}}\right) d\mathrm{l} + \int_{d^{\alpha_{2,L}}}^{d^{\alpha_{2,N}}} H(l) \exp\left(-\pi\lambda_2 p_L d^2\right) d\mathrm{l} +
\end{aligned}$$

$$\int_{d^{\alpha_{2,N}}}^{\infty} H(l) \exp\left(-\pi\lambda_2\Big[p_L d^2 + p_N\left(l_1^{\frac{2}{\alpha_{2,N}}} - d^2\right)\Big]\right) dl\Bigg\},$$

(B.5)

where (a) follows from the definition of $\hat{a} \triangleq \frac{P_2 B_2 G_2}{P_1 B_1 G_1}$ and (b) follows from the fact that $\mathbb{P}(X > Y) = \int_0^\infty \mathbb{P}(X > y) f_Y(y) dy$, (c) follows from this change of variable $l = \hat{a} l_1$, and (d) follows from the definition of $H(l) \triangleq \left(\frac{l}{\hat{a}}\right)^{\frac{2}{\alpha_1}-1} \exp\left(-\pi\lambda_1 \left(\frac{l}{\hat{a}}\right)^{\frac{2}{\alpha_1}}\right)$. ■

## B.2 Proof of Lemma 7

The probability of a typical device to associate with mm-wave SBS can be defined as $\mathcal{A}_2 = \mathcal{A}_{2,LOS} + \mathcal{A}_{2,NLOS}$. The intensity measures of the path loss process for LOS and NLOS mm-wave SBSs are[25]:

$$\Lambda_{2,LOS}([0,x)) = \pi\lambda_2\left[p_L\left(d^2 \mathbb{1}(x > d^{\alpha_{2,L}}) + x^{\frac{2}{\alpha_{2,L}}} \mathbb{1}(x < d^{\alpha_{2,L}})\right)\right], \tag{B.6}$$

$$\Lambda_{2,NLOS}([0,x)) = \pi\lambda_2\left[p_N\left(x^{\frac{2}{\alpha_{2,N}}} - d^2\right) \mathbb{1}(x > d^{\alpha_{2,N}})\right]. \tag{B.7}$$

Therefore, $\Lambda'_{2,LOS}([0,x))$ and $\Lambda'_{2,NLOS}([0,x))$ are given as follows:

$$\Lambda'_{2,LOS}([0,x)) = \frac{d\Lambda_{2,LOS}([0,x))}{dx} = \frac{2\pi\lambda_2 p_L}{\alpha_{2,L}} x^{\frac{2}{\alpha_{2,L}}-1} \mathbb{1}(x < d^{\alpha_{2,L}}), \tag{B.8}$$

$$\Lambda'_{2,NLOS}([0,x)) = \frac{d\Lambda_{2,NLOS}([0,x))}{dx} = \frac{2\pi\lambda_2 p_N}{\alpha_{2,N}} x^{\frac{2}{\alpha_{2,N}}-1} \mathbb{1}(x > d^{\alpha_{2,N}}). \tag{B.9}$$

The PDF of the path loss for a user device associated with LOS or NLOS mm-wave SBSs is given as:

$$f_{2,Q} = \frac{-\mathrm{d}F_{2,Q}}{\mathrm{d}x} = \Lambda'_{2,Q}([0,x)) \exp(-\Lambda_{2,Q}([0,x))), \tag{B.10}$$

where $Q \in \{\mathrm{LOS}, \mathrm{NLOS}\}$. Therefore, the probability of a user device to associate with LOS or NLOS mm-wave SBSs is $\mathcal{A}_{2,Q}$, where $Q$, $Q' \in \{\mathrm{LOS}, \mathrm{NLOS}\}$ and $Q \neq Q'$, can be derived as follows:

$$\mathcal{A}_{2,Q} = \mathbb{P}(P_2 B_2 G_2 L_{2,Q}^{-1} > P_1 B_1 G_1 L_1^{-1}) \mathbb{P}(L_{2,Q'} > L_{2,Q}),$$

$$
\begin{aligned}
&\overset{(a)}{=} \mathbb{P}(L_1 > \bar{a}L_{2,Q})\mathbb{P}(L_{2,Q'} > L_{2,Q}),\\
&\overset{(b)}{=} \int_0^\infty \bar{F}_1(\bar{a}l_{2,Q}) f_{2,Q}(l_{2,Q}) e^{-\Lambda_{2,Q'}([0,l_{2,Q}))} d\mathrm{l}_{2,Q},\\
&= \int_0^\infty \exp\left(-\pi\lambda_1 \left(\bar{a}l_{2,Q}\right)^{\frac{2}{\alpha_1}}\right) \Lambda'_{2,Q}([0,l_{2,Q})) e^{-\Lambda_{2,Q}([0,l_{2,Q}))} e^{-\Lambda_{2,Q'}([0,l_{2,Q}))} d\mathrm{l}_{2,Q},\\
&\overset{(c)}{=} \int_0^\infty \exp\left(-\pi\lambda_1 \left(\bar{a}l_{2,Q}\right)^{\frac{2}{\alpha_1}}\right) \Lambda'_{2,Q}([0,l_{2,Q})) e^{-\Lambda_2([0,l_{2,Q}))} d\mathrm{l}_{2,Q}, \qquad \text{(B.11)}
\end{aligned}
$$

where (a) follows from the definition of $\bar{a} \triangleq \frac{P_1B_1G_1}{P_2B_2G_2}$, (b) follows from the definition of $f_{2,Q}$ in Eq. (B.10), and $\bar{F}_1(x)$ in Eq. (B.3). The step in (c) follows from $\Lambda_{2,Q}([0,l_{2,Q})) + \Lambda_{2,Q'}([0,l_{2,Q})) = \Lambda_2([0,l_{2,Q}))$. Using Eq. (B.11), we can derive the probability of association to LOS and NLOS mm-wave SBS as follows:

$$
\begin{aligned}
\mathcal{A}_{2,LOS} &= \int_0^\infty \exp\left(-\pi\lambda_1 \left(\bar{a}l_{2,L}\right)^{\frac{2}{\alpha_1}}\right) \left\{\frac{2\pi\lambda_2 p_L}{\alpha_{2,L}} l_{2,L}^{\frac{2}{\alpha_{2,L}}-1} \mathbb{1}(l_{2,L} < d^{\alpha_{2,L}})\right\} \times \\
&\quad e^{\left(-\pi\lambda_2\left[p_L l_{2,L}^{\frac{2}{\alpha_{2,L}}} \mathbb{1}(l_{2,L}<d^{\alpha_{2,L}}) + p_L d^2 \mathbb{1}(d^{\alpha_{2,L}} \le l_{2,L} < d^{\alpha_{2,N}}) + p_L d^2 + p_N\left(l_{2,L}^{\frac{2}{\alpha_{2,N}}} - d^2\right)\mathbb{1}(l_{2,L} > d^{\alpha_{2,N}})\right]\right)} d\mathrm{l}_{2,L},\\
&= \frac{2\pi\lambda_2 p_L}{\alpha_{2,L}} \int_0^{d^{\alpha_{2,L}}} l_{2,L}^{\frac{2}{\alpha_{2,L}}-1} \exp\left(-\pi\lambda_1 \left(\bar{a}l_{2,L}\right)^{\frac{2}{\alpha_1}} - \pi\lambda_2 p_L l_{2,L}^{\frac{2}{\alpha_{2,L}}}\right) d\mathrm{l}_{2,L}. \qquad \text{(B.12)}
\end{aligned}
$$

Similarly, we use Eq. (B.11) to derive the association probability to NLOS mm-wave SBS as follows:

$$
\begin{aligned}
\mathcal{A}_{2,NLOS} &= \int_0^\infty \exp\left(-\pi\lambda_1 \left(\bar{a}l_{2,N}\right)^{\frac{2}{\alpha_1}}\right) \left\{\frac{2\pi\lambda_2 p_N}{\alpha_{2,N}} l_{2,N}^{\frac{2}{\alpha_{2,N}}-1} \mathbb{1}(l_{2,N} > d^{\alpha_{2,N}})\right\} \times \\
&\quad e^{\left(-\pi\lambda_2\left[p_L l_{2,N}^{\frac{2}{\alpha_{2,L}}} \mathbb{1}(l_{2,N}<d^{\alpha_{2,L}}) + p_L d^2 \mathbb{1}(d^{\alpha_{2,L}} \le l_{2,N} < d^{\alpha_{2,N}}) + p_L d^2 + p_N\left(l_{2,N}^{\frac{2}{\alpha_{2,N}}} - d^2\right)\mathbb{1}(l_{2,N} > d^{\alpha_{2,N}})\right]\right)} d\mathrm{l}_{2,L},\\
&= \frac{2\pi\lambda_2 p_N}{\alpha_{2,N}} \int_{d^{\alpha_{2,N}}}^\infty l_{2,N}^{\frac{2}{\alpha_{2,N}}-1} \exp\left(-\pi\lambda_1 \left(\bar{a}l_{2,N}\right)^{\frac{2}{\alpha_1}} - \pi\lambda_2\left[p_L d^2 + p_N(l_{2,N}^{\frac{2}{\alpha_{2,N}}} - d^2)\right]\right) d\mathrm{l}_{2,N}. \qquad \text{(B.13)}
\end{aligned}
$$

■

## B.3 Proof of Lemma 9

The $b^{\text{th}}$ moment of the CSP of a typical device served by the mm-wave SBS can be derived as:

$$
M_{b,2}(\theta_{\mathcal{D}}) = \mathbb{E}_l\left[\underbrace{\mathbb{P}(n = 2 | L_{2,min} = l_2)}_{\bar{\mathcal{A}}_2(l_2)} P_{s,2}(\theta_{\mathcal{D}})^b\right],
$$

$$
\begin{aligned}
&= \mathbb{E}_l\left[\bar{\mathcal{A}}_2(l_2)\left(p_L P_{s,2,L}(\theta_{\mathcal{D}}) + p_N P_{s,2,N}(\theta_{\mathcal{D}})\right)^b\right],\\
&\overset{(a)}{=} \mathbb{E}_l\left[\bar{\mathcal{A}}_2(l_2)\left(p_L\frac{\Gamma\left(m_L, \frac{m_L}{\Omega_L}\nu_L\right)}{\Gamma(m_L)} + p_N\frac{\Gamma\left(m_N, \frac{m_N}{\Omega_N}\nu_N\right)}{\Gamma(m_N)}\right)^b\right],\\
&= \mathbb{E}_l\left[\left(\bar{\mathcal{A}}_{2,L}(l_{2,L}) + \bar{\mathcal{A}}_{2,N}(l_{2,N})\right)\times\left(p_L\frac{\Gamma\left(m_L, \frac{m_L}{\Omega_L}\nu_L\right)}{\Gamma(m_L)} + p_N\frac{\Gamma\left(m_N, \frac{m_N}{\Omega_N}\nu_N\right)}{\Gamma(m_N)}\right)^b\right],\\
&\overset{(b)}{=} \mathbb{E}_l\left[\bar{\mathcal{A}}_{2,L}(l_{2,L})\left(p_L\frac{\Gamma\left(m_L, \frac{m_L}{\Omega_L}\nu_L\right)}{\Gamma(m_L)}\right)^b\right] + \mathbb{E}_l\left[\bar{\mathcal{A}}_{2,N}(l_{2,N})\left(p_N\frac{\Gamma\left(m_N, \frac{m_N}{\Omega_N}\nu_N\right)}{\Gamma(m_N)}\right)^b\right],\\
&\overset{(c)}{=} \mathbb{E}_l\left[\bar{\mathcal{A}}_{2,L}(l_{2,L})\,p_L^b\left(1-\frac{\gamma\left(m_L, \frac{m_L}{\Omega_L}\nu_L\right)}{\Gamma(m_L)}\right)^b\right] + \mathbb{E}_l\left[\bar{\mathcal{A}}_{2,N}(l_{2,N})\,p_N^b\left(1-\frac{\gamma\left(m_N, \frac{m_N}{\Omega_N}\nu_N\right)}{\Gamma(m_N)}\right)^b\right],\\
&\overset{(d)}{\approx} \mathbb{E}_l\left[\bar{\mathcal{A}}_{2,L}(l_{2,L})p_L^b\left(1-[1-e^{-\zeta_L\nu_L}]^{m_L}\right)^b\right] + \mathbb{E}_l\left[\bar{\mathcal{A}}_{2,N}(l_{2,N})\,p_N^b\left(1-[1-e^{-\zeta_N\nu_N}]^{m_N}\right)^b\right],\\
&\overset{(e)}{=} \mathbb{E}_l\left[\bar{\mathcal{A}}_{2,L}(l_{2,L})p_L^b\sum_{k=0}^{b}\binom{b}{k}\left(-[1-e^{-\zeta_L\nu_L}]^{m_L}\right)^k\right]+\\
&\qquad\qquad\qquad\qquad \mathbb{E}_l\left[\bar{\mathcal{A}}_{2,N}(l_{2,N})\,p_N^b\sum_{k=0}^{b}\binom{b}{k}\left(-[1-e^{-\zeta_N\nu_N}]^{m_N}\right)^k\right],\\
&\overset{(f)}{=} \mathbb{E}_l\left[\bar{\mathcal{A}}_{2,L}(l_{2,L})p_L^b\sum_{k=0}^{b}\sum_{\ddot{k}=0}^{m_L k}\binom{b}{k}\binom{m_L k}{\ddot{k}}(-1)^{\ddot{k}+k}e^{-\zeta_L\nu_L\ddot{k}}\right]+\\
&\qquad\qquad\qquad \mathbb{E}_l\left[\bar{\mathcal{A}}_{2,N}(l_{2,N})p_N^b\sum_{k=0}^{b}\sum_{\ddot{k}=0}^{m_N k}\binom{b}{k}\binom{m_N k}{\ddot{k}}(-1)^{\ddot{k}+k}e^{-\zeta_N\nu_N\ddot{k}}\right],
\end{aligned}
$$

where (a) follows from substituting the value of $P_{s,2,L}(\theta_{\mathcal{D}})$ and $P_{s,2,N}(\theta_{\mathcal{D}})$ from Eq. (4.16) and Eq. (4.17), respectively, (b) follows from $l_{2,\mathrm{L}} = r_{2,\mathcal{D}}^{\alpha_{2,L}}$ and $l_{2,\mathrm{N}} = r_{2,\mathcal{D}}^{\alpha_{2,N}}$ and the considered blockage model where $p_L = 1$ when mm-wave intended link distance $r_{2,\mathcal{D}} < d$ and $p_N = 1$ when mm-wave intended link distance $r_{2,\mathcal{D}} > d$, (c) follows from $\Gamma(s) = \gamma(s,x) + \Gamma(s,x)$, (d) follows from the CDF of Gamma random variable which can be tightly upper bounded by $\frac{\gamma\left(m_L, \frac{m_L}{\Omega_L}\nu_L\right)}{\Gamma(m_L)} < [1-e^{-\zeta_L\nu_L}]^{m_L}$ [150], where $\zeta_L \triangleq m_L(m_L!)^{-1/m_L}$, $\nu_L \triangleq \frac{\theta_{\mathcal{D}} r_{2,\mathcal{D}}^{\alpha_{2,L}}\sigma_2^2}{P_2G_2}$, $\zeta_N \triangleq m_N(m_N!)^{-1/m_N}$, and $\nu_N \triangleq \frac{\theta_{\mathcal{D}} r_{2,\mathcal{D}}^{\alpha_{2,N}}\sigma_2^2}{P_2G_2}$ [29]. The steps in (e) and (f) are done by following the binomial expansion theorem. Finally, the Lemma 4 follows from de-conditioning on $l$ and using the definitions $\ddot{\nu}_L \triangleq \frac{\nu_L}{r_{2,\mathcal{D}}^{\alpha_{2,L}}} = \frac{\nu_L}{l_{2,\mathrm{L}}} = \frac{\theta_{\mathcal{D}}\sigma_2^2}{P_2G_2}$ and $\ddot{\nu}_N \triangleq \frac{\nu_N}{r_{2,\mathcal{D}}^{\alpha_{2,N}}} = \frac{\nu_N}{l_{2,\mathrm{N}}} = \frac{\theta_{\mathcal{D}}\sigma_2^2}{P_2G_2}$. ■

## B.4 Proof of Lemma 10

The $b^{\text{th}}$ moment of the CSP of a typical device when associated to $\mu$wave MBS can be derived as follows:

$$
\begin{aligned}
M_{b,1}(\theta_{\mathcal{D}}) &= \mathbb{E}_{l_1}\left[\underbrace{\mathbb{P}(n=1|L_{1,min}=l_1)}_{\bar{\mathcal{A}}_1(l_1)} P_{s,1}(\theta_{\mathcal{D}})^b\right],\\
&\overset{(a)}{=} \mathbb{E}_{l_1}\left[\bar{\mathcal{A}}_1(l_1)\prod_{\mathbf{y}_{1,i}\in\mathbf{\Phi}_1\setminus\{\mathbf{y}_{1,0}\}}\frac{1}{\left(1+\theta_{\mathcal{D}}\left(\frac{r_{1,\mathcal{D}}}{\|\mathbf{y}_{1,i}\|}\right)^{\alpha_1}\right)^b}\right],\\
&\overset{(b)}{=} \mathbb{E}_{l_1}\left[\bar{\mathcal{A}}_1(l_1)\exp\left(\int_r^\infty -2\lambda_1\pi\left[1-\frac{1}{\left(1+\theta_{\mathcal{D}}\left(\frac{r}{y}\right)^{\alpha_1}\right)^b}\right]y\mathrm{d}y\right)\right],\\
&\overset{(c)}{=} \mathbb{E}_{l_1}\left[\bar{\mathcal{A}}_1(l_1)\exp\left(\int_{l_1^{\frac{1}{\alpha_1}}}^\infty -2\lambda_1\pi\left[1-\frac{1}{\left(1+\theta_{\mathcal{D}}\frac{l_1}{y^{\alpha_1}}\right)^b}\right]y\mathrm{d}y\right)\right.,\\
&\overset{(d)}{=} \mathbb{E}_{l_1}\left[\bar{\mathcal{A}}_1(l_1)\exp\left(\int_0^1 -2\lambda_1\pi\left[1-\frac{1}{(1+\theta_{\mathcal{D}}v)^b}\right]v^{-1}\frac{y^2}{\alpha_1}\mathrm{d}v\right)\right],\\
&\overset{(e)}{=} \mathbb{E}_{l_1}\left[\bar{\mathcal{A}}_1(l_1)\exp\left(\frac{-2\lambda_1\pi l_1^{\frac{2}{\alpha_1}}}{\alpha_1}\int_0^1\left[1-\frac{1}{(1+\theta_{\mathcal{D}}v)^b}\right]\frac{1}{v^{\frac{2}{\alpha_1}+1}}\mathrm{d}v\right)\right],
\end{aligned}
$$

where (a) follows from taking expectation over $l_1 = r^{\alpha_1}$ and considering the conditional association probability for the typical device connecting to the MBSs tier given in Lemma (6) and substituting the value of $P_{s,1}(\theta_{\mathcal{D}})$ from Eq. (4.21). In step (b) we apply PGFL of the PPP [61, Chapter 4]. Step (c) follows from averaging over $l_1$. In step (d), we use the change of variable $v = \frac{l_1}{y^{\alpha_1}}$, $dy = \frac{-1}{\alpha_1 l_1 y^{-\alpha_1-1}}dv = \frac{-1}{\alpha_1}v^{-1}ydv$, when $y = l_1^{\frac{1}{\alpha_1}} \rightarrow v = 1$ and when $y = \infty \rightarrow v = 0$ and we swap the integral limits and multiply by $-1$, (e) follows from $y^2 = l_1^{\frac{2}{\alpha_1}}/v^{\frac{2}{\alpha_1}}$ and doing some mathematical manipulations. ■

## B.5 Proof of Lemma 11

While taking the association biases effect in consideration, the $b^{\text{th}}$ moment of the CSP $P_{s,k}(\theta_{\mathcal{D}})$ of the typical device when it is served by the $k^{\text{th}}$ tier is given as follows:

$$
\begin{aligned}
&M_{b,\mathrm{k}'}(\theta_{\mathcal{D}}) = \mathbb{E}_{r_{k,\mathcal{D}}}\Bigg[\mathbb{P}(n=k|r_{k,\mathcal{D}})P_{s,k'}(\theta_{\mathcal{D}})^b\Bigg],\\
&\overset{(a)}{=} \mathbb{E}_{r_{k,\mathcal{D}}}\Bigg[\prod_{j\neq k} e^{-\pi\lambda_j(\hat{P}_{jk}\hat{B}_{jk})^{2/\alpha_j}r^2} \times \prod_{\mathbf{y}_{k,i}\in\mathbf{\Phi}_k\setminus\{\mathbf{y}_{k,0}\}} \frac{1}{\left(1+\theta_{\mathcal{D}}\left(\frac{r_{k,\mathcal{D}}}{\|\mathbf{y}_{k,i}\|}\right)^{\alpha_k}\right)^b}\Bigg],\\
&\overset{(b)}{=} \mathbb{E}_{r_{k,\mathcal{D}}}\Bigg[\prod_{j\neq k} e^{-\pi\lambda_j(\hat{P}_{jk}\hat{B}_{jk})^{2/\alpha_j}r^2} \times \exp\left(\int_{r_{k,\mathcal{D}}}^{\infty} -2\lambda_k\pi\left[1-\frac{1}{\left(1+\theta_{\mathcal{D}}\left(\frac{r_{k,\mathcal{D}}}{y}\right)^{\alpha_k}\right)^b}\right]y\mathrm{d}y\right)\Bigg],\\
&\overset{(c)}{=} \int_0^{\infty} 2\lambda_k\pi r e^{-\lambda_k\pi r^2} e^{-\sum\limits_{j\neq k}\lambda_j(\hat{P}_{jk}\hat{B}_{jk})^{2/\alpha_j}\pi r^2} \times \exp\left(\int_{r}^{\infty} -2\lambda_k\pi\left[1-\frac{1}{\left(1+\theta_{\mathcal{D}}\left(\frac{r}{y}\right)^{\alpha_k}\right)^b}\right]y\mathrm{d}y\right)\mathrm{d}r,\\
&\overset{(d)}{=} \int_0^{\infty} e^{-q} e^{-q\sum\limits_{j\neq k}\hat{\lambda}_{jk}(\hat{P}_{jk}\hat{B}_{jk})^{2/\alpha_j}} \times \exp\left(-2q\int_0^1\left[1-\frac{1}{(1+\theta_{\mathcal{D}}v^{\alpha_k})^b}\right]v^{-3}\mathrm{d}v\right)\mathrm{d}q,\\
&\overset{(e)}{=} \int_0^{\infty} e^{-q} e^{-q\sum\limits_{j\neq k}\hat{\lambda}_{jk}(\hat{P}_{jk}\hat{B}_{jk})^{2/\alpha_j}} \times \exp\left(-q\int_1^{\infty}\left[1-\frac{1}{(1+\theta_{\mathcal{D}}u^{-\alpha_k/2})^b}\right]\mathrm{d}u\right)\mathrm{d}q,\\
&\overset{(f)}{=} \int_0^{\infty} e^{-q} e^{-q\sum\limits_{j\neq k}\hat{\lambda}_{jk}(\hat{P}_{jk}\hat{B}_{jk})^{2/\alpha_j}} \times \exp\left(-q\left[\,{}_2F_1(b,-\frac{2}{\alpha_k};1-\frac{2}{\alpha_k};-\theta_{\mathcal{D}})-1\right]\right)\mathrm{d}q,\\
&= \frac{1}{\sum\limits_{j\neq k}\hat{\lambda}_{jk}(\hat{P}_{jk}\hat{B}_{jk})^{2/\alpha_j} + \,{}_2F_1(b,-\frac{2}{\alpha_k};1-\frac{2}{\alpha_k};-\theta_{\mathcal{D}})}.
\end{aligned}
$$

where (a) follows from considering the conditional association probability for the typical device connecting to the $k^{\text{th}}$ tier given in Eq. (4.30). In step (b), we apply PGFL of the PPP [61, Chapter 4]. Step (c) follows from averaging over $r_{k,\mathcal{D}}$, step (d) is by using variable substitution $q=\pi\lambda_k r^2$ and $v=r/y$. In step (e), we perform variable substitution $v=u(\hat{P}_{jk}\hat{B}_{jk})^{-1/\alpha_j}$ and step (f) follows from the fact that ${}_2F_1(b,-\frac{2}{\alpha};1-\frac{2}{\alpha};-\theta)\equiv 1+\int_1^{\infty}(1-\frac{1}{(1+\theta h^{-\alpha/2})^b})\mathrm{d}h$. ■

# Appendix C

# Derivations and Proofs in Chapter 5

## C.1 Proof of Lemma 12

The phantom cells dedicate $\eta$ and $(1-\eta)$ fraction of the time to serve biased and non-biased users, respectively. Consider a time interval of $t$ seconds. Then the numbers of data bits sent by each phantom BS to non-biased and biased users are $(1-\eta)t\mathcal{R}_{d2}$ bits and $\eta t\mathcal{R}_{dB}$ bits, respectively. On average, there are $\frac{\lambda_2}{\lambda_1}$ phantom BSs per MBS, and hence, the MBS should be able to convey control signaling amounts of $\frac{\lambda_2}{\lambda_1}\frac{\mu_C(1-\eta)t\mathcal{R}_{d2}}{\gamma}$ bits and $\frac{\lambda_2}{\lambda_1}\frac{\mu_C\eta t\mathcal{R}_{dB}}{\gamma}$ bits to non-biased and biased users, respectively, during time interval $t$. However, the MBS sends the control bits with the rates of $\mathcal{R}_{c2}$ and $\mathcal{R}_{cB}$ for non-biased and biased phantom cell users, respectively. Hence, the amount of time required to send the control signaling by the MBS is $\frac{\lambda_2}{\lambda_1}\frac{\mu_C(1-\eta)t\mathcal{R}_{d2}}{\gamma\mathcal{R}_{c2}}$ seconds and $\frac{\lambda_2}{\lambda_1}\frac{\mu_C\eta t\mathcal{R}_{dB}}{\gamma\mathcal{R}_{cB}}$ seconds for non-biased and biased phantom cell users, respectively. Consequently, the remaining time for the MBS to serve macrocell users is $\left(t-\frac{\lambda_2}{\lambda_1}\frac{\mu_C(1-\eta)t\mathcal{R}_{d2}}{\gamma\mathcal{R}_{c2}}-\frac{\lambda_2}{\lambda_1}\frac{\mu_C\eta t\mathcal{R}_{dB}}{\gamma\mathcal{R}_{cB}}\right)$ seconds. Hence, the average number of bits the MBS conveys to macrocell users during time interval $t$ is $\mathcal{R}_1^{(s)}\left(t-\frac{\lambda_2}{\lambda_1}\frac{\mu_C(1-\eta)t\mathcal{R}_{d2}}{\gamma\mathcal{R}_{c2}}-\frac{\lambda_2}{\lambda_1}\frac{\mu_C\eta t\mathcal{R}_{dB}}{\gamma\mathcal{R}_{cB}}\right)$ bits. Dividing the above expression by $t$, we obtain the average rate at which data is delivered to macrocell users as $\mathcal{R}_1^{(s)}\left(1-\frac{\lambda_2}{\lambda_1}\frac{\mu_C(1-\eta)\mathcal{R}_{d2}}{\gamma\mathcal{R}_{c2}}-\frac{\lambda_2}{\lambda_1}\frac{\mu_C\eta\mathcal{R}_{dB}}{\gamma\mathcal{R}_{cB}}\right)$. Then (5.7) is obtained by replacing $(1-\eta)\mathcal{R}_{d2}$ by $\mathcal{T}_2^{(s)}$, replacing $\eta\mathcal{R}_{dB}$ by $\mathcal{T}_B^{(s)}$ and multiplying the above expression by $(1-\mu_C)$.
■

## C.2 Proof of Lemma 13

From the independence of the PPPs of the macro and phantom BSs , the joint pdf of the distances between a generic user and his nearest phantom BS and nearest MBS is given by $f_{r_1,r_2}(x,y) = 4\pi^2 xy\lambda_1\lambda_2 e^{-\pi(\lambda_1 x^2+\lambda_2 y^2)}$, $x, y > 0$. The control link distributions are given by

$$\begin{aligned}\mathbb{P}\left\{r_1 < x|\mathcal{U}_2\right\} &= \frac{\mathbb{P}\left\{r_1 < x, \mathcal{U}_2\right\}}{\mathbb{P}\left\{\mathcal{U}_2\right\}} = \frac{\mathbb{P}\left\{r_1 < x, P_1 r_1^{-\alpha_1} < P_2 r_2^{-\alpha_1}\right\}}{\mathbb{P}\left\{P_1 r_1^{-\alpha_1} < P_2 r_2^{-\alpha_1}\right\}} \\ &= \frac{\mathbb{P}\left\{r_1 < x, r_2 < \left(\frac{P_2}{P_1}\right)^{\frac{1}{\alpha_2}} r_1^{\frac{\alpha_1}{\alpha_2}}\right\}}{\mathcal{A}_2}. \end{aligned} \tag{C.1}$$

Hence, the pdf of $R_{c2}$ is given by

$$\begin{aligned} f_{R_{c2}}(x) &= \frac{1}{\mathcal{A}_2} \frac{\mathrm{d}\mathbb{P}\left\{r_1 < x, r_2 < \left(\frac{P_2}{P_1}\right)^{\frac{1}{\alpha_2}} r_1^{\frac{\alpha_1}{\alpha_2}}\right\}}{\mathrm{d}x} \\ &= \frac{1}{\mathcal{A}_2} \int_0^{\left(\frac{P_2}{P_1}\right)^{\frac{1}{\alpha_2}} x^{\frac{\alpha_1}{\alpha_2}}} f_{r_1,r_2}(x,y)dy. \end{aligned} \tag{C.2}$$

Similarly, the pdf of $R_{cB}$ is derived as follows.

$$f_{R_{cB}}(x) = \frac{1}{\mathcal{A}_B} \int_{\left(\frac{P_2}{P_1}\right)^{\frac{1}{\alpha_2}} x^{\frac{\alpha_1}{\alpha_2}}}^{\left(\frac{BP_2}{P_1}\right)^{\frac{1}{\alpha_2}} x^{\frac{\alpha_1}{\alpha_2}}} f_{r_1,r_2}(x,y)dy. \tag{C.3}$$

■

## C.3 Proof of Lemma 14

The coverage probability, which is the *ccdf* of the SINR, can be expressed in terms of the Laplace transform (LT) of the aggregate interference. Using the general SINR model in (5.23), the coverage probability is given by

$$\begin{aligned}\mathbb{P}[\text{SINR} > \theta] &= \mathbb{P}\left[\frac{P_{BS} H {r_o}^{-\alpha}}{\mathcal{I}_{agg} + \sigma^2} > \theta\right] \\ &\overset{(a)}{=} \int_0^{\infty} \exp\left(-\frac{\sigma^2 \theta r_o^{\alpha}}{P_{BS}}\right) \mathcal{L}_{\mathcal{I}_{agg}}(\theta \frac{r_o^{\alpha}}{P_{BS}}) f_{r_o}(r) dr, \end{aligned} \tag{C.4}$$

where (a) follows from the exponential distribution of $H$ and the definition of the LT [63,75], and the parameters in (C.4) can be obtained for each user case from Table 5.2. In the case of shared spectrum access, $\mathcal{I}_{agg}$ is the superposition of two independent interferences from the two tiers 1 and 2, and hence, can be decomposed to the multiplications of the LTs of the interferences from each tier as follows:

$$\mathcal{L}_{\mathcal{I}_{agg}}(s) = \mathcal{L}_{\mathcal{I}_1}(s)\mathcal{L}_{\mathcal{I}_2}(s). \tag{C.5}$$

In the other cases, the aggregate interference is simply single-tier interference. The LT of the interference for a given network tier $k \in \{1, 2\}$ is calculated as:

$$\begin{aligned}\mathcal{L}_{\mathcal{I}_k}(s) &= \mathbb{E}\left[e^{-sP_k \sum\limits_{x\in\mathbf{\Phi_k}\setminus b_o} H_x x^{-\alpha_k}}\right] = \mathbb{E}\left[\prod_{x\in\mathbf{\Phi_1}\setminus b_o} e^{-sP_k H_x x^{-\alpha_k}}\right] \\ &\overset{(b)}{=} \exp\left\{-2\pi\lambda_k \int_{\|b_o\|}^{\infty} \frac{sP_k x}{x^{\alpha_k} + sP_k}\mathrm{d}x\right\}.\end{aligned} \tag{C.6}$$

where (b) follows by from the probability generating functional of the PPP and the i.i.d. exponential distribution of $H_x$, and $b_o$ is the location of the serving BS determined by the employed association criterion. The lemma is obtained by calculating the LT of the aggregate interference affecting the test user according to Table 5.2 using (C.5) and (C.6), in which the the location of the serving BS $b_o$ is obtained via the association criterion given in (5.1). Then, by substituting the LT of the interference in (C.4) and integrating over the appropriate link distance given in Table 5.2, we obtain the coverage probabilities. ■

# Bibliography

[1] Javier Gozalvez, "5G tests and demonstrations mobile radio," *IEEE Vehicular Technology Magazine*, vol. 10, no. 2, pp. 16–25, 2015.

[2] Jeffrey G Andrews, Stefano Buzzi, Wan Choi, Stephen V Hanly, Aurelie Lozano, Anthony CK Soong, and Jianzhong Charlie Zhang, "What will 5G be?," *IEEE Journal on Selected Areas in Communications*, vol. 32, no. 6, pp. 1065–1082, 2014.

[3] Han-Shin Jo, Young Jin Sang, Ping Xia, and Jeffrey G Andrews, "Heterogeneous cellular networks with flexible cell association: A comprehensive downlink SINR analysis," *IEEE Transactions on Wireless Communications*, vol. 11, no. 10, pp. 3484–3495, 2012.

[4] Christodoulos Skouroumounis, Constantinos Psomas, and Ioannis Krikidis, "Heterogeneous FD-mm-Wave cellular networks with cell center/edge users," *IEEE Transactions on Communications*, vol. 67, no. 1, pp. 791–806, 2018.

[5] L Ericsson, "Cellular IoT evolution for industry digitalization," *White Paper*, vol. 17, January 2019.

[6] Jeffrey G Andrews, Tianyang Bai, Mandar N Kulkarni, Ahmed Alkhateeb, Abhishek K Gupta, and Robert W Heath, "Modeling and analyzing millimeter wave cellular systems," *IEEE Transactions on Communications*, vol. 65, no. 1, pp. 403–430, 2016.

[7] Michele Polese, Marco Giordani, Marco Mezzavilla, Sundeep Rangan, and Michele Zorzi, "Improved handover through dual connectivity in 5G mmwave mobile networks,"

*IEEE Journal on Selected Areas in Communications*, vol. 35, no. 9, pp. 2069–2084, 2017.

[8] Peng Wang, Yonghui Li, Lingyang Song, and Branka Vucetic, "Multi-gigabit millimeter wave wireless communications for 5G: From fixed access to cellular networks," *IEEE Communications Magazine*, vol. 53, no. 1, pp. 168–178, 2015.

[9] Derya Malak, Harpreet S Dhillon, and Jeffrey G Andrews, "Modeling uplink coverage and rate with aggregation in Machine-to-Machine communication networks," in *IEEE International Conference on Communications (ICC)*, 2016, pp. 1–6.

[10] Derya Malak, Harpreet S Dhillon, and Jeffrey G Andrews, "Optimizing data aggregation for uplink Machine-to-Machine communication networks," *IEEE Transactions on Communications*, vol. 64, no. 3, pp. 1274–1290, 2016.

[11] Martin Haenggi and Daniele Puccinelli, "Routing in ad hoc networks: a case for long hops," *IEEE Communications Magazine*, vol. 43, no. 10, pp. 93–101, 2005.

[12] Jing Guo, Salman Durrani, Xiangyun Zhou, and Halim Yanikomeroglu, "Massive machine type communication with data aggregation and resource scheduling," *IEEE Transactions on Communications*, vol. 65, no. 9, pp. 4012–4026, 2017.

[13] Onel L Alcaraz López, Hirley Alves, Pedro H Juliano Nardelli, and Matti Latva-aho, "Aggregation and resource scheduling in machine-type communication networks: A stochastic geometry approach," *IEEE Transactions on Wireless Communications*, vol. 17, no. 7, pp. 4750–4765, 2018.

[14] Dong Min Kim, Rene Brandborg Sorensen, Kashif Mahmood, Olav Norvald Osterbo, Andrea Zanella, and Petar Popovski, "Data aggregation and packet bundling of uplink small packets for monitoring applications in LTE," *IEEE Network*, vol. 31, no. 6, pp. 32–38, 2017.

[15] Giovanni Rigazzi, Nuno K Pratas, Petar Popovski, and Romano Fantacci, "Aggregation and trunking of M2M traffic via D2D connections," in *IEEE International Conference on Communications (ICC)*. IEEE, 2015, pp. 2973–2978.

[16] Shilpa Rao and Rajeev Shorey, "Efficient device-to-device association and data aggregation in industrial IoT systems," *International Conference on Communication Systems and Networks*, pp. 314–321, 2017.

[17] Guowang Miao, Amin Azari, and Taewon Hwang, "$E^2$-MAC: Energy efficient medium access for massive M2M communications," *IEEE Transactions on Communications*, vol. 64, no. 11, pp. 4720–4735, 2016.

[18] Amin Azari and Guowang Miao, "Network lifetime maximization for cellular-based M2M networks," *IEEE Access*, vol. 5, pp. 18927–18940, 2017.

[19] Amin Azari and Guowang Miao, "Fundamental tradeoffs in resource provisioning for IoT services over cellular networks," in *IEEE International Conference on Communications (ICC)*. IEEE, 2017, pp. 1–7.

[20] Zhaohui Yang, Wei Xu, Yijin Pan, Cunhua Pan, and Ming Chen, "Energy efficient resource allocation in machine-to-machine communications with multiple access and energy harvesting for IoT," *IEEE Internet of Things Journal*, vol. 5, no. 1, pp. 229–245, 2018.

[21] Liang Liang, Lu Xu, Bin Cao, and Yunjian Jia, "A cluster-based congestion-mitigating access scheme for massive M2M communications in internet of things," *IEEE Internet of Things Journal*, vol. 5, no. 3, pp. 2200–2211, 2018.

[22] Wael Fatnassi and Zouheir Rezki, "Reliability enhancement of smart metering system using millimeter wave technology," *IEEE Transactions on Communications*, vol. 66, no. 10, pp. 4877–4892, 2018.

[23] Marco Di Renzo, "Stochastic geometry modeling and analysis of multi-tier millimeter wave cellular networks," *IEEE Transactions on Wireless Communications*, vol. 14, no. 9, pp. 5038–5057, 2015.

[24] Tianyang Bai and Robert W Heath, "Coverage and rate analysis for millimeter-wave cellular networks," *IEEE Transactions on Wireless Communications*, vol. 14, no. 2, pp. 1100–1114, 2014.

[25] Esma Turgut and M Cenk Gursoy, "Coverage in heterogeneous downlink millimeter wave cellular networks," *IEEE Transactions on Communications*, vol. 65, no. 10, pp. 4463–4477, 2017.

[26] Na Deng, Yi Sun, and Martin Haenggi, "Success probability of millimeter-wave D2D networks with heterogeneous antenna arrays," in *Wireless Communications and Networking Conference (WCNC)*. IEEE, 2018, pp. 1–5.

[27] Sarabjot Singh, Mandar N Kulkarni, Amitava Ghosh, and Jeffrey G Andrews, "Tractable model for rate in self-backhauled millimeter wave cellular networks," *IEEE Journal on Selected Areas in Communications*, vol. 33, no. 10, pp. 2196–2211, 2015.

[28] Hisham Elshaer, Mandar N Kulkarni, Federico Boccardi, Jeffrey G Andrews, and Mischa Dohler, "Downlink and uplink cell association with traditional macrocells and millimeter wave small cells," *IEEE Transactions on Wireless Communications*, vol. 15, no. 9, pp. 6244–6258, 2016.

[29] Tianyang Bai and Robert W Heath, "Coverage and rate analysis for millimeter-wave cellular networks," *IEEE Transactions on Wireless Communications*, vol. 14, no. 2, pp. 1100–1114, 2015.

[30] Na Deng and Martin Haenggi, "A fine-grained analysis of millimeter-wave device-to-device networks," *IEEE Trans. Commun*, vol. 65, no. 11, pp. 4940–4954, 2017.

[31] Sarabjot Singh and J Andrews, "Joint resource partitioning and offloading in heterogeneous cellular networks," *IEEE Transaction on Wireless Communication*, vol. 13, pp. 888–901, 2013.

[32] Han-Shin Jo, Young Jin Sang, Ping Xia, and Jeffrey G Andrews, "Outage probability for heterogeneous cellular networks with biased cell association," in *Proc. of the IEEE GLOBECOM*, Houston, Texas, USA, December 2011, pp. 1–5, 2011.

[33] Hesham ElSawy and Ekram Hossain, "On stochastic geometry modeling of cellular uplink transmission with truncated channel inversion power control," *IEEE Transactions on Wireless Communications*, vol. 13, no. 8, pp. 4454–4469, August 2014.

[34] Harpreet S Dhillon, Thomas David Novlan, and Jeffrey G Andrews, "Coverage probability of uplink cellular networks," in *IEEE Global Communications Conference (GLOBECOM)*, Anaheim, California, USA, 2012, pp. 2179–2184.

[35] M. Di Renzo and Peng Guan, "A mathematical framework to the computation of the error probability of downlink MIMO cellular networks by using stochastic geometry," *IEEE Transaction on Wireless Communications*, vol. 62, no. 8, pp. 2860–2879, August 2014.

[36] H.S. Dhillon, M. Kountouris, and J.G. Andrews, "Downlink MIMO HetNets: Modeling, ordering results and performance analysis," *IEEE Transactions on Wireless Communications*, vol. 12, no. 10, pp. 5208–5222, October 2013.

[37] Dongxu Cao, Sheng Zhou, and Zhisheng Niu, "Optimal base station density for energy-efficient heterogeneous cellular networks," in *IEEE International Conference on Communications (ICC)*, 2012, pp. 4379–4383.

[38] Sayan Mukherjee and Hiroyuki Ishii, "Energy efficiency in the phantom cell enhanced local area architecture," in *IEEE Wireless Communications and Networking Conference (WCNC)*, 2013, pp. 1267–1272.

[39] Shan Zhang, Jie Gong, Sheng Zhou, and Zhisheng Niu, "How many small cells can be turned off via vertical offloading under a separation architecture?," *IEEE Transactions on Wireless Communications*, vol. 14, no. 10, pp. 5440–5453, 2015.

[40] Hazem Ibrahim, Hesham ElSawy, Uyen T Nguyen, and Mohamed-Slim Alouini, "Modeling virtualized downlink cellular networks with ultra-dense small cells," in *IEEE International Conference on Communications (ICC)*, 2015, pp. 5360–5366.

[41] Xingqin Lin, Radha Krishna Ganti, Philip J Fleming, and Jeffrey G Andrews, "Towards understanding the fundamentals of mobility in cellular networks," *IEEE Transactions on Wireless Communications*, vol. 12, no. 4, pp. 1686–1698, 2013.

[42] Wei Bao and Ben Liang, "Stochastic geometric analysis of user mobility in heterogeneous wireless networks," *IEEE Journal on Selected Areas in Communications*, 2015.

[43] Sanam Sadr and R Adve, "Handoff rate and coverage analysis in multi-tier heterogeneous networks," *IEEE Transactions on Wireless Communications*, vol. 14, no. 5, pp. 2626 – 2638, 2015.

[44] Gongzheng Zhang, Tony QS Quek, Aiping Huang, and Hangguan Shan, "Delay and reliability tradeoffs in heterogeneous cellular networks," *IEEE Transactions on Wireless Communications*, pp. 1101–1113, 2016.

[45] Xiaohu Ge, Junliang Ye, Yang Yang, and Qiang Li, "User mobility evaluation for 5G small cell networks based on individual mobility model," *IEEE Journal on Selected Areas in Communications*, vol. 34, no. 3, pp. 528–541, 2016.

[46] John A Silvester and Leonard Kleinrock, "On the capacity of multihop slotted ALOHA networks with regular structure," *IEEE Transactions on Communications*, vol. 31, no. 8, pp. 974–982, 1983.

[47] Rudolf Mathar and Jürgen Mattfeldt, "On the distribution of cumulated interference power in Rayleigh fading channels," *Wireless Networks*, vol. 1, no. 1, pp. 31–36, 1995.

[48] Vivek P Mhatre and Catherine P Rosenberg, "Impact of network load on forward link inter-cell interference in cellular data networks," *Wireless Communications, IEEE Transactions on*, vol. 5, no. 12, pp. 3651–3661, 2006.

[49] F Garcia, I Stojmenovic, and J Zhang, "Addressing and routing in hexagonal networks with applications in location update and connection rerouting in mobile phone networks," *IEEE Trans. Parallel and Distributed Systems*, vol. 13, no. 9, pp. 963–971, 2002.

[50] Peter Friess, *Internet of Things-Global Technological and Societal Trends From Smart Environments and Spaces to Green ICT*, River Publishers, 2011.

[51] Jayavardhana Gubbi, Rajkumar Buyya, Slaven Marusic, and Marimuthu Palaniswami, "Internet of things (IoT): A vision, architectural elements, and future directions," *Future generation computer systems*, vol. 29, no. 7, pp. 1645–1660, 2013.

[52] Sergey Andreev, Olga Galinina, Alexander Pyattaev, Mikhail Gerasimenko, Tuomas Tirronen, Johan Torsner, Joachim Sachs, Mischa Dohler, and Yevgeni Koucheryavy, "Understanding the IoT connectivity landscape: a contemporary M2M radio technology roadmap," *IEEE Communications Magazine*, vol. 53, no. 9, pp. 32–40, 2015.

[53] Afif Osseiran, Federico Boccardi, Volker Braun, Katsutoshi Kusume, Patrick Marsch, Michal Maternia, Olav Queseth, Malte Schellmann, Hans Schotten, Hidekazu Taoka, et al., "Scenarios for 5G mobile and wireless communications: the vision of the METIS project," *IEEE Communications Magazine*, vol. 52, no. 5, pp. 26–35, 2014.

[54] Jeffrey G Andrews, François Baccelli, and Radha Krishna Ganti, "A tractable approach to coverage and rate in cellular networks," *IEEE Transactions on Communications*, vol. 59, no. 11, pp. 3122–3134, 2011.

[55] Adrian Baddeley, Imre Bárány, and Rolf Schneider, "Spatial point processes and their applications," *Stochastic Geometry: Lectures given at the CIME Summer School held in Martina Franca, Italy, September 13–18, 2004*, pp. 1–75, 2007.

[56] Martin Haenggi, Jeffrey G Andrews, François Baccelli, Olivier Dousse, and Massimo Franceschetti, "Stochastic geometry and random graphs for the analysis and design of wireless networks," *IEEE Journal on Selected Areas in Communications*, vol. 27, no. 7, pp. 1029–1046, 2009.

[57] Paulo Cardieri, "Modeling interference in wireless ad hoc networks," *Communications Surveys & Tutorials, IEEE*, vol. 12, no. 4, pp. 551–572, 2010.

[58] François Baccelli, Maurice Klein, Marc Lebourges, and Sergei Zuyev, "Stochastic geometry and architecture of communication networks," *Telecommunication Systems*, vol. 7, no. 1-3, pp. 209–227, 1997.

[59] François Baccelli and Serguei Zuyev, "Stochastic geometry models of mobile communication networks," 1996.

[60] Martin Haenggi and Radha Krishna Ganti, *Interference in large wireless networks*, Now Publishers Inc, 2009.

[61] Martin Haenggi, *Stochastic geometry for wireless networks*, Cambridge University Press, 2012.

[62] Theodore S Rappaport et al., *Wireless communications: principles and practice*, vol. 2, prentice hall PTR New Jersey, 1996.

[63] Hesham ElSawy, Ekram Hossain, and Martin Haenggi, "Stochastic geometry for modeling, analysis, and design of multi-tier and cognitive cellular wireless networks: A survey," *IEEE Communications Surveys & Tutorials*, vol. 15, no. 3, pp. 996–1019, 2013.

[64] Chia-han Lee and Martin Haenggi, "Interference and outage in poisson cognitive networks," *Wireless Communications, IEEE Transactions on*, vol. 11, no. 4, pp. 1392–1401, 2012.

[65] Naga Bhushan, Junyi Li, Durga Malladi, Rob Gilmore, Dean Brenner, Aleksandar Damnjanovic, Ravi Sukhavasi, Chirag Patel, and Stefan Geirhofer, "Network densification: the dominant theme for wireless evolution into 5G," *Communications Magazine, IEEE*, vol. 52, no. 2, pp. 82–89, 2014.

[66] Hazem Ibrahim, Hesham Elsawy, Uyen T Nguyen, and Mohamed-Slim Alouini, "Modeling virtualized downlink cellular networks with ultra-dense small cells," in *IEEE International Conference on Communications (ICC)*. IEEE, 2015, pp. 5360–5366.

[67] Jagadish Venkataraman, Martin Haenggi, and Oliver Collins, "Shot noise models for the dual problems of cooperative coverage and outage in random networks," in *44st Annual Allerton Conference on Communication, Control, and Computing*, 2006.

[68] Elvino S Sousa, John Silvester, et al., "Optimum transmission ranges in a direct-sequence spread-spectrum multihop packet radio network," *Selected Areas in Communications, IEEE Journal on*, vol. 8, no. 5, pp. 762–771, 1990.

[69] Steven P Weber, Xiangying Yang, Jeffrey G Andrews, and Gustavo De Veciana, "Transmission capacity of wireless ad hoc networks with outage constraints," *Information Theory, IEEE Transactions on*, vol. 51, no. 12, pp. 4091–4102, 2005.

[70] Ting-Chao Hou and Victor OK Li, "Transmission range control in multihop packet radio networks," *Communications, IEEE Transactions on*, vol. 34, no. 1, pp. 38–44, 1986.

[71] A. Guo and M. Haenggi, "Spatial stochastic models and metrics for the structure of base stations in cellular networks," *IEEE Transactions on Wireless Communications*, vol. 12, no. 11, pp. 5800–5812, 2013.

[72] B. Blaszczyszyn, M.K. Karray, and H.P. Keeler, "Using Poisson processes to model lattice cellular networks," in *Proc.32th Annual IEEE International Conference on Computer Communications (INFOCOM'13)*, Turin, Italy, April 2013, pp. 773–781.

[73] Marco Di Renzo, Alessandro Guidotti, and Giovanni Emanuale Corazza, "Average rate of downlink heterogeneous cellular networks over generalized fading channels: a stochastic geometry approach," *Communications, IEEE Transactions on*, vol. 61, no. 7, pp. 3050–3071, 2013.

[74] Sayandev Mukherjee, "Distribution of downlink sinr in heterogeneous cellular networks," *IEEE Journal on Selected Areas in Communications*, vol. 30, no. 3, pp. 575–585, 2012.

[75] Harpreet S Dhillon, Radha Krishna Ganti, François Baccelli, and Jeffrey G Andrews, "Modeling and analysis of k-tier downlink heterogeneous cellular networks," *IEEE Journal on Selected Areas in Communications*, vol. 30, no. 3, pp. 550–560, April 2012.

[76] Harpreet S Dhillon, Radha Krishna Ganti, and Jeffrey G Andrews, "Load-aware modeling and analysis of heterogeneous cellular networks," *Wireless Communications, IEEE Transactions on*, vol. 12, no. 4, pp. 1666–1677, 2013.

[77] Thomas D Novlan, Harpreet S Dhillon, and Jeffrey G Andrews, "Analytical modeling of uplink cellular networks," *IEEE Transactions on Wireless Communications*, vol. 12, no. 6, pp. 2669–2679, 2013.

[78] Steven Weber, Jeffrey G Andrews, and Nihar Jindal, "The effect of fading, channel inversion, and threshold scheduling on ad hoc networks," *Information Theory, IEEE Transactions on*, vol. 53, no. 11, pp. 4127–4149, 2007.

[79] Steven P Weber, Jeffrey G Andrews, Xiangying Yang, and Gustavo De Veciana, "Transmission capacity of wireless ad hoc networks with successive interference cancellation," *IEEE Transactions on Information Theory*, vol. 53, no. 8, pp. 2799–2814, 2007.

[80] Zih-Siang Syu and Chia-Han Lee, "Spatial constraints of Device-to-Device communications," in *First International Black Sea Conference on Communications and Networking (BlackSeaCom)*, 2013, pp. 94–98.

[81] Xingqin Lin, Jeffrey G Andrews, and Amitava Ghosh, "Spectrum sharing for Device-to-Device communication in cellular networks," *arXiv preprint arXiv:1305.4219*, 2013.

[82] Nihar Jindal, Steven Weber, and Jeffrey G Andrews, "Fractional power control for decentralized wireless networks," *IEEE Transactions on Wireless Communications*, vol. 7, no. 12, pp. 5482–5492, 2008.

[83] Sunil Srinivasa and Martin Haenggi, "Modeling interference in finite uniformly random networks," in *International Workshop on Information Theory for Sensor Networks (WITS'07)*, 2007, pp. 1–12.

[84] Sunil Srinivasa and Martin Haenggi, "Distance distributions in finite uniformly random networks: Theory and applications," *IEEE Transactions on Vehicular Technology*, vol. 59, no. 2, pp. 940–949, 2010.

[85] Radha Krishna Ganti and Martin Haenggi, "Interference and outage in clustered wireless ad hoc networks," *IEEE Transactions on Information Theory*, vol. 55, no. 9, pp. 4067–4086, 2009.

[86] Martin Haenggi, "Mean interference in hard-core wireless networks," *IEEE Communications Letters*, vol. 15, no. 8, pp. 792–794, 2011.

[87] Jesper Møller, Mark L Huber, and Robert L Wolpert, "Perfect simulation and moment properties for the matérn type iii process," *Stochastic Processes and their Applications*, vol. 120, no. 11, pp. 2142–2158, 2010.

[88] Huu Quynh Nguyen, François Baccelli, and Daniel Kofman, "A stochastic geometry analysis of dense ieee 802.11 networks," in *INFOCOM 2007. 26th IEEE International Conference on Computer Communications. IEEE.* IEEE, 2007, pp. 1199–1207.

[89] François Baccelli and Bartlomiej Blaszczyszyn, *Stochastic geometry and wireless networks: Theory*, vol. 1, Now Publishers Inc, 2009.

[90] Mark L Huber and Robert L Wolpert, "Likelihood-based inference for matérn type-iii repulsive point processes," *Advances in Applied Probability*, pp. 958–977, 2009.

[91] Bertil Matérn, *Spatial variation*, vol. 36, Springer Science & Business Media, 2013.

[92] Jeemin Kim, Hyun-Kwan Lee, Dong Min Kim, and Seong-Lyun Kim, "Delay performance of two-stage access in cellular Internet-of-Things networks," *IEEE Transactions on Vehicular Technology*, vol. 67, no. 4, pp. 3521–3533, 2018.

[93] Guang Yang, Martin Haenggi, and Ming Xiao, "Traffic allocation for low-latency multi-hop networks with buffers," *IEEE Transactions on Communications*, vol. 66, no. 9, pp. 3999–4013, 2018.

[94] Vikram Chandrasekhar and Jeffrey G Andrews, "Spectrum allocation in tiered cellular networks," *IEEE Transactions on Communications*, vol. 57, no. 10, 2009.

[95] Harpreet S Dhillon, Howard Huang, and Harish Viswanathan, "Wide-area wireless communication challenges for the internet of things," *arXiv preprint arXiv:1504.03242*, 2015.

[96] Shahid Mumtaz, Ahmed Alsohaily, Zhibo Pang, Ammar Rayes, Kim Fung Tsang, and Jonathan Rodriguez, "Massive Internet of Things for industrial applications: Addressing wireless IIoT connectivity challenges and ecosystem fragmentation," *IEEE Industrial Electronics Magazine*, vol. 11, no. 1, pp. 28–33, 2017.

[97] Jeffrey G Andrews, Stefano Buzzi, Wan Choi, Stephen V Hanly, Angel Lozano, Anthony CK Soong, and Jianzhong Charlie Zhang, "What will 5G be?," *IEEE Journal on Selected Areas in Communications*, vol. 32, no. 6, pp. 1065–1082, 2014.

[98] Federico Boccardi, Robert W Heath, Angel Lozano, Thomas L Marzetta, and Petar Popovski, "Five disruptive technology directions for 5g," *IEEE Communications Magazine*, vol. 52, no. 2, pp. 74–80, 2014.

[99] "Cisco visual networking index: Global mobile data traffic forecast update, 2014–2019," *White Paper, Cisco*, 2015.

[100] Konstantinos Ntontin, Marco Di Renzo, and Christos Verikoukis, "On the feasibility of full-duplex relaying in multiple-antenna cellular networks," *IEEE Transactions on Communications*, vol. 65, no. 5, pp. 2234–2249, 2017.

[101] Hazem Ibrahim, Hesham ElSawy, Uyen Trang Nguyen, and Mohamed-Slim Alouini, "Mobility-aware modeling and analysis of dense cellular networks with C-plane/U-plane split architecture," *IEEE Transactions on Communications*, vol. 64, no. 11, pp. 4879 – 4894, 2016.

[102] Praful D Mankar, Goutam Das, and Sant Sharan Pathak, "Load-aware performance analysis of cell center/edge users in random HetNets," *IEEE Transactions on Vehicular Technology*, vol. 67, no. 3, pp. 2476–2490, 2018.

[103] Wen Sun and Jiajia Liu, "Coordinated multipoint-based uplink transmission in internet of things powered by energy harvesting," *IEEE Internet of Things Journal*, vol. 5, no. 4, pp. 2585–2595, 2018.

[104] Yun Li, Jie Liu, Bin Cao, and Chonggang Wang, "Joint optimization of radio and virtual machine resources with uncertain user demands in mobile cloud computing," *IEEE Transactions on Multimedia*, 2018.

[105] Kan Zheng, Fanglong Hu, Wenbo Wang, Wei Xiang, and Mischa Dohler, "Radio resource allocation in LTE-advanced cellular networks with M2M communications," *IEEE communications Magazine*, vol. 50, no. 7, 2012.

[106] Tabinda Salam, Waheed Ur Rehman, and Xiaofeng Tao, "Cooperative data aggregation and dynamic resource allocation for massive machine type communication," *IEEE Access*, 2018.

[107] Yue Li and Lin Cai, "Cooperative device-to-device communication for uplink transmission in cellular system," *IEEE Transactions on Wireless Communications*, vol. 17, no. 6, pp. 4510–4524, 2018.

[108] Zaher Dawy, Walid Saad, Arunabha Ghosh, Jeffrey G Andrews, and Elias Yaacoub, "Toward massive machine type cellular communications," *IEEE Wireless Communications*, vol. 24, no. 1, pp. 120–128, 2017.

[109] Qiaoyang Ye, Beiyu Rong, Yudong Chen, Mazin Al-Shalash, Constantine Caramanis, and Jeffrey G Andrews, "User association for load balancing in heterogeneous cellular networks," *IEEE Transactions on Wireless Communications*, vol. 12, no. 6, pp. 2706–2716, 2013.

[110] Sarabjot Singh, Harpreet S Dhillon, and Jeffrey G Andrews, "Offloading in heterogeneous networks: Modeling, analysis, and design insights," *IEEE Transactions on Wireless Communications*, vol. 12, no. 5, pp. 2484–2497, 2013.

[111] Nuno K Pratas and Petar Popovski, "Zero-outage cellular downlink with fixed-rate d2d underlay," *IEEE Transactions on Wireless Communications*, vol. 14, no. 7, pp. 3533–3543, 2015.

[112] Amin Azari, "Energy-efficient scheduling and grouping for machine-type communications over cellular networks," *Ad Hoc Networks*, vol. 43, pp. 16–29, 2016.

[113] Wei Bao and Ben Liang, "Rate maximization through structured spectrum allocation and user association in heterogeneous cellular networks," *IEEE Transactions on Communications*, vol. 63, no. 11, pp. 4510–4524, 2015.

[114] Yicheng Lin, Wei Bao, Wei Yu, and Ben Liang, "Optimizing user association and spectrum allocation in HetNets: A utility perspective," *IEEE Journal on Selected Areas in Communications*, vol. 33, no. 6, pp. 1025–1039, 2015.

[115] Ingram Olkin and Albert W Marshall, *Inequalities: theory of majorization and its applications*, vol. 143, Academic press, 2016.

[116] Stephen Boyd and Lieven Vandenberghe, *Convex optimization*, Cambridge university press, 2004.

[117] Hyoungju Ji, Sunho Park, Jeongho Yeo, Younsun Kim, Juho Lee, and Byonghyo Shim, "Ultra-reliable and low-latency communications in 5G downlink: Physical layer aspects," *IEEE Wireless Communications*, vol. 25, no. 3, pp. 124–130, 2018.

[118] Jeffrey G Andrews, Stefano Buzzi, Wan Choi, Stephen V Hanly, Angel Lozano, Anthony CK Soong, and Jianzhong Charlie Zhang, "What will 5G be?," *IEEE Journal on selected areas in communications*, vol. 32, no. 6, pp. 1065–1082, 2014.

[119] Martin Haenggi, "The meta distribution of the SIR in Poisson bipolar and cellular networks," *IEEE Transactions on Wireless Communications*, vol. 15, no. 4, pp. 2577–2589, 2016.

[120] Mehdi Bennis, Mérouane Debbah, and H Vincent Poor, "Ultrareliable and low-latency wireless communication: Tail, risk, and scale," *Proceedings of the IEEE*, vol. 106, no. 10, pp. 1834–1853, 2018.

[121] Sanket S Kalamkar and Martin Haenggi, "Per-link reliability and rate control: Two facets of the SIR meta distribution," *IEEE Wireless Communications Letters*, 2019.

[122] Mohammad Salehi, Abbas Mohammadi, and Martin Haenggi, "Analysis of D2D underlaid cellular networks: SIR meta distribution and mean local delay," *IEEE Transactions on Communications*, vol. 65, no. 7, pp. 2904–2916, 2017.

[123] Mohammad Salehi, Hina Tabassum, and Ekram Hossain, "Meta distribution of the SIR in large-scale uplink and downlink NOMA networks," *arXiv preprint arXiv:1804.02710*, 2018.

[124] Na Deng and Martin Haenggi, "The energy and rate meta distributions in wirelessly powered D2D networks," *IEEE Journal on Selected Areas in Communications*, vol. 37, no. 2, pp. 269–282, 2019.

[125] Amitava Ghosh, Timothy A Thomas, Mark C Cudak, Rapeepat Ratasuk, Prakash Moorut, Frederick W Vook, Theodore S Rappaport, George R MacCartney, Shu Sun, and Shuai Nie, "Millimeter-wave enhanced local area systems: A high-data-rate approach for future wireless networks," *IEEE Journal on Selected Areas in Communications*, vol. 32, no. 6, pp. 1152–1163, 2014.

[126] Jeffrey G Andrews, Tianyang Bai, Mandar N Kulkarni, Ahmed Alkhateeb, Abhishek K Gupta, and Robert W Heath, "Modeling and analyzing millimeter wave cellular systems," *IEEE Transactions on Communications*, vol. 65, no. 1, pp. 403–430, 2017.

[127] Hazem Ibrahim, Wei Bao, and Uyen T Nguyen, "Data rate utility analysis for uplink two-hop internet-of-things networks," *IEEE Internet of Things Journal*, 2018.

[128] George R MacCartney, Junhong Zhang, Shuai Nie, and Theodore S Rappaport, "Path loss models for 5G millimeter wave propagation channels in urban microcells.," in *Globecom*, 2013, pp. 3948–3953.

[129] Talha Ahmed Khan, Ahmed Alkhateeb, and Robert W Heath, "Millimeter wave energy harvesting," *IEEE Transactions on Wireless Communications*, vol. 15, no. 9, pp. 6048–6062, 2016.

[130] Wenqiang Yi, Yuanwei Liu, and Arumugam Nallanathan, "Modeling and analysis of D2D millimeter-wave networks with poisson cluster processes," *IEEE Transactions on Communications*, vol. 65, no. 12, pp. 5574–5588, 2017.

[131] Minoru Nakagami, "The m-distribution—A general formula of intensity distribution of rapid fading," in *Statistical methods in radio wave propagation*, pp. 3–36. Elsevier, 1960.

[132] Marvin K Simon and Mohamed-Slim Alouini, *Digital communication over fading channels*, vol. 95, John Wiley & Sons, 2005.

[133] Kiran Venugopal, Matthew C Valenti, and Robert W Heath, "Device-to-device millimeter wave communications: Interference, coverage, rate, and finite topologies," *IEEE Transactions on Wireless Communications*, vol. 15, no. 9, pp. 6175–6188, 2016.

[134] Tianyang Bai, Rahul Vaze, and Robert W Heath, "Analysis of blockage effects on urban cellular networks," *IEEE Transactions on Wireless Communications*, vol. 13, no. 9, pp. 5070–5083, 2014.

[135] J Gil-Pelaez, "Note on the inversion theorem," *Biometrika*, vol. 38, no. 3-4, pp. 481–482, 1951.

[136] Radha Krishna Ganti and Martin Haenggi, "Asymptotics and approximation of the SIR distribution in general cellular networks," *IEEE Transactions on Wireless Communications*, vol. 15, no. 3, pp. 2130–2143, 2016.

[137] Yuanjie Wang, Martin Haenggi, and Zhenhui Tan, "The meta distribution of the SIR for cellular networks with power control," *IEEE Transactions on Communications*, vol. 66, no. 4, pp. 1745–1757, 2018.

[138] MJ Kronenburg, "The binomial coefficient for negative arguments," *arXiv preprint arXiv:1105.3689*, 2011.

[139] Yuanjie Wang, Martin Haenggi, and Zhenhui Tan, "Sir meta distribution of k-tier downlink heterogeneous cellular networks with cell range expansion," *IEEE Transactions on Communications*, 2018.

[140] Woon Hau Chin, Zhong Fan, and Russell Haines, "Emerging technologies and research challenges for 5G wireless networks," *IEEE Wireless Communications*, vol. 21, no. 2, pp. 106–112, 2014.

[141] Hiroyuki Ishii, Yoshihisa Kishiyama, and Hideaki Takahashi, "A novel architecture for LTE-B: C-plane/U-plane split and Phantom Cell concept," in *IEEE Globecom Workshops*, Anaheim, CA, USA, December 2012, pp. 624–630.

[142] Christian Hoymann, Daniel Larsson, Havish Koorapaty, and Jung-Fu Cheng, "A lean carrier for LTE," *IEEE Communications Magazine*, vol. 51, no. 2, pp. 74–80, 2013.

[143] Peter F Ash and Ethan D Bolker, "Generalized Dirichlet tessellations," *Geometriae Dedicata*, vol. 20, no. 2, pp. 209–243, 1986.

[144] Toktam Mahmoodi and Srini Seetharaman, "On using a SDN-based control plane in 5G mobile networks," *Wireless World Research Forum*, vol. 32.

[145] R. K. Ganti and M. Haenggi, "Spatial and Temporal Correlation of the Interference in ALOHA Ad Hoc Networks," *IEEE Communications Letters*, vol. 13, no. 9, pp. 631–633, Sept. 2009.

[146] Duckdong Hwang, Dong In Kim, and Tae-Jin Lee, "Throughput maximization for multiuser MIMO wireless powered communication networks," *IEEE Transactions on Vehicular Technology*, vol. 65, no. 7, pp. 5743–5748, 2015.

[147] Theodore S Rappaport, Shu Sun, Rimma Mayzus, Hang Zhao, Yaniv Azar, Kevin Wang, George N Wong, Jocelyn K Schulz, Mathew Samimi, and Felix Gutierrez, "Millimeter wave mobile communications for 5g cellular: It will work!," *IEEE access*, vol. 1, pp. 335–349, 2013.

[148] Seyed Mohammad Azimi-Abarghouyi, Behrooz Makki, Martin Haenggi, Masoumeh Nasiri-Kenari, and Tommy Svensson, "Stochastic geometry modeling and analysis of single-and multi-cluster wireless networks," *IEEE Transactions on Communications*, vol. 66, no. 10, pp. 4981–4996, 2018.

[149] Jeffrey G Andrews, Abhishek K Gupta, and Harpreet S Dhillon, "A primer on cellular network analysis using stochastic geometry," *arXiv preprint arXiv:1604.03183*, 2016.

[150] Horst Alzer, "On some inequalities for the incomplete gamma function," *Mathematics of Computation of the American Mathematical Society*, vol. 66, no. 218, pp. 771–778, 1997.